UTS UNIVERSITY OF TECHNOLOGY SYDNEY

Targeting cancer cell-derived small extracellular vesicles (sEVs) to develop nanoparticle-integrated detection systems

by Pritam Bordhan

Thesis submitted in fulfilment of the requirements for the degree of

Doctor of Philosophy

under the supervision of Prof. Dayong Jin and Prof. Majid Warkiani

University of Technology Sydney
Faculty of Science, School of Mathematical and Physical Sciences, Institute for Biomedical Materials and Devices.

29/05/2024

CERTIFICATE OF ORIGINAL AUTHORSHIP

I, *Pritam Bordhan*, declare that this thesis is submitted in fulfilment of the requirements for the award of *Doctor of Philosophy (Science)*, in the *School of Mathematics and Physical Science, Faculty of Science* at the University of Technology Sydney.

This thesis is wholly my own work unless otherwise referenced or acknowledged. In addition, I certify that all information sources and literature used are indicated in the thesis.

This document has not been submitted for qualifications at any other academic institution.

This research is supported by the Australian Government Research Training Program.

Signature: Production Note:
Signature removed prior to publication.

Date: 29/05/2024

ACKNOWLEDGEMENT

I want to express my profound gratitude to the exceptional individuals who have been instrumental in shaping my PhD journey. First and foremost, I extend my deepest thanks to Prof. Dayong Jin, my principal supervisor, whose unwavering support and belief in my potential granted me the privilege to contribute to his esteemed research group. Prof. Majid Warkiani deserves special recognition for his invaluable mentorship and guidance, which have significantly influenced the trajectory of my research endeavours.

A heartfelt acknowledgment goes to the dedicated colleagues who have enriched my PhD experience. Dr. Shihui Wen and Dr. Libing Fu stand out for their continuous support, offering valuable guidance and hands-on assistance throughout the intricate UCNP-LFA studies. My gratitude extends further to Dr Mahnaz Maddahffar, Dr Jiayan Liao, and Dr Tesfaye Asrat, whose expertise and collaboration greatly contributed to the success of the UCNP synthesis and surface modification processes. Special thanks are extended to Dr. Sareh Zhand for her invaluable direction, guidance and assistance in navigating the complex sEV isolation and characterisation processes. This collective effort and guidance from these remarkable individuals have been indispensable, fostering an environment of collaboration and knowledge exchange that has significantly propelled the progress of my research.

Finally, I sincerely appreciate the International Research Scholarship, the IDEAL HUB scholarship, and the HDR Seed Funding Award for their generous financial support throughout my PhD tenure. Their contributions eased the financial burden and played a pivotal role in my research journey. I sincerely apologise if I have forgotten to acknowledge anyone.

In conclusion, my gratitude extends to all those who have been a part of my academic odyssey and contributed in various capacities. The collaborative spirit and support I have received have been instrumental in shaping my research and academic pursuits.

Impact of COVID-19 and illness during PhD study

My candidature for the PhD program commenced in August 2020, and unfortunately, the progression of my research was markedly impacted by the onset of the COVID-19 pandemic. The ensuing restrictions on access to laboratory facilities, campus lockdowns, and persistent funding complexities causing delays in obtaining necessary experimental materials presented considerable challenges. Adding to the complications, in February 2022, I faced a severe health setback due to acute pancreatitis and diabetic ketoacidosis, leading to my hospitalisation and admission to the ICU (St. Vincent's Hospital, Sydney) on 09.02.2022. I was subsequently released on 22.02.2022, but the aftermath of my health ordeal required an extended period of rest and recovery, during which I was physically weakened and reliant on assistance for daily tasks. It was not until early May 2022 that I could resume my PhD studies, losing nearly three critical months of my PhD candidature. Furthermore, following this illness, I was diagnosed with diabetes, necessitating long-term medication that will persist throughout my life, thereby exerting enduring effects on my daily activities. The compounding influence of this health setback, coupled with the constraints imposed by the pandemic and ongoing funding challenges, has substantially hindered the trajectory of my research endeavours throughout the course of my PhD tenure. Despite my resilient efforts, these multifaceted challenges have posed formidable obstacles, impeding the smooth advancement of my research and hindering the realization of its full potential.

List of Publications, Awards and Conferences

Publications

1. P. Bordhan, S. Razavi Bazaz, D. Jin and M. E. Warkiani. "Advances and enabling technologies for phase-specific cell cycle synchronisation" Lab on a chip. DOI: 10.1039/D1LC00724F

2. V.Y. Naei, P. Bordhan, F. Mirakhorli, M. Khorrami, J. Shrestha, H. Nazari, A. Kulasinghe, M.E. Warkiani, "Advances in novel strategies for isolation, characterization and analysis of CTCs and ctDNA", Therapeutic Advances in Medical Oncology, DOI:10.1177/17588359231192401

3. S. Zhand, K. Xiao, S. Razavi Bazaz, Y. Zhu, P. Bordhan, D. Jin and M. E. Warkiani. "Improving capture efficiency of human cancer cell derived exosomes with nanostructured metal organic framework functionalized beads." Applied Materials Today 23: 100994. DOI: https://doi.org/10.1016/j.apmt.2021.100994.

4. P. Bordhan, S. Zhand, L. Fu, Y.Y. Cheng, D. Jin, M.E. Warkiani, S. Wen, “Up-conversion Nanoparticle-Integrated Lateral Flow Assay for Detecting Small Extracellular Vesicles (sEV) PD-L1.” (in preparation)

Conferences

Pritam Bordhan. Ultrasensitive lateral flow assay using up-conversion nanoparticles for the detection of PD-L1 in sEVs (Presentation). Institute for Biomedical Materials and Device (IBMD) Research Week, 2-10 June, 2023. University of Technology Sydney, Australia

Pritam Bordhan. Ultrasensitive lateral flow assay using up-conversion nanoparticles for the detection of PD-L1 in sEVs (Oral Presentation) Australia and New Zealand Society for

Extracellular Vesicles Conference (ANZSEV) 2023, 7th - 10th November 2023, Barossa Valley, Adelaide, South Australia

Awards

1. UTS Science PhD Scholarship Top-up Awards.
2. UTS Science HDR Seed Funding scheme, 2023, Research Session 1

Table of Contents

Impact of COVID-19 and illness during PhD study 3

List of Publications, Awards and Conferences 4

Publications 4

Conferences 4

Awards 5

ABBREVIATIONS 9

Thesis Abstract 13

1. Literature Review 15

1.1. Liquid Biopsy in Cancer Diagnosis 15

1.1.1. Circulating Tumour Cells (CTCs 17

1.1.2. Circulating Tumour DNA (ctDNA) 18

1.1.3. Extracellular Vesicles (EVs) 19

1.2. Significance of sEVs in Liquid Biopsy 20

1.3. Isolation and Characterisation of sEVs 25

1.4. Limitations in sEV Analysis 26

1.5. Nanoparticle integrated biosensors 28

Advantages of using nanoparticles in biosensors 28

Magnetic Nanoparticles (MNPs) 31

Carbon Nanostructures 31

Gold Nanoparticles (AuNPs) 31

Quantum Dots (QDs) 32

Luminescent Nanoparticles: 32

Up-conversion Nanoparticles (UCNPs) 35

1.6. Nanoparticle-based and Integrated sEV-detecting sensors 35

Challenges of NP-based biosensors towards sEV detection 36

1.6.1. Fluorescence-based Detection 38

1.6.2. Colorimetric Based Detection 42

1.6.3. Electrochemical-based Detection 45

1.6.4. Surface-Enhanced Raman Scattering (SERS) based detection 49

1.6.5. Surface Plasmon Resonance (SPR) Detection 53

1.6.6. Single EV analysis 54

1.6.7. Lateral Flow Immunoassays for sEV detection 57

1.7. UCNPs in bio-sensing applications 66

1.7.1. UCNP Mechanism and Synthesis 68

1.7.2. Surface Modification of UCNPs 73

Ligand exchange 73
Ligand oxidation 73
Ligand removal 74
Lipid encapsulation 74
Polymer/Silica Encapsulation 74
1.7.3. UCNP Application in sEV detection/analysis 75
1.8. Aim, Hypothesis and Expmerimental Results Chapters Outline 80
2. Methodology 81
2.1. Cell Culture and conditioned medium 81
2.2. Isolation of extracellular vesicles by ultracentrifugation 81
2.3. Nanoparticle tracking analysis 82
2.4. Western Blotting 83
2.5. Transmission electron microscopy (TEM) 83
2.6. Synthesis of upconversion nanoparticles 84
2.7. Surface modification of UCNPs 85
2.8. Bioconjugation of UCNPs with antibody using conjugation kit 86
2.9. Bioconjugation of gold nanoparticles (AuNPs) with antibodies using conjugation optimisation kit 87
2.10. Lateral Flow Strip Design 88
2.11. Operational procedure of the UCNP Lateral Flow Assay 89
2.12. Operational Procedure of the AuNP ELISA and UCNP-based Microplate Immunoassays 90
2.13. Enzyme-Linked Immunosorbent Assay (ELISA) for detection of CD63, PD-L1, GPC-1 and PSA on the surface of sEVs 91
2.14. Data and Statistical Analysis 91
3. Design and Characterisation of Nanoparticles 93
Abstract 93
3.1. Introduction 94
3.2. Results and Discussion 97
3.2.1. Structural and Functional characterisation of AuNPs and AuNP-HRP conjugates 97
3.2.2. Synthesis, Surface Modification and Characterisation of UCNPs 102
3.3. Conclusion 108
4. Developing nanoparticle-integrated ELISA formats for sensitive detection of sEV surface markers with potential POC applications 110
Abstract 110
4.1. Introduction 111
4.2. Experimental Results 116

4.2.1. Cell Culture and Isolation of sEVs 116
4.2.2. Optimisation of the sandwich ELISA components 117
4.2.3. AuNP enhanced colorimetric sandwich ELISA 123
4.2.4. UCNP-based microplate Sandwich Immunoassay 128
4.3. Discussion and Conclusion 133
5. Up-conversion Nanoparticle-Integrated Lateral Flow Assay for Detecting Small Extracellular Vesicles (sEV) PD-L1 137
Abstract 137
5.1. Introduction 137
5.2. Experimental Results 140
5.2.1. sEV characterisation 140
5.2.2. Detection of CD63 and PD-L1 proteins using UCNP-LFA 142
5.2.3. Detection of CD63 and PD-L1 biomarkers on the surface of sEVs 147
5.3. Discussion and Conclusion 153
6. Detecting Small Extracellular Vesicles (sEV) GPC-1 using a quantitative, up-conversion nanoparticle-based quantitative lateral flow assay (UCNP-LFA) technology 156
Abstract 156
6.1. Introduction 156
6.2. Experimental Results 158
6.2.1. Characterisation of isolated sEVs 158
6.2.2. Detection of GPC-1, PD-L1 and PSA in sEVs using commercial ELISA kits 160
6.2.3. UCNP-LFA-based detection of GPC-1 and PD-L1 antigens 162
6.2.4. Detection of sEV-GPC-1 and sEV-PD-L1 using the UCNP-LFA 165
6.3. Discussion and Conclusion 168
7. Conclusion, Perspectives and Future Directions 171
7.1. Thesis Summary 171
7.2. Technical Limitations 176
7.3. Perspectives and Future Research Directions 178
7.4. Conclusion 184
8. Appendix 185
9. References 186

ABBREVIATIONS

ALP: Alkaline Phosphatase

Au: Gold

Au-NPFe_2O_3NCs: Gold-loaded Ferric Oxide Nanocubes

AuNPs: Gold nanoparticles

BCA: Bicinchoninic Acid Protein Assay

BSA: Bovine Serum Assay

CEA: Carcinoembryonic Antigen

cfDNA: Circulating free DNA

CMOS: Complementary Metal Oxide Semiconductor

CNTs: Carbon Nanotubes

CRISPR: Clustered Regularly Interspaced Short Palindromic Repeats

CTCPA: 4-((((2-carboxyethyl) thio) carbonothioyl) thio)-4-cyanopentanoic acid

CTCs: Circulating Tumour Cells

ctDNA: circulating tumour DNA

CuNPs: Copper Nanoparticles

CuO: Copper Oxide

CV: Coefficient of Variation

DAB: Diaminobenzidine

ddPCR: Droplet Digital PCR

DLS: Dynamic Light Scattering

DMF: Dimethyl Formamide

DNA: Deoxyribonucleic acid

dPCR: Digital PCR

ECM: Extracellular Matrix

EGFR: Epidermal Growth Factor Receptor

ELISA: Enzyme-Linked Immuno-Sorbent Assay

EMT: Epithelial Mesenchymal Transition

EpCAM: Epithelial Cell Adhesion Molecule

EphA2: Ephrin Type-A Receptor 2

ESA: Excited State Absorption

ESCRT: Endosomal Sorting Complex for Transport

ETU: Energy Transfer Up-conversion

EVs: Extracellular Vesicles

FACS: Fluorescence Activated Cell Sorting

FBS: Fetal Bovine Serum

FDA: United States Food and Drug Administration

FN-NS: Fluorescent Nanospheres

FRET: Fluorescence Resonance Energy Transfer

FTIR: Fourier Transform Infrared Spectroscopy

GPC-1: Glypican 1

HCC: Hepatocellular Carcinoma

HCR: Hybridisation Chain Reaction

HER2: Human Epidermal Growth Factor Receptor 2

HRP: Horseradish Peroxidase

HSP: Heat Shock Protein

HSPGs: Heparan Sulfate Proteoglycans

ICP-MS: Inductively Coupled Plasma Mass Spectrometry

LCM: Laser Capture Microdissection

LDA: Linear Discriminant Analysis

LED: Light Emitting Diode

LFA: Lateral Flow Assay

lncRNA: Long Non-Coding RNA

LOD: Limit of Detection

LSPR: Localised Surface Plasmon Resonance

MAA: Methyl methacrylic acid

MBs: Magnetic Beads

MIO: Macro-porous Inverse Opal

miRNA: Micro RNA

MMPs: Matrix Metalloproteases

MNPs: Magnetic Nanoparticles

MOEP: 2-(methacryloyloxy) ethyl phosphate

MOF: Metal-Organic Framework

mRNA: Messenger RNA

MW: Molecular Weight

NALFA: Nucleic Acid LFA

NC membrane: Nitrocellulose Membrane

NIR light: Near Infrared light

NN: Neural Network

NPs: Nanoparticles

NRs: Nanorods

NSCLC: Non-Small Cell Lung Cancer

NTA: Nanoparticle Tracking Analysis

NTH: Nano-Tetrahedron

OA: Oleic Acid

ODE: 1-Octadecene

OEGMA: Oligo Ethylene Glycol Methyl Methacrylate

PAA: Polyacrylic Acid

PADs: Paper-based Analytical Devices

PBS: Phosphate Buffered Saline

PCA: Principal Component Analysis

PCa: Prostate Cancer

PCR: Polymerase Chain Reaction

PDAC: Pancreatic Ductal Adenocarcinoma

PD-L1: Programmed Cell Death Ligand 1

PEG: Poly Ethylene Glycol

PM: Pleural Mesothelioma

POC: Point of Care

POCT: Point of Care Testing

PS: Phosphatidylserine

PSA: Prostate-Specific Antigen

PVDF: Polyvinylidene Difluoride

QDs: Quantum Dots

QY: Quantum Yield

RAFT polymerisation: Reversible Addition−Fragmentation Chain Transfer polymerisation

RCA: Rolling Circle Amplification

RF: Random Forests

RIPA buffer: Radioimmunoprecipitation Assay buffer

RNA: Ribonucleic acid

RPA: Recombinase Polymerase Amplification

SEC: Size Exclusion Chromatography

SERS: Surface Enhanced Raman Spectroscopy

sEVs: Small Extracellular Vesicles

SiMoA: Single-Molecule Arrays

SPR: Surface Plasmon Resonance

ssDNA: Single-Stranded DNA

STED: Stimulated Emission Depletion

SVM: Support Vector Machine

SWCNTs: Single-Walled Carbon Nanotubes

TAMRA: Tetramethyl Rhodamine

TEM: Transmission Electron Microscopy

THF: Tetrahydrofuran

TIRF: Total Internal Reflection Fluorescence

TMA: Transcription-Mediated Amplification

TMB: 3,3',5,5'-tetramethylbenzidine

TSA: Tyramine Signal Amplification

UCL: Up-conversion Luminescence

UCNPs: Up-conversion Nanoparticles

ULISA: Up-conversion-Linked Immunosorbent Assay

VEGF: Vascular Endothelial Growth Factor

Thesis Abstract

Small extracellular vesicles (sEVs) hold immense significance as potential biomarkers for cancer-specific diagnosis due to their role in intercellular communication and the transport of bioactive molecules. Their unique cargoes, comprising proteins, nucleic acids and lipids, reflect the originating cells' status, providing valuable insights into the disease microenvironment. Harnessing sEVs as biomarkers offers a minimally invasive approach for early cancer detection and a deeper understanding of disease progression.

Nanoparticle-assisted technologies play a crucial role in sensitively detecting sEVs. Their unique physicochemical properties enhance the sensitivity and specificity of detection methods, allowing for precise identification of sEV-associated biomolecules.

In Chapter 1, we present a comprehensive review of novel approaches involving nanoparticle-assisted and integrated strategies for the sensitive detection and characterisation of sEV markers. Chapter 2 summarises the experimental methodologies implemented during the course of the PhD study. In Chapter 3, we summarise the structural and functional characterisation of the AuNPs and UCNPs and their conjugation to signalling and/or detector antibodies for use in the AuNP-ELISA, UCNP based microplate immunoassasy and UCNP-LFA analytical systems as probes.

For Chapter 4, we functionalised AuNPs and UCNPs with relevant antibodies to use as probes in a nanoparticle-modified ELISA format. The aim was to leverage the high loading capacity and biocompatibility of these nanoparticles to enhance the detection sensitivity of target analytes in a standard microplate immunoassay format with potential POC applications. In the study, we performed colorimetric ELISAs in a hand-held, portable plate reader, with the AuNP-ELISA achieving a ~2-fold improvement in the detection limit of CD63 compared to the

conventional ELISA. Concurrently, the UCNP immunoassasy was performed in a customised bench-top plate reader and achieved a ~10-fold enhancement in the detection limit of CD63 compared to the AuNP-ELISA. The findings of this results chapter establish the utility of nanoparticles in enhancing the sensitivity of conventional immunoassay formats that can potentially be implemented in POC settings to detect cancer-specific sEV markers.

In Chapter 5, we introduce a novel quantitative lateral flow assay (LFA) for sensitively detecting CD63 and PD-L1 using highly doped up-conversion nanoparticles (UCNPs). sEV-PD-l plays a significant role in tumour progression, particularly in immune response, and the UCNP-LFA successfully detected sEV-CD63 and sEV-PD-L1 from multiple cell-derived sEVs with its detection performance being comparable to sEV marker detection using commercial ELISA kits. In Chapter 6, we extend the use of the UCNP-LFA to sensitively detect GPC-1 and PD-L1 in sEVs isolated from relevant cell lines. sEV-GPC-1 has significant clinical significance, with studies establishing its role in promoting cancer-promoting behaviour. The study was the first of its kind that used an LFA technology to quantitatively detect sEV-GPC-1, which it did at an improved sensitivity compared to a commercial ELISA kit. The findings of these two result chapters advance the implementation of quantitative UCNP-LFA systems towards sensitive and accurate detection of cancer-specific sEV markers, specifically in POC settings. Finally, in Chapter 7, we summarise the overall findings of the PhD thesis, discuss technical limitations and highlight the future research directions to enable the implementation of rapid, reliable and sensitive detection of sEV markers in diagnostic settings.

1. Literature Review

1.1. Liquid Biopsy in Cancer Diagnosis

Cancer diagnostics remains to be one of the biggest challenges of the healthcare industry, being one of the leading causes of mortality worldwide [1]. Cancer cells exhibit a wide degree of morphological and phenotypical heterogeneity, which limits the improvement of cancer management strategies (Fig 1). The gold standard for cancer diagnosis has traditionally been tumour biopsy and targeted therapies, which provide insight into tumours' morphology and gene expression profile. Assessments are performed after detecting a mass lesion that is normally evident long after the onset of cancer. Patients usually miss the chance for treatment at this stage [2]. Moreover, biopsies are generally invasive, requiring physical sampling of a segment of the tumour for pathologic analysis and resection of primary tumour tissues, and do not represent the real-time status of molecular markers and tumour heterogeneity that are altered in the process of tumour progression and evolution [3-5]. Additionally, single biopsies do not represent the overall genomic landscape of a tumour and bring evaluation bias due to intertumoral and intertumoral heterogeneity [6]. For effective early-stage cancer diagnosis, platforms that allow for multiple and serial sampling for the dynamic monitoring of cancer progress is highly desirable.

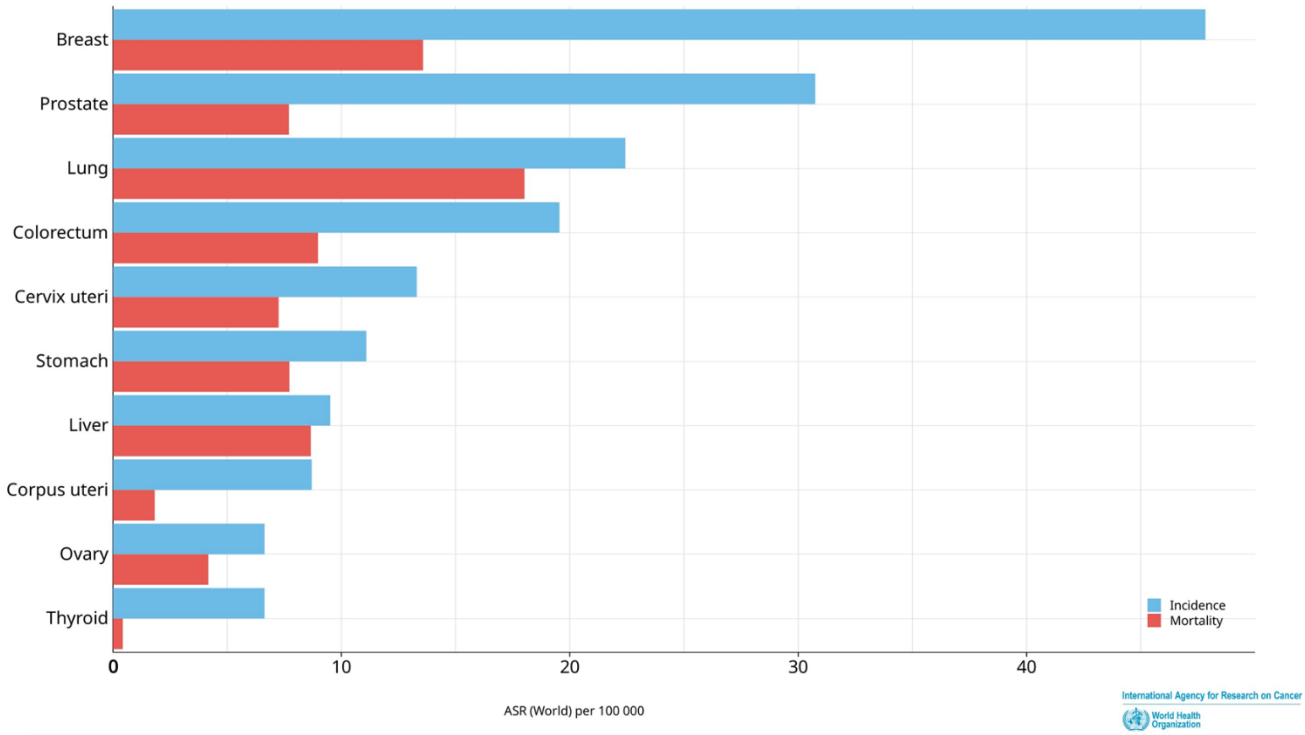

Fig 1: Global age-standardised cancer incidence and mortality rates in 2022. Cancer continues to be a leading cause of mortality globally, mainly due to the absence of rapid, reliable, and sensitive early-stage detection systems. Data generated from Global Cancer Observatory, International Agency for Research on Cancer 2022 [1].

Liquid biopsy facilitates dynamic analyses of molecular or cellular biomarkers and holds great potential for the diagnosis, prognosis, monitoring of disease progress and treatment efficacy, understanding of disease mechanisms, and identification of therapeutic targets for drug development [7]. It offers several advantages over conventional tissue biopsies by focusing on minimally invasive analyses of analytes that are released from the primary tumour sites and circulated elsewhere through body fluids. Moreover, liquid biopsy has been shown to reflect intratumoral heterogeneity better than tissue biopsies and are suitable for longitudinal monitoring of cancer evolution and detection of resistance-conferring tumor cells [8]. Liquid biopsy analysis of tumours presents an ideal diagnostic and prognostic option for molecular diagnosis of cancer. This promises a shift in medical paradigms towards personalised medicine and show promise of revolutionising diagnostic and disease monitoring applications [9, 10]. Multiple studies have shown that some unique components sourced from biofluids are

favourable for early stage cancer detection [11-14]. These include circulating tumour cells (CTCs), extracellular vesicles (EVs) and circulating tumour DNA (ctDNA) (Fig 2) [11, 15, 16]. Systems that characterise and analyse these components in the biofluids of patients, facilitate the monitoring of cancer development [17].

1.1.1. Circulating Tumour Cells (CTCs)

CTCs are tumour derived cells that have separated from the tumour and entered biofluids like blood [18]. CTCs contribute to the spread of metastasis and subsequent growth of tumour cells at distant sites within the body. The presence and frequency of these rare cells are pivotal to early cancer detection and monitoring and their isolation and retrieval is pivotal in furthering our understanding of cancer biology [19]. The inherent rarity and fragility of CTCs in biofluids like blood, makes existing technologies like fluorescence-activated cell sorting (FACS), laser capture microdissection (LCM), etc. suffer from low yield, damage of cell viability and poor repeatability. The techniques are also constrained by total input cell number and do not allow for the collection of live cells for further analysis [20]. The key priorities for progress in CTC enrichment are efficiency and high-volume sample throughput, minimising bias and capturing viable CTCs for live analyses. Most CTC enrichment methods cannot meet one or more of these criteria. For instance, the most common method for CTC enrichment-CELLSEARCH®$^{\text{Veridex LLC}}$ (FDA approved CTC-based diagnostic) relies on positive immunogenic selection with antibodies against EpCAM [21]. This biases against CTCs that have undergone partial or complete epithelial-mesenchymal transition (EMT), which has a significant role in metastasis, but is still poorly understood [22]. Some other CTC enrichment methods include immunogenic negative selection, density-based filtering, and microfiltration all have their own limitations [23]. Apart from this, to be able to sample and decode cancer heterogeneity, CTC analyses must also occur at the single cell level [24]. Traditional methods

for single cell isolation are not able to track single cells over time and therefore is not feasible for establishing the association of cell biomarkers with dynamic cell behaviour.

1.1.2. Circulating Tumour DNA (ctDNA)

Circulating cell-free DNA (cfDNA) are shed both actively and passively from cells and are detected in biofluids like plasma, urine. These are double-stranded small extracellular DNA (~70-200 base pairs) [25-27]. A small fraction of cfDNA (<0.01% of the total non-cell DNA), called circulating tumour DNA (ctDNA) specifically in cancer samples contain tumour specific molecular alterations and have been studied for detection of cancer specific markers [28, 29]. ctDNA is highly fragmented, associated with nucleosomes and are released into circulation through apoptosis, necrosis, secretion of tumour cells and circulating tumour cells (CTCs) or metastatic lesions [28, 30, 31]. The type of cancer and the staging of disease progression are prominent determinants of the ctDNA levels in circulation. Studies have established that ctDNA levels is significantly higher in cancerous samples compared to healthy populations and it varies with different cancer progression stages. Additionally, factors like tumour size, metabolism and proliferation also correlate with the amount of ctDNA in plasma [32-34]. Despite this, the implementation of ctDNA analyses in clinical settings experience some critical challenges including very low concentrations and differentiation from cfDNA to allow for accurate detection of rare mutations. The ratio of ctDNA is as low as 1-10% of cfDNA at advanced diseased stages and < 0.1% at early stages [29, 35]. The variability in concentrations of ctDNA in circulation also hinder the definition of a concentration range for detection [30, 36, 37].

1.1.3. Extracellular Vesicles (EVs)

EVs are lipid bilayer encapsulated bodies released from most mammalian cells. They can be broadly classified into three subsets based on their size and biogenesis, which include apoptotic bodies (>1000 nm), microvesicles (100-1000nm) and small extracellular vesicles (~30-150nm) (previously named as exosomes) [38]. Small extracellular vesicles (sEVs) are formed by inward budding of late endosomes and are enriched sources of biomolecules like proteins, mitochondrial/nuclear DNA, mRNA/microRNA, lipids and other metabolites, which contain molecular information about their tissue of origin [39]. These vesicles impact physiological and pathological processes, including cancer metastasis, tumour progression and intercellular communication [40, 41]. sEVs are secreted by cells and are present in all bodily fluids (plasma, saliva, urine, ascites, cerebrospinal fluid, etc.) and can induce different molecular pathways and act as potent biomarkers of early diagnosis of cancers. sEV proteins associated with endosomes typically provide generic markers or disease-specific signatures that shed light on the biological status of their parental cells in clinical diagnosis (Fig 2) [42].

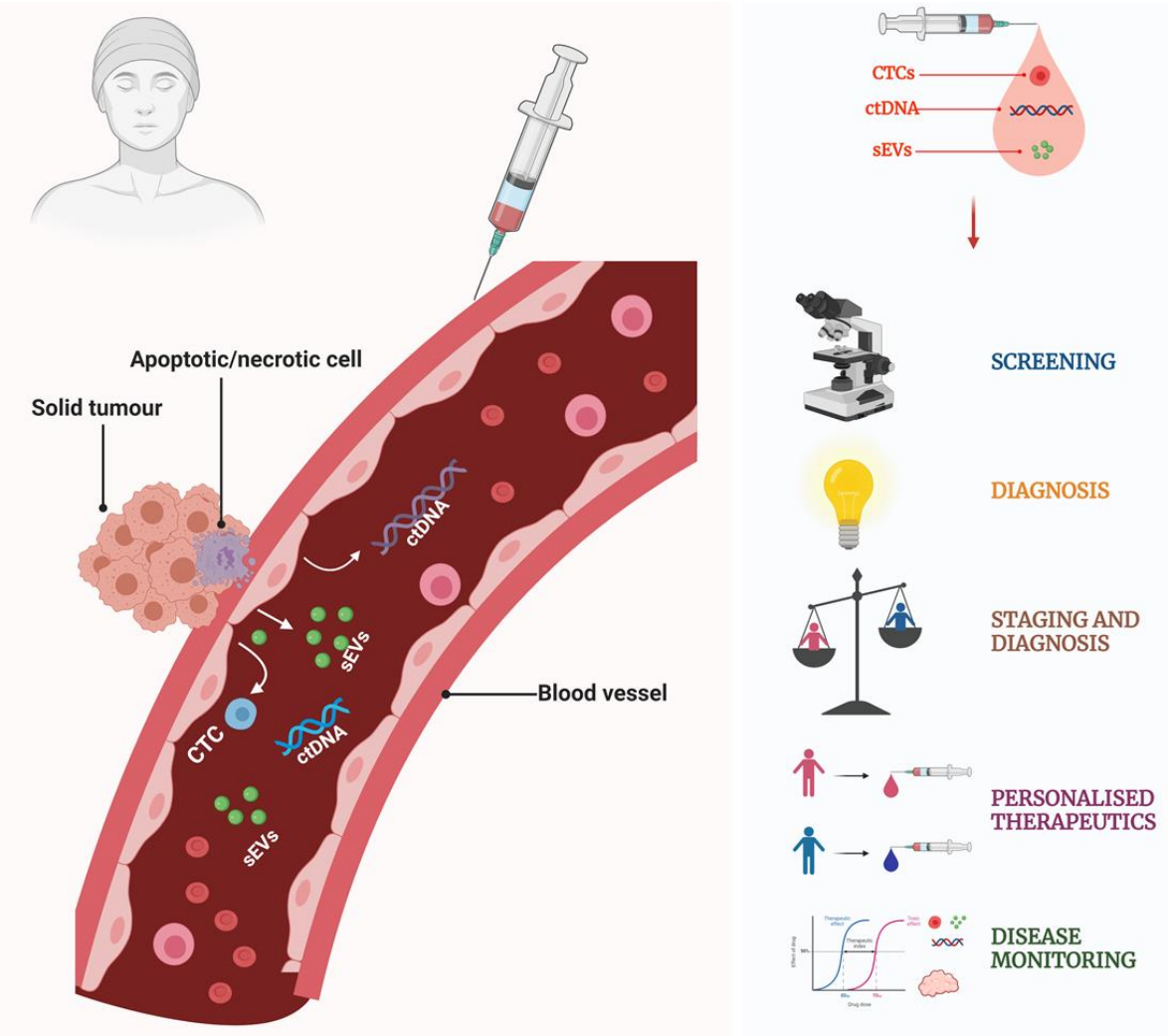

Fig 2: Significance of liquid biopsy: Liquid biopsy allows for detection of cancer related biomarkers in body fluids, eliminating the need for invasive tissue samples and facilitating early-stage cancer marker detection across diverse sample types. Liquid biopsy aids in monitoring the effectiveness of treatments and identifying genetic changes during the course of therapy. The common cell components exploited for liquid biopsy include CTCs, ctDNA and sEVs. In contrast to CTCs and ctDNA, sEVs exhibit distinct advantages. sEVs are secreted by living cells existing in large quantities, and maintaining stable circulation.

1.2. Significance of sEVs in Liquid Biopsy

sEVs are promising biomarkers with superiority in several aspects compared to the other liquid biopsy targets, specifically for tumour detection and screening. In contrast to the inherent rarity of CTCs in biofluids, sEVs are relatively abundant with concentrations being $>10^9$ vesicles/mL [43]. Moreover, sEVs play a significant role in intercellular communication and molecular

exchange and reflect valuable information about the genetic and epigenetic alterations of the cells of origin, making them more representative than ctDNA. The liposome-like membrane structures of EVs also give them inherent stability and protects them from degradation and maintain the integrity of EV associated molecular cargoes (Fig 3) [44, 45].

For clinical sEV analysis, a wide range of associated proteins have been identified as potential biomarkers for various diseases, among which cancer is a pivotal target [46]. These protein biomarkers are engaged in either capture or detection processes of sEVs from different biofluid samples. While sEVs exhibit broad diversity in their origin, they are made of some common structural and functional proteins, which include tetraspanins (CD9, CD63 and CD81), heat shock proteins (HSP60, HSP70) and endosomal sorting complex for transport (ESCRT) associated components (Alix and TSG101) (Fig 3) [47]. Apart from these, cancer-specific sEV markers like HER2, CEA, GPC-1, EGFR, EpCAM, and PD-L1 have been implicated in hepatocellular carcinoma (HCC), pancreatic ductal adenocarcinoma (PDAC), non-small cell lung cancer (NSCLC), breast and prostate cancers [11, 48-50] (Table 1). Other than proteins, associated nucleic acids like miRNA, mRNA, lncRNA and DNA are also detected in tumour-derived sEVs [51]. sEV-associated nucleic acids are transferred cell-to-cell by membrane fusion, spreading cancer-promoting cellular contents to surrounding cells, thus facilitating cancer progression [52, 53]. sEV miRNAs are conspicuous cancer biomarkers because of their stability against RNase-dependent degradation [54, 55]. Studies have implicated the expression of miRNAs like miR-21, miR-10b, miRN-378, miR-139 and miR-222 in multiple cancer types, including HCC, PDAC, NSCLC and breast cancer [56-59]. sEV glycans and lipids also mediate vesicle biogenesis, intercellular recognition, communication and disease progression [60, 61]. Glycans have structural and compositional diversity, and their varied incorporation leads to different biophysical properties and functionalities [62]. Studies have also shown a 2-3-fold enrichment of lipids in sEVs compared to cells, with select lipids like phosphatidylserine (PS)

being highly expressed in cancer cell-derived sEVs [63, 64]. Strategies that allow sensitive and multiplexed profiling of EV glycans and/or lipids have been explored for a better understanding of EV mechanisms for application in diagnostics [46, 65, 66].

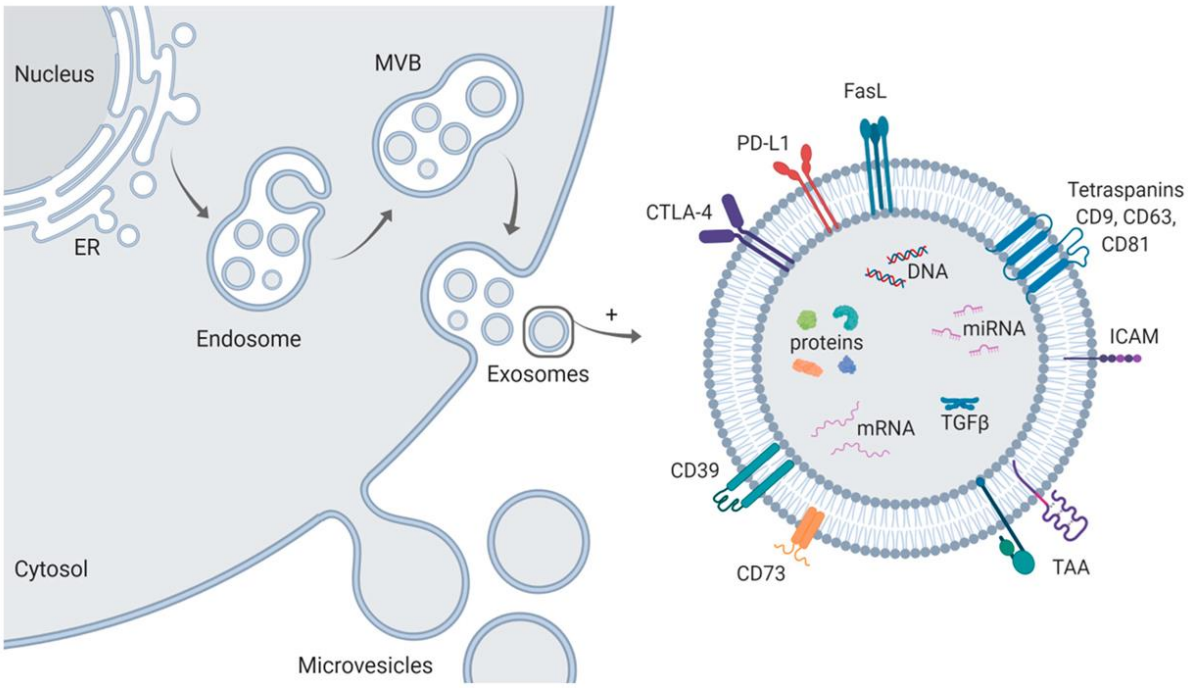

Fig 3: sEVs originate from the endosomal membrane, forming through inward budding, resulting in multivesicular bodies (MVB). When MVBs fuse with the plasma membrane, sEVs are released into the extracellular space. The molecular content of sEVs encompasses proteins, miRNA, mRNA, DNA, and lipids. sEVs are characterised by surface markers, including tetraspanins CD9, CD63, and CD81, termed “sEV structural markers," as well as adhesion molecules like intercellular adhesion molecule ICAM, and, in the case of tumour-derived sEVs, tumour-associated antigens (TAA) specific to the cell of origin. sEVs play a pivotal role in tumorigenesis, tumour progression, and metastasis, and their enrichment in body fluids renders them key players in these processes. Identifying specific molecules within sEVs presents a novel approach for cancer diagnosis, monitoring progression, and predicting prognosis. Reproduced with permission from [67].

Table 1: Significance of cancer-specific sEV markers in Liquid Biopsy

Cancer types	sEV sources	sEV biomarker	Clinical significance	Ref.
Gastric Cancer	Serum	lnc HOTTIP	Early diagnosis	[68]
	Serum	miR-15b-3p	Early diagnosis	[69]
Hepatocellular Carcinoma (HCC)	Serum	miRNA-21; lncRNA-A TB	Prognostic significance	[70]
	Serum	miR-21	Early diagnosis	[71]
	Serum	miR-92b	Early recurrence diagnosis after LDLT	[72]
	Serum	CEA; GPC-3 and PD-L1	Early diagnosis and progression monitoring	[73]
Pancreatic Cancer (PDAC)	Plasma	miRNA-10b	Early diagnosis and progression monitoring	[74]
	Plasma	miRNA-10b	Early diagnosis	[75]
	Serum	Glypican1	Early diagnosis	[76]
	Plasma	Glypican1	Stage classification	[77]
	Serum	EpCAM, Glypican1	Early diagnosis	[78]
Colorectal Cancer (CRC)	Serum	hsa-circ-0004771	Early diagnosis	[79]
	Plasma	EpCAM-CD63	Early diagnosis; prognosis prediction	[80]
	Serum	GPC-1	Early diagnosis; prognosis prediction	[81]
Non-small cell lung cancer (NSCLC)	Plasma	miRNA-21	Early diagnosis and drug resistance in advanced cancers	[79]
	Plasma	CD63; EGFR; EpCAM	Early diagnosis and therapeutic effect evaluation	[82]
	Serum	PD-L1	Early diagnosis	[83]
Malignant Pleural Mesothelioma (MPM)	Serum	miR-16-5p	Early diagnosis; prognosis prediction	[84]
	Serum	PD-L1	Early diagnosis; prognosis prediction	[85]
Breast Cancer	Plasma	EpCAM	Early diagnosis	[86]
	Plasma	HER2	Early diagnosis	[87]

	Serum	PD-L1	Prognosis prediction and progression monitoring	[88]
	Blood	CA153	Differential diagnosis	[89]
	Serum	miR-21; miR-222; miR-200c	Classification of molecular subtypes of breast cancer	[90]
	Plasma	CA153; CEA, EGFR, Her-2	Differential diagnosis of BC and healthy donors	[91]
Prostate Cancer	Serum	GPC-1	Prognosis	[92]
	Plasma	miR-217; miR-23b-3p	Early diagnosis	[93]
	Serum	EphrinA2	Early diagnosis; distinguish PCA from BPH patients	[94]
	Serum	EpCAM and PSMA	Early diagnosis	[95]
	Serum	TUBB3 mRNA	Prognosis	[96]
Ovarian Cancer	Ascites	EpCAM; CD24	Early diagnosis	[97]
	Plasma	CA125; EpCAM; CD24	Early diagnosis	[98]
	Plasma	CD24; FRα	Early diagnosis	[99]
	Plasma	miR-4732-5p	Early diagnosis	[100]

1.3. Isolation and Characterisation of sEVs

In recent years, studies have developed several approaches towards the isolation and characterisation of sEVs. Most conventional strategies exploit either the physical characteristics like size, density and surface charge or biological characteristics like sEV surface markers to facilitate the separation and identification of sEVs [101]. sEVs are isolated from body fluids like blood and urine, with the former being the most abundant source of sEVs, with the average concentration being between 5 - 15 × 10^{18} particles per mL [102, 103]. Conventional strategies like ultracentrifugation [104], size exclusion chromatography (SEC) [105], EV filtration, polymer precipitation and microfluidics have been implemented towards sEV isolation [106, 107]. These techniques have their advantages and disadvantages with regard to purity and sample recovery, all of which have been extensively reviewed in multiple published works. Among these, ultracentrifugation is the most common technique, relying on the sequential separation of particles by sedimentation based on size and density by a series of centrifugal forces and duration [108]. Additionally, techniques like transmission electron microscopy (TEM) have been used to investigate the morphology of sEVs and dynamic light scattering (DLS) and NTA (Nanoparticle Tracking Analysis) is implemented to assess the concentration and size distribution of sEVs (Fig 4) [109].

Following the extraction process, sEV proteins are identified and quantified by Enzyme Linked Immunosorbent Assay (ELISA), Flow Cytometry, while sEV nucleic acid content is analysed by PCR and sequencing techniques [110-113]. Immunoaffinity-based methods rely on the identification of specific sEVs based on the surface proteins; this includes the common surface markers (CD63, CD9 and CD81) as well as disease-specific markers like epithelial cellular adhesion molecule (EpCAM), Programmed death-ligand 1 (PD-L1), glypican 1 (GPC-1) or heat shock protein and heparin [114]. Flow-cytometry has also proven to be advantageous for the analysis and characterisation of particles, including sEVs attached to microbeads [115, 116]

and has been used effectively to characterise sEVs from multiple cell types, including Mel526 melanoma cells [117], K562 human erythromyeloblastoid leukemia cells [63] and PC3 prostate cancer cells [118].

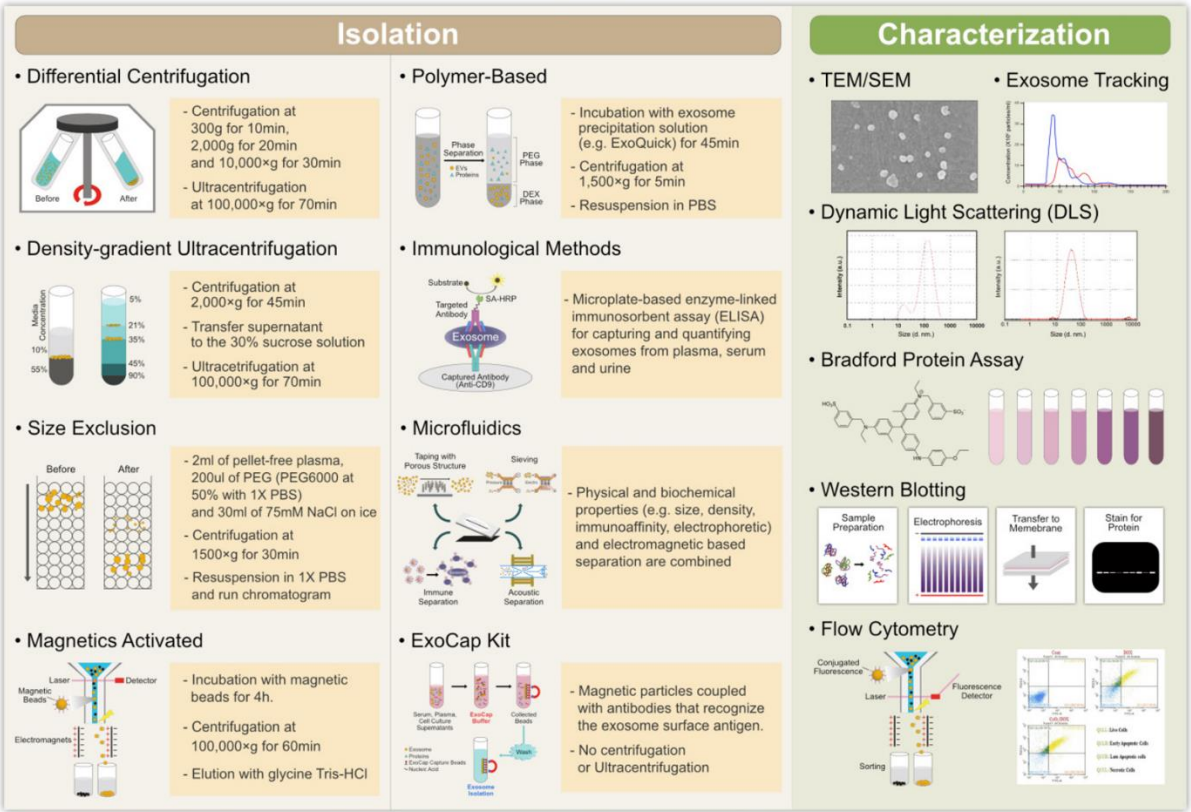

Fig 4: Techniques for isolation, characterisation and functional analysis of sEVs. Ultracentrifugation is the current gold standard method for isolation of sEVs. Following isolation, sEVs are typically characterised for their size, morphology and functional expression using techniques like NTA, TEM and Flow Cytometry, respectively. Reproduced with permission from [119].

1.4. Limitations in sEV Analysis

The small size, low density, and heterogeneity of sEVs significantly hinder the application of standardised methods for sEV characterisation. Most conventional sEV isolation methods require large sample consumption and tedious isolation steps [10]. Concurrently, conventional sEV analysis techniques necessitate sophisticated instrumentation and complex multi-step workflows that restrict the implementation of these sEV-based detection strategies in clinical settings [120]. The other major complexity is the existing heterogeneity in sEV populations,

where sEVs isolated from the same batch of cells vary extensively regarding size, morphology, lipid, protein and nucleic acid composition. This heterogeneity disrupts the reproducibility of sEV studies and limits their application in diagnostic settings [121]. While immune-isolation methods can selectively isolate specific sEV subpopulations, the biogenesis of EV subsets involves the same plasma membrane and endocytic pathways that prevent the identification of a specific marker for particular EV subpopulations [122]. To address this, there has been a push to develop more accessible cancer diagnostic technologies, including novel assay formats that are integrated with miniaturisation, automation and advanced engineering operations [123]. Most liquid biopsy platforms require the enrichment of limited target analytes from body fluids such as blood, urine, saliva, and subsequent analysis and characterisation of the isolated components [124]. Towards this, micro-scale materials have been combined with emerging engineering tools to create integrated diagnostic platforms, among which microfluidic systems have had the biggest impact [125, 126]. Microfluidics have been rapidly developed over the past few decades and have significant potential for application in biological analysis. They offer several advantages over conventional diagnostic strategies, including minimal consumption of samples and reagents, high resolution and sensitivity, low cost and significant reduction in assay time [127, 128]. These platforms allow for better control over multiple aspects of assays, including sample filtration, analyte transport, mixing, heating and analysis through integrated optical and electrical sensors, with most of these microfluidic devices allowing for automation and parallelisation [129, 130]. These features potentiate the development of ultrasensitive integrated bio-sensing platforms that can run multiple analytical processes.

1.5. Nanoparticle integrated biosensors

Advantages of using nanoparticles in biosensors: In the context of biosensor development, nanomaterials play a pivotal role, characterised by their unique properties on the nanoscale. Nanomaterials are natural or manufactured particles in unbound or aggregate states, where >50% of the particles are in the size range of 10-100nm [131]. These materials have unique optical, electronic and magnetic properties that are different from the bulk material. Moreover, their physico-chemical properties can be changed by tuning the shape and size of the nanoparticles (NPs) (Fig 5) [132, 133]. NP-based biosensors offer numerous advantages, including high specificity, enabling the precise detection of target analytes [134]. They also facilitate label-free detection, thereby streamlining assay procedures and reducing functional complexity. NP-based sensors typically require small sample volumes, making them suitable for applications where sample availability is limited [135, 136]. Studies have leveraged the large surface area to volume ratio of nanoparticles, to enhance the sensitivity and improve the detection limit of sEV based biosensors that have potential to be implemented in clinical diagnostics [133, 137].

The evolution of NP-based sensor technologies also holds the potential to revolutionize point-of-care (POC) diagnostic applications [138]. POCs aim to remove processing times that is caused by the conventional workflow, where samples are collected and transported to central labs for testing [139]. POCs offer an excellent solution for accurate, quality-assured tests that allow for rapid detection and expedite diagnosis and treatment initiation in resource poor settings [140, 141]. These systems allow for reduced consumption of power and expensive reagents, while offering multiplexed ultrasensitive analysis of diseased samples in an economical and portable setting [142, 143]. The move to POC systems represents a paradigm shift from conventional diagnostic methods to personalised diagnostics that allow for rapid,

low cost, reliable quantitative analysis of biomarkers. For the development of reliable POC cancer diagnostic platforms, devices need to meet the ASSURED criteria outlined by WHO, i.e. these systems must be affordable, sensitive with minimal false negative rates, specific with minimal false positive rates, user friendly, rapid and robust operation process and equipment free which can operate without the need for extensive instruments and is easily accessible in resource-limited settings [144, 145].

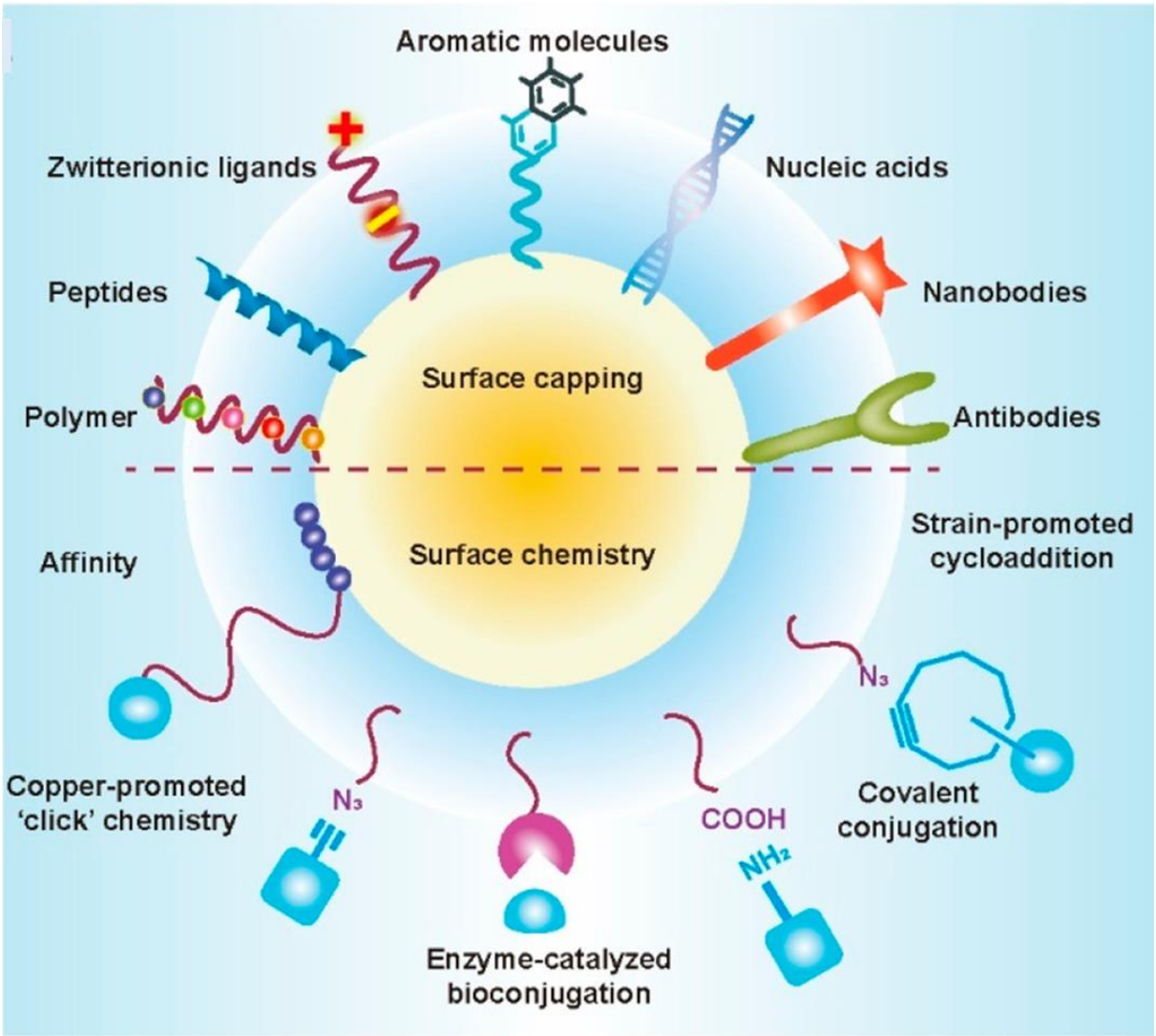

Fig 5: Bioconjugation of target recognition molecules on nanoparticles: Nanoparticles serve as versatile probes in biosensors due to their unique properties and adaptability. Through bioconjugation with a diverse array of target recognition molecules such as antibodies, aptamers, or enzymes, nanoparticles can selectively bind to specific analytes, enabling highly sensitive detection. Reproduced with permission from [146].

For use in bio-sensors, NPs are typically functionalised with target analyte recognition molecules like antibodies, aptamers, molecular beacons, etc. to selectively recognise target analytes with improved sensitivity compared to conventional strategies without the integration of nanoparticles. Recognition molecules are typically functionalized on nanoparticle surfaces through methods such as physical adsorption, covalent binding, or the use of specific adaptor molecules. The choice of strategy during nanoparticle functionalization must prioritise achieving optimal orientation of the recognition molecule on the nanoparticle surface with the aim to enhance the functionality of the molecule in a biosensor, serving as an effective probe for the detection of sEVs [147, 148]. The most common strategies for functionalisation are physical adsorption and covalently link antibodies to nanoparticles to the former's amine group. However, these approaches often block the antigen binding sites that reduce the recognition efficacy of the target moieties [148]. To resolve this, alternate conjugation approaches have been studied, which include bio-orthogonal chemistry and use of coupling between avidin modified antibodies with biotin conjugated nanoparticles, to amplify signal intensity. Additionally, the density/concentration of the target molecule is also critical to ensure the best bio-analytical performance of the functionalised nanoparticles [148, 149]. This is most relevant in conjugation protocols like passive adsorption which exploits the electrostatic and hydrophobic interactions between the protein and the surface layer of the nanoparticles, only at an optimised pH and protein amount to generate stable nanoparticle probes. The same is true for functionalisation of nucleic acid recognition molecules like aptamers, which are synthetic single-stranded oligonucleotides to target nucleic acids with high selectivity and sensitivity [150]. The most commonly implemented nanoparticles, particularly in sEV detection sensors include magnetic nanoparticles, carbon nanostructures, gold nanoparticles, quantum dots and upconversion nanoparticles.

Magnetic Nanoparticles (MNPs): Magnetic Nanoparticles (MNPs) are nanoscale aggregates of iron oxide or ferrite particles that are valuable in biosensing due to their ability to concentrate analytes or recognition molecules on them [151]. When modified with receptor units, MNPs can either interact with the analyte or, under the influence of an external magnetic field, agglomerate for easy separation [152]. MNPs are ideal for biosensing because they ensure minimal interference during signal capture, and their transportability to microfluidic transduction platforms enables complex multiplexed analyses for simultaneous detection of diverse analytes [153].

Carbon Nanostructures: Nanostructured carbons like carbon nanotubes (CNTs) and graphene are widely employed as electrochemical transducers in biosensor devices, given their beneficial properties [154, 155]. CNTs, in particular, with their nanowire morphology, biocompatibility, and electronic properties, enhance capacities such as approaching active sites of redox enzymes and facilitating their wiring to the bulk electrode [156]. Their easily functionalised organic nature introduces new features to nanostructured electrodes, including specific docking sites for biomolecules and redox mediation of bio-electrochemical reactions [157], while the formation of highly porous three-dimensional networks in CNT films provides a large electroactive surface area, enabling high sensitivities [158, 159].

Gold Nanoparticles (AuNPs): AuNPs are the most extensively utilised in biosensors due to their biocompatibility, optical and electronic properties, and uncomplicated production and modification processes [160, 161]. Notably, their optical behaviour involves surface plasmon resonance (SPR), where irradiation induces electron oscillation, resulting in a colour change observable with the naked eye upon recognition events in bioanalytical applications [162, 163]. Additionally, AuNPs are a robust transduction platform for single-molecule detection, demonstrated through refractive index sensing of localised surface plasmon resonance (LSPR) coupled with enzyme-linked immunosorbent assay (ELISA). For instance, Chen et al. utilised

60 nm gold nanoparticles, immobilising the model enzyme horseradish peroxidase (HRP) via biotin-streptavidin linkage. HRP catalysed the oxidation of soluble monomer 3,3'-Diaminobenzidine (DAB), forming coloured polybenzimidazole that aggregated around the enzyme, leading to an additional shift in LSPR scattering wavelength and enabling the detection of few or even single HRP proteins attached to the AuNPs [164]. The advantages of AuNPs in high-sensitivity biosensing were further validated through surface-enhanced Raman spectroscopy (SERS), achieving detection limits down to the single-molecule level [165-167].

Quantum Dots (QDs): QDs are luminescent semiconducting nanocrystals, which are a prominent nanomaterial in bio-analytics. Predominantly composed of cadmium chalcogenides (S, Se, Te), QDs exhibit a broad absorption spectrum and a size-dependent, narrow emission spectrum, offering diverse emission wavelengths for multiplexed analysis [168]. The distinct emission wavelengths result from the varying band gaps of the semiconductor material with different nanocrystal sizes, facilitating efficient optical transduction in bioanalytical applications [169]. QDs are commonly integrated in Fluorescence Resonance Energy Transfer (FRET)-based biosensors, which involves a non-radiative energy transfer between the excited QDs (donor) and a quencher (acceptor) like organic fluorophores [170]. This FRET quenching technique is notably applied in optical DNA and oligonucleotide sensors [171, 172], with QD fluorescence reappearing upon quencher removal, achieved through strategic approaches like hybridization with gold nanoparticles [173, 174]. Moreover, QDs possess high quantum yields, ensuring efficient signal generation in bio-analytical assays and can be easily functionalized with various biomolecules, enabling targeted binding to specific molecular targets and facilitate precise and selective bio-sensing applications [169].

Luminescent Nanoparticles:

Luminescent nanoparticles have attracted significant attention in biosensor development due to their superior optical properties, including high brightness, photostability, and tunable emission [175-179]. Inorganic nanoparticles, such as quantum dots, dye-loaded silica nanoparticles, and up-converting nanoparticles, have largely dominated this field [180-182]. However, to achieve greater control over properties such as emission behaviour, size, and surface chemistry, recent advancements have focused on organic materials, particularly dye-loaded polymer nanoparticles [183]. These nanoparticles encapsulate large quantities of small organic dyes within lipid or polymer matrices, offering advantages over both free dyes and traditional inorganic nanoparticles like quantum dots. Specifically, dye-loaded nanoparticles exhibit higher brightness, broader absorption and emission spectra, and biodegradability, making them particularly appealing for biological applications [181]. Dye-loaded nanoparticles are synthesised using strategies such as emulsion polymerisation or the assembly of pre-formed polymers. Achieving superior brightness often requires high dye loading, which can lead to aggregation-caused quenching (ACQ) [184]. To address this, recent innovations in dye design have incorporated strategies such as aggregation-induced emission (AIE), dye modifications with bulky side groups, and the use of bulky hydrophobic counterions [185, 186]. These approaches mitigate ACQ and produce brighter nanoparticles with emerging applications in in vitro and in vivo bioimaging.

Lanthanide-doped (in)organic nanoparticles have also gained prominence for their unique optical properties, which stem from their 4f electronic configurations and intraconfigurational 4f-4f transitions [177, 187]. Incorporating lanthanide ions such as Eu^{3+}, Tb^{3+}, and Er^{3+} into inorganic matrices (e.g., oxides or fluorides) or organic frameworks stabilises the ions and enhances their luminescent characteristics [188]. Lanthanide-doped nanoparticles exhibit several advantages, including narrow and long-lived luminescence, high photostability, large Stokes or anti-Stokes shifts, and tunable emission wavelengths, making them highly valuable

in bioimaging and biosensing applications [178]. Lanthanide-doped NPs typically rely on direct excitation, but this approach is often inefficient due to lanthanide ions' inherently low absorption cross-sections. This limitation is particularly significant in aqueous or in vivo environments, where autofluorescence and photobleaching can further reduce emission intensity [189]. To overcome this, lanthanide ions are often indirectly sensitised using coordinated aromatic ligands, known as antenna molecules [190]. These antennas efficiently absorb light and transfer the energy non-radiatively to the lanthanide ions, significantly enhancing excitation efficiency and luminescence intensity. The antenna effect not only boosts brightness but also allows excitation with lower-energy light, which reduces tissue absorption and scattering in biological settings [191, 192].

Down-shifting photosensitised lanthanide nanoparticles represent an important refinement, wherein high-energy photons absorbed by photosensitisers are converted to lower-energy emissions via energy transfer to lanthanide ions [193]. This process improves excitation efficiency and reduces issues caused by autofluorescence and photobleaching in biological environments, as it allows excitation in shorter wavelength regions while emitting in the near-infrared or visible spectrum [194]. Down-shifting mechanisms are particularly advantageous for biological imaging applications, as they enable deep-tissue penetration and improved signal clarity by minimising scattering and attenuation at higher wavelengths [195]. Furthermore, this approach enhances compatibility with multiplexed detection systems by reducing spectral overlap and facilitating simultaneous monitoring of multiple targets [196].

Recent advances have also integrated organic dyes with lanthanide-doped nanoparticles, creating hybrid nanosystems with improved light absorption efficiency and efficient energy transfer [197, 198]. This integration considerably enhances the emission brightness of lanthanide nanoparticles and enables fine-tuning of excitation ranges while maintaining a large separation between excitation and emission wavelengths [177]. Such hybrid systems have

shown promising potential in photonic materials and emerging biomedical applications, offering versatility and functionality for imaging, biosensing, and other cutting-edge technologies [199, 200].

Up-conversion Nanoparticles (UCNPs): Among luminescent nanoparticles, lanthanide doped upconversion nanoparticles (UCNPs) have gained significant importance in biosensing applications due to their unique optical properties. Unlike conventional luminescent systems, UCNPs can convert low-energy near-infrared (NIR) light into high-energy visible or ultraviolet light. This capability provides key advantages for biological applications, including deeper tissue penetration and reduced background interference, making them highly effective in complex biological environments [201, 202]. UCNPs find utility in bioimaging and biosensing applications, offering enhanced sensitivity and specificity. Their ability to emit distinct and tunable colours enhances multiplexed detection capabilities, enabling simultaneous analysis of multiple analytes [203]. Additionally, the biocompatibility and low cytotoxicity of UCNPs contribute to their suitability for various biomedical applications, making them promising tools in the field of biosensing [204].

1.6. Nanoparticle-based and Integrated sEV-detecting sensors

Tumour-derived sEVs are promising liquid biopsy markers owing to the abundant molecular information they contain from tumour cells, including proteins and nucleic acids. The overall sEV levels or their associated contents have a strong correlation with tumorigenesis and disease progression [205, 206]. The common target includes structural sEV markers, including CD63, CD9, CD81, ALIX or TSG101. Apart from these, the functionalised nanoparticle also targets sEV nucleic acids, specifically miRNA, that can be used as disease-specific biomarkers [207-209].

Challenges of NP-based biosensors towards sEV detection: The limited availability of tumour derived sEVs in peripheral biofluids like blood, urine, and saliva makes it difficult to develop highly sensitive sEV detection platforms for cancers. Moreover, the inherent heterogeneity of sEVs hinders a comprehensive understanding of the molecular messaging machinery of sEVs [210, 211]. While NP-based technologies offer numerous advantages, they are not without their constraints. One such challenge is the detection of sEVs at the single vesicle level [212]. The inherent heterogeneity of sEVs hampers accurate disease analysis, as patient samples typically exhibit a mixture of tumour-derived and non-tumour sEVs. Conventional bulk analytical methods struggle to discern disease-specific sEVs amidst the background of non-target sEVs in typical clinical samples, thereby compromising sensitivity in detection [213]. Analysing sEVs at the single vesicle level allows for enhanced sensitivity and accuracy in detection of sEV markers. Most NPs are relatively large (< 20nm), and when functionalised with target recognition ligands (e.g. antibodies) their effective dimensions further expand. This is problematic due to the diverse size variations of sEVs, and achieving high detection sensitivity becomes challenging when the dimensions of nanoparticles and the sEVs are not comparable [214]. Beyond size-based limitations, the effectiveness of NP-based biosensors is contingent upon their unique structural and functional attributes. For e.g. NPs like QDs, MNPs, UCNPs are intricate and demand specialised expertise for operation; similarly, certain sensor technologies like electrochemical sensors are operationally complex and necessitate very specific technical proficiency [134]. On the other hand, methods like colorimetric detection technologies may offer simplicity and cost-effectiveness but are not as sensitive at detecting target analytes [212, 214].

Despite these limitations, NP-based biosensors have immense research interest, specially towards the development of highly sensitive sEV detection platforms facilitating improved detection limits [215]. The biggest advantage of NPs is their large surface area to volume ratio,

allowing the attachment of an enhanced number of biomolecules. Moreover, the comparable size variations between NPs and biomolecules, allow them to interact more effectively [133]. Moreover, the advantages of miniaturization, automatization and enhanced sensitivity offered by integrated sensor systems, have prompted innovation towards developing total sEV analysis systems that incorporate both sEV isolation systems with downstream analytical systems to form highly sensitive integrated sEV sensor platforms. These integrated systems are an improvement over conventional techniques and allow for high throughput analysis of small sample volumes and achieve detection of low concentrations of sEVs and associated proteins and nucleic acids [99, 216]. Advancements in NP-based and novel integrated systems can facilitate the development of highly sensitive, 'sample-to-answer' sEV detection and analysis systems that allow high-throughput platforms that can detect low concentrations of sEVs from minimal sample volumes. Moreover, integrated systems can also be used to perform multiplexed detection of multiple sEV markers thereby improving the diagnostic accuracy of EV detection platforms [217-220]. The evolution of NP-based/integrated sEV sensor technologies holds the potential to revolutionize point-of-care (POC) diagnostic applications. POCs aim to remove processing time that is caused by the conventional workflow, where samples are collected and transported to central labs for testing [139]. POC systems offer an excellent solution for accurate, quality-assured tests that allow for rapid detection and expedite diagnosis and treatment initiation in resource poor settings [140, 141]. These systems are ideally. POC testing systems allow for reduced consumption of power and expensive reagents, while offering multiplexed ultrasensitive analysis of diseased samples in an economical and portable setting [142, 143]. The move to POC systems represents a paradigm shift from conventional diagnostic methods to personalised diagnostics that allow for rapid, low cost, reliable quantitative analysis of biomarkers. For the development of reliable POC cancer diagnostic platforms, devices need to meet the ASSURED criteria outlined by WHO, i.e. these

systems must be affordable, sensitive with minimal false negative rates, specific with minimal false positive rates, user friendly, rapid and robust operation process and equipment free which can operate without the need for extensive instruments and is easily accessible in resource-limited settings [144, 145].

Despite numerous studies extensively reviewing nanoparticle-assisted and microfluidic sEV isolation strategies, there is a notable gap in the literature concerning a comprehensive review of novel approaches that involve nanoparticle-based/integrated strategies to facilitate sEV detection and analysis. These strategies aim to provide heightened sensitivity for the detection of both structural and cancer-specific sEVs along with their associated cargoes. In this chapter, we present a broad comparison of novel integrated sEV detection strategies and discuss their operational principles and efficiency at detection of sEVs and their associated proteins and nucleic acids. Additionally, we highlight emerging opportunities to enable ultrasensitive detection and analysis of sEVs and facilitate the development of rapid, reliable and sensitive sEV-based diagnostics. The strategies involved in the detection and quantification of sEV cargoes discussed in this study include Fluorescence Detection, Colorimetric Detection, Electrochemical Detection, Surface Enhanced Raman Spectroscopy (SERS), Surface Plasmon Resonance (SPR), Single EV Analysis and Lateral Flow Immunoassays (LFAs) [137, 221].

1.6.1. Fluorescence-based Detection

Fluorescence-based detection strategies have been widely implemented towards sEV detection due to their compatibility with multiplexed sensing platforms and their integration with microfluidic systems [45, 104]. Generally, fluorescence detection approaches involve labelling the sEVs with fluorescent tags conjugated with antibodies or aptamers to improve the detection efficiency and analytical accuracy of EVs. The labelled sEVs are captured and detected in biosensor chips based on immunoaffinity, external force or nanostructure trapping strategies

[98]. Other strategies involve signal amplification, where the fluorescent substrate is catalysed by an enzyme, hybridisation chain reaction, etc., to enhance the signal intensity, thus improving the detection sensitivity [222].

Immunoaffinity-based approaches, leveraging specific antibody interactions for highly sensitive and selective identification of sEV markers, are the most common methods for sEV detection. In that regard, Kanwar et al. designed a microfluidic "ExoChip' device functionalised with anti-CD63 antibodies to allow on-chip capture of serum-derived sEVs within circular chambers. The detection was achieved through a fluorescent carbocyanine dye (DiO), and quantification was performed using a standard plate reader. The device demonstrated a substantial elevation (~ 2.34-fold) in sEVs among cancer patients compared to their healthy counterparts [223]. In a similar system, Fang et al. developed a microfluidic chip that allowed for immunocapture and quantitative analysis of $EpCAM^+$ and $HER2^+$ sEVs in small sample volumes isolated from breast cancer patients (Fig 6a, 6b) [224].

The versatility and robustness of fluorophores offer an extensive array of labelling possibilities, paving the way for exploring diverse integrated strategies that facilitate precise targeting of sEV markers. Studies have implemented bead-based approaches in microfluidic systems to achieve integrated isolation and ultrasensitive detection of sEVs markers [225, 226]. In this regard, Gao et al. employed quantum dot (QDs) nanoprobes in a micro-chip to allow bead-based isolation and multiplexed detection of sEV markers. The method employed anti-CD9-labeled magnetic beads for sEV isolation and three QD probes labelled with antibodies in conjunction with fluorescence microscopy to enable the multiplexed detection of sEV surface markers, including carcinoma embryonic antigen (CEA), Cytokeratin 19, and Progastrin-releasing peptide (proGRP) [227]. While CdSe-based QDs are the most commonly used fluorescent probes, studies have explored other QDs like InP/ZnS, silicon, and gold–carbon dots for sEV detection in similar platforms [228-230]. Expanding beyond the conventional

reliance on antibodies, studies have explored using sEV-targeting aptamers in combination with metallic NPs to quantify sEV markers. For instance, He et al. designed an assay for direct capture and rapid detection of sEVs, using a copper-mediated signal amplification strategy. It employed a three-step method, which involved cholesterol-modified magnetic beads (MBs) for initial sEV capture, aptamer-modified copper oxide nanoparticles (CuO NPs) to form sandwich complexes, and subsequent dissolution to generate fluorescent copper nanoparticles (CuNPs). The study enabled quantitative sEV analysis, with a detection limit of 4.8×10^4 particles/μL in biological samples (Fig 6c, 6d) [231]. In another aptamer-based strategy, Gao et al. employed rolling circle amplification (RCA) to generate an extended DNA hairpin structure with functional domains, including CD63 aptamer sequences, linker sequences, and spacer sequences with complementary base pairs, forming a dynamic hairpin structure. Upon binding to sEVs, the RCA product unravels its hairpin structure, exposing a linker sequence, and subsequent interaction with a fluorescent AuNP-linker/complementary bioconjugate (AuNP-L/cL) through toehold-mediated strand displacement releases the fluorescent cL probe. The fluorescence signal directly correlated with sEV concentration, reaching a detection limit of 1×10^8 particles/mL [232].

Fluorescence-based microfluidic strategies have also been explored towards the detection and characterisation of sEV-associated nucleic acids [233]. sEV-RNAs, specifically, are actively involved in tumorigenesis, angiogenesis, metastasis and drug resistance, making them promising cancer biomarkers for liquid biopsy. To address this, studies have explored the use of microfluidics-integrated cationic nanoparticle-based systems that can sensitively detect sEV-RNAs without requiring isolation procedures [234-236]. Cao et al. integrated the RCA process in a microfluidic platform for sensitive and specific detection of miRNAs directly in minimally processed samples. The system combined solid-phase miRNA isolation, miRNA ligation and a dual-phase exponential RCA assay in a unified workflow to enable the detection

of low-level sEV-miRNA in as few as 2 × 10^6 sEVs [237]. A number of fluorescence detection systems have also used molecular beacons (nano-sized, dual-labelled oligonucleotide hairpin probes with a fluorophore and a quencher at each end) to detect disease-specific sEV-nucleic acids in clinically diverse samples [234, 238-240]. Yang et al. developed an immune-biochip that selectively enriched $EGFR^+$ and $PD\text{-}L1^+$ sEVs using surface-tethered antibodies and achieved *in-situ* sEV RNA detection through electrostatic interactions with cationic lipoplexes containing RNA-target sensing molecular beacons. Utilising Total Internal Reflection Fluorescence (TIRF) microscopy, the system exhibited superior performance in related applications compared to traditional workflows, while consuming reduced sample volume (~30 µL) and a shortened assay time (~24 hours to 4 hours) (Fig 6e, 6f) [241].

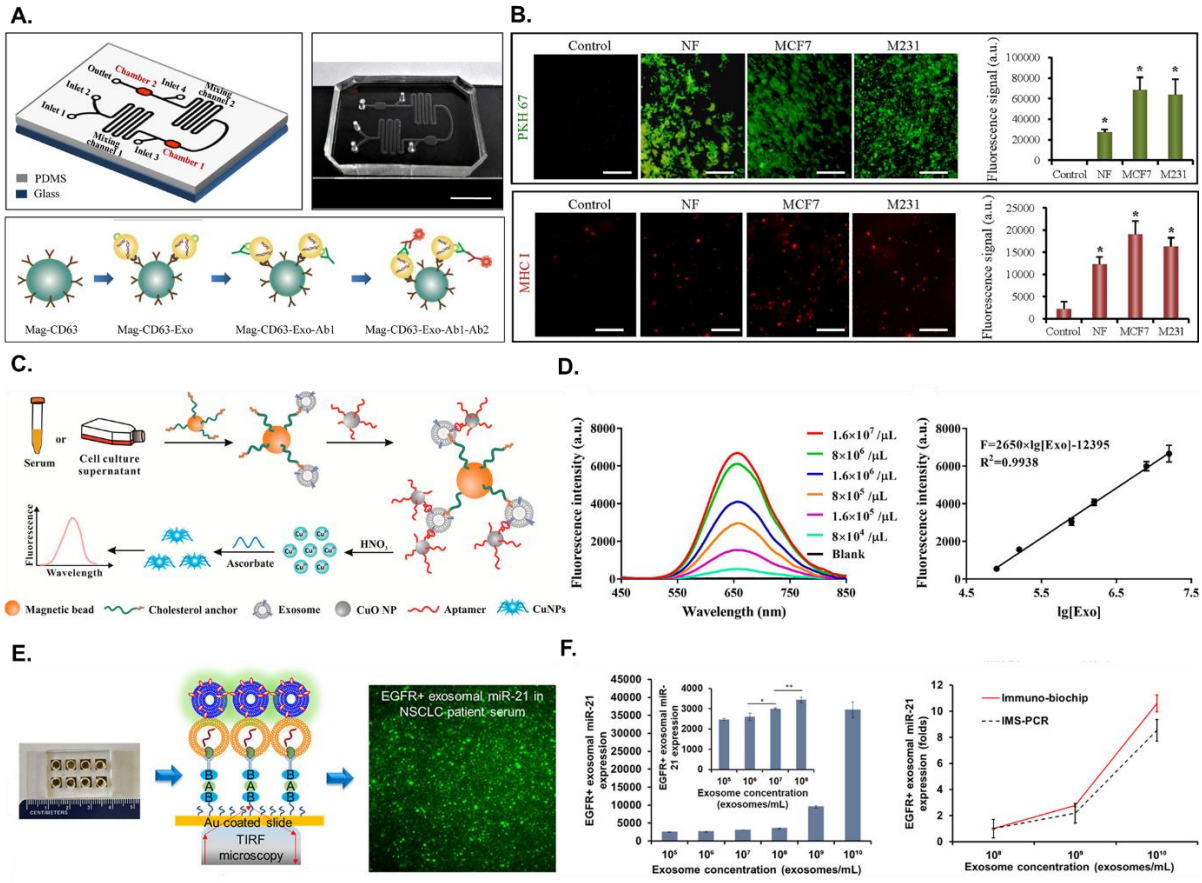

Fig 6: Fluorescence-based sEV detection: (a.) Immunomagnetic capture and fluorescence-labelled detection of breast cancer-specific sEVs, integrated into a microfluidic chip. (b.) Images and quantification of total sEVs and sEV-MHC I isolated from control, MCF7 and M231 cells. Reproduced with permission from ref [86] (c.) Copper-mediated signal amplification strategy for sEV detection

involving cholesterol-modified magnetic beads, aptamer-modified copper oxide nanoparticles, and the dissolution process to generate fluorescent copper nanoparticles. (d.) Sensitivity of the assay for sEV detection: Emission spectra and linear plot of fluorescence intensity obtained at different concentrations of sEVs ranging from 8×10^4 to 1.6×10^7 particles/µL. Reproduced with permission from ref [231](e.) Immuno-biochip for detecting sEV-RNA. In the chip, sEVs are initially captured by specific antibodies, where CLP-modified magnetic beads (MBs) bind to sEV RNAs, and the resulting restored fluorescence is analysed for quantifying sEV-RNA biomarkers. (f.) Expression of sEV-miR-21 on $EGFR^+$ sEVs at concentrations ranging from 10^5 to 10^{10} sEVs/mL. Detection sensitivity of the immunochip was 106 sEVs/mL. The immunochip showed higher sensitivity than the conventional IMS-PCR workflow. Reproduced with permission from ref [241].

1.6.2. Colorimetric Based Detection

Colorimetric detection platforms are the most straightforward methods to determine target analyte concentration, making them desirable for developing highly sensitive POC devices [242]. However, colorimetric sensors often suffer from low sensitivity and necessitate the development of integrated sensor setups to enhance the signal intensity and detection sensitivity. These integrated approaches rely on chemical reaction-based colour changes to nanoparticle aggregation or on the peroxidase (HRP)- like activity that catalyses a colorimetric signal in the presence of a relevant chromogenic substrate [104, 242]. For instance, Xia et al. incorporated water-soluble single-walled carbon nanotubes (s-SWCNTs) and CD63-specific aptamers, which, when absorbed into s-SWCNTs enhance their peroxidase activity and facilitate the oxidation of TMB from colourless to blue. In the presence of sEVs, the aptamers bind with CD63, causing a conformational change in s-SWCNTs and altering the solution's colour from deep to moderate, detectable by the naked eye or spectrometry. Under optimal conditions, the system achieved a detection limit of 5.2×10^5 particles/µL [243]. A similar aptamer-based approach was explored using graphitic nitride nanosheets to establish the differential expression of CD63 in sEVs from breast cancer cells compared to controls (Fig 7a) [244].

AuNPs are the most frequently employed NPs in colorimetric biosensors since they undergo a shift in their extinction coefficient upon aggregation, leading to a noticeable change in colour

[245]. In this context, Jiang et al. created a multiplexed sensor platform by constructing AuNPs with a range of aptamers targeting surface proteins on sEVs. Upon sEV binding to CD63 aptamers, ligands were displaced from the AuNP surface, inducing destabilisation and subsequent AuNP aggregation. This colour change, from red to blue, was measured via UV-vis spectroscopy, and when integrated with a microfluidic chip featuring gold pattern arrays, the system enabled both visual and quantitative detection of multiple proteins on sEVs derived from cancer cells [246]. Aggregation of AuNPs have also been combined with other processes, like DNA hybridisation chain reaction (HCR), to amplify the signal in colorimetric bio-sensors [247]. For instance, Zhang et al. used aptamer-conjugated MNPs to isolate sEVs from cell culture media. Subsequently, a bivalent-cholesterol-labelled DNA probe was hydrophobically incorporated into the sEV membrane, initiating an enzyme-linked HCR involving alkaline phosphatase (ALP). The ALP-mediated reduction of ascorbic acid 2-phosphate to ascorbic acid facilitated Ag^{+} reduction, resulting in silver shell formation on gold nanorods (AuNRs) and a colour change from pink to brown, green, or purple with increasing sEV concentration, offering a visually distinguishable sEV detection system [248].

Studies have explored integrating on-chip systems with colorimetry detection platforms to detect sEVs sensitively [249-251]. One such application is integrated ELISA, which offers efficient, miniaturised platforms, enabling rapid and sensitive analyte detection, making them suitable for high-throughput screening and POC applications [10]. For instance, Woo et al. designed an 'Exodisc' platform that allowed on-chip ELISA for the detection of bladder cancer-associated sEVs in urine. The system integrated nano-filters for sEV isolation, followed by on-disc ELISA and absorbance measurement at 450nm using a customised detection system. The analysis revealed elevated CD9 and CD81 expression in diseased sEV samples compared to healthy controls (Fig 7b) [252]. In a similar approach, Liang et al. engineered a dual-filtration microfluidic device featuring two distinct membranes (200nm and 30nm pores) to effectively

isolate and enrich sEVs from bladder cancer urine samples. The integration of a smartphone camera interface facilitated sEV quantification through a microchip-based colorimetric ELISA. The system demonstrated a notable sensitivity of 81.3% and specificity of 90% in discerning sEVs originating from bladder cancer patients and those from healthy controls (Fig 7c) [218]. The utilisation of nanoparticles and on-chip immunoassays enables the development of highly sensitive and specific sEV detection systems.

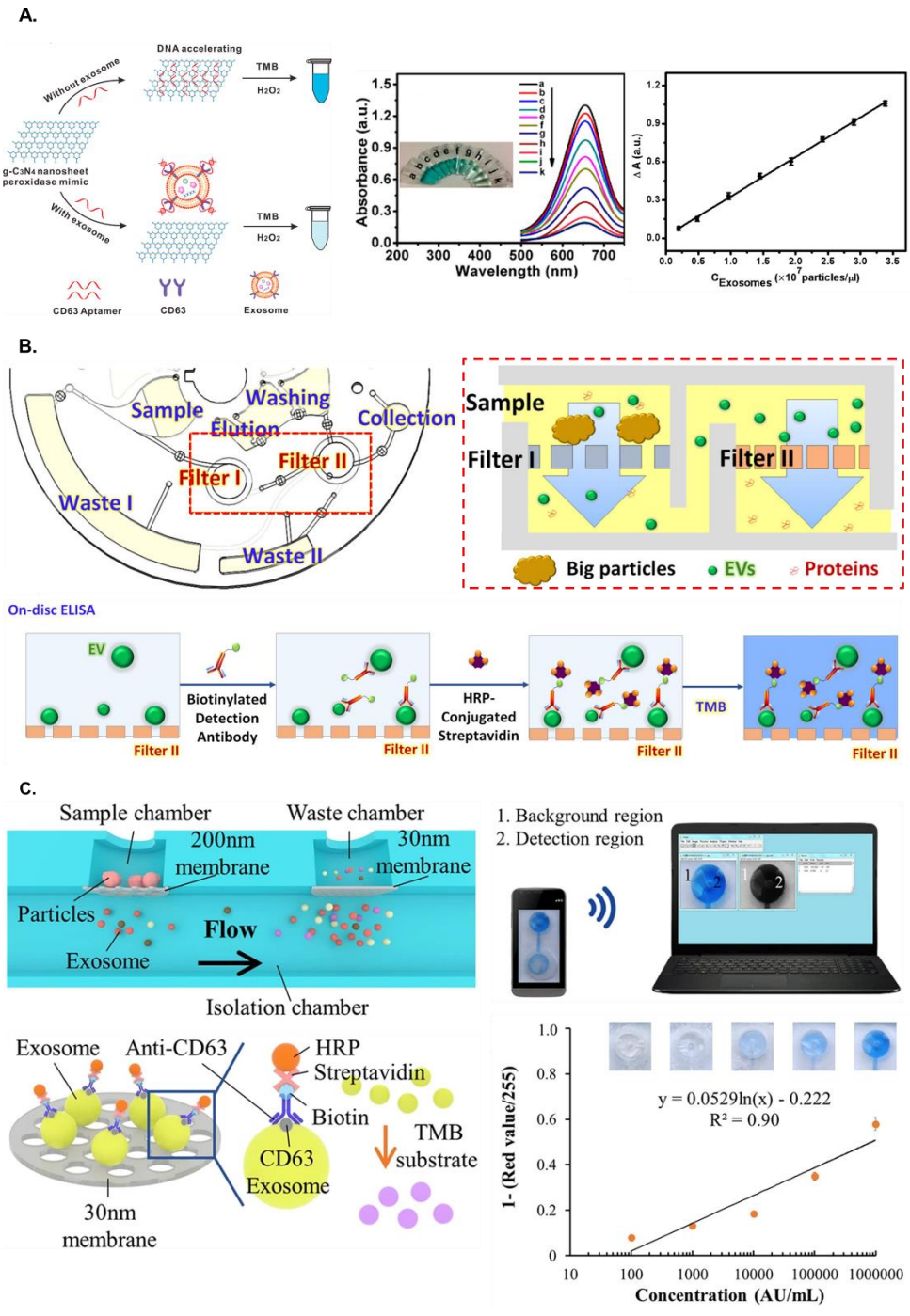

Fig 7: Colorimetric sEV detection strategies: (a.) (left) Colorimetric Detection of sEVs based on single-stranded DNA (ssDNA) accelerating the peroxidase-like activity of graphitic nitride nanosheets (NS). The ssDNA-NSs hybrid demonstrated a catalytic efficiency facilitated by robust interactions with TMB, resulting in a minimum fourfold increase in the reaction rate compared to unmodified NSs. (Top right) UV-vis absorption spectra at different concentrations of sEVs (a-k: 0, 0.19, 0.48, 0.97, 1.45, 1.93, 2.41, 2.89, 3.38, 3.86, 4.35 × 10^7 particles/μL). (Bottom right) Linear relationship between net absorbance (652nm) and concentration of sEVs; the system achieved a LOD of 13.52 × 10^5 particles/μL. Reproduced with permission from ref [244] (b.) Exodisc is a rapid, label-free, and highly sensitive approach for isolating and quantifying sEVs), where it is integrated with two nanofilters, enabling automated sEV enrichment from both cell-culture supernatant or cancer-patient urine within 30 minutes using a compact centrifugal microfluidic system. Reproduced with permission from ref [253] (c.) Double-filtration integrated microfluidic device for efficient isolation and detection of sEVs. By employing size exclusion, this device selectively captures sEVs with sizes ranging from 30 to 200 nm, facilitating on-chip direct ELISA for efficient sEV detection and imaging using a smartphone, potentiating future POC applications. (Bottom right) Standard curve of microchip ELISA for detection of sEVs and the images of colorimetric signal at each concentration. Reproduced with permission from ref [254].

1.6.3. Electrochemical-based Detection

Electrochemical detection involves the detection of target analytes as a result of changes in electrical signals like potential, current and impedance [255]. Electrochemical assays have shown excellent sensitivity and specificity for detecting biomolecules within complex matrices. These sensors allow for affordable, label-free, miniaturised sEV detection, thereby showing promise for potential POC systems [242]. Moreover, electrochemical sensors can be conveniently integrated with other systems for rapid and real-time analysis of sEV markers.

Nanomaterials like metal oxides, QDs, and CNTs have unique properties that make them appealing to incorporate into these biosensor systems [256, 257]. For instance, Boriachek et al. reported a voltammetric immunoassay for the detection of disease-specific sEVs using quantum dots for signal amplification. The method involved initial magnetic capture of sEVs with a CD63/CD9 antibody and subsequent identification of breast and colon cancer-specific sEVs using quantum dots functionalised with the corresponding antibodies. Anodic stripping voltammetric quantification was employed to enable the sensitive detection of sEVs with a detection limit of 100 sEVs per μL (Fig 8a, 8b) [258]. In a more recent study, the same group

developed an integrated sEV isolation and electrochemical detection system using gold-loaded ferric oxide nanocubes (Au-NPFe_2O_3NCs) functionalised with CD63 antibodies. sEVs were initially isolated using placental choriocarcinoma cells using the magnetic nanocubes, following which the sEVs were transferred to screen-printed electrodes, functionalised with anti-placental sEV antibody. The HRP-like activity of Au-NPFe_2O_3NCs facilitated TMB oxidation, resulting in diimine formation for both visual and electrochemical detection, achieving a low detection limit of 10^3 sEVs per mL [259].

The flexibility and simplicity of electrochemical sensors, along with their adaptability to miniaturised and automated systems, have driven the advancement of modified versions of traditional bio-analytical techniques. For instance, Dodan et al. integrated a sandwich ELISA format with an electrochemical immunosensor to detect and quantify sEV-associated CD9 based on the electrochemical reduction of TMB after the addition of HRP-conjugated antibodies. The system operated with a minimal sample volume (1.5 µL) and achieved a LOD of 200 sEVs/µL [260]. In another study, Zhou et al. modified an apatsensor by immobilising CD63 binding aptamers onto a gold electrode within a microfluidic system. Redox labelled probing strands were then hybridised onto aptamer molecules on the electrode surface, and in the presence of sEVs, the released probing strands with redox reporters led to a diminished electrochemical signal. The system was successful at detecting sEVs at concentrations as low as 1×10^6 particles/mL, and a ~100-fold improved sensitivity compared to analogous immunoassays [261]. The ease of engineering aptamers to emit specific signals upon analyte binding allows for designing easy-to-operate detection systems that can be used in resource-limited settings as a reliable and sensitive sEV-based diagnostic. Wang et al. leveraged the strengths of advanced aptamer technology, DNA-based nanostructures, and portable electrochemical devices to develop a nano tetrahedron (NTH)-assisted aptasensor that facilitates the direct capture and detection of hepatocellular sEVs. The oriented immobilisation

of aptamers enhanced the accessibility of a nucleobase-containing aptamer to sEVs, resulting in a ~100-fold higher sensitivity compared to the single-stranded aptamer-functionalized aptasensor (Fig 8c, 8d) [262].

While a majority of the sEV detection strategies target sEV surface protein markers, electrochemical sensor strategies can also be implemented to detect sEV-associated nucleic acids sensitively. In that context, Wang et al. developed a highly integrated enzyme-based electrochemical platform using a metal-organic framework (MOF)-based sensing interface for comprehensive profiling of tumour-specific sEVs. The multifunctional sensing interface, created through MOF self-assembly on DNA-modified electrodes, efficiently collected sEVs from biofluids and simultaneously detected sEV-associated proteins and RNA molecules on a single sensor chip. The platform successfully detected sEV-miRNA-21 at concentrations as low as 3.6 fM in a 10 μL sample and outperformed traditional immunoassays by enabling multiparametric analysis of breast cancer [263] (Fig 8e, 8f). The continuous development of electrochemical sensors equipped with robust design architecture will allow for reliable profiling and sensitive detection of tumour-specific sEVs in clinical settings.

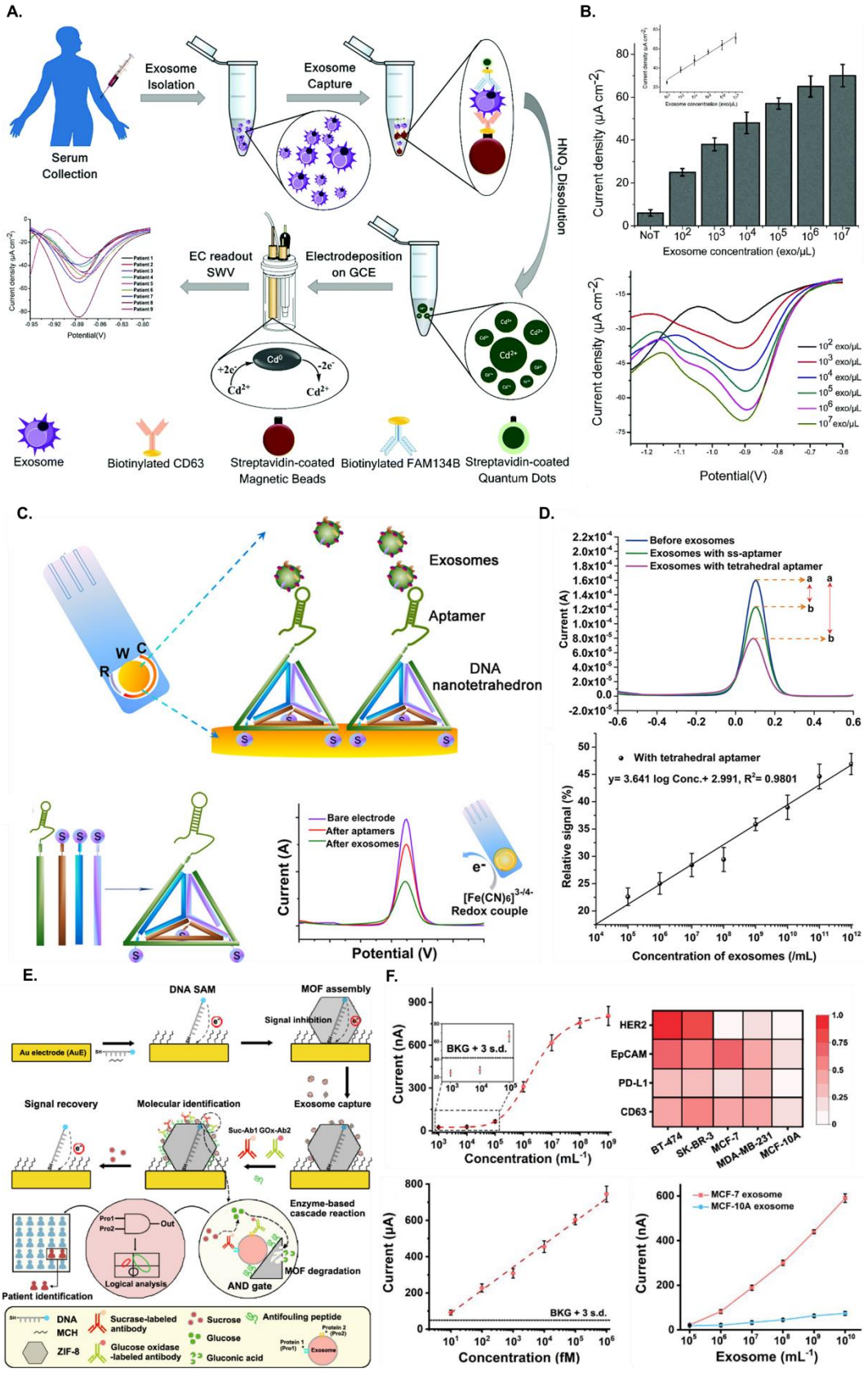

Fig 8: Electrochemical-based sEV detection: (a.) QD-based electrochemical detection of sEV markers. sEVs were first magnetically captured using a general antibody (CD63 or CD9), and subsequently, cancer-specific sEVs were isolated through CdSeQD-functionalized specific antibodies (FAM134B for

colon and HER2 for breast cancer). The quantification of disease-specific sEVs was accomplished by acid dissolution of CdSeQDs and subsequent anodic stripping voltammetric measurement of Cd^{2+}. (b.) Square-wave anodic stripping voltammetry (SWASV) current densities at different concentrations of sEVs isolated from BT474 breast cancer cells. The system achieved a detection limit of 100 sEVs/µL. Reproduced with permission from [258] (c.) DNA-NTH assisted electrochemical aptasensor-based detection of EVs. The electrochemical aptasensor employed NTHs for immobilising aptamers onto gold electrodes, allowing the direct capture of sEVs in suspension. The facile self-assembly of DNA NTH and subsequent redox signal changes after aptamer immobilisation and incubation with sEVs demonstrated effective signal generation and amplification on the electrode. (d.)(Top right) Electrochemical current collection of a single-stranded aptamer and NTH-assisted aptasensor for detection of 10^{13} sEVs/mL and current signal before and after aptamer capture of sEVs for each electrode. (Bottom right) Calibration curve of the NTH-assisted aptasensor with sEV concentration ranging from 10^5 to 10^{12} sEVs/mL, achieving a LOD of 2.09×10^4 sEVs/mL. Reproduced with permission from ref [264] (e.) MOF functionalised sensing electrochemical interface designed to analyse both sEV protein and RNA markers on a single integrated chip. The study leveraged the bio-analytical applications of ZIF-8-Modified Gold Electrode (ZIF-8/AuE) for sEV Capture and Analysis. (f.) (Top right) Calibration curves for quantifying MCF-7 sEVs with the dashed line (inset) indicating the LOD of the sensor and profiling of four protein markers on multiple cell-derived sEVs. (Bottom right) Calibration curve of quantifying miR-21 and detection of sEV-miR-21 in MCF-7 and MCF-10A sEVs at different concentrations. Reproduced with permission from ref [263].

1.6.4. Surface-Enhanced Raman Scattering (SERS) based detection

SERS is a spectroscopic technique based on plasmonics that employs a laser and leverages the optical properties of metallic nanostructures to extract detailed chemical information from molecules adsorbed or attached to them. SERS strengthens Raman scattering by molecules adsorbed on rough metal surfaces or by nanostructures [265, 266]. There are two main enhancement modes of SERS, namely electromagnetic enhancement and chemical enhancement. The former is attributed to a local increase in the electromagnetic field induced by surface plasmon resonance; the latter is achieved by charge transfer between a metal nanoparticle and target molecule [267]. SERS is a highly effective and selective analytical method and has attracted attention in sEV detection due to its high sensitivity and multiplex detection capability [268, 269]. SERS detection strategies, with robust Raman spectra and customisable nanostructured substrates, are well-suited for obtaining high-quality signals from sEV-associated surface proteins and internalised nucleic acids, enabling comprehensive

diagnostic information extraction through single-molecule detection and efficient multiplexing capabilities [267].

SERS biosensors achieve high performance when integrated with nanomaterials and nanostructures. Zong et al. was the first study to report a SERS-based approach to detect tumour-specific sEVs. Utilising magnetic beads and SERS functionalised with specific antibodies targeting CD63 and the tumoral marker HER2, the method formed a sandwich-type immunocomplex in the presence of sEVs. Employing magnetic beads to separate sEVs from the cell media facilitated the detection of SERS signals in the isolated sEVs, achieving specific detection of sEVs at a detection limit of 6×10^4 sEVs per mL [270]. In a more recent study, Wang et al. integrated aptamers instead of antibodies in a SERS platform to simultaneously detect multiple sEVs. Silica-coated magnetic beads functionalised with CD63 aptamers captured sEVs, while SERS probes (AuNP@aptamer) with different reporters were synthesised for multiplexing. The sensor achieved a detection limit of ~10^3 sEVs across multiple sEV types and successfully distinguished cancer-specific sEVs from healthy patient sEVs (Fig 9a, 9b) [271].

SERS based sensors have also explored the detection of sEVs in a label-free approach without using antibodies or aptamers to recognise sEVs. For instance, Lee et al. designed a 3D nano bowl SERS system based on the thin silver film for time-dependent detection of SKOV3-derived EVs [272]. In a more recent study, Dong et al. designed a bee-hive resembling an Au-coated TiO_2 macroporous inverse opal (MIO) structure, leveraging a tailored "slow light effect" for enhanced SERS performance. This MIO structure enabled label-free capture and analysis of sEVs from cancer patients' plasma, with the SERS intensity of the 1087 cm–1 peak serving as a diagnostic criterion for tumor liquid biopsies. The system achieved at least a twofold increase in the 1087 cm–1 SERS peak intensity for sEVs from cancer patients compared to healthy patients, establishing the method's simplicity and versatility in cancer diagnostics

[273]. Apart from sEV surface protein markers, the clinical significance of sEV-nucleic acids has also inspired the application of SERS sensors towards the sensitive detection of sEV-miRNAs [75, 79].

SERS systems have also been combined with microfluidic platforms in integrated sensors to facilitate the separation and detection of sEVs, while ensuring high purity, high efficiency and sensitive detection of sEVs [99, 274, 275]. Integrated SERS systems have applied both label-based and label-free approaches to detect sEV markers [251-253] sensitively. Recently, Zhao et al. targeted sEV-miRNA to develop an integrated SERS sensor, which employed an RCA and tyramine signal amplification (TSA) strategy. The system integrated a magnetic enrichment chamber, a serpentine fluid mixer, and a plasmonic SERS substrate with capture probes. In the presence of target miRNA, the capture probes triggered RCA, leading to tyramine cascade amplification, generating multiple 'hot spots' and significantly enhancing SERS signals. The system successfully detected miR-21 in breast cancer cell-derived sEVs, with a detection limit of 1 pmol/L (Fig 9c, 9d) [276].

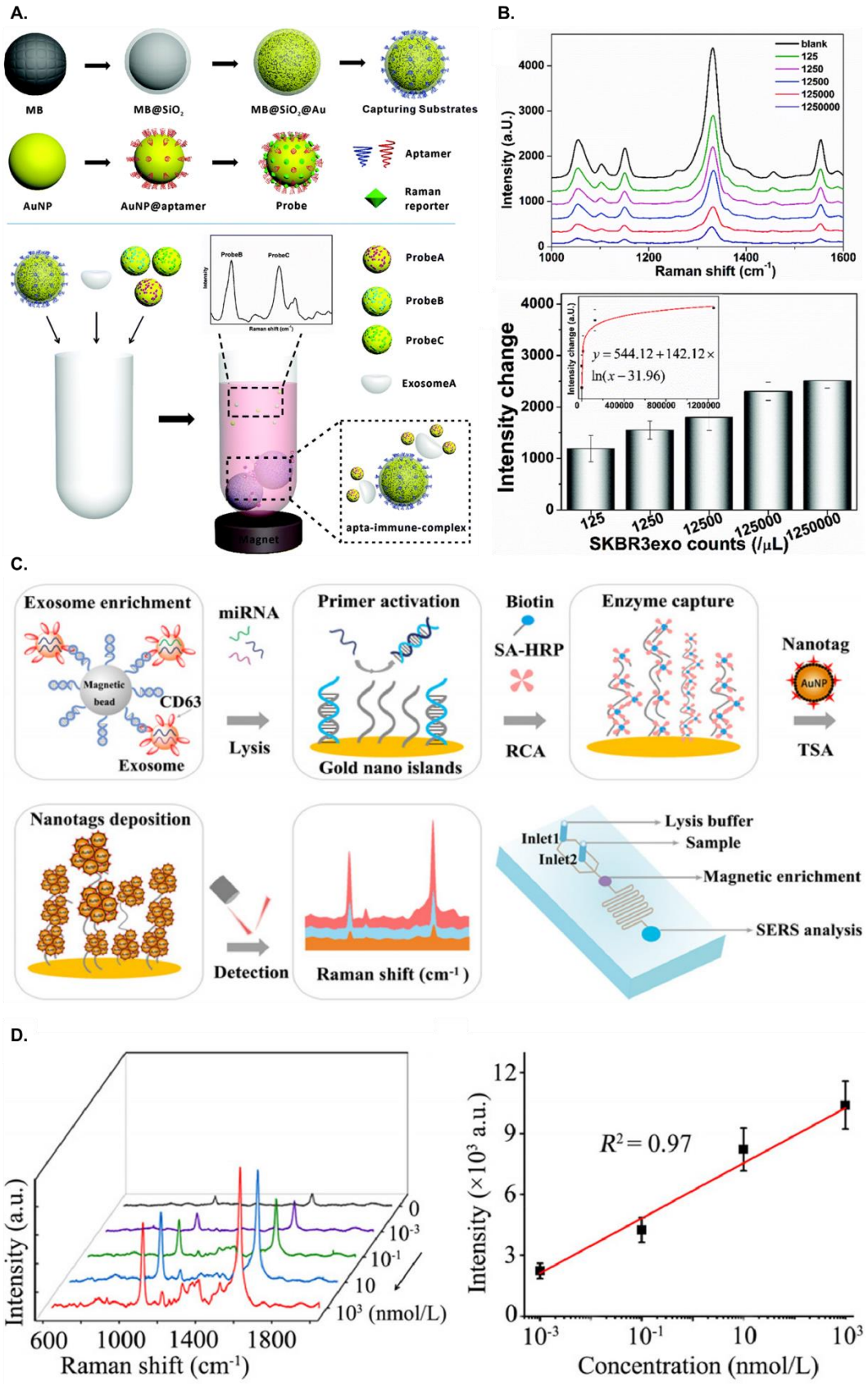

Fig 9: SERS based sEV detection: (a.) Screening and detection of multiple cancer specific sEVs using a SERS based sensor. The study used magnetic substrates and SERS probes for the simultaneous and multiple detection of sEVs. The gold shell magnetic nanobeads modified with aptamers served as

capturing substrates, recognising sEV through the surface protein CD63, while gold nanoparticles with specific aptamers acted as SERS probes for different sEVs types, generating a decreased SERS signal intensity in the presence of the target sEVs. (b.) (Top) SERS spectra of the supernatant after adding SKBR3 sEVs at different concentrations. (Bottom) The change in intensity of the 1326 cm^{-1} band of the spectra was recorded at different sEV concentrations; the system achieved a detection limit of 32 SKBR3 sEVs/µL. Reproduced with permission from ref [271] (c.) Schematic of an integrated SERS sensor for detecting sEV miRNA with nucleic acid-tyramine cascade amplification. The chip integrated a magnetic enrichment chamber, a serpentine fluidic mixer, and a plasmonic SERS substrate with capture probes. The released miRNA initiated a cascade, including RCA reaction and catalyzed nanotag deposition via TSA, creating abundant "hot spots" to amplify SERS signals. (d.) (Left) SERS measurements of DmiR-21 at various concentrations. (Right) Linear relationship between signal intensity of the band at 1583cm-1 and DmiR-21 concentrations, achieving a detection limit of 1pmol/L. Reproduced with permission from ref [276].

1.6.5. Surface Plasmon Resonance (SPR) Detection

SPR is a resonant oscillation of conduction electrons at the interface between a negative and a positive dielectric constant material under stimulation by incident light. This oscillation is very sensitive to changes resulting from the interaction of molecules on the conductive surface, making them suitable for application in biosensors [277, 278]. The high sensitivity and rapid label-free detection of sEVs using SPR-based methods make them suitable for implementation in sEV-based liquid biopsy systems [279]. One of the best examples of an SPR-based platform employed towards sEV detection was a nanoplasmonic sEV (nPLEX) sensor designed by Im et al., where the sensor featured periodic nanohole arrays in a gold film strategically designed for matching sEV dimensions (<200 nm) and facilitating enhanced sensitivity. Employing a multichannel microfluidic system, the sensor integrated PEG passivation and anti-CD63 antibody functionalisation, enabling high-throughput analyses. The sensor was successful at detecting CaOV3 sEVs at a detection limit of ~3000 sEVs, which was a ~102-fold improvement over parallelly conducted ELISA analyses. The study also demonstrated a ~300% enhanced signal intensity by using AuNPs as secondary labels [97]. In another study, Zhu et al. designed an integrated microfluidic chip that facilitated real-time quantitative detection of tumour derived sEVs. The system combined SPR imaging with antibody microarrays specific

to the extracellular domains of sEV markers and accurately quantified multiple sEV markers, reaching a detection limit of ~4.87 × 10^7 sEVs/cm^2 with a throughput of 300μL/min [280]. Similar systems combining antibody immunoaffinity approaches within SPR-based detection platforms have proven successful in detecting both structural and disease-specific surface markers on sEVs with high sensitivity [278, 281-283].

1.6.6. Single EV analysis

The identification of sEV subpopulations in a background of heterogenous EVs is difficult by analytical methods relying on bulk EV measurements for EV analysis. Intrinsic heterogeneity is one of the main hindrances to sEV analysis in biofluids. Single EV detection allows for more accurate information on tumour progression and would be immensely valuable for early detection and assessing tumour heterogeneity and phenotypic variations [45]. Microfluidics have permitted automated and integrated systems to compartment samples into single EV resolution, minimising sample consumption and enhancing sensitivity [284]. Several microfluidic applications have been implemented towards EV analysis both at the single-cell and single-vesicle level, including microwell/chamber-based systems [192, 260-262], microchannel-based systems [263, 264] and droplet-based-microfluidics [205, 285].

Digital techniques like digital PCR (dPCR) and digital ELISA have enabled ultrasensitive digital detection of single molecules, making them suitable for single EV analysis. These methods generally quantify the fluorescence signals from spatially isolated labelled beads [286-289]. However, these strategies individually are unable to achieve the sensitivity to detect single EVs and the specificity to differentiate specific/rare EV subsets based on their surface protein expression. Lin et al. integrated digital droplet PCR with aptamer-based proximity ligation assay for digital quantification of sEV-associated PD-L1. The study exploited the high binding affinity and selectivity of aptamers combined with the sensitivity of droplet digital PCR

(ddPCR) to sensitively quantitate tumour-derived sEV-associated PD-L1 at a detection limit of 0.0735 pg/mL [290]. Integrated ELISA strategies have also been explored to achieve ultrasensitive detection of sEVs and specific EV subpopulations. Liu et al. developed an immunomagnetic droplet system to quantify the number of sEVs (ExoELISA). EVs were anchored to the magnetic micro-beads through a sandwich ELISA with a fluorescent enzymatic reporter. The fluid volume in a droplet was enough to encapsulate a single bead. The droplet-based digital ELISA system allowed for very accurate sEV detection and could detect as low as 10EVs/μL. The study also accurately quantified GPC-1^+ sEVs in plasma samples in breast cancer samples and differentiated them from healthy controls (Fig 10a) [205]. More recently, a droplet-based optofluidic digital ELISA system was reported to quantify specific EV subpopulations at a throughput 100 times greater than typical microfluidics (~20 million droplets/minute). The system implemented parallelisation of droplet generation, processing and analysis to achieve an ultrasensitive detection limit of 9EVs/μL, which is ~100 times more sensitive than conventional gold standard methods (Fig 10b) [291]. These studies demonstrate the potential of microfluidics to develop a powerful single EV analysis approach to investigate the heterogeneity of EVs. Single-molecule arrays (SiMoA) have established themselves as an ultrasensitive digital ELISA platform that can detect single protein molecules in complex samples [289, 292] and has been implemented to sensitively detect EVs in cell-derived and plasma samples at single EV resolutions [80]. Future studies should explore the integration of the SiMoA technology with EV separation strategies to achieve integrated sEV isolation from complex sample types that facilitate enhanced detection sensitivity of sEVs.

Integrated digital systems have also been combined with microfluidic systems to facilitate the detection of EVs at the single vesicle resolution [293, 294]. Lee et al. integrated an inverted microscope setup with a scientific complementary metal oxide semiconductor (sCMOS) camera in a microfluidic chip to facilitate multiplexed profiling of single sEVs. The system

allowed for stable capture of EVs and on-chip immune-staining and imaging of immobilised EVs in the microfluidic chamber. The imaging cycles were repeated for multiple target biomarkers over multiple rounds and was successful at realising multiplexed analysis of 11 different surface proteins on individual EVs derived from a glioblastoma cell line [295]. Raghu et al. implemented a similar imaging setup in an SPR-based microfluidic chip to achieve label-free and multiplexed single sEV detection. The study implemented a nano-sensing array tailored towards single sEV detection and achieved three orders magnitude of improved sensitivity compared to previously reported real time, multiplexed platforms [296]. The major hindrance in single EV detection systems is the relatively low abundance of specific surface proteins. Since amplification of the target protein in single EVs is not possible, studies have explored strategies where protein profiles are transformed to DNA sequences followed by sequencing to characterise proteins of EVs [285, 294]. Ko et al. devised an antibody-based immune-sequencing system that facilitated multiplexed analysis of proteins from individual EVs. The study incorporated droplet microfluidics to compartmentalise and individual EVs. Following this, the barcodes/antibody-DNA are sequenced to profile protein composition allowing for highly sensitive, multiplexed detection of specific proteins at the single EV resolution [285]. The system provides an improvement in throughput compared to analogous approaches and can be implemented to profile large numbers of EVs, making them scalable and applicable in the profiling of rare proteins in diverse nanoparticles [294].

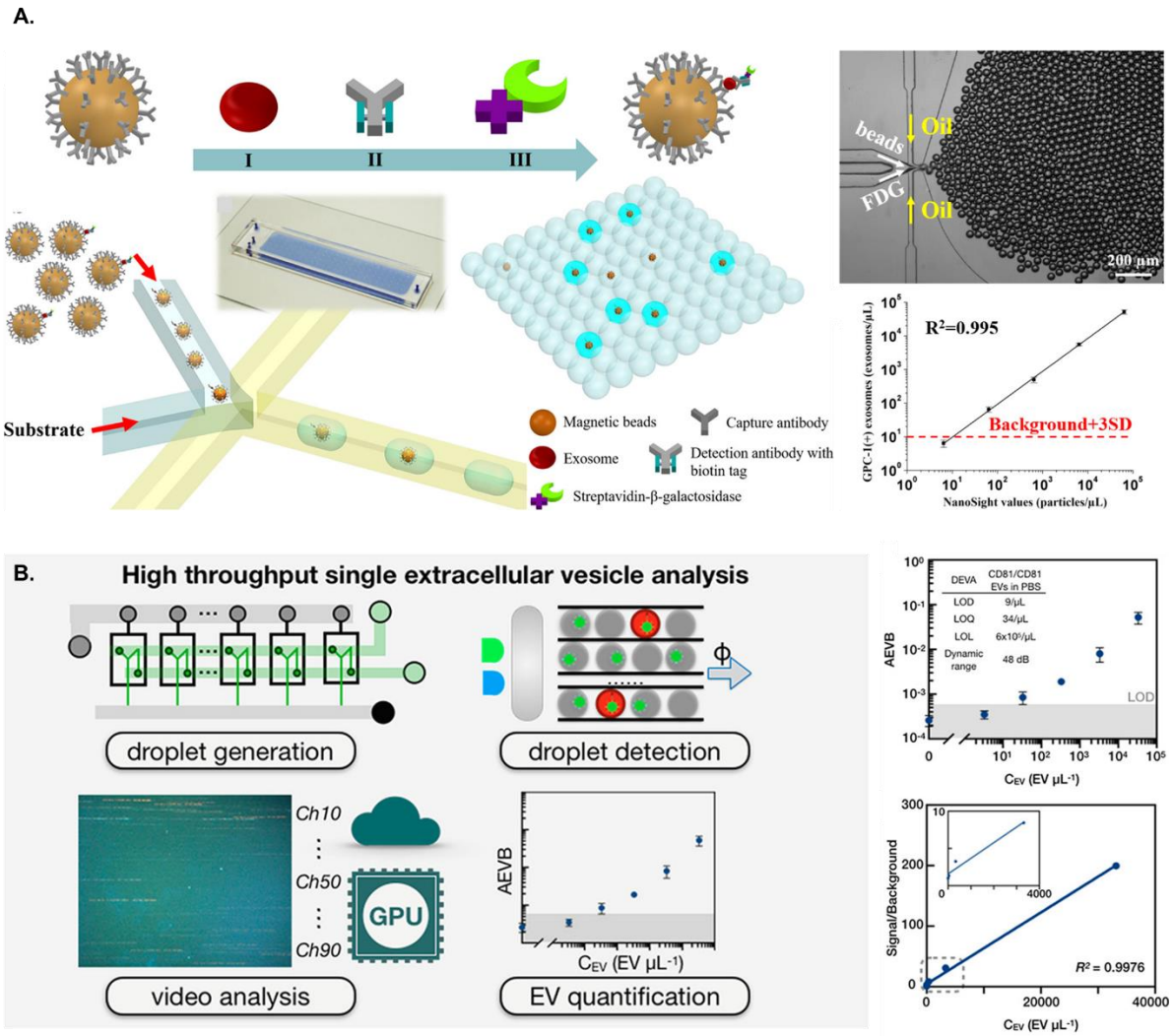

Fig 10: (a.) Schematic of the droplet digital ExoELISA for sEV quantification. Magnetic beads construct a single sEV immunocomplex and the microdroplets encapsulate both the substrate and beads. The ExoELISA chip employs droplet digital technology to counting positive droplets with target sEVs is achieved through fluorescent readout. The calibration curve shows the dynamic range of sEV concentrations across 5 orders of magnitude. The system achived a detection limit if 10 sEVs/μL (indicated by red dash line). Reproduced with permission from ref [205]. (b.) High throughput droplet digital ELISA for sEV analysis. The platform parallelised droplet generation, detection and digital analysis to achieve an ultrasensitive detection limit of 9EVs/μL, a ~100× improvement over gold standard methods. Reproduced with permission from [297].

1.6.7. Lateral Flow Immunoassays for sEV detection

Lateral flow assays (LFAs) have emerged as a widely recognised and adaptable technology for rapidly identifying target analytes. Particularly well-suited for point-of-care diagnostics (POC), they offer numerous benefits in contrast to alternative analytical approaches. Notably, their

rapid and economical characteristics make them advantageous, requiring no sophisticated equipment [298]. In a typical LFA setup, the sample is introduced onto the sample pad and moves through capillarity to the conjugate pad. At this stage, the analyte in the sample interacts with a conjugate consisting of a detection antibody linked to relevant nanoparticles (Fig 9a) [299, 300]. The resulting complex travels across the nitrocellulose membrane, where the analyte is recognised by the capture antibody immobilised at the test line. Simultaneously, any excess substance reaches the control line, where a secondary antibody is immobilised to confirm the proper functioning of the test. In summary, the test and control lines display positive results if the target analyte is present in the sample. Conversely, if the analyte is absent, only the control line registers a positive outcome (Fig 11a). The most prominent illustration of this bioanalytical approach is demonstrated by the human pregnancy test, which operates by detecting human Chorionic Gonadotropin (hCG) in urine [301, 302].

The simplicity in operation and rapid identification of target analytes have motivated the implementation of LFAs towards the detection of sEV markers. Oliveira-Rodriguez et al. was among the earliest to facilitate LFA-based detection of tetrasparins as targets from purified sEVs from cell culture supernatants of Ma-Mel-86c melanoma cells. The study used 40nm gold nanoparticles (AuNPs)-conjugated anti-CD63 as detection antibody and a combination of anti-CD9 and anti-CD81 as capture antibodies to detect 8.54×10^8 sEVs per mL. The study was also successful at sEV markers on sEVs isolated from plasma and urine samples [215]. Cobo et al. demonstrating a similar strategy of AuNP-labelled LFAs, to detect the tumour-derived antigen MICA in sEVs, marking a novel application in LFA. The study highlighted crucial optimisation strategies in the context of LFAs, including addressing competition events and steric effects, to target scarce proteins like MICA with the detection antibodies on AuNPs, and facilitate improved detection limits [303]. Studies have also assessed the comparative performance of diverse nanoparticles in LFAs, including AuNPs, Carbon Black dots and

magnetic nanoparticles (MNPs), with the AuNPs showing superior performance, specifically in the context of ease of functionalisation and better linear range fitting [304, 305]. The sensitivity of LFAs can also be improved by signal enhancement of the nanoprobes. Towards this, Dong et al. combined the simple, rapid quantification of LFAs with a membrane biotinylation strategy by labelling sEVs with a biotin-tagged DSE-PEGbiotin, forming a complex with streptavidin-conjugated fluorescent nanospheres (FNs-SA) for detection. Streptavidin deposition at the LFA test strip's test line facilitated the interaction, enabling the testing of Cal-27 cell-derived sEVs with a minimal detectable concentration of 2.0×10^6 particles per mL (Fig 11b) [306]. In another signal enhancement technique, Wang et al. integrated Fe_3O_4 nanozymes in an LFA format to detect sEVs. Iron oxide superparamagnetic nanoparticles (Fe_3O_4 MNPs), known for their peroxidase-like capabilities, were coated with oleic acid and employed as colorimetric labels and LFA strips were immersed into TMB and H_2O_2 mixed solution to facilitate signal amplification. This strategy significantly enhanced visual signals and reduced the detection limit from 5.73×10^7 EVs/μL to 2.49×10^7 EVs/μL [307].

Apart from optimising assay and nanoparticle-probe conditions and chemical/signal enhancement used in LFAs, studies have also implemented pre-concentration and pre-amplification steps to facilitate sample enrichment and enhanced detection sensitivity. While pre-concentration steps have facilitated improved detection of sEV-proteins [308], the pre-amplification step is more relevant for detection of sEV-nucleic acids. In that context, Kim et al. presented a DNA barcode-based nucleic acid LFA (NALFA) for the identification of colorectal cancer-specific sEV-miRNA. The study integrated reverse transcription with a stem-loop primer to amplify the target RNA, and the technology generated a colorimetric signal exclusively in the presence of target sEV-miRNA. The system also achieved 95.24% sensitivity and 100% specificity in the detection of target miRNA in sEVs isolated from plasma samples

(Fig 11c) [309]. As an alternative to traditional LFAs, Wang et al. developed a competitive LFA that relies on a CD63 aptamer-functionalised AuNP format, where in the presence of sEV-CD63, the interaction between the aptamer on AuNPs and sEV-CD63 prevented binding to the test line. In the absence of sEV-CD63, the AuNPs@aptamer interacted with the complementary aptamer present at the test line to generate a positive signal. The system achieved a detection limit of 6.4×10^8 particles per mL for lung carcinoma A459 cell-derived sEVs, but further refinement is needed, such as validating with a control line on test strips, managing AuNP aggregation, and enhancing reproducibility during strip assembly [310].

However, a majority of the LFA strategies involve colorimetric interpretation, which have limited sensitivity in the absence of pre-treatment and/or signal enhancement and do not allow quantitative detection of target analytes [311, 312]. Overcoming these constraints can be achieved by incorporating highly stable and sensitive fluorescent nanoparticles into LFAs, facilitating the development of robust quantitative analytical assays. Lanthanide-doped upconversion nanoparticles (UCNPs) are especially valuable in this context, exhibiting the ability to merge lower-energy photons into a higher-energy photon, making them well-suited for single-molecule biosensing and bioimaging applications [177]. The nonbleaching, nonblinking, and anti-Stokes emissions of UCNPs, along with their adjustable colours, position them as ideal probes for multiplexed assays. The application of UCNP-based LFAs in various studies has demonstrated improved accuracy and sensitivity in detecting disease-specific target biomarkers, showcasing significant potential for point-of-care testing applications [313-317]. The application of UCNP-based LFAs in various studies has demonstrated improved accuracy and sensitivity in detecting disease-specific target biomarkers, showcasing significant potential for POCT applications [318-321].

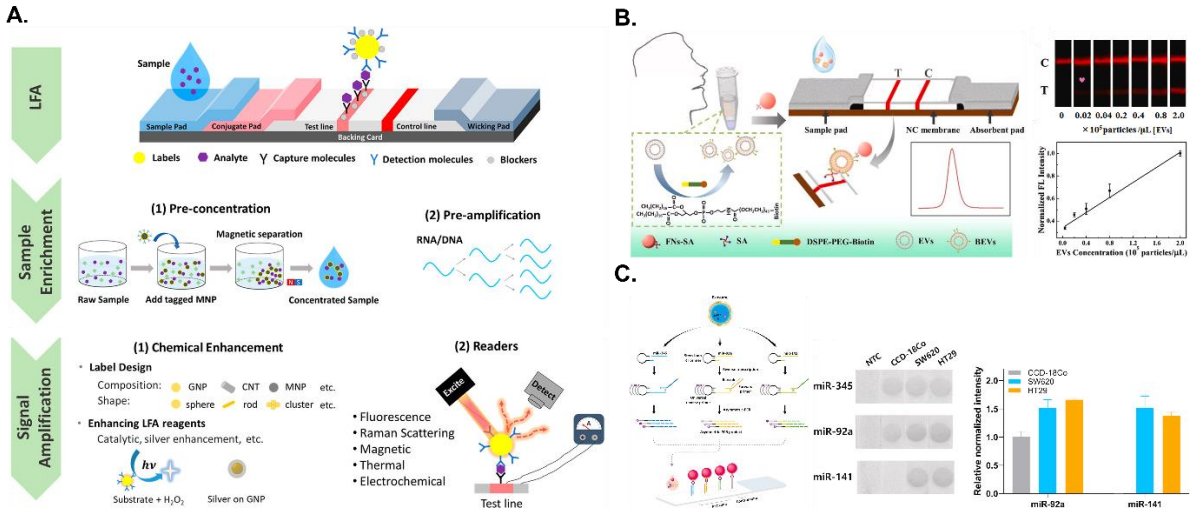

Fig 11: LFA based detection of sEV protein markers or nucleic acids (a.) Schematic representation of a sandwich LFA. Approaches aimed at enhancing the sensitivity of LFAs include sample enrichment techniques, allowing for preconcentration and amplification of analytes to improve detection limits, as well as signal amplification methods, involving chemical enhancements or the incorporation of readers to directly enhance LFA signals. Reproduced with permission from ref [322] (b.) Combining membrane biotinylating strategy and FNs-based LFA for simple and rapid sEV. T line and C line were immobilised with streptavidin (SA) and biotin respectively. Reproduced with permission from ref [306] (c.) Schematic illustration of the DNA barcode-based nucleic acid LFA (NALFA) for the analysis of multiple sEV miRNA markers on a single LFA strip. The system successfully identified miR-92a and miR-141 in colorectal cancer sEVs, generating a colorimetric signal discernible to the naked eye only in the presence of the target sEV miRNA. Reproduced with permission from ref [309].

Table 2: Summary of nanoparticle-based and integrated sEV detection platforms

Methods	sEV sources	sEV targets	Sensing mechanism	Detection limit	Ref.
Fluorescence Detection	Cell culture supernatant/pancreatic cancer serum	CD63	CD63 antibody-functionalized EXOchip; Fluorescent carbocyanine dye (DiO)	Not Specified	[223]
	Breast Cancer Cell culture supernatant/Samples	EpCAM, Her2	Microfluidic Immunomagnetic Capture and Fluorescent Detection	Not Specified	[224]
	Cell culture supernatant/clinical samples	PD-L1	Magnetic Beads Isolation and Fluorescence Detection	10.76 sEVs/μL	[226]
	Cell Culture Supernatant	CD63	Copper-mediated Signal Amplification	4.8×10^4 particles/μL	[231]
	Cell Culture Supernatant	CD63	DNP-AuNP Satellite Network and aptamer-based Rolling Circle Amplification	$\sim 10^5$ particles/μL	[232]
	Cell Culture Supernatant	sEV-miR-21	Microfluidic Exponential Rolling Circle Amplification	<10 zeptomole; 2×10^6 sEVs	[237]
	Cell Culture Supernatant	sEV-miR-21, sEV-miR-375, sEV-miR-27a	Molecular beacons and fluorophore-based multiplexed detection of sEV-miRNAs	Not Specified	[238]
	Cell Culture Supernatant/Pancreatic Cancer Serum	sEV-GPC-1 mRNA	Signal-amplifiable biochip based on Lipid-Polymer Hybrid NPs (LPHNs) containing catalysed hairpin DNA Circuit (CHDC)	0.01 pg (0.46 amol)	[240]
	Cell Culture Supernatant/Lung Cancer Sera	sEV-miR-21, sEV-TTF-1 mRNA	Immuno-biochip-based isolation of sEVs and quantification of sEV-RNA using cationic lipoplexes containing molecular beacons	Not Specified	[241]

Colorimetric Detection	Cell Culture Supernatant	CD63	Aptasensor based on DNA-capped single-walled carbon nanotubes catalysing H_2O_2-based TMB oxidation	5.2×10^5 particles/μL	[243]
	Cell Culture Supernatant	CD63	ssDNA-based enhancement of peroxidase-like activity (TMB oxidation) of graphitic carbon nitride nanosheets	13.52×10^5 particles/μL	[244]
	Cell Culture Supernatant/Breast Cancer Samples	CD63	Dual Signal Amplification Strategy of Enzyme-Catalyzed Metallization of Au Nanorods and Hybridization Chain Reaction	9×10^3 particles/μL	[248]
	Cell Culture Supernatant/Bladder Cancer Samples	CD9, CD81	ExoDisc: On-Chip TMB-based ELISA detection of sEV	Not Specified	[253]
Electrochemical Detection	Cell Culture Supernatant	CD63	Direct Isolation and Sensitive Detection of sEVs using Gold-Loaded Nanoporous Ferric Oxide Nanozymes	10^3 sEVs/mL	[249]
	Cell Culture Supernatant	CD9	Electrochemical Sandwich Immunosensor Based on Surface Marker-Mediated Signal Amplification	10^3 particles/μL	[260]
	Cell Culture Supernatant	CD63	Aptamer based electrochemical detection	10^6 particles/mL	[261]
	Cell Culture Supernatant	EpCAM	Aptasensor with Expanded Nucleotide Using DNA Nanotetrahedra for Electrochemical Detection	2.09×10^4 sEVs/mL	[262]
	Cell Culture Supernatant/Breast Cancer Samples	Her-2, EpCAM; sEV-miR-21	Metal–Organic Framework-Based Sensing Interface and an Enzyme-Based Electrochemical Logic Platform	2.3×10^6 sEVs/mL; 3.6 fM	[263]
SERS based detection	Cell Culture Supernatant	CD63, Her-2	Magnetic nanobeads and SERS probes based sEV detection	~1200 sEVs	[270]
	Cell Culture Supernatant	CD63	Magnetic substrates and SERS probes	~203 sEVs/μL	[271]

	Plasma of cancer patients	Label-free sEV detection	Beehives-like Au-coated TiO_2 macroporous inverse opal	Not Specified	[323]
	Cell Culture Supernatant/Lung Cancer Samples	sEV-miR-21	Combination of SERS reporter element and duplex-specific nuclease (DSN)-assisted signal amplification	~5 fM	[79]
	Cell Culture Supernatant	sEV-miR-21	Microfluidic SERS sensor for miRNA in sEVs with nucleic acid-tyramine cascade amplification	1 pmol/L	[276]
SPR Detection	Cell Culture Supernatant	CD24, EpCAM	Nano-plasmonic exosome (nPLEX) assay based on transmission surface plasmon resonance through periodic nanohole arrays	~3000 sEVs (670 aM)	[97]
	Cell Culture Supernatant/Breast Cancer Samples	Her-2	Label-free approach for on-chip profiling of sEVs using a SPR sensor	2070 sEVs/μL	[281]
	Multiple Myeloma Patient Samples	Label-free sEV detection	Merging colloidal nanoplasmonics and surface plasmon resonance spectroscopy	~10 pM	[283]
Single EV Detection	Cell Culture Supernatant/Breast Cancer Samples	GPC-1	Droplet Digital ExoELISA	~10 sEVs/μL	[205]
	Cell Culture Supernatant/Human Plasma Samples	CD81	Droplet-based optofluidic platform for single sEV detection	9 EVs/μL	[297]
	Cell Culture Supernatant	CD9, CD63, CD81, EGFR, PD-L1, PD-L2	Microfluidic multiplexed profiling of single Evs	Not Specified	[295]
Lateral Flow Assay based sEV detection	Cell Culture Supernatant	CD9, CD81, CD63	Gold Nanoparticle based Lateral flow Assay	8.54×10^5 sEVs/μL	[215]

	Cell Culture Supernatant	MICA, CD9	Gold Nanoparticle based Lateral flow Assay	Not Specified	[303]
	Cell Culture Supernatant	CD63, CD147	Magnetic Nanoparticle based Lateral Flow Assay	~10^7 EVs/μL	[324]
	Cell Culture Supernatant	Biotin tagged EVs	Membrane biotinylation strategy coupled with fluorescent nanospheres-based lateral flow assay	2×10^3 particles/μL	[306]
	Plasma Samples	CD63, CD9	Nanozyme-Based Lateral Flow Immunoassay	2.49×10^7 EVs/μl	[325]
	Cell Culture Supernatant/Colorectal Cancer Samples	sEV-miR-345, sEV-miR-92a, sEV-miR-141	DNA barcode-based nucleic acid lateral flow assay	Not Specified	[309]

Table 2 comprehensively compares nanoparticle-based and integrated platforms for sEV detection, showcasing their strengths and applications (Table 2). Fluorescence-based detection remains one of the most widely employed approaches due to its high sensitivity and versatility, particularly for multiplexed analyses of sEV proteins and nucleic acids. Colorimetric strategies, while practical and cost-effective, can achieve comparable sensitivity through advanced signal amplification strategies. Electrochemical platforms demonstrate enhanced sensitivity, with detection limits as low as ~10^3 sEVs/mL, offering robust quantification and suitability for profiling low-abundance sEV markers. Similarly, SERS-based methods exhibit exceptional sensitivity (~10^2 sEVs/μL) and enable detailed molecular profiling, though their reliance on specialized equipment limits their clinical implementation. Single sEV detection platforms are particularly valuable for characterising the heterogeneity of sEV populations, achieving unparalleled sensitivity (~10 sEVs/μL) and enabling detailed molecular analysis at the single-vesicle level. Among these methods, LFAs and nanoparticle-based immunoassays stand out for their potential to be developed into POC sEV diagnostic systems. Their rapid, user-friendly design and compatibility with minimal instrumentation make them particularly suitable for integration into clinical settings, offering a promising pathway for accessible and reliable sEV detection systems.

1.7. UCNPs in bio-sensing applications

UCNPs, recognised as a prominent luminescent nanomaterial in biomedicine fields, offer unique advantages for fluorescence detection (Fig 12) [326, 327]. The anti-Stokes process of upconversion luminescence (UCL), converting longer-wavelength light into shorter-wavelength light through photon energy transfer, particularly stands out [328, 329]. Lanthanide-doped UCNPs, especially under near-infrared (NIR) light, exhibit distinctive UCL properties such as sharp emission lines, substantial anti-Stokes shift, extended lifetimes, non-

blinking, and remarkable photostability. The NIR light used for UCNPs excitation has advantages like low phototoxicity, deep penetration, minimal photobleaching, and weak autofluorescence [202, 328]. These outstanding features make NIR-excited UCNPs highly sought-after in fluorescence detection, garnering substantial research interest.

Comparatively, UCNPs offer unique advantages over other approaches like small molecules and gene coding. While small molecules have been used to detect biomarkers, their stability in the physiological environment is often compromised due to a lack of biocompatibility [330, 331]. In contrast, UCNPs, with reasonable modification, remain biocompatible and can effectively carry small molecules, making them suitable for constructing highly stable and sensitive biosensors [332]. Moreover, UCNP-based sensing devices can identify analytes by detecting luminescence intensity, offering ease of manufacturing and adaptability to various scenarios. Additionally, UCNPs, being biocompatible, can enter various cell types, making them a focus of research for nanocarriers loaded with components that facilitate precise tumour targeting [201, 333].

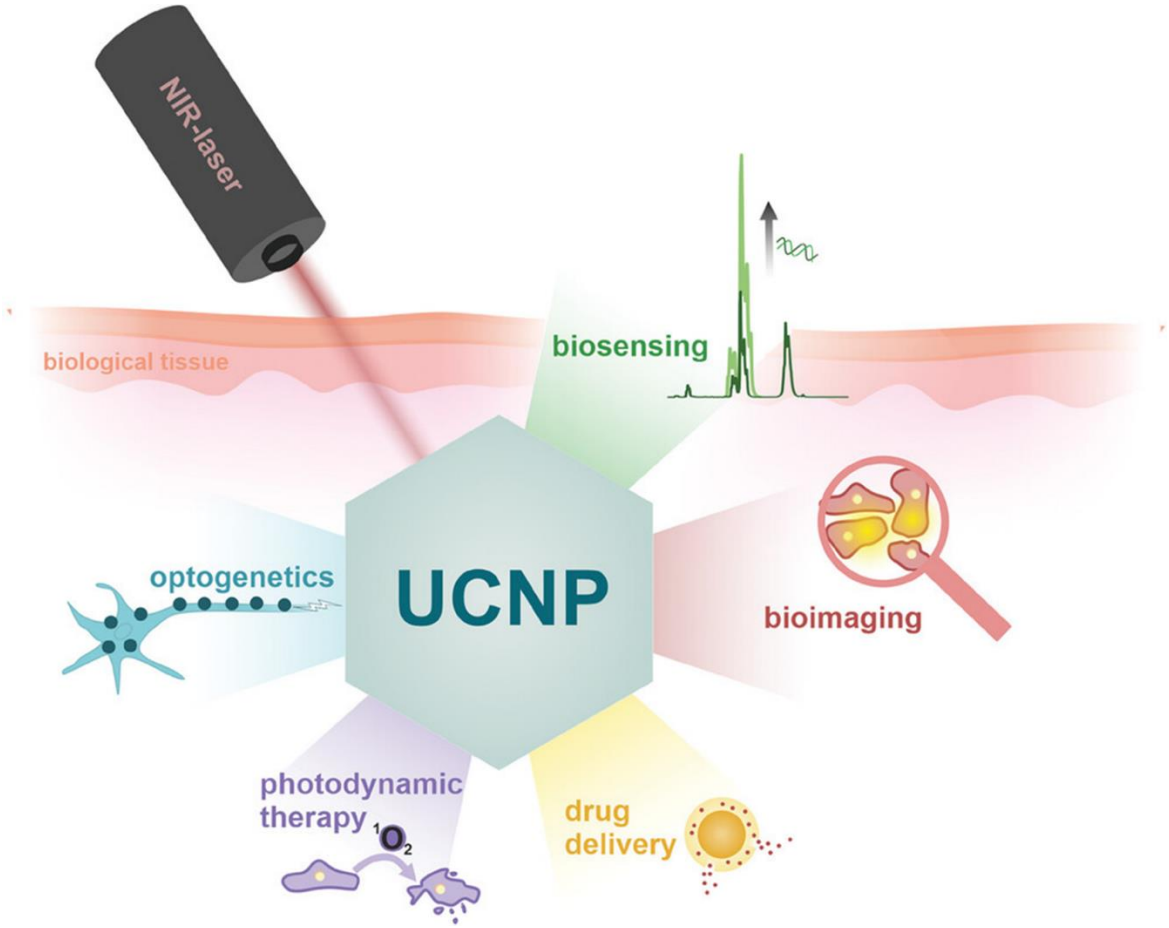

Fig 12: Range of potential applications of UCNPs in bioanalytical and medical sciences. Reproduced with permission from [334].

1.7.1. UCNP Mechanism and Synthesis

The lanthanide (Ln) ions in UCNPs arise from electronic transitions within the 4f orbitals. These transitions are intraconfigurational (4f-4f) and are shielded from external influences by the outer 5s and 5p orbitals, giving rise to highly distinctive and stable emission characteristics [188, 335]. Each Ln ion has a 'signature' emission spectrum defined by its specific electronic energy levels, making them highly valuable in diverse applications like bioimaging, sensing, and photonics [336-338].

Lanthanides exhibit sharp, narrow emission peaks due to discrete 4f electronic transitions, with highly specific spectra for each ion, such as Eu^{3+} (~615 nm) and Tb^{3+} (~545 nm), enabling

precise multiplexing in imaging and biosensing [339]. Their long-lived excited states, lasting milliseconds to microseconds, facilitate time-resolved fluorescence techniques, reducing background interference in biological assays [340]. Lanthanides also feature anti-Stokes emission, minimising spectral overlap and converting low-energy NIR light to higher-energy visible or UV light for applications like deep-tissue imaging [341]. Additionally, their high photostability, resulting from the shielding of 4f orbitals by outer 5s and 5p orbitals, makes them suitable for long-term and consistent performance [342].

UCNPs are composed of multiple integral elements, among which is a host lattice that serves as a conducting structure, doped with activator and sensitiser ions for the transfer of energy [202]. The UCNP-emitted light can also be customised by altering the dopants, thus potentiating the development of multiplexing assays. In contrast to luminescence processes typically involving a single electron transitioning from the ground state to the excited state, UCNPs employ multiple low-energy photons to produce high-energy emissions [343].

Signature Emission Spectra of Key Lanthanide Ions in UCNPs

Eu^{3+} (Europium): Eu^{3+} is known for its bright red luminescence and exhibits sharp emission lines, the most prominent being at ~615 nm ($^5D_0 \rightarrow {}^7F_2$). This transition is hypersensitive to the surrounding environment, making Eu^{3+} a valuable probe for monitoring chemical changes or binding events [339, 344].

Tb^{3+} (Terbium): Tb^{3+} emits intense green luminescence, with the most prominent transition at ~545 nm ($^5D_4 \rightarrow {}^7F_5$). Its high quantum efficiency makes it suitable for applications requiring bright and stable green emission [345, 346].

Er^{3+} (Erbium): Er^{3+} is commonly used in upconversion applications, emitting green (~525 nm, $^2H_{11/2} \rightarrow {}^4I_{15/2}$; ~550 nm, $^4S_{3/2} \rightarrow {}^4I_{15/2}$) and red light (~655 nm, $^4F_{9/2} \rightarrow {}^4I_{15/2}$) upon NIR excitation. These emissions are useful in bioimaging and photonics [341, 347].

Tm^{3+} (Thulium): Tm^{3+} also features prominently in upconversion systems, emitting blue (~450 nm, $^1D_2 \rightarrow {}^3F_4$) and NIR light (~800 nm, $^3H_4 \rightarrow {}^3H_6$). Its distinct emission peaks make it ideal for multiplexed imaging [348, 349].

Yb^{3+} (Ytterbium): Yb^{3+} is primarily used as a sensitiser in upconversion processes due to its strong absorption of NIR light (~980 nm, $^2F_{7/2} \rightarrow {}^2F_{5/2}$) and efficient energy transfer to activator ions like Er^{3+} or Tm^{3+}. While its own emission is weak (NIR ~1000 nm), it plays a crucial role in driving upconversion luminescence [340, 350].

Lanthanide-doped nanoparticles undergo upconversion primarily through excited state absorption (ESA) and energy transfer upconversion (ETU). Activators such as Er^{3+}, Tm^{3+}, and Ho^{3+} are commonly utilised for their capacity to produce visible optical emissions at low excitation power densities, with Yb^{3+} serving as a widely employed sensitiser due to its straightforward two-energy level system and significant absorption cross-section at ~ 980 nm (Fig 13) [351]. Lanthanide-doped UCNPs can be synthesised using various methods, each offering specific advantages in controlling size, morphology, and luminescent properties. Thermal decomposition involves the thermal breakdown of lanthanide precursors with surfactants, producing highly monodisperse nanoparticles with controlled sizes [352, 353]. Hydrothermal synthesis uses lanthanide salts in an aqueous solution under high temperature and pressure, resulting in nanoparticles with uniform morphology and crystalline phases [354]. Coprecipitation involves mixing lanthanide chlorides with sodium hydroxide and ammonium fluoride in methanolic solutions, precipitating UCNPs with desirable structural and optical characteristics [355].

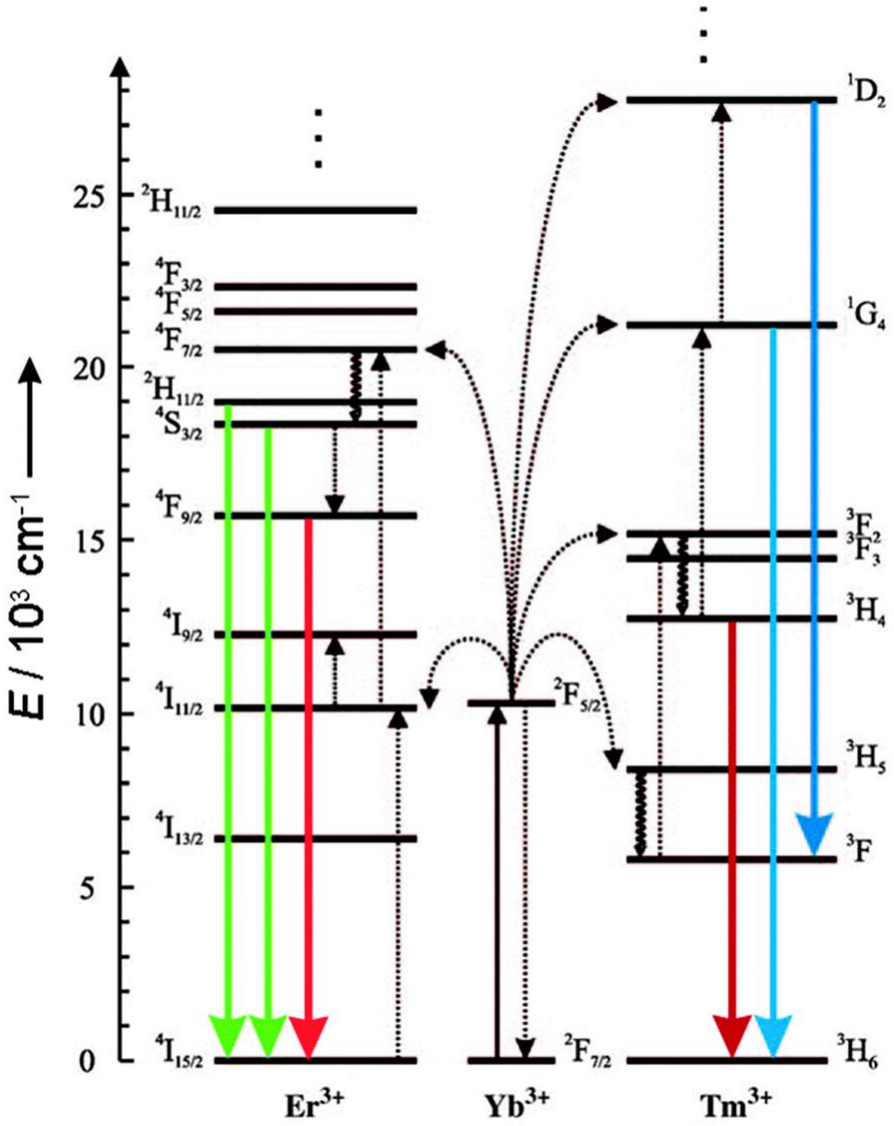

Fig 13: The diagram illustrates the anti-Stokes processes in UCNPs of $NaYF_4$: Yb,Er/Tm, depicting the absorption of near-infrared (NIR) light by the sensitizer ion Yb^{3+} and the subsequent emission of visible or NIR light by the activator ions Er^{3+} or Tm^{3+}. These ions are incorporated within a hexagonal nanocrystal structure of $NaYF_4$, with full arrows representing radiative transitions, dotted arrows indicating non-radiative energy transfer, and curled arrows denoting multiphoton relaxation. Reproduced with permission from ref [356].

Achieving high upconversion efficiency in UCNPs requires co-doping sensitiser and activator ions with closely matched intermediate-excited states [357, 358]. Increasing the doping concentration can initially enhance emission brightness and luminescence by shortening the sensitizer-to-activator distance and increasing the number of photon sensitisers and emitters [359]. However, surpassing a critical concentration threshold leads to concentration quenching,

where excessive dopant levels disrupt the cascade energy transfer process. This results in energy migration among closely spaced ions and significant non-radiative losses, ultimately reducing luminescence efficiency [359-361]. Several strategies have been developed to overcome concentration quenching [361, 362]. One approach involves coating the luminescent core of UCNPs with an inert shell to shield it from surface quenchers, effectively minimising energy loss and preserving emission intensity [360]. Another method is increasing excitation power density, where high-power lasers or focused photon flux are used to excite more ions, reducing energy loss to ground-state ions and enhancing luminescence in highly doped UCNPs [363, 364]. The third strategy targets uniform dopant distribution to prevent local concentration quenching from clustering [365]. Techniques like layer-by-layer hot injection ensure precise dopant placement, optimise spacing, enhance energy transfer, and minimise non-radiative losses, enabling brighter, more efficient UCNPs [359, 365].

In this thesis, we synthesised core and core-shell $NaYF_4$:40%Yb^{3+}, 4%Er^{3+} nanoparticles using a standard co-precipitation procedure, allowing for cost-effective, straightforward synthesis while facilitating the consistent production of uniformly sized nanoparticles. The high doping concentration of Yb^{3+} is critical, as it serves as an efficient sensitiser, absorbing near-infrared (NIR) light at approximately 980 nm and transferring energy to Er^{3+} ions. This energy transfer process underpins the strong upconversion luminescence of the system [366]. Yb^{3+} possesses a high absorption cross-section in the NIR region, enabling effective excitation and enhancing overall luminescence performance [367]. Early work, such as that by Li et al., demonstrated the synthesis of Yb/Er-doped UCNPs, highlighting the importance of high Yb^{3+} and moderate Er^{3+} doping levels for optimal upconversion luminescence [368]. These doping concentrations have been successfully employed in various studies as luminescent probes for precisely detecting specific analytes [366, 369]. The exact composition of $NaYF_4$:40%Yb^{3+}, 4%Er^{3+} has

previously been synthesised within our group and applied specifically in UCNP-LFA systems, demonstrating its utility in biosensing platforms [370, 371].

1.7.2. Surface Modification of UCNPs

Most UCNPs are prepared in organic solvents and capped with hydrophobic ligands, such as oleic acid, which render them hydrophobic and dispersible only in solvents like chloroform and hexane. A crucial step to render them suitable for biomedical applications involves surface modification to achieve a hydrophilic composition [372, 373]. This modification introduces functional groups or imparts a strong charge to the nanoparticle surface, allowing conjugation with antibodies, aptamers and other target recognition molecules. The ideal surface modification should ensure colloidal stability in water and provide functionality for the covalent attachment of biomarkers, facilitating active targeting [374]. The most common surface modification strategies include ligand oxidation, ligand exchange, ligand removal, lipid encapsulation, and polymer/silica encapsulation (Fig 14).

Ligand exchange is the most common method employed to displace the original oleate ligands on the surface and allow them to be coated with a hydrophilic organic ligand [375]. This project mainly employed this surface modification procedure to facilitate the replacement of hydrophobic ligands with bifunctional polymers. Various ligands, such as polyethylene glycol-phosphate ligand, polymers like polyacrylic acid (PAA), acid derivatives such as 3-mercaptopropionic acid, and certain amine derivatives like cysteine, are suitable for ligand exchange [376-380]. This approach holds significant advantages as it is a straightforward method that does not impact nanoparticle size, owing to the minute size of the exchange agent [381].

Ligand oxidation is a relatively new, versatile technique to convert the hydrophobic UCNPs to hydrophilic by oxidising the ligand into functionalised derivatives [374, 382]. In employing

this approach, the Lemieux-von Rudloff reagent (aqueous mixture of $KMnO_4$ and $NaIO_4$) selectively oxidizes carbon–carbon double bonds, converting them into carboxylic groups for enhanced reactivity. The resulting oxidized UCNPs, featuring free carboxylic groups, enable direct conjugation with proteins, and other recognition molecules [382].

Ligand removal serves as a direct approach to acquire water-soluble UCNPs by eliminating oleate ligands that coat the surfaces of the nanoparticles. This elimination process can be carried out through either treating UCNPs with excess ethanol under sonication or exposing them to strong acid [383, 384]. This method aims to ease the conjugation of electronegative ligands without encountering steric hindrance. Consequently, the nanoparticles acquire a negative charge and colloidal stability through electrostatic forces, although this approach falls short in conferring enduring colloidal stability in water or buffers [385].

Lipid encapsulation involves the linkage between the oleate ligands and the hydrophobic tail of the lipids driven by hydrophobic interactions [386, 387]. This configuration results in the formation of stable aqueous dispersions for lipid-coated UCNPs, preventing any undesirable aggregation. This facilitates an effective shielding of the UCNP surface by the lipids when exposed to water and enhances the accessibility of the platform for conjugating diverse functional groups, such as with dyes, maleimide, or carboxylic groups [388]. This adaptability allows the UCNPs to be readily employed in various bioanalytical applications.

Polymer/Silica Encapsulation: Amphiphilic copolymers, featuring both hydrophobic and hydrophilic components, have proven effective in stabilizing OA-capped UCNPs [389]. The nanoparticles find stability as the hydrophobic ligand component interacts with the oleates, while the hydrophilic ligand component ensures colloidal stability in water. Notably, this method offers the benefits of maintaining the native ligands without causing surface disruptions [390]. Silica coatings have also been employed as a means to confer water dispersibility upon

UCNPs [391, 392]. Silica's chemical inertness and hydrophilicity create stable, water-dispersible coated nanoparticles. The biocompatible and non-toxic nature of silica shells makes them ideal for optical bioanalytical applications, which not only facilitates additional surface functionalisation but also allows application in biosensors [393, 394].

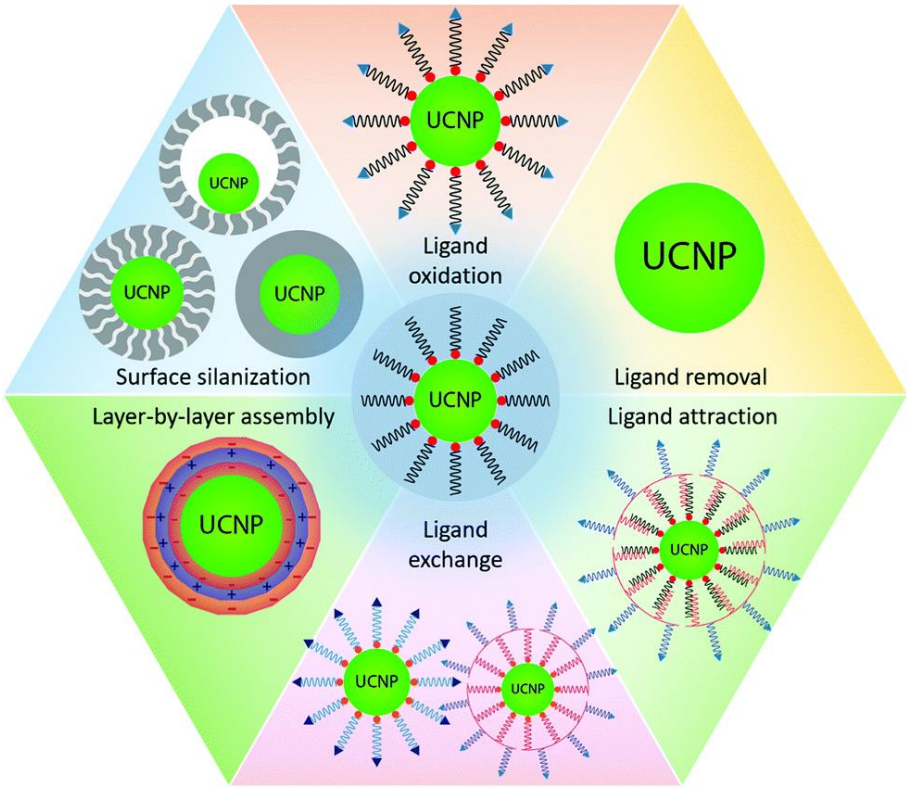

Fig 14: Illustration of the various techniques employed for modifying the surface chemistry of UCNPs. These modifications enhance the stability and biocompatibility of UCNPs, rendering them suitable for bio-conjugation with target recognition molecules such as antibodies and aptamers. Consequently, this enhances their performance as bioanalytical probes. Reproduced with permission from ref [395].

1.7.3. UCNP Application in sEV detection/analysis

The continuous synthesis and utilisation of UCNPs have enabled the development of reliable sensors tailored for the highly sensitive and specific detection of tumour biomarkers in cancer cell components like CTCs, ctDNA and sEVs [396]. The significance of sEV markers in disease-specific clinical diagnosis has prompted the utilisation of UCNP sensors for sensitively detecting relevant sEV markers. UCNPs serve as efficient energy donors, contributing to the

success of fluorescence/luminescence resonance energy transfer (FRET/LRET) assays with significantly reduced detection limits. Chen et al. exploited LRET from UCNPs (NaYF4:Yb^{3+}, Er^{3+} synthesised by thermal decomposition) to gold nanorods (AuNRs) to develop a paper-based biosensor for detecting sEV-specific markers. The sensor employed a CD63 aptameric sequence, split into two parts—one bound to UCNPs (energy donors) and the other to Au nanorods (energy receptors). In the absence of sEVs, UCNPs exhibited green fluorescence upon excitation at 980 nm. However, in the presence of sEVs, the formation of complexes led to fluorescence quenching proportional to the concentration of sEVs. The system achieved a LOD of 1.1×10^3 particles/μL within ~ 30 mins [397]. In a similar strategy, Wang et al. used a FRET-based aptasensor using UCNPs (NaYF4:Yb^{3+}, Er^{3+} synthesised by thermal decomposition) as donors and tetramethyl rhodamine (TAMRA) as acceptors for detecting $EpCAM^+$ sEVs with high sensitivity. Under excitation by NIR light at 980nm, TAMRA emitted yellow fluorescence at 585nm, exhibiting linear correlation with sEV concentration. This system achieved a notably low LOD of 80 particles/μL for $EpCAM^+$ sEVs (Fig 15a, 15b) [398]. UCNPs have also integrated more robust bio-analytical strategies like inductively coupled plasma mass spectrometry (ICP-MS) to analyse cancer-related sEV biomarkers quantitatively. Zhang et al. designed DNA-programmed UCNP–AuNP nanosatellite assemblies, where AuNPs, coupled with aptamers targeting tumour-associated proteins (CD63, HER2, and EpCAM), acted as cores linking different elements (Y, Tb, and Eu) doped UCNPs ($NaYF_4$:Yb,Er, $NaEuF_4$:Yb,Er and $NaTbF_4$:Yb,Er synthesised by co-precipitation). Upon encountering target sEVs, specific aptamers recognised surface proteins, releasing corresponding UCNPs, enabling simultaneous and accurate differentiation of sEVs from various cell lines through ICP-MS detection [399].

The superior bio-analytical performance offered by UCNPs has prompted their application in diverse point-of-care testing (POCT) formats, including paper-based analytical devices

(PADs), lateral flow assays (LFAs), microfluidic devices, and microarrays. PADs incorporate 3D networks of cellulose fibres, where PAA-modified UCNPs have been used as nanoprobe elements for detecting target DNA sequences, allowing for sensitive assays that can be recorded using a cell phone camera or even by naked eye observation, post-irradiation with a handheld NIR laser [400, 401]. Our group have previously reported the use of a UCNP-LFA system (core/core-shell $NaYF_4$:2%Er/20%Yb, $NaYF_4$:8%Er/60%Yb@$NaYF_4$, $NaYF_4$:0.5%Tm/20%Yb and NaYF4:8%Tm/60%Yb@$NaYF_4$ nanocrystals) for the sensitive detection of prostate-specific antigen (PSA) and ephrin type-A receptor 2 (EphA2) biomarkers, providing a rapid and accessible platform for analyte detection [402]. Wang et al. incorporated magnetic UCNPs ($NaYF_4$: Yb, Er; Y:Yb:Er = 69:30:1) in a microfluidic nanoplatform to enable the detection of CTCs [403]. Microarray technology has facilitated high-throughput and multiplexed detection from small sample volumes by utilising two different UCNPs ($NaYF_4$:Yb^{3+},Er^{3+} and $NaYF_4$:Yb^{3+},Tm^{3+} synthesised by thermal coprecipitation) to create a spectrally and spatially multiplexed serological assay for detecting various viruses and antigens [404]. These applications showcase the adaptability and efficacy of UCNP nanoprobes in enhancing diagnostic capabilities, particularly in resource-limited settings.

UCNP-based sEV detection has also been implemented in ELISA-like sandwich immunoassays to detect sEV markers. Lan et al. synthesised $NaYF_4$:Yb^{3+}, Er^{3+} nanoparticles through the thermal decomposition of rare earth stearates. They designed a VEGF-specific aptamer with functionalised and fixed portions, forming a complex in the presence of the target protein, and achieved a remarkable LOD of 6pM for VEGF in breast cancer patient samples by measuring the intensity of the luminescent signal produced at 540nm upon 980nm laser excitation [405]. Similarly, Farka et al. introduced a single molecule upconversion-linked immunosorbent assay (ULISA) for the detection of PSA in prostate cancer patients, synthesising β-$NaYF_4$: 18 mol % Yb^{3+}, 2 mol % Er^{3+} type UCNPs through high-temperature

coprecipitation. Silica-coated and anti-PSA antibody-functionalized particles were implemented in a sandwich immunoassay format, and the resulting complexed UCNPs were quantified using upconversion epiluminescence microscopy, achieving a remarkable LOD of 42 fM for PSA in prostate cancer patient samples [406].

In a previous study from our group, lanthanide-doped UCNPs were used in conjunction with TIRF microscopy imaging to enable the detection of single sEVs. In the study, sEV-specific tetraspanin antibodies (CD63, CD81, CD9) are functionalised on the surface of glass slides to first capture sEVs, which were subsequently detected by UCNP conjugated anti-EpCAM antibodies. The uniformity, brightness, and photostability of highly doped UCNPs (NaYF4:20%Yb^{3+},2%Er^{3+} nanocrystals) significantly enhance the optical signal of individual molecules, enabling the counting of single sEVs based on the presence of bright spots. The assay achieved a detection limit of 1.8×10^6 EVs/mL, surpassing the standard ELISA by approximately three orders of magnitude (Fig 15c, 15d) [407]. More recently, the group further improved imaging resolution by using a strategy of stimulated emission depletion (STED)-like super-resolution microscopy of UCNPs ($NaYF_4$:20%Yb^{3+},2%Er^{3+}, $NaYF_4$:40%Yb^{3+},4%Tm^{3+} and $NaYF_4$:20%Yb^{3+},6%Tm^{3+} nanocrystals) to characterise the expression of surface markers on single EVs. In contrast to traditional fluorescence microscopy, the super-resolution method attains imaging resolutions finer than 50 nm, enabling the detailed examination of individual sEVs, facilitating the visualisation of singular EVs, and identifying distinct surface-marker subgroups within diverse EV populations [408]. These studies underscore the significant potential of UCNPs towards quantitatively assessing the expression of surface antigens on single sEVs. The strategies offer a means to digitally monitor EV heterogeneity digitally, presenting a means for tracking development.

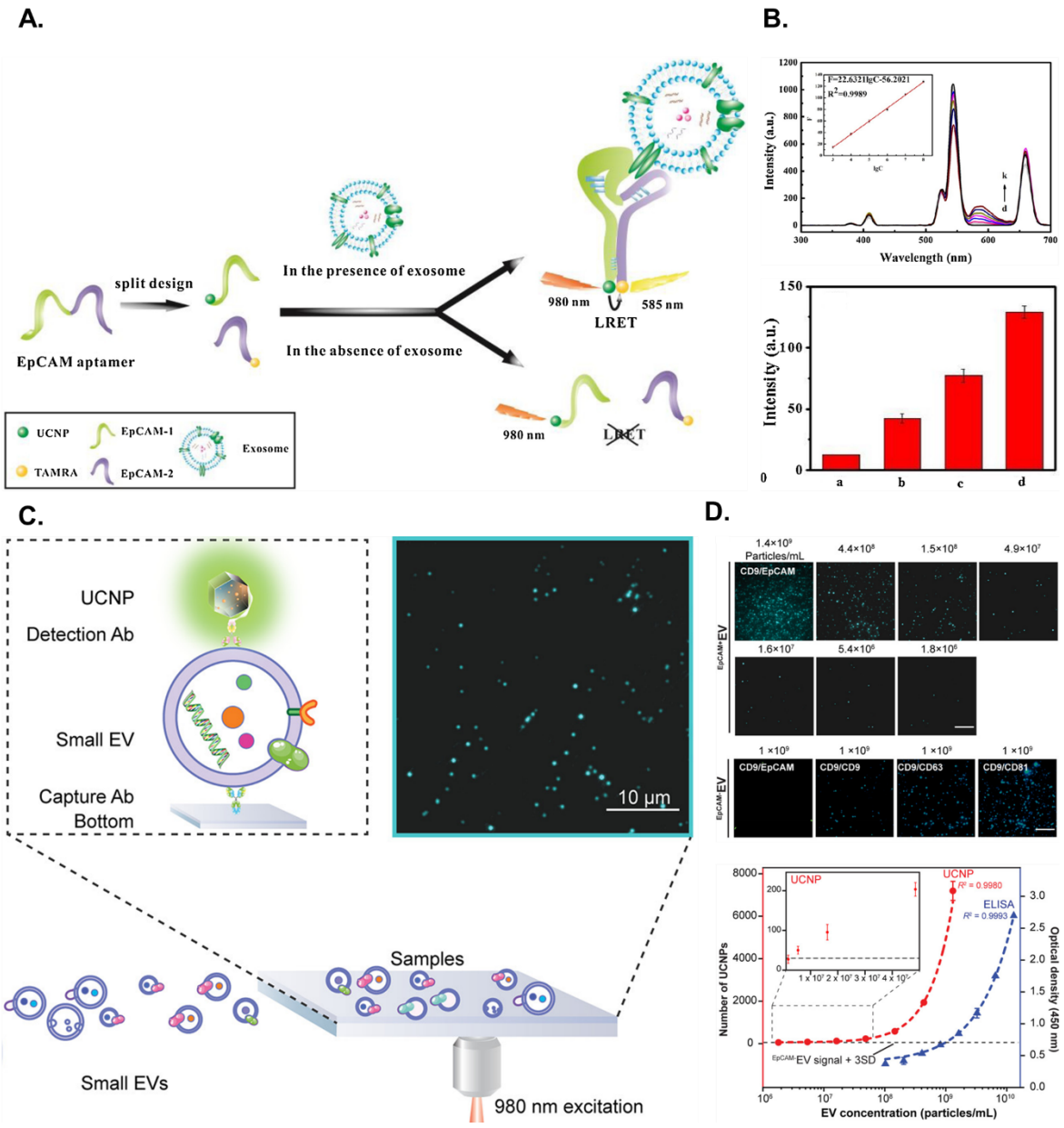

Fig 15: (a.) An aptasensor that employed luminescence resonance energy transfer (LRET) between rare-earth doped UCNPs and TAMRA for highly sensitive sEV detection. The system utilized EpCAM-coupled aptamers, allowing the UCNPs-TAMRA to emit yellow fluorescence at 585 nm upon near-infrared light excitation at 980 nm, providing a linear correlation between fluorescence intensity and sEV concentration for effective detection and quantification. (B.) Linear Curve for fluorescence intensity (585nm) at different concentrations of sEVs (d to k: 0, 10^3, 10^4, 10^5, 10^6, 10^7, 10^8 sEVs/μL), with the assay achieving a detection limit of 80 sEVs/μL. Resulting fluorescent intensity from the UCNPs-TAMRA system for MCF-10A (b), MCF-7 (c), MDA-MB-231 (d) cell-derived sEVs. Reproduced with permission from ref [398] (C.) Quantitative analysis of single sEVs isolated from cancer cells using UCNPs as a luminescent probe in a TIRF microscopy setup. (D.) (Top right) Single-molecule quantification of $^{CD9+EpCAM+}$EVs at a range of EV concentrations. (Bottom right) Comparative analysis of calibration curves for detecting $^{CD9+EpCAM+}$EVs between the UCNP-based assay (red) and ELISA (blue). The LOD of the UCNP-assay was 1.8×10^6 sEVs/mL, which is ~3 orders of magnitude lower than the ELISA. Reproduced with permission from [407].

1.8. Aim, Hypothesis and Expmerimental Results Chapters Outline

The diverse applications discussed in the literature highlight the versatility and effectiveness of integrated sensor technologies and nanoparticles, including UCNP nanoprobes, in advancing diagnostic capabilities, inspiring the goals of this thesis. The aim of my thesis was to leverage the superior bio-analytical performance of nanoparticles, specifically UCNPs and AuNPs, to facilitate enhanced detection sensitivity of sEV markers. I hypothesise that the unique physio-chemical properties of the nanoparticles and the optimised functionalised strategies implemented in the study will allow improved detection sensitivity of target analytes, specifically sEV markers and contribute towards the continuous development of sEV-based sensor technologies.

The experimental results are summarised as follows. Chapter 3 discusses the results that validate the structural and functional characterisation of the nanoparticles for effective probes in the immunoassays to detect sEV surface markers sensitively. Chapter 4 explores two nanoparticle-modified microplate ELISA formats using AuNPs and UCNPs to enhance the detection sensitivity of CD63 with potential POC applications. In Chapter 5, I introduced a quantitative UCNP-LFA with potential POC applications to detect sEV-CD63 and sEV-PD-L1 in sEVs isolated from H1975, MM05 and MSTO-211H cells. Chapter 6 uses the UCNP-LFA to detect sEV-GPC-1 and sEV-PD-L1 from sEVs isolated from LnCap, DU145 and HCT116 cell lines. The overall objective of the experimental work in the PhD was to introduce nanoparticle-based systems to enable improved detection of sEV surface markers with potential applications in diagnostic settings.

2. Methodology

2.1. Cell Culture and conditioned medium

H1975, MSTO-211H (Asbestos and Dust Diseases Research Institute, Sydney, Australia), MM05 (University of Queensland Thoracic Research Centre, Prince Charles Hospital, Brisbane, Australia), LnCap (American Type Culture Collection, CRL-1740), DU145 (American Type Culture Collection, HTB-81) and HCT116 (American Type Culture Collection, CCL-247) cells were cultured in RPMI 1640 (Gibco, UK) supplemented with 10% (v/v) fetal bovine serum (FBS, Gibco, UK), 100 U/mL penicillin and 100 mg/mL streptomycin (Gibco, UK) in T175 culture flasks (Thermofisher, USA) and incubated at 37°C in a 5% CO_2 humidified incubator. Once the cells reached 70% confluency (~ 3×10^7 cells), the supernatant was carefully discarded, and the cells were washed twice with phosphate buffer saline (PBS). Then, the cells were cultured in an FBS-free medium under hypoxic condition for 48 h at 37°C in a 5% CO_2 humidified incubator and the culture medium was collected for subsequent isolation of sEVs.

2.2. Isolation of extracellular vesicles by ultracentrifugation

The media containing the released EVs was collected and subjected to multiple centrifugation steps including 300 × g for 10 min and 2000 × g for 10 min followed by 10,000 × g (R18A rotor, HITACHI CR22N, Japan) for 30 min to remove cells, dead cells and cell debris, then filtrated through a sterile 0.22 μm syringe filter (Merck Millipore, USA). The conditioned medium further underwent ultracentrifugation at 100,000 × g for 120 min (F37L carbon fiber rotor, Sorvall WX ultra series, Thermofisher, USA). The supernatant was removed, and pellets that contained EVs were re-suspended in a separate ultracentrifuge tube in PBS (previously filtered through a 0.22 μm syringe filter) and centrifuged a second time at 100,000 × g for 120

min. The supernatant was removed, and the sEV pellet was re-suspended in ~100 µL filtrated PBS. The sEVs were stored at -80°C until use. All centrifugation steps were performed at 4°C. For the plasma samples, sEVs were isolated using a similar protocol. Briefly, 500µL of plasma was subjected to multiple centrifugation steps, 2,000 ×g (19776 rotor, Sigma, USA) for 10 min to remove any cell debris and larger protein aggregates. The supernatant was centrifuged at 10,000× g (19776 rotor, Sigma, USA) for 20 min to pellet out microvesicles. The Supernatant was transferred to fresh polycarbonate UC tubes and further centrifuged at 100,000 ×g (TLA 55 S/N15U1275 rotor, Optima MAX-XP ultracentrifuge, Beckman Coulter, USA) in 70 min to pellet out sEVs. The supernatant was discarded, and the pellet was resuspended in 500 filtered PBS and further centrifuged at 100,000 ×g for 70 min. All centrifugation steps were performed at 4 ºC. The sEVs were stored at -80°C until use.

2.3. Nanoparticle tracking analysis

Nanoparticle tracking analysis (NTA) was performed on a ZetaView ® PMX-420 QUATT system (Particle Metrix, Germany) equipped with a 532nm green laser for determining the sEV concentration and size distribution. 100µL of isolated sEV samples were diluted to 500µL with freshly filtered PBS (0.22µm filter) and loaded into the detection chamber by syringe. The camera was manually set and kept the same for all samples with a slider shutter 650 and slider gain 50. 30s videos were recorded, and the number of captures was 5. The detection threshold was set to 6, and blur and max jump distance were automatically set. The temperature was maintained at 25ºC. The data were processed by the NTA software (8.05.14 SP7 version).

2.4. Western Blotting

The isolated sEVs were lysed by adding an equal volume of RIPA lysis and extraction buffer (Cat#89900, Thermofisher, USA). The protein concentration of the sEVs was measured using a Pierce BCA protein assay kit (Cat#23227, Pierce Biotechnology, CT, USA) as per the manufacturer's instructions. For Western Blot analysis, sEV proteins (2×10^8 particles; 5µg) were resolved using Bolt™ 4-12% Bis-Tris Plus Gels (Cat#NW04120BOX, Invitrogen, USA). Samples were diluted in 4 X Bolt™ LDS Sample Buffer (Cat#B0007, ThermoFisher, USA) and heated up to 70°C for 10 min, then transferred on polyvinylidene difluoride (PVDF) membranes (Cat#88585, ThermoFisher, USA). The PVDF membrane was blocked for 30 min at room temperature at 5% non-fat powdered milk in PBS-T (PBS and 0.5% Tween-20) and incubated overnight at 4°C with the following primary antibodies: anti-human CD63 (Cat# 353004, Biolegend, USA), anti-human CD9 (Cat# 312106, BioLegend, USA) and anti-human CD81 (Cat# 349506, BioLegend, USA). Then, the blots were incubated with an appropriate HRP-conjugated IgG secondary antibody (1:2000) (Cat# 405306, BioLegend, USA) in PBS-T for 1 h at 37°C. The blot was washed three times with a PBS-T buffer for 14 min after each incubation step. It was then visualised under SuperSignal™ West Dura Extended Duration Substrate (Cat#37071, ThermoFisher, USA). The mentioned proteins were resolved under non-reducing conditions.

2.5. Transmission electron microscopy (TEM)

To investigate the morphology of the sEVs isolated by ultracentrifugation, TEM was used. Briefly, 5 µl of sEV sample (~10^6 particles) was fixed with 2.5% formaldehyde and applied to 300-square mesh copper grids coated with a thin formvar carbon film. The grids were subsequently negatively stained with 1% UAR-EMS Uranyl acetate replacement stain and

incubated for 30 minutes. Grids were then washed with PBS and dried with filter paper. The sEV samples were observed using a TEM JEOL F200 microscope operating at 200 kV.

2.6. Synthesis of upconversion nanoparticles

$NaYF_4$:40%Yb^{3+},4%Er^{3+} nanocrystals were synthesized according to our previously reported method [409]. In a typical experiment, 1 mmol $RECl_3 \cdot 6H_2O$ (RE = Y, Yb, Er) with the desired molar ratio was added to a flask containing 6 mL OA and 15 mL ODE. The mixture was heated to 160°C under argon flow for 30 min to obtain a clear solution and then cooled down to ~50°C, followed by adding 5 mL methanol solution of NH_4F (4 mmol) and NaOH (2.5 mmol). After stirring for 30 min, the solution was heated to 150°C under argon flow for 20 min to expel methanol, and then the solution was further heated to 310°C for another 90 min. Finally, the reaction solution was cooled down to room temperature. The products were precipitated by ethanol and centrifuged (9000 rpm for 5 min), then washed three times with cyclohexane, ethanol and methanol to get the nanoparticles.

To get the nanoparticles with the core-shell structure, layer-by-layer epitaxial growth was employed. The shell precursor's ($NaYF_4$) preparation was similar to that for the core nanoparticles synthesis except the step where the reaction solution was slowly heated to 150°C for 20 min. Instead of further heating to 300 °C to trigger nanocrystal growth, the solution was cooled down to room temperature to yield the shell precursors. For epitaxial growth, 0.15 mmol as-prepared core nanocrystals were added to 6 mL OA and 6 mL ODE. The mixture was heated to 170 °C under argon for 30 min, and then further heated to 300°C. Next, 0.25 mL as prepared shell precursors were injected into the reaction mixture and ripened at 300°C for 4 min, followed by the same injection and ripening cycles several times to get the nanocrystals with

the desired size. Finally, the slurry was cooled down to room temperature and the formed nanocrystals were purified according to the same procedure used for the core nanocrystals.

The morphological characterisation of the nanoparticles was performed by transmission electron microscope (TEM). The FEI Tecnai T20 microscope was operated under an accelerating voltage of 200 kV. The UCNPs in cyclohexane were dropped onto carbon-coated copper grids and dried.

2.7. Surface modification of UCNPs

As UCNPs with tuneable optical properties were synthesized at high temperatures with oleic acid (OA) as a surface ligand, surface modification was required to transition UCNPs from hydrophobic to hydrophilic state. Polymers containing multiple anchoring ligands were extensively used to modify the as-synthesized UCNPs with improved colloidal stability, biocompatibility and immunogenicity. In this project, we modified the UCNPs with tri-block polymer.

Tri-block copolymers were synthesized by photo-induced RAFT polymerization using a blue LED strip (460 nm) based on a previously established protocol [410]. Briefly, a 25 mL Schleck tube was charged with 4-((((2-carboxyethyl) thio) carbonothioyl) thio)-4-cyanopentanoic acid (CTCPA), 0.1g, 0.33 mmol, 0.35 g MAA (4 mmol) and with 5.0 mL DMF. The mixture was degassed through a three-cycle freeze-pump-thaw. The LED light was then 'turned on,' marking the start of the polymerization reaction. After 12 hours of irradiation, the polymerization was stopped at a monomer conversion of 70 %. The synthesis of the di-block copolymer was continued by adding 5 g of OEGMA-500 (10 mmol). The mixture was degassed, reacted for 10 hours, and at 80 % monomer conversion, the reaction was stopped. The polymer was precipitated in diethyl ether, and the tri-block copolymer was synthesized by

taking 1.5 g (0.21 mmol) of obtained di-block with 0.3 g (1.4 mmol) MOEP in 5.0 mL DMF. After degassing, the reaction was carried out for 11 hours, and the final tri-block polymer was purified via precipitation in diethyl ether.

Then, 500 µL of OA-coated UCNPs (20 mg/mL) kept in cyclohexane were centrifuged and re-dispersed in 1 mL tetrahydrofuran (THF), followed by the addition of 1 mL THF solution with 10 mg copolymer. The resulting dispersion was sonicated for 1 min followed by incubation in a shaker overnight at room temperature. The polymer-coated UCNPs were purified four times by washing/centrifugation at 14860 rpm for 30 min. The supernatant was removed and the nanoparticles were re-dispersed in water and stored at 4 ºC for further use. The Polymer modified UCNPs were characterised using Dynamic Light Scattering (DLS) and Zeta Potential to determine the hydrodynamic sizes and the surface charge of the modified nanoparticles. These measurements were performed on a Malvern Instruments Zetasizer Nano ZS instrument equipped with a 4 mV He-Ne laser operating at 633 nm with a 173º backscatter measurement angle. All measurements were done in triplicates to determine the reproducibility and standard deviation of the data. The modified nanoparticles were also subjected to Fourier Transform Infrared Spectroscopy (FTIR), where the samples were dried in a 60ºC in a vacuum oven overnight and the spectral data was obtained within the range 4000 to 500 cm^{-1} with 64 scans. The FTIR spectra was performed using a Nicolet 7650 system. The upconversion emission spectra were measured using a custom-built spectroscopic system equipped with a 980 nm continuous-wave diode laser.

2.8. Bioconjugation of UCNPs with antibody using conjugation kit

Paired capture and detector antibodies and proteins for CD63 (capture antibody: Cat# 11271-T16; detector antibody: Cat# 11271-R142; CD63 protein: Cat# 11271-H08H, SinoBiological,

China), PD-L1 (capture and detector antibody pair: Cat# ab253485, PD-L1 protein: ab280943, Abcam, UK) and GPC-1 (capture antibody: Cat# ab283523; detector antibody: Cat# ab272300; GPC-1 protein: Cat# ab114484, Abcam, UK). Bioconjugation of UCNPs with antibody was done using the Particle Conjugation Kit (Cat# A-PCKS-10, AnteoTech, Queensland, Australia) as per the manufacturer's protocol with minor modifications. Briefly, 10 µL of UCNPs-Polymer (20 mg/mL) were mixed with 190 µL activation buffer containing 5 mM sodium fluoride and incubated on a shaker (500 rpm) for one hour at room temperature. Following this, the activated nanoparticles were washed with particle washing and conjugation solutions by centrifugation at 15,000 rpm for 40 minutes at 4°C. Subsequently, 40 µL of activated UCNPs-Polymer were mixed with 108 µL of conjugation buffer containing 5 mM sodium fluoride and 2 µL of 1 mg/mL detector antibody. The mixture was incubated on a shaker (500 rpm) for one hour at room temperature. Next, 20 µL of BSA solution (20% w/w) was added to the mixture, followed by another one-hour incubation. The UCNPs-Polymer-Antibody were then centrifuged at 15,000 rpm for 40 minutes at 4°C and washed with the storage buffer. Finally, the antibody-modified nanoparticles were resuspended in 200 µL of storage buffer and stored at 4°C for further use.

2.9. Bioconjugation of gold nanoparticles (AuNPs) with antibodies using conjugation optimisation kit

The AuNPs were conjugated to IgG-HRP antibody (Cat# 31431, Thermofisher, USA) using the Gold Nanoparticle (50nm) Conjugation Optimisation Kit (Cat# 50-100 Cytodiagnostics, USA). The kit included citrate-capped 50 nm AuNPs and a range of buffers with pH values from 5.7 to 10, designed to determine the optimal pH and antibody loading amount for forming stable AuNP-antibody conjugates. The passive adsorption technique was employed to conjugate antibodies to the AuNPs. Since this process is highly sensitive to factors such as pH

and antibody loading, a standardised commercial optimisation kit was used to improve the likelihood of developing stable and functional conjugates.

A titration experiment was performed to find the optimal pH and protein concentration to ensure colloidal stability, as per the manufacturer's instructions. At the optimised pH and protein concentration, AuNPs were incubated at room temperature for 30 minutes with continuous stirring. The AuNPs were centrifuged at 2000 × g for 30 minutes, after which the pellet was resuspended in conjugate resuspension buffer (0.1 mM PBS, 1% BSA) and stored at 4ºC until further use. The AuNP-antibody conjugates were characterised using UV-vis spectroscopy, dynamic light scattering (DLS) and zeta potential, to determine the hydrodynamic diameter of AuNPs before and after conjugation with antibody. Additionally, the functionality of the AuNP@IgG-HRP conjugates was validated using a Conjugation QC Lateral Flow Dipstick kit (Cat# LF-018-10, Cytodiagnostics, USA). The dipstick is a rapid immunochromatographic test for quality control of gold nanoparticle-antibody conjugation, with IgG antispecies antibodies immobilised on the test lines of the strip membrane. A red line at the test site indicates successful conjugation, while its absence confirms that the conjugation was unsuccessful. The HRP functionality of the AuNP-antibody conjugates was assessed by adding 3,3′,5,5′-Tetramethylbenzidine (TMB) substrate (Cat# TO440, Sigma Aldrich, USA). The characteristic blue colour, produced when HRP catalyses the oxidation of TMB in the presence of hydrogen peroxide, confirmed that the HRP functionality was retained in the conjugates, whereas the absence of colour indicated that the HRP antibody conjugation was unsuccessful.

2.10. Lateral Flow Strip Design

The UCNP-LFAs were fabricated based on a previous protocol [402]. While detector antibodies were conjugated with surface-modified UCNPs to make detection probes, the

capture antibodies were immobilised on the surface of NC membranes. Capture antibodies were prepared at 0.3 mg/mL in buffer (50mM Tris-HCl, 1% w/v BSA, 0.5% w/v sucrose). The test line was fabricated by dispersing the capture antibodies through Dispenser HM3030 (Goldbio Co., China) on separate NC membranes and dried in an oven at 37ºC for 30 minutes. Then, the sample pad, conjugate pad, NC membrane and absorption pad were assembled and mounted on an adhesive backing pad with 1-2mm overlap between two adjoining pads. Finally, the assembled pads were cut into 6 cm × 2.73 mm (length × wide) strips and loaded into plastic cartridges.

2.11. Operational procedure of the UCNP Lateral Flow Assay

We used a double-antibody sandwich-format LFA strip to detect corresponding antigens and sEV markers in samples. For the test, 3 µl antibody-coated UCNP were transferred to 177 µl running buffer (20 mM Tris·HCl buffer, pH 7.6, with 1% BSA and 1% Tween-20) with 0.01-100 ng/mL of the antigens. The same procedure was followed for preparing the sEV samples with concentrations between ~10^2 – 10^7 sEVs/µL. After incubation on a shaker (800 rpm) for 10 min at 30°C, 50 µL of sample solutions were added onto the sample pad of the strip. After 10 min, the strip was detected at the test line by our strip reader (designed by UTS team and engineered previously by Lastek Photonic Technology Solutions, Australia) equipped with 980 nm laser and emission intensity of the nanoprobes at the testline area of nitrocellulose membrane was analysed. In the presence of target epitopes in the samples, the UCNP probes complexed with the targets, which were recognised by the immobilised antibodies in the membrane. The UCNP emission signal peaks at 654nm is proportional to the concentration of the target analytes present in the sample, thus enabling the detection and quantification of target epitopes.

2.12. Operational Procedure of the AuNP ELISA and UCNP-based Microplate Immunoassays

We used a sandwich format ELISA system and a paired antibody set for CD63 to sensitively detect target analytes. High-binding microplates (Cat#655061, Greiner Bio-One, Germany) were coated with the optimised concentration of capture antibody in PBS (pH 7.4) and incubated at 4ºC overnight. Plates were washed three times with washing buffer (PBS, 0.05% Tween 20) and blocked using a buffer with an optimised concentration of BSA. After rinsing the wells with washing buffer, 100µL of CD63 antigen (Cat# 11271-H08H, Sino Biological, China) at varying concentrations (0.39-50ng/mL) or 50 µL sEV samples at different concentrations (~10^5 – 10^7 sEVs/µL) were added to the wells and allowed to incubate at 4ºC overnight. After incubation, wells were washed with washing buffer, and 100µL of detector antibody was added to wells and allowed to incubate at room temperature for 2 hours. The washing step was repeated, and 100µL of anti-IgG-HRP antibody and/or 100µL of AuNP conjugated IgG-HRP was added to each well and allowed to incubate at room temperature for 1.5 h. Wells were washed five times with PBS and patted dry. 100µL of TMB substrate solution was added to each well and allowed to develop colour for 15-30 minutes, after which 100µL of stop solution (2M H_2SO_4) was added to the wells to stop the reaction. After stopping the reaction, optical density of the well plates was measured at 450nm in a conventional microplate (Varioskan LUX Reader, Thermofisher, USA) and/or a portable microplate reader (Absorbance 96 plate reader, Byonoy, Germany).

Black walled-clear bottomed high binding microplates (Cat# 655097 Greiner Bio-One, Germany) were used for the UCNP microplate immunoassasy format and the capture antibody coating and blocking steps followed were identical to the AuNP-ELISA format. Following this, 50µL of antigen (0.1-1000ng/mL) or sEV samples (~10^5 – 10^7 sEVs/µL) were added to wells and incubated at 4ºC overnight. The washing steps were repeated and the UCNP probes

conjugated to the detector antibody were added to the wells and allowed to incubate for 2h at room temperature. Wells were washed five times with 10mM Tris-HCl buffer (pH 7.4) and patted dry. Once dry, the UCNP luminescence signals in the wells were recorded in our customised UCNP 96-well microplate reader (designed by UTS team and engineered by Lastek Photonic Technology Solutions, Australia) equipped with a 980nm laser.

2.13. Enzyme-Linked Immunosorbent Assay (ELISA) for detection of CD63, PD-L1, GPC-1 and PSA on the surface of sEVs

The concentration of CD63, PD-L1, GPC-1 and PSA on the surface of sEVs isolated from the cell lines- H1975, MM05, MSTO-211H, LnCap, DU145 and HCT116- were quantified using the following commercial ELISA kits - Human CD63 SimpleStep ELISA (Cat# 275099, Abcam, UK), Human PD-L1 SimpleStep ELISA (Cat# 277712, Abcam, UK), Human GPC-1 ELISA (Cat# ab270217, Abcam, UK) and Human PSA ELISA kits (Cat#264615, Abcam, UK) as per the manufacturer's protocol with minor modifications. Briefly, 50 µL of standard or sample were added to wells of the provided 96-well plate. To this, 50 µL of antibody cocktail consisting of capture and detector antibody were added to the wells and incubated at room temperature for 1 hour. Following this, the wells were aspirated and washed three times with Wash Buffer, and 100 µL of TMB Solution was added and incubated for 10 minutes to develop colour. Finally, 100 µL of Stop Solution was added to the wells and the optical density was measured at 450 nm using a microplate reader (Varioskan LUX Reader, Thermofisher, USA).

2.14. Data and Statistical Analysis

Calibration curves were generated by plotting the signal intensity ratios against the concentration range. The limit of detection (LOD) was defined as the sum of the signal at blank concentration and three times the standard deviation of the blank measurements.

The data were reported as mean ± standard deviation (SD). Two-tailed unpaired T-test or one-way ANOVA with post hoc multiple comparison tests were applied for normally distributed data. Statistical analysis was performed using OriginLab (version 2020b) and GraphPad Prism (version 8.4.3 Software, USA). P-values <0.05 were considered statistically significant.

3. Design and Characterisation of Nanoparticles

Abstract

This chapter focuses on the design, synthesis, and characterisation of two key types of nanoparticles — AuNPs and UCNPs — engineered for bioanalytical applications. Citrate capped AuNPs were conjugated to HRP tagged antibodies for use as colorimetric signal enhancing probes in the AuNP ELISA format. The AuNP-IgG-HRP conjugates were prepared using passive adsorption at optimised pH and antibody loading concentration determined by successive titration experiments, which was critical for maintaining colloidal stability and preventing aggregation. The conjugates were functionally characterised to ensure they successful use in the AuNP ELISA to amplify detection signals.

Highly doped ($NaYF_4$:40%Yb^{3+},4%Er^{3+}) core and core@shell UCNPs were synthesised, leveraging their unique upconversion luminescence properties for biosensing applications in the UCNP microplate immunoassay and the UCNP-LFA. Surface modification with tri-block copolymers transitioned the UCNPs from hydrophobic to hydrophilic states, enhancing their colloidal stability and biocompatibility. Structural characterisation of the UCNPs were done using TEM, DLS, and zeta potential measurements, demonstrating the uniformity and stability of the nanoparticles. The nanoparticles exhibited sharp and stable emissions at ~540 nm and ~654 nm under 980 nm excitation. These luminescent properties, combined with inert shell passivation to mitigate surface quenching, ensured the UCNPs were well-suited for applications requiring high sensitivity towards detection low abundancxe sEV target analytes.

This chapter underscores the importance of systematic nanoparticle design and characterisation in developing robust bioanalytical platforms. The integration of optimised AuNPs and UCNPs into their respective immunoassay systems provides a strong foundation for the sensitive detection of sEV surface markers, as detailed in subsequent chapters.

3.1. Introduction

The synthesis, bioconjugation, and characterisation of nanoparticles form a pivotal component of this thesis, as their structural and functional integrity directly underpin the experiments and results presented in subsequent chapters (Chapters 4, 5, and 6). Nanoparticles have emerged as powerful tools in bioanalytical systems, particularly for enhancing the sensitivity and specificity of immunoassay platforms, including LFAs and ELISAs. This chapter details the synthesis, surface functionalisation, and characterisation of two key types of nanoparticles—UCNPs and AuNPs—for use as probes in UCNP-LFA, UCNP microplate immunoassay and AuNP ELISA, respectively.

In this thesis, UCNPs and AuNPs were synthesised and/or bioconjugated to act as highly efficient and stable probes within their respective assay systems, ensuring optimal sensitivity and specificity in detecting low-abundance sEV surface markers. The integration of these NPs into the assays was tailored to achieve reliable signal amplification and to address challenges associated with detecting low-abundance target analytes.

The use of AuNPs in this nanoparticle-based ELISA platform aimed to develop a simple, enhanced sandwich ELISA for detecting low-abundance sEV surface markers, potentially in a POC setting. AuNPs offer highly versatile surface chemistry, enabling stable and efficient functionalisation with recognition molecules like antibodies [411]. Compared to other nanoparticles, such as silica or polymer-based NPs, AuNPs provide stronger and more stable conjugations, which are critical for preserving functional integrity during the repeated washing and incubation steps inherent in ELISA protocols [411, 412]. Their unique SPR property enhances localised electromagnetic fields, improving HRP catalytic activity for substrate conversion (e.g., TMB in ELISA), an advantage not shared by silica or polymer NPs [413]. AuNPs are also highly biocompatible and oxidation-resistant, unlike silver or iron oxide NPs,

which degrade in biological buffers, ensuring stability and reproducibility in ELISA systems [414, 415]. Additionally, AuNPs are widely used in immunoassays, with established protocols minimising the need for extensive optimisation. While other NPs could theoretically function as HRP carriers, AuNPs uniquely combine optical properties, biocompatibility, and stability, making them the ideal choice for enhancing detection sensitivity in this system. In this thesis, commercial citrate-capped AuNPs (50 nm) were included in a Conjugation Optimisation kit (Cytodiagnostics, USA), and titration experiments were performed to determine optimal pH and antibody loading capacity for use as conjugates in the AuNP ELISA format. These experiments aimed to achieve the highest sensitivity and specificity possible, with a focus on low-abundance sEV surface markers.

The rationale for choosing UCNPs ($NaYF_4$:40%Yb^{3+}, 4%Er^{3+}) lies in their superior upconversion luminescence properties, which are particularly well-suited for detecting low-abundance sEV surface markers. These UCNPs efficiently convert NIR light (~980 nm) into visible emissions, enabling highly sensitive detection with minimal background interference [416, 417]. Yb^{3+} ions, present at a high doping concentration (40%), act as efficient sensitisers with a strong NIR absorption cross-section, while Er^{3+} ions serve as activators to facilitate energy transfer and produce sharp, bright emissions [321, 418]. This doping combination is optimised for strong luminescence and robust performance in biosensing applications [419]. In this project, UCNPs ($NaYF_4$:40%Yb^{3+}, 4%Er^{3+}) were integrated into a UCNP-based lateral flow assay (UCNP-LFA) and a UCNP-based microplate immunoassay, both aimed at detecting low-abundance sEV surface markers. The bright and stable luminescence of these UCNPs improved the sensitivity and reliability of these systems, enabling effective signal amplification [419, 420]. Their high photostability, biocompatibility, and ability to support functionalisation with recognition molecules such as antibodies made them an ideal choice for detecting low-abundance biomarkers in complex biological samples [421, 422].

A critical factor in these NP-based assays was the size variability of NPs employed in the immunoassays. Given the heterogeneous nature of sEVs, in the context of size, morphology and composition, it was important to ensure that the size of the NPs was appropriately considered to allow for effective marker detection. Larger NPs restrict access to smaller sEVs, affecting binding kinetics, while smaller NPs exhibit reduced loading capacity of capture antibodies, thus compromising capture efficiency [214, 423]. sEVs range in size from 30 to 150 nm in diameter, and NPs in the size range of ~ 40–60 nm strike an ideal balance, being large enough to provide sufficient surface area for functionalisation while remaining small enough to ensure effective interaction with sEVs [424, 425]. This size range enhances the binding efficiency of NPs to sEVs, thereby improving detection sensitivity. The appropriate NP size depends on the specific application, particularly the targeted sEV cargo. In this thesis, the focus was on sEV surface markers, making NPs in the 40–60 nm range especially suitable. These NPs provide adequate surface area for loading recognition molecules, such as antibodies, while minimising steric hindrance commonly associated with larger NPs [426]. Additionally, NPs of this size have been shown to enhance signal amplification, particularly for AuNPs, which exhibit strong SPR and this property amplifies signals in SERS and colorimetric assay-based detection systems, significantly improving the sensitivity of sEV detection [427]. Specifically, in the context of sEVs, NPs within this size range have demonstrated efficacy in nanoparticle-based immunoassays for detecting sEV surface markers [215, 303, 428]. Additionally, it was crucial to ensure that the NPs possessed the appropriate chemistry for high stability, biocompatibility and immunogenicity, facilitating the formation of immunocomplexes with target analytes on sEVs and serving as sensitive probes in the immunoassays.

The synthesis, surface modification and bioconjugation of UCNPs and the assembly of LFA strips for the UCNP-LFA were conducted under the expert guidance and direction of Dr Shihui

Wen, Dr Libing Fu and Dr Jiayan Liao, whose invaluable assistance was instrumental in the successful execution of these endeavours.

3.2. Results and Discussion

3.2.1. Structural and Functional characterisation of AuNPs and AuNP-HRP conjugates

AuNPs are highly stable and have well-defined surface chemistry, allowing for functionalising sEV-specific capture antibodies. These properties make AuNPs ideal for use as probes that can amplify signal output in colorimetric detection methods like ELISA, leading to enhanced sensitivity and detection limits of sEV markers [429, 430]. In Results Chapter 4, commercial citrate-capped AuNPs (50nm) were used to bioconjugate to HRP antibodies, which increases the availability of HRP for catalysing the TMB substrate, resulting in amplified colorimetric signals and markedly improved detection sensitivity for sEV surface markers. The absorbance spectra and average hydrodynamic size of the AuNPs were analysed by UV-Vis spectroscopy, Dynamic Light Scattering (DLS) and Zeta Potential measurements, respectively. The absorbance spectra peak was found at 523.3 nm, the average hydrodynamic size of AuNPs was found to be 53.61 ± 1.29 nm and the zeta potential was found to be -36.4 mV (Fig 16).

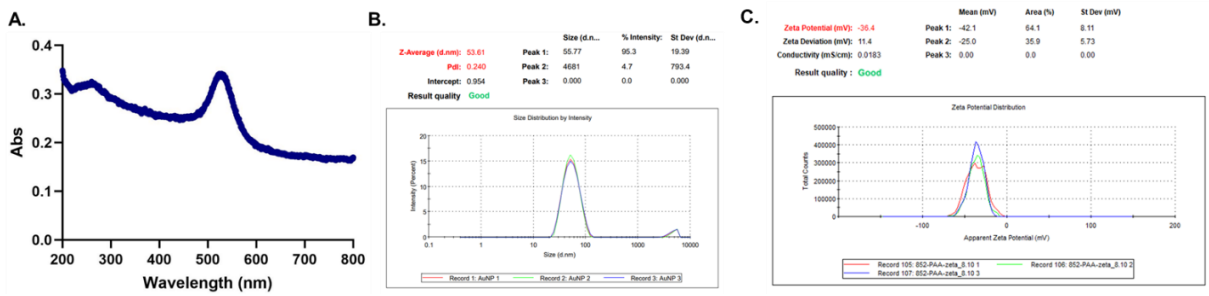

Fig 16: (a.) UV-Vis spectra of AuNPs (b.) Dynamic light scattering (DLS) measurements of the average hydrodynamic diameter of AuNPs (c.) Zeta Potential measurements of AuNPs

Passive adsorption was employed to conjugate AuNPs to the HRP-Antibody using a Gold Nanoparticle (50 nm) Optimisation kit. The passive adsorption method was selected to prepare AuNP-antibody conjugates over methods like covalent bonding because multiple studies indicated that the former achieved the most effective enhancement of colorimetric signal intensities in ELISA setups [429-431]. This is because covalent-based conjugation methods target the constant region of the antibody where the HRP is located, creating more bulk around the HRP, making it less likely to respond to its substrates and generating a colorimetric signal. The passive adsorption conjugation process exploits the electrostatic and hydrophobic interactions between the protein and the surface layer of the AuNP at an optimised pH and protein amount to generate stable AuNP complexes. Titration experiments were performed to determine the optimal pH and antibody concentration to ensure the highest level of nanoparticle surface coverage by the antibody and generate stable AuNP-antibody conjugates. The results indicated that a pH of 5.7 and an antibody concentration exceeding 10 µg were the optimal conditions for maintaining the colloidal stability of the AuNPs (Fig 17). At non-optimal pH levels or lower antibody concentrations, the insufficient surface coverage of the AuNPs by the antibody resulted in aggregation, leading to a loss of the characteristic red colouration of the colloidal AuNPs and reduced stability. Additionally, functional characterisation of AuNP-HRP conjugates was conducted using a QC Conjugate Lateral Flow Dipstick kit, with test strips pre-coated with the corresponding antispecies IgG antibody on the test line. The AuNP-HRP complexes recognised the epitope on the test line where the AuNPs aggregated, yielding a positive result (red line) and indicating stable functional integrity of the conjugates; upon adding TMB substrate to the AuNP-IgG-HRP complexes, an immediate colorimetric product was generated due to the catalytic activity of HRP. In the presence of hydrogen peroxide, HRP oxidizes TMB, producing a distinct blue-colored product, which is characteristic of HRP-tagged antibodies. This reaction contrasts with the unchanged color of unconjugated AuNPs,

confirming the successful conjugation and functional activity of the AuNP-IgG-HRP complexes (Fig 18).

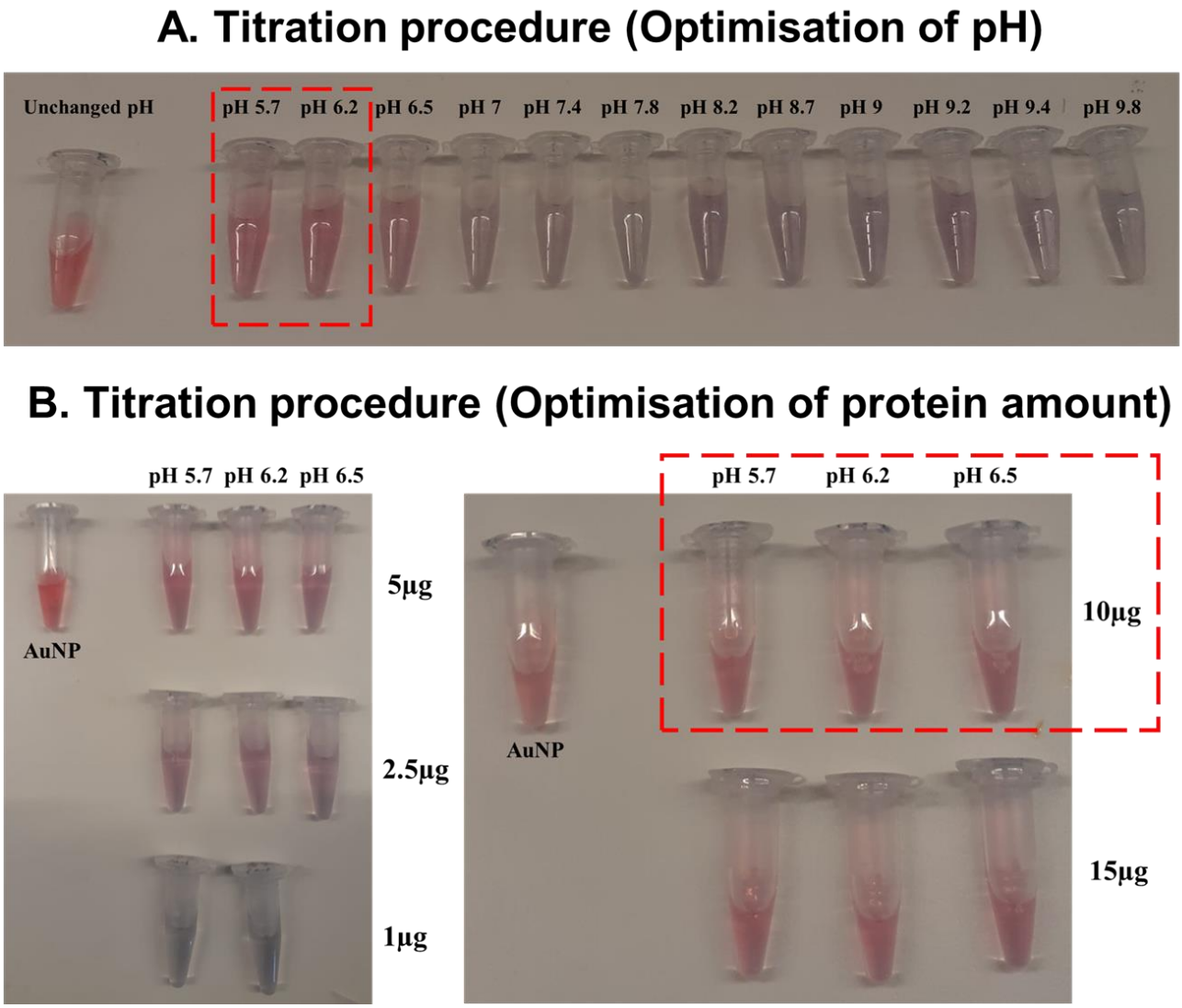

Fig 17: Titration experiments to determine the optimal pH (a.) and antibody-HRP concentrations (b.) for passive adsorption of HRP-Antibody to gold nanoparticles. At pH 5.7 and at antibody concentrations > 10 µg, the AuNP-HRP complexes maintained good colloidal stability and did not aggregate. At suboptimal pH levels or lower antibody concentrations, inadequate antibody coverage on the AuNP surface caused aggregation, which led to the loss of the colloidal AuNPs' characteristic red coloration and reduced their stability.

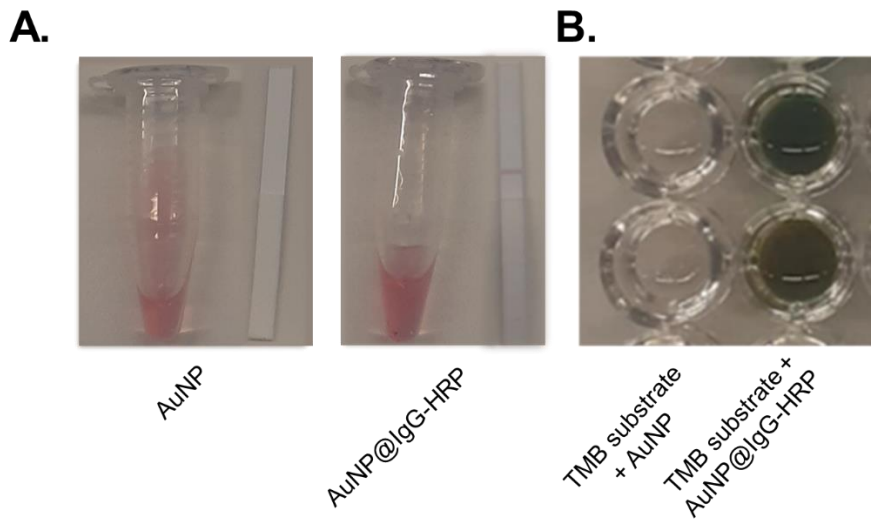

Fig 18: (a.) Functionality of AuNP-HRP conjugates: AuNP-HRP complexes were mixed with a running buffer and introduced into QC Conjugate Lateral Flow Dipsticks, which were pre-coated with the corresponding antibody on the test line. The AuNP-HRP complexes recognised the epitope on the test line where the AuNPs aggregated, indicating stable functional integrity of the conjugates. (b.) 50 µL of TMB substrate was added to 10 µL of AuNPs and AuNP-HRP conjugates, with the latter immediately generating a colorimetric product, while the former maintained an unchanged colour.

While titration experiments were performed to determine the optimal antibody loading amount required to generate stable and functional AuNP-antibody conjugates via passive adsorption, ensuring sufficient coverage to prevent aggregation and maintain assay functionality, another important parameter to consider was the equivalent number of antibodies conjugated per nanoparticle, as this plays a key role in the performance of the AuNP-ELISA.

The estimated number of antibodies conjugated per AuNP was calculated based on the commercial 50 nm citrate-capped AuNPs used in this study. The surface area of a spherical AuNP was determined using the formula:

Surface Area = $4\pi r^2$, where r is the radius of the AuNP,

For a 50 nm AuNP, the radius is r=25 nm,

Surface Area = $4 \times \pi \times (25)^2$ nm^2 = 7.85×10^3 nm^2

The footprint of an untagged IgG antibody is approximately 123 nm², derived from its dimensions (14.5 nm × 8.5 nm) [432]. The addition of an HRP enzyme increases steric hindrance and the effective footprint of each IgG antibody. This increase arises from the bulkiness of HRP (~ 40–44 kDa) and the random orientation inherent to passive adsorption [433, 434]. Practically, this spatial footprint can increase by ~30–50%, depending on the size of HRP and its orientation on the IgG molecule. For HRP-tagged IgG antibodies, the effective footprint is estimated to be 160–185 nm².

The maximum number of antibodies conjugated per AuNP can be calculated by dividing the total AuNP surface area by the antibody footprint:

Number of antibodies per NP= Total Surface Area / Antibody Footprint

Number of antibodies per NP= 7854 / 160 – 185 ≈42 – 49

Passive adsorption introduces randomness in antibody orientation, unlike covalent conjugation, which enables more controlled orientation and efficient surface coverage. In passive adsorption, antibodies may bind through various regions (e.g., Fc or Fab), reducing functional binding capacity [435]. HRP-tagged antibodies are bulkier than regular IgG due to the enzyme attachment. This bulk creates additional steric hindrance, preventing efficient packing on the nanoparticle surface [436]. Given these factors, a reduction of 20–30% in the theoretical antibody number is expected under realistic conditions.

Adjusting the upper limit values: 49 – 42 × 0.7 ≈ 29 – 34 antibodies per AuNP.

This estimation aligns with the observed colloidal stability and functionality of the AuNP-HRP conjugates, validated through the QC lateral flow dipstick test and functional HRP enzymatic activity.

3.2.2. Synthesis, Surface Modification and Characterisation of UCNPs

The luminescent properties of $NaYF_4$:40%Yb^{3+},4%Er^{3+} UCNPs, including quantum yield (QY) and brightness, are key factors contributing to their suitability for biosensing applications [437]. Yb^{3+} ions act as efficient sensitisers due to their strong absorption cross-section in the near-infrared (NIR) region (~980 nm), facilitating energy transfer to Er^{3+} activators and resulting in visible emission [438]. The brightness of these UCNPs, defined as the product of QY and absorption cross-section, is significantly influenced by the high doping concentration of Yb^{3+}. Studies indicate that Yb^{3+} doping at 40% achieves an optimal balance, enhancing brightness while avoiding concentration-quenching effects commonly observed at higher dopant levels [439, 440]. Quantum yields for $NaYF_4$:Yb^{3+},Er^{3+} UCNPs are often reported in the range of 0.1–5% under continuous-wave excitation at 980 nm, depending on synthesis conditions, particle size, and the use of core-shell structures [359, 441]. For instance, the incorporation of an inert shell, such as $NaYF_4$ or $NaGdF_4$, passivates surface quenching sites and improves QY by reducing non-radiative energy losses, with some studies reporting up to a twofold increase in QY for core@shell UCNPs compared to core-only counterparts [439, 442]. These enhancements are particularly critical for applications requiring high signal-to-background ratios, such as biosensing in complex biological environments [441].

Brightness, defined as the product of QY and absorption cross-section, is another critical parameter for evaluating the performance of UCNPs. Yb^{3+} ions act as efficient sensitisers, with a high absorption cross-section for NIR light (~980 nm) [443]. This energy is transferred non-radiatively to Er^{3+} ions, resulting in sharp dual-band emissions (~540 nm and ~654 nm), corresponding to the $^4S_{3/2} \rightarrow {}^4I_{15/2}$ and $^4F_{9/2} \rightarrow {}^4I_{15/2}$ transitions, respectively [193, 444]. Notably, the brightness of $NaYF_4$:40%Yb^{3+},4%Er^{3+} UCNPs is significantly higher under NIR excitation, offering distinct advantages, particularly in biological imaging where NIR

excitation reduces tissue autofluorescence and scattering [440, 442]. The doping concentration of Yb^{3+} (40%) is carefully optimised to achieve maximum brightness while avoiding concentration quenching, which occurs when excessive dopant levels lead to energy migration to quenching sites. This balance ensures efficient energy transfer to Er^{3+} activators while minimising non-radiative losses [359, 441]. The addition of an inert shell further enhances brightness by mitigating surface quenching effects, which can otherwise compromise luminescence. This shell also improves QY, contributing to overall brightness improvement [202]. Moreover, tailoring nanoparticle size is another critical factor influencing brightness. Smaller nanoparticles exhibit higher surface-to-volume ratios, which increases the likelihood of surface quenching. Therefore, optimised core sizes, typically in the range of 30–40 nm, combined with an inert shell thickness of ~3–5 nm, have been shown to maximise luminescence, striking a balance between reducing surface quenching and maintaining efficient luminescent properties [441, 445].

While the absolute values of QY and brightness can vary depending on experimental conditions, the selection of $NaYF_4$:40%Yb^{3+},4%Er^{3+} UCNPs in this thesis is consistent with their demonstrated performance in our previous studies [359, 439, 442]. This includes the use of the exact composition of these UCNPs in our group's UCNP-LFA studies [370, 371], where they have proven to be highly sensitive, photostable, and efficient luminescent probes for the detection of low-abundance analytes.

Core and core@shell UCNPs were synthesised following a previously published co-precipitation method [409, 446]. The morphology of the synthesised UCNPs was characterised using TEM, showing that the $NaYF_4$:40%Yb^{3+},4%Er^{3+} core nanocrystals had a size of approximately ~34 nm and exhibited a high degree of homogeneity with a narrow size distribution (Fig 19a). The growth of inert shells was used to passivate non-radiative pathways to surface quenchers, forming core@shell nanoparticles. The passivation of non-radiative

pathways to surface quenchers through shell coating is crucial for maximising upconversion luminescence and improving sensitivity for detecting target analytes. Following the shell coating, the size of UCNPs increased from 34 nm to 40 nm (Fig 19b), indicating the addition of a 3 nm thick inert shell. The observed narrow size distribution, with a coefficient of variation (CV) below 5%, signifies the uniformity of the as-synthesized core@shell nanocrystals. This uniformity ensures consistency in size, rendering them suitable for subsequent surface modification.

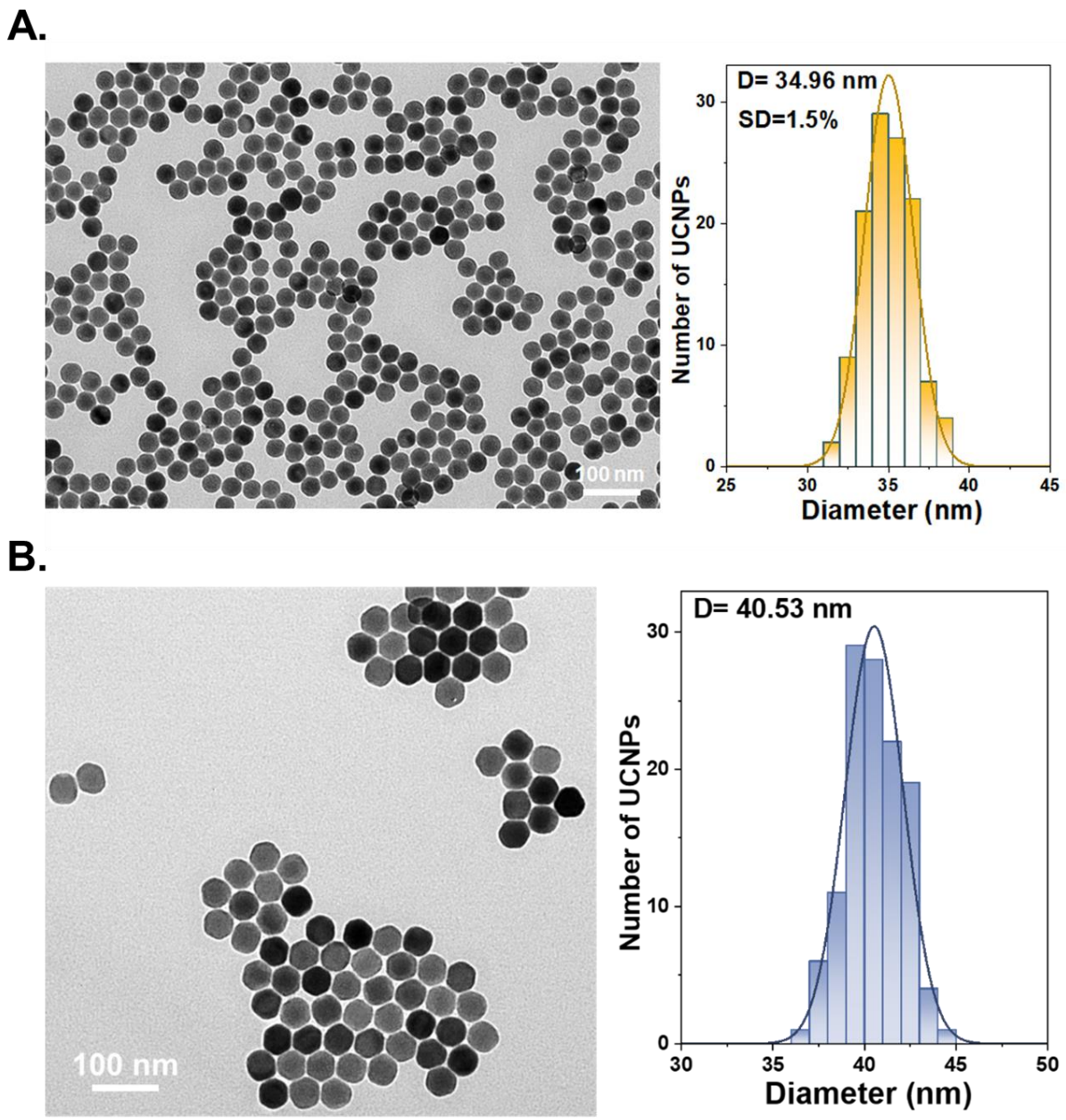

Fig 19: TEM of the core (A) and core@shell UCNPs (B), size distribution diagram

Surface modification of UCNPs is a vital step in making the particles suitable for use as probes in biomedical applications. The surface of as-synthesized UCNPs is hydrophobic and requires surface modification to make them hydrophilic [447, 448]. Polymers containing multiple anchoring ligands have been extensively used to modify the as-synthesized UCNPs and improve colloidal stability, biocompatibility and immunogenicity [410, 449]. In this project,

we modified the UCNPs with copolymers (Fig 20a) to form UCNPs with surface carboxyl groups based on a previously optimised protocol [410]. Fourier transform infrared (FTIR) spectroscopy also confirmed the successful coating of copolymer on the surface of UCNPs, as evidence by the absorption bands of copolymer at 1638 cm^{-1} (asymmetric stretching vibrations of CO_2), and 1048 cm^{-1} (stretching vibrations of CH_2O) (Fig 20b). When excited at 980 nm, UCNPs display two prominent emission bands, located at ~540 nm and ~654 nm. These bands correspond to the $^4S_{3/2} \rightarrow {}^4I_{15/2}$ and $^4F_{9/2} \rightarrow {}^4I_{15/2}$ electronic transitions of Er^{3+}, respectively (Fig 20c).

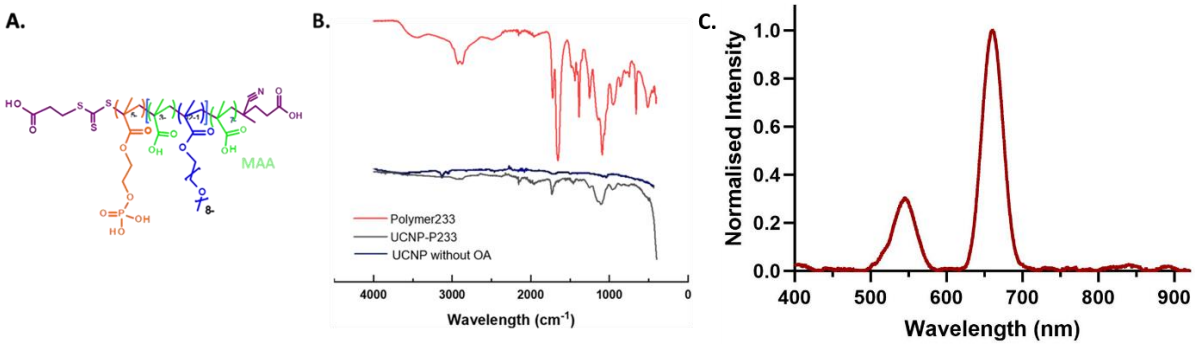

Fig 20: The structure (A) and Fourier transform infrared spectra (FTIR) (B) of as-synthesized polymer, UCNP without OA and UCNPs modified with polymer (C) Luminescence spectra of UCNPs under excitation at 980 nm.

For bioanalytical applications, the UCNPs were transitioned from an oil phase to an aqueous phase, using a ligand exchange strategy to replace OA with a co-polymer, as discussed previously. DLS measurements were employed to validate that the successful surface modification of the as-synthesised UCNPs. As illustrated in Fig. 21a, the size of the UCNP-Polymer was found to be 69 nm, which indicates a uniformly distributed hydrodynamic size without aggregation. Zeta potential was used to assess the surface charge of polymer-modified UCNPs. The carboxylic functional group on the polymer surface, when in an aqueous medium, is deprotonated, generating a negative charge. The zeta potential of the UCNP-Polymer was

found to be -24.5 mV (Fig. 21b), confirming the successful modification of the UCNPs with the polymer. These modified UCNPs were further utilised for bioconjugation with CD63 and PD-L1 detector antibodies, employing the AnteoTech Nano kit to generate probes for subsequent use in the UCNP microplate immunoassay (Results Chapter 4) and the UCNP-LFA (Results Chapters 5 and 6).

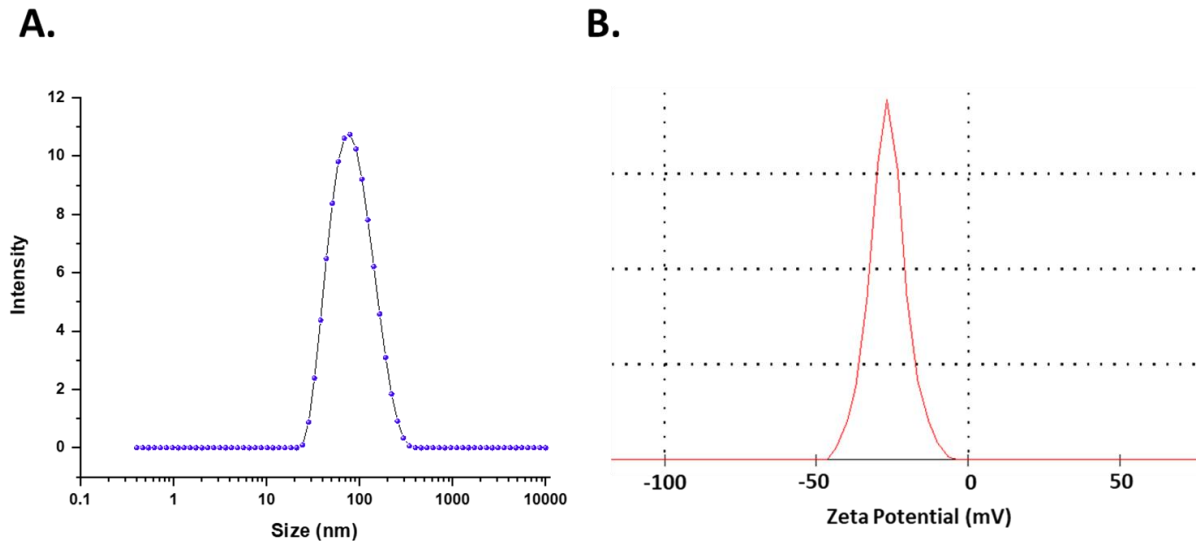

Fig 21: Characterisation of surface-modified UCNPs (diluted in ultra-pure water, pH 7). Dynamic light scattering CONTIN plot (a.) and Zeta potential (b.) measurements were performed on Malvern Zetasizer Nano ZS equipped with 633nm laser and 173° backscattering detector. The size of the UCNPs-Polymer was found to be 69 nm, and the zeta potential measurement was found to be -24.5 mV.

Following surface modification, antibodies for CD63, PD-L1, and GPC-1 were conjugated to UCNPs using a Particle Conjugation Kit, enabling their use as probes in Results Chapters 4, 5, and 6. An important parameter to evaluate in this process was the mole ratio of antibodies to UCNPs in the conjugated probes. The conjugation was carried out using the exact same kit and protocol that our group has successfully applied in multiple published studies, particularly those involving the UCNP-LFA. In these previous projects, the conjugation process consistently achieved a high efficiency of ~80%, ensuring the reliability and reproducibility of the antibody-UCNP functionalisation [370, 371].

Calculation of mole ratio of Antibody/UCNPs

Moles of UCNPs = Mass of UCNPs (g) / Molecular weight of UCNPs (g/mol)

$= 2 \times 10^{-4} / 90 \times 10^{6} = 2.22 \times 10^{-12}$ moles

Moles of Antibody = Mass of Antibody (g) / Molecular weight of antibody (g/mol)

CD63 Antibody = $2 \times 10^{-6} / 25{,}000 = 8 \times 10^{-11}$ moles

PD-L1 Antibody = $2 \times 10^{-6} / 33{,}000 = 6.06 \times 10^{-11}$ moles

GPC-1 Antibody = $2 \times 10^{-6} / 62{,}000 = 3.23 \times 10^{-11}$ moles

Adjusted for estimated conjugation efficiency (80%)

CD63 Antibody: $8 \times 10^{-11} \times 0.8 = 6.4 \times 10^{-11}$ moles

PD-L1 Antibody = $6.06 \times 10^{-11} \times 0.8 = 4.85 \times 10^{-11}$ moles

GPC-1 Antibody = $3.23 \times 10^{-11} \times 0.8 = 2.58 \times 10^{-11}$ moles

Mole ratio of modified Antibody to UCNPs

CD63: $6.4 \times 10^{-11} / 2.22 \times 10^{-12} \approx 28.8$

PD-L1: $4.85 \times 10^{-11} / 2.22 \times 10^{-12} \approx 21.8$

GPC-1: $2.58 \times 10^{-11} / 2.22 \times 10^{-12} \approx 11.6$

The calculated mole ratios of antibodies to UCNPs were approximately 29 for CD63, 22 for PD-L1, and 12 for GPC-1, reflecting successful conjugation and providing a reliable basis for their use in downstream bioanalytical applications.

3.3. Conclusion

This chapter detailed the design, synthesis, surface modification, and characterisation of nanoparticles crucial for developing nanoparticle-based immunoassay platforms. AuNPs and UCNPs were carefully optimised and evaluated to meet the specific requirements for their respective roles in AuNP-ELISA, UCNP-based microplate immunoassay and UCNP-LFA.

These nanoparticles not only facilitated improved signal amplification but also addressed the unique challenges associated with detecting low-abundance sEV surface markers. AuNPs were successfully characterised and optimised as HRP-antibody conjugates for use in the AuNP-ELISA. Titration experiments were performed to determine the optimal pH and antibody loading concentration for maintaining colloidal stability and achieving high antibody surface coverage. Functional testing of the AuNP-HRP conjugates confirmed their stability and activity, with robust colorimetric signals generated upon exposure to TMB substrate, validating their utility in the AuNP ELISA format for sensitive detection of sEV surface markers. Similarly, UCNPs were synthesised, passivated with inert shells, and surface-modified with copolymers to ensure colloidal stability, biocompatibility, and functional integrity. These modified UCNPs were further conjugated with detector antibodies using optimised protocols and tested as probes in UCNP-based LFAs and microplate immunoassays. The upconversion efficiency, stable luminescence and ability to support bioconjugation with antibodies make UCNPs highly effective for the sensitive and reliable detection of low-abundance target analytes.

The results and discussions in this chapter highlight the importance of systematic nanoparticle optimisation in bioanalytical systems. The characterisation and functionalisation processes described herein established the structural and functional integrity of AuNPs and UCNPs, ensuring their suitability for use in the experiments presented in subsequent chapters. For AuNPs, optimising antibody conjugation efficiency and stability was critical for enhancing ELISA sensitivity. For UCNPs, the combination of stable luminescence and and tailored surface chemistry ensured their effectiveness in UCNP-LFA and microplate immunoassays. The insights gained here will directly inform the experiments and results detailed in Chapters 4, 5 and 6, underscoring the broader impact of nanoparticle-based bioanalytical innovations.

4. Developing nanoparticle-integrated ELISA formats for sensitive detection of sEV surface markers with potential POC applications

Abstract

ELISA is a widely used technique employed in detecting target analytes and is widely used in scientific and clinical settings. However, conventional ELISAs often face limitations in sensitivity, making it unable to detect and quantify low-abundance analytes accurately. Moreover, traditional ELISAs are performed in benchtop plate readers that require well-equipped lab settings, making them unsuitable for POC testing in resource-limited environments. To address this, the integration of nanoparticles has emerged as a strategic enhancement, significantly amplifying sensitivity and expanding the detection limits of ELISAs for improved precision in identifying target analytes. In this study, we explored two modified ELISA formats to facilitate enhanced sensitivity towards the detection of CD63, which is an integral structural marker of sEVs. The first technique involved an AuNP-enhanced colorimetric ELISA system, performed in a portable, hand-held plate reader device, wherein the signalling HRP antibody was conjugated to AuNPs and the modified ELISA generated a ~2-fold enhancement in detection sensitivity compared to the conventional ELISA format. The second technique involved the use of a UCNP-based microplate-ELISA immunoassay, performed in a bench-top, custom built plate reader where the HRP-tagged signalling antibody was replaced by a UCNP-conjugated detector antibody to function as a luminescent signal-generating probe. The system achieved a LOD of 0.036 ng/mL (1.578 pM) and a ~10-fold enrichment in detection sensitivity compared to the AuNP-ELISA. While the UCNP microplate immunoassay has limited feasibility for use as a POC testing system, the enhanced sensitivity of the modified ELISA systems have significant clinical relevance, specifically towards detecting low-abundance target analytes from diverse sample types in diagnostic settings.

4.1. Introduction

The Enzyme-Linked Immunosorbent Assay (ELISA) detection system is a widely used biochemical technique designed to detect and quantify target analytes in a sample [450, 451]. They are based on very specific antigen-antibody binding and the binding of an enzyme-labelled antibody to a specific target molecule, generating a measurable signal, typically colorimetric or fluorescent, enabling the quantification of the target's presence in a sample [452]. Colorimetric ELISAs commonly use enzyme labels, including horseradish peroxidase (HRP), alkaline phosphatase (ALP) and β-galactosidase. These enzymes catalyse the oxidation of reducing substrates like 3,3',5,5'-tetramethylbenzidine (TMB) by H_2O_2, generating a coloured reaction product in the presence of target analytes [453]. Contrastingly, other ELISA formats utilise fluorescent or luminescent labels to produce light as a signal-generating product in the presence of target analytes [454].

sEVs are formed by the inward budding of late endosomes and contain molecular information about their tissue of origin. They have gained attention as enriched sources of biomolecules, including proteins, nucleic acids and other metabolites [39]. While sEVs originate from diverse sources, they share common structural and functional proteins, including tetraspanins (CD9, CD63 and CD81), heat shock proteins (HSP60, HSP70) and endosomal sorting complex for transport (ESCRT) associated components (Alix and TSG101) [47]. Studies have implicated tumour-derived sEVs in promoting aspects of tumour progression, including cell apoptosis suppression, angiogenesis, invasiveness and metastasis, genomic stability and inflammation [40, 41].

While studies have used conventional ELISA to detect sEV surface markers to accurately detect and quantify minimal quantities of sEV target analytes, the detection sensitivity of conventional ELISAs can be improved by integrating an additional signal amplification step.

Multiple studies have explored signal amplification strategies like tyramide signal amplification, liposomes and nanoparticles to enhance the sensitivity of immunoassays [455-457]. In this context, AuNPs are considered an appealing choice for integration into immunoassays owing to their unique structural, optical and catalytic properties. AuNPs have a high surface-volume ratio, high loading capacity and biocompatibility [458] and studies have employed AuNPs to function as signal indicators and carriers to load more signalling molecules and facilitate improved sensitivity in immunoassays [459, 460]. Moreover, traditional ELISAs typically rely on bulky instruments that are not practical for use in resource-constrained settings. To address this, portable ELISA systems offer handheld plate reader devices with user-friendly interfaces that function similarly to conventional ELISA setups, while enabling rapid detection of sEV-specific analytes [461, 462]. Integrating nanoparticle immunoassays into these portable platforms can enhance the sensitivity of sEV marker detection, particularly in setups with limited resources.

While traditional ELISAs generally employ a colorimetric signal readout, efforts have been made to replace the enzyme-mediated signal development process using nanoparticles like quantum dots, magnetic NPs, metal NPs and fluorescent polymers [463-465]. UCNPs represent a new generation of luminescent labels for sensitive detection of target analytes in immunoassays. They exhibit the unique ability to be stimulated by near-infrared light and subsequently emit shorter wavelength light (anti-Stokes emission). This reduces autofluorescence and light scattering in bio-analytical applications [445, 466]. Moreover, UCNPs offer high photostability, and the large anti-Stokes shifts allow for the separation of excitation and detection channels, making them ideal for use in sensitive immunoassays [467-469]. Previous research conducted by our group has successfully utilised UCNPs in TIRF and super-resolution microscopy formats to detect and quantify sEVs at the single vesicle level [407, 408]. Studies have also incorporated UCNPs into microplate-based ELISA formats to

detect target analytes at improved detection sensitivity and an expanded concentration range compared to traditional ELISAs [470, 471]. While these studies have employed the UCNP microplate immunoassay format to detect target analytes, it has not been used to detect and quantify sEV surface markers.

In this study, we explore two nanoparticle-enhanced ELISA formats to allow for sensitive detection of target analytes. The first is a colorimetric ELISA system performed in a portable, hand-held plate reader, where the signalling antibody was conjugated to AuNPs to function as signal enhancers and improve the sensitivity of traditional ELISAs (Fig 22). The second is a UCNP-based microplate immunoassay system performed in a customised plate reader integrated with a 980 nm laser to excite UCNPs and record the resultant emission signals at ~654 nm. In the UCNP immunoassasy, the signalling antibody is replaced by a UCNP probe that functions as a signal transducer by emitting luminescent signals in the presence of target analytes instead of an enzyme-mediated generation of a coloured product (Fig 23). The objective of the study was to harness the enhanced sensitivity of the nanoparticle-modified ELISA/microplate immunoassasy systems for the sensitive detection of CD63, an integral structural surface marker for sEVs.

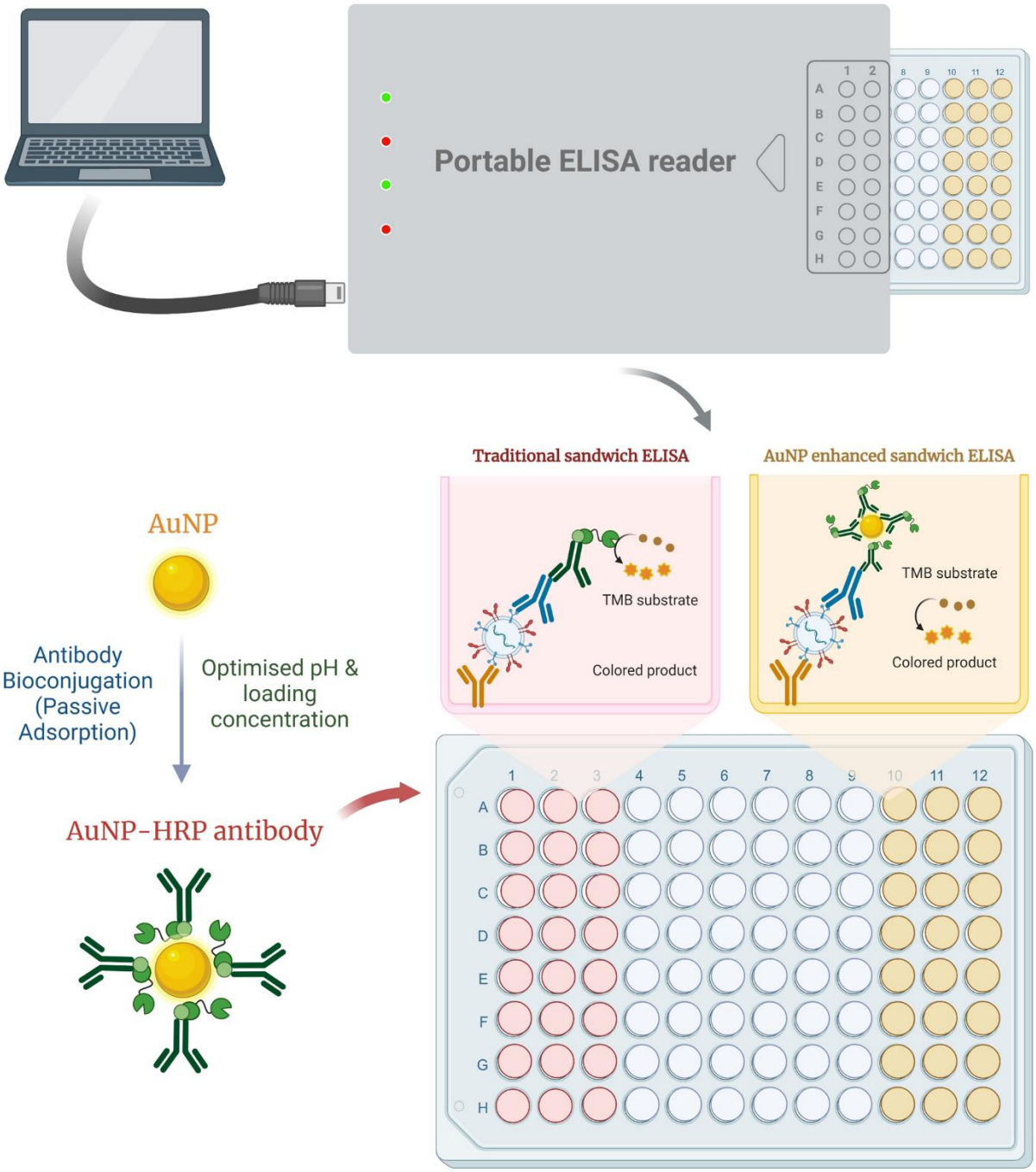

Fig 22: Schematic illustration of the colorimetric AuNP-enhanced sandwich ELISA (AuNP-ELISA), implemented in a portable, hand-held plate reader. The conventional sandwich ELISA format was modified using AuNP-conjugated HRP-labelled antibodies that act as a colorimetric signal amplifier and consequently enhance the detection sensitivity of target analytes using the ELISA format.

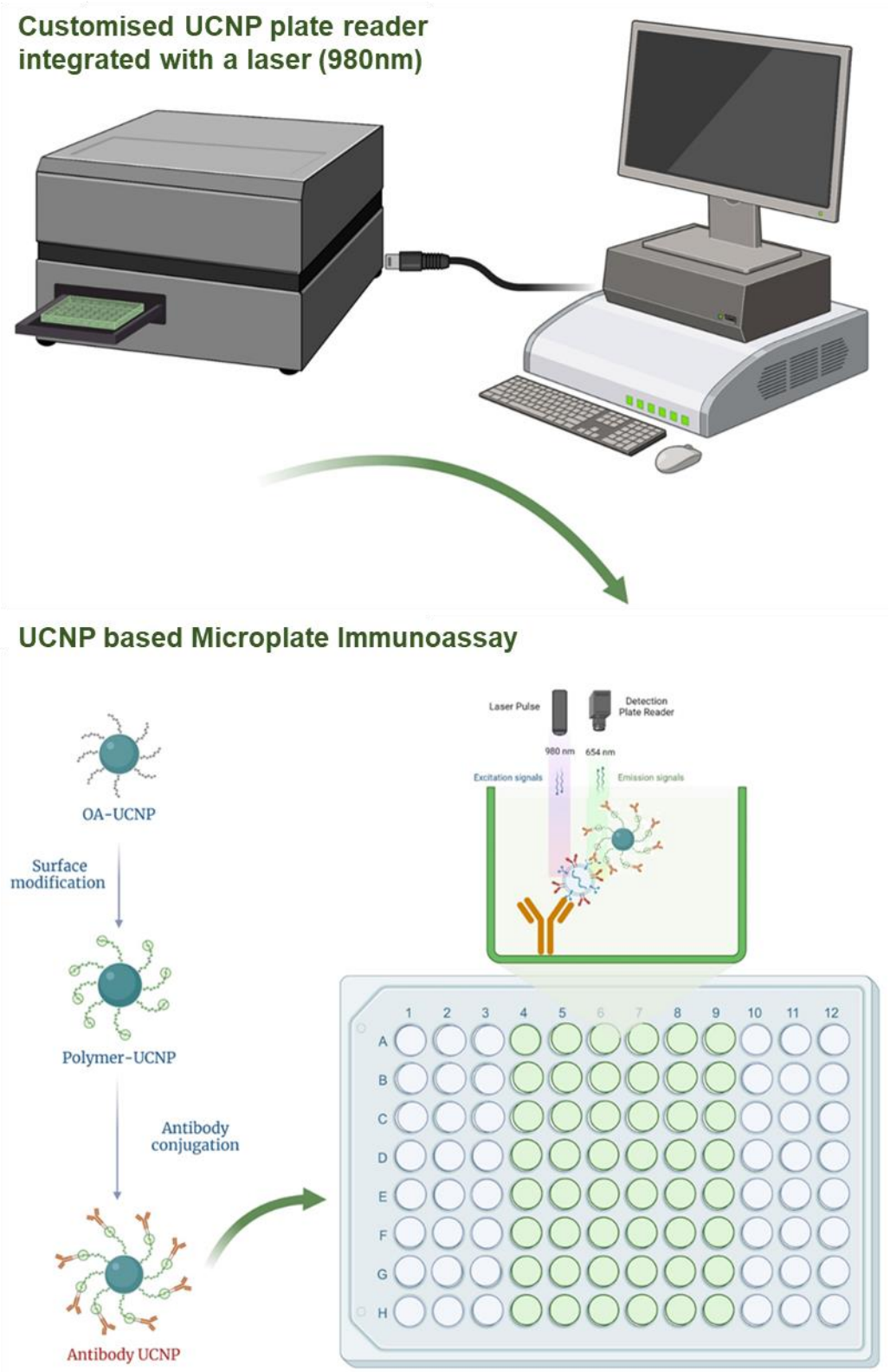

Fig 23: Schematic representation of the UCNP-enhanced microplate immunoassay. UCNP conjugated antibody complexes were used in a microplate-based sandwich immunoassay, where the probes replaced the colorimetric signal-generating compounds of a traditional ELISA detection system. A custom-built plate reader equipped with a 980nm laser was used to excite the UCNP probes and record the emission as 654nm.

4.2. Experimental Results

4.2.1. Cell Culture and Isolation of sEVs

H1975 and MSTO-211H cells (Fig 24) were cultured in T175 flasks until they reached ~70% confluence. Subsequently, hypoxic conditions were induced on the cells for 48 h, following which the culture medium underwent to isolate sEVs. The size and concentration of the isolated sEVs were assessed by NTA. The average sizes of the H1975 and MSTO sEVs were found to be 108.7 nm and 125.1 nm, respectively, consistent with the reported size range of sEVs. The concentration of the isolated sEVs were found to be 4.4×10^9 particles/mL and 1.2×10^9 particles/mL, respectively (Fig 25). sEVs from H1975 and MSTO cells were also used for Chapter 5, where Western Blotting and TEM validated the morphology and sEV specific surface marker expression of sEVs (Fig 36).

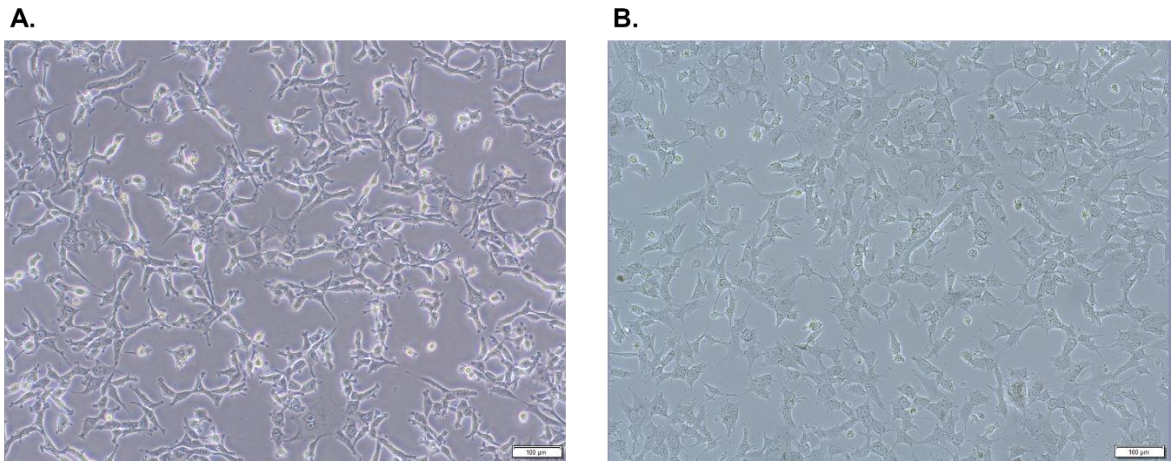

Fig 24: Representative phase-contrast images of (a.) H1975 and (b.) MSTO cells. These cells were cultured till they reached ~70% confluence and cultured in hypoxic conditions for 48 hours before the culture medium was collected to isolate sEVs (Scale bar: 100 µm)

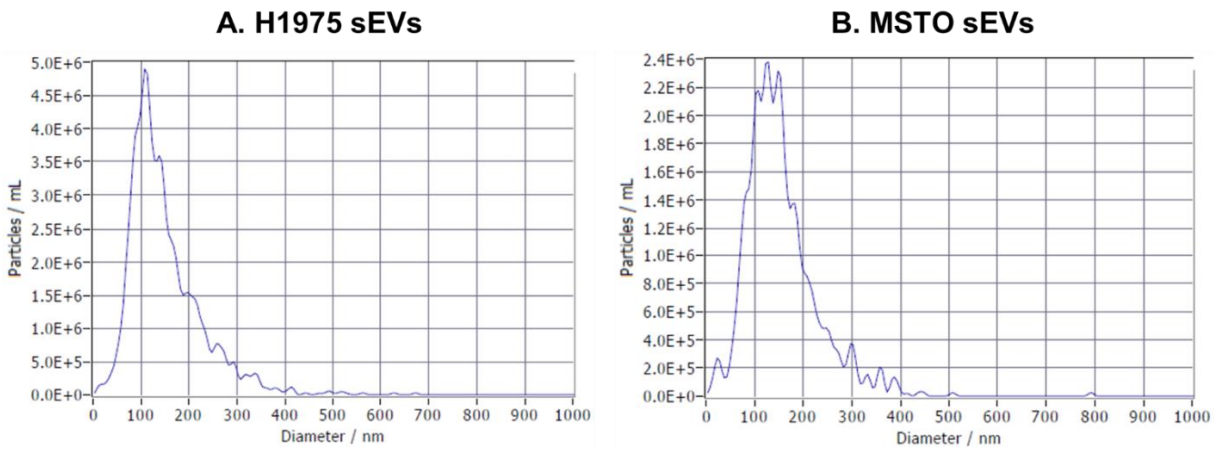

Fig 25: NTA analysis of the H1975 (a.) and MSTO-211H (B.) cell-derived sEVs. The mean sizes of the H1975 and MSTO sEVs were found to be 108.7 nm and 125.1 nm, respectively, and the concentrations of the sEVs were found to be 4.4×10^9 particles/mL and 1.2×10^9 particles/mL, respectively.

4.2.2. Optimisation of the sandwich ELISA components

The AuNP-enhanced colorimetric immunoassay exploits the unique properties of AuNPs employed as carriers of the signalling HRP-labelled antibody in the traditional sandwich ELISA process. Traditional colorimetric ELISAs use an HRP-labelled antibody to catalyse the oxidation of a substrate to generate a coloured product, the absorbance which can be quantitated using a microplate reader. With the enhanced surface area of AuNPs, they are able to bind to more molecules of the antibody and hence generate a significant amplification of the colorimetric signal in comparison to the traditional ELISA format. In this study, AuNP-HRP conjugates were prepared to be integrated for use in the ELISA system and facilitate enhanced sensitivity in detecting target analytes, specifically sEV surface markers. Having previously established the excellent bio-analytical performance offered by high-quality UCNPs, detector antibodies were conjugated with surface-modified UCNPs and used directly in a microplate-based immunoassay, where the UCNP-antibody complex functioned as signal probes instead of coloured product-generating compounds of conventional ELISA. A customised plate reader

that can excite UCNPs and record their emission signals in a microplate setup was used to detect and quantify target analytes in samples sensitively.

In this project, the capture antibody and blocking buffer concentrations were optimised independently, as they do not directly interact with the detection antibody or HRP antibody in the ELISA setup [472-475]. However, the simultaneous optimisation of the detection antibody and HRP antibody concentrations was crucial due to their interdependent roles in the sandwich ELISA format [476-478]. In the context of the AuNP-ELISA platform, conjugation of HRP to AuNPs introduced unique dynamics compared to free HRP antibodies, necessitating a tailored approach to optimise both detection and HRP antibody concentrations simultaneously [479, 480]. This is particularly important for low-abundance targets, such as sEV surface markers, where limited antigen availability requires a precise balance between detection antibody and HRP antibody concentrations to maximise antigen capture and signal amplification [481, 482]. Moreover, simultaneous optimisation is essential to account for sandwich ELISA systems' non-linear nature and the components' synergistic effects. This ensures the assay operates within its optimal dynamic range, delivering accurate and reproducible results [483, 484]. Independent optimisation of these parameters could overlook their interplay, potentially leading to suboptimal signal amplification and reduced sensitivity; therefore, optimising both antibodies in tandem gives a better chance of achieving the desired assay performance [485-487].

To ensure the best analytical performance of both sandwich ELISA formats, it was vital to optimise the multiple components of the sandwich ELISA setup, namely the concentrations of capture antibody, blocking buffer (% BSA), detector antibody and the HRP-labelled antibodies. The optimised ELISA conditions were found to be – capture antibody: 5 μg/mL, blocking buffer: 7.5% BSA, detector antibody: 4 μg/mL and HRP-antibody: 250 ng/mL (Fig 26); and these optimised concentrations of the ELISA components were used for the remainder of the nanoparticle integrated immunoassay experiments. Additionally, to assess if the immunoassays

maintained a high level of specificity in detection of target analytes, experiments were performed to check for cross-reactivity/non-specific binding. The results showed that absorbance readings of the control and 12.5 ng/mL PD-L1 antigen were similar in a CD63 ELISA detection setup, and the absorbance readings between 25 ng/mL CD63 antigen and 25 ng/mL + 12.5 ng/mL PD-L1 antigen were indistinguishable (Fig 27). Similarly, for a PD-L1 detection setup, absorbance readings of the control and 25 ng/mL CD-63 antigen were similar and the readings between 50 ng/mL PD-L1 antigen and 25 ng/mL CD63 + 50 ng/mL antiegn were indistinguishable. These findings establish the sandwich ELISA's specificity in detection of target analytes.

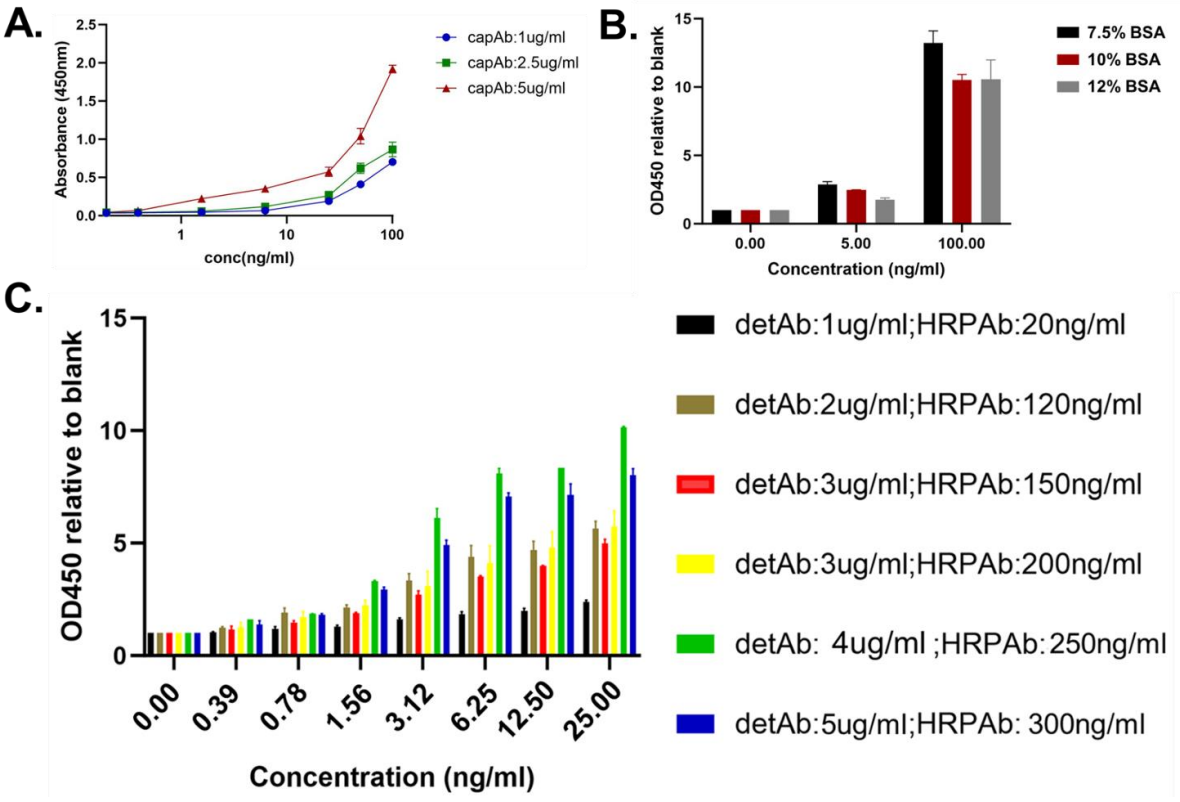

Fig 26: Optimisation of sandwich ELISA components. (a). Capture Antibody (capAb: 1 µg/mL, 2 µg/mL and 5 µg/mL) (b.) Blocking Buffer (7.5% BSA, 10 % BSA and 12 % BSA) (c.) Detector Antibody (detAb) and HRP-labelled Antibody (HRPAb). Data plotted as Mean ± S.D (n=3)

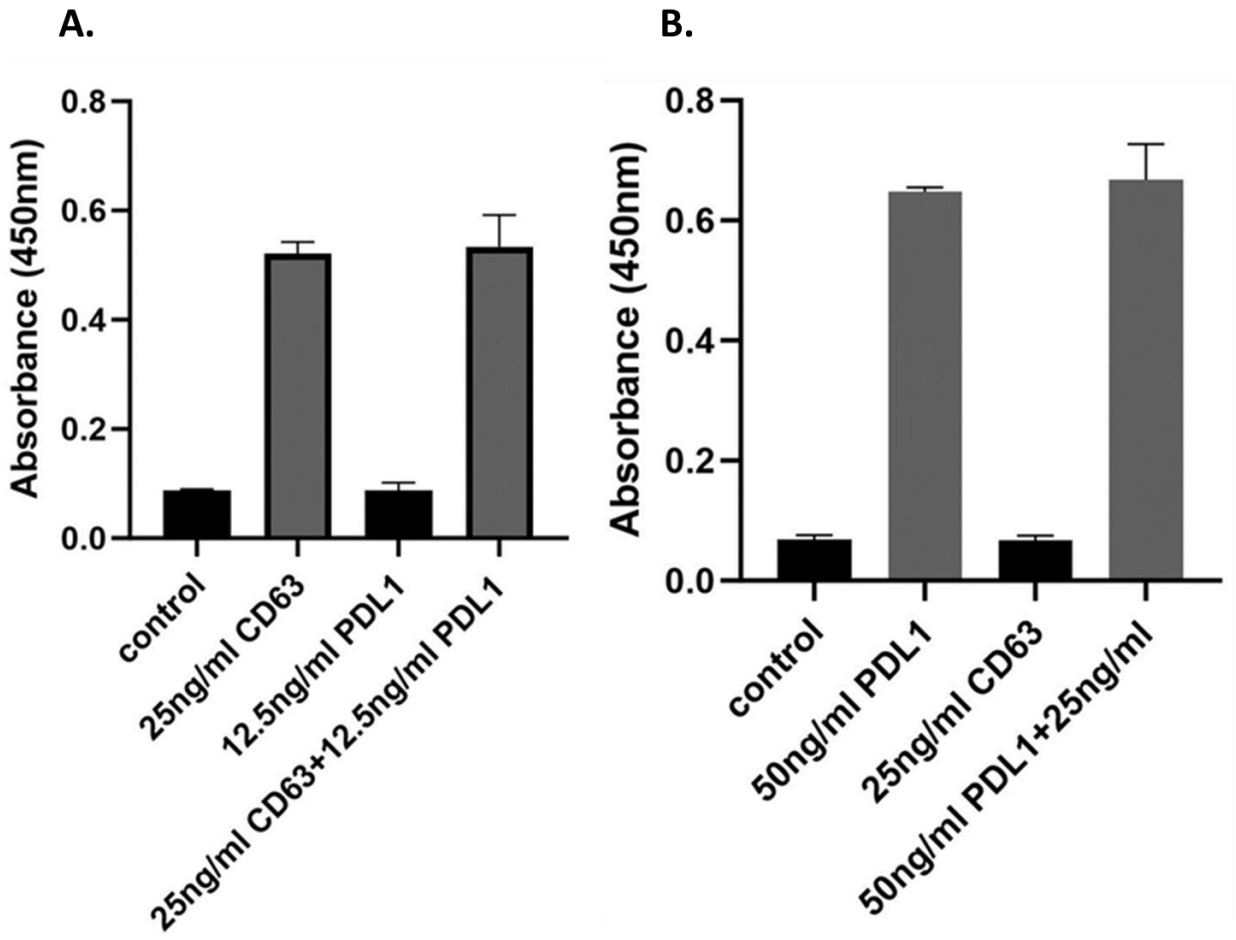

Fig 27: Detection of cross interactions in CD63 and PD-L1 in the sandwich ELISA format. Microplate wells with the CD63 antibody pair showed no positive signal in the presence of high concentrations of PD-L1 (12.5 ng/mL). Importantly, the high concentration of PD-L1 did not affect the detection of 25 ng/mL CD63. Microplate wells with the PD-L1 antibody pair have no positive signal in the presence of high concentrations of CD63 (125 ng/mL); also, the high concentration of CD63 did not affect the detection of 50 ng/mL PD-L1. Data plotted as Mean ± S.D. (n=3)

Apart from optimising the concentrations of BSA in the blocking buffer, the capture, detector, and HRP antibodies, several other parameters were considered, tested, and optimised to ensure the ELISA performed as robustly as possible. These additional factors were critical in refining the assay's performance and addressing the challenges inherent in developing a reliable homemade ELISA platform. The optimisation process, including the concentration ranges of antibodies used and the antigen to be tested, was informed both by findings from relevant studies on sEV-specific ELISA development [488-490] and by the specific needs of our experimental setup, ensuring the approach was tailored to achieve the best possible analytical

performance. Unlike commercial ELISA kits, which benefit from industrially optimised and controlled surface chemistries, we had limited control over the microplate surface properties. Nevertheless, to give us the best chance of developing a reliable assay, we selected high-binding polystyrene microplates to ensure consistent antibody and antigen immobilisation [491, 492]. The choice of the coating buffer was critical, as the AuNP-IgG-HRP conjugates used in subsequent experiments were pH-sensitive and prone to aggregation under alkaline conditions. While carbonate buffer (pH 9.6) is commonly used in ELISA protocols, we opted for PBS (pH 7.4) as the coating buffer [493]. This adjustment improved the stability of the AuNPs and enhanced the reliability of the ELISA results by preventing aggregation. The ionic strength and pH of buffers at various stages of the ELISA were systematically adjusted. Higher salt concentrations were avoided to maintain optimal antibody binding efficiency [494]. For the washing steps, PBS-Tween (0.05% Tween-20) was used to reduce background noise. However, during the final washing step for the UCNP-based microplate immunoassay, Tween-20 was excluded from the wash buffer to avoid excess detergent interference, as Tween-20 was already present in the UCNP probe dilution buffer. This modification significantly improved the reproducibility and signal specificity of the UCNP-based assay. The number of washing cycles was increased from three to five to further reduce background signals and non-specific interactions [495]. This adjustment demonstrated the importance of stringent washing steps in achieving reliable results, particularly in custom ELISA setups. The incubation temperature and duration for antigen binding, blocking, and antibody interactions were systematically optimised. While most commercial ELISA protocols recommend incubating the antigen/sample for 1.5–2 hours at 37°C, our experiments demonstrated that overnight incubation at 4°C yielded more consistent results. This adjustment accounts for the low abundance of target analytes in our samples and the absence of industrial optimisation in our setup, as the extended incubation period allowed sufficient time for stable immunocomplex

formation between the antigen and antibody, ultimately enhancing assay sensitivity and reproducibility. The reaction time for TMB substrate development was optimised to prevent overdevelopment, which can result in signal saturation or variability [496]. Careful monitoring ensured that the colorimetric signals remained within the quantifiable range. To ensure accurate quantification, different curve-fitting models were evaluated, including linear regression and 4-parameter logistic (4PL) regression. ELISA standard curves are typically fitted using the 4PL model, but in our dataset, the R-squared values for both models were comparable. To ensure consistency across assays, particularly since the UCNP microplate immunoassay employed a linear curve fit, we chose to analyse the ELISA data using a linear regression model as well. This ensured methodological uniformity in data interpretation and facilitated direct comparisons between the two assay systems.

The iterative optimisation of ELISA conditions addressed specific challenges associated with a home-made assay system, such as limited control over surface chemistries and detecting low-abundance target analytes. Key adjustments, such as the use of high-binding plates, specific buffer formulations, and prolonged incubation times, were guided by both experimental evidence and insights from the literature. assumed that these factors would enhance immunocomplex stability and overall assay performance. While certain conditions, such as shorter incubation times, higher temperatures, or buffers with pH incompatible with nanoparticles, were tested and discarded due to inconsistent results, these setbacks informed a more robust optimisation strategy. These insights not only strengthen the current assay's performance but also provide a foundation for further refinement and adaptation to other analytes or assay platforms.

4.2.3. AuNP enhanced colorimetric sandwich ELISA

The optimised sandwich ELISA conditions were used to detect CD63 using both the conventional ELISA and the AuNP-enhanced ELISA formats. Samples with a concentration range of CD63 antigen (0.39 ng/mL–50 ng/mL) were concurrently analysed to establish calibration curves for both systems, to serve as references for quantifying the concentration of CD63 on the surface of sEVs. Fig 28 shows a proportional increase in absorbance readings with increasing concentration of CD63 antigen in the range of 0.39 ng/mL–50 ng/mL, corresponding to molar concentration range of 0.0171 nM - 2.19 nM. The results clearly show that the AuNP-ELISA generated higher signals compared to the conventional ELISA, resulting in sensitive detection of target analytes (Fig 28). LODs were calculated as per the standard formula reported in the literature [497, 498]. The LOD of CD63 antigen with AuNP-ELISA was found to be 0.493 ng/mL (0.0216 nM), which exceeded that of the conventional ELISA (1.191 ng/mL, 0.0522 nM), establishing the superiority of the format. Additionally, the generation of coloured products with the addition of TMB substrate with the AuNP-ELISA took only 10 mins, while the classic ELISA took up to 30 mins. The improved LOD was a result of the AuNPs functioning as carriers of the HRP signalling molecules to the binding sites of the target epitope and can be implemented to accurately detect minute quantities of target analytes, including sEV surface markers.

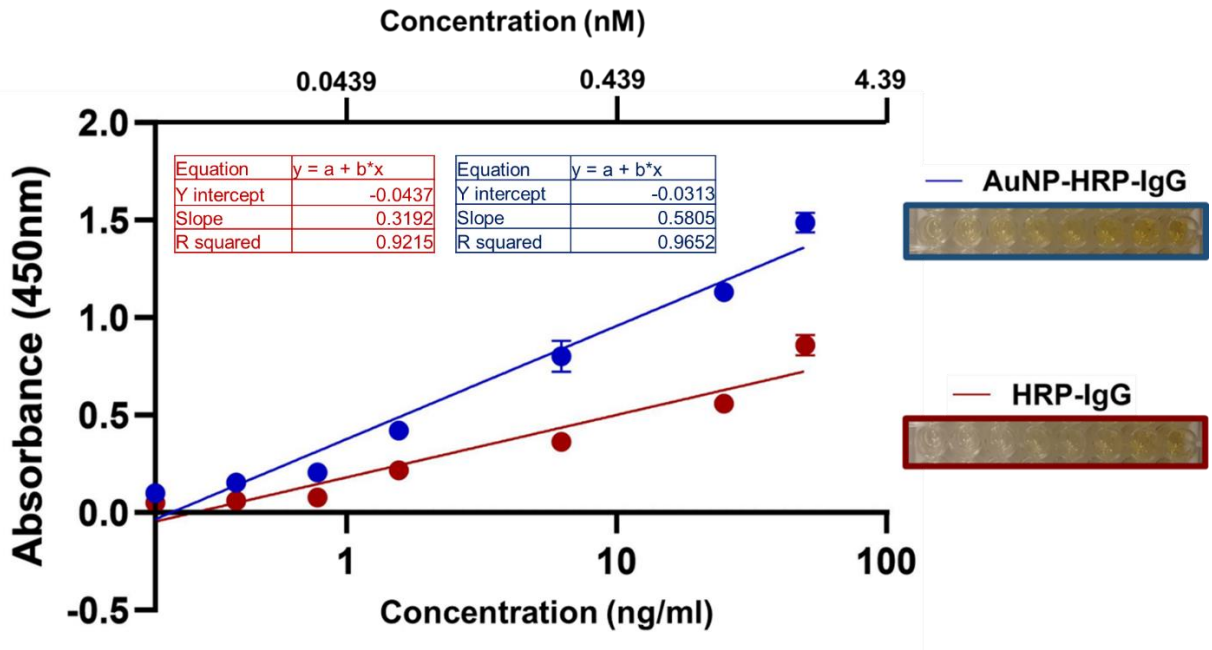

Fig 28: Detection of CD63 antigen using the (red) Conventional colorimetric ELISA and the (blue) AuNP-enhanced ELISA. Calibration curves for the detection of CD63 at concentrations of 0.39 ng/mL–50 ng/mL, corresponding to a molar concentration range of 0.0171 nM - 2.19 nM. The absorbance readings showed a proportional increase with increasing concentration of the protein between this concentration range [(a.) R^2=0.9215; (b.) R^2=0.9652]. Data plotted as Mean ± S.D. The AuNP ELISA clearly generated higher colorimetric signals than the conventional ELISA format, resulting in enhanced sensitivity towards detection of CD63 antigen. The AuNP ELISA produced colorimetric signals in 10 minutes, compared to the conventional ELISA, which took up to 30 minutes for colour development. Data plotted as Mean ± S.D. (n=3)

The AuNP-ELISA was used to detect CD63 on the surface of sEVs isolated from H1975 and MSTO cells. sEV samples were prepared at varying concentrations (~ 10^5 – 10^6 sEVs/µL) to quantitate the CD63 on the surface of sEVs. Consistent with the calibration curve findings (CD63 antigen), the AuNP-ELISA generated higher absorbance readings and allowed for enhanced sensitivity in the detection of sEV CD63. The conventional ELISA had limited sensitivity, hindering accurate CD63 quantitation in sEVs. In contrast, the AuNP-ELISA was able to detect CD63 at concentrations as low as 1.87 × 10^6 sEVs/µL and 8.21 × 10^5 sEVs/µL for H1975 and MSTO sEVs, respectively (Fig 29).

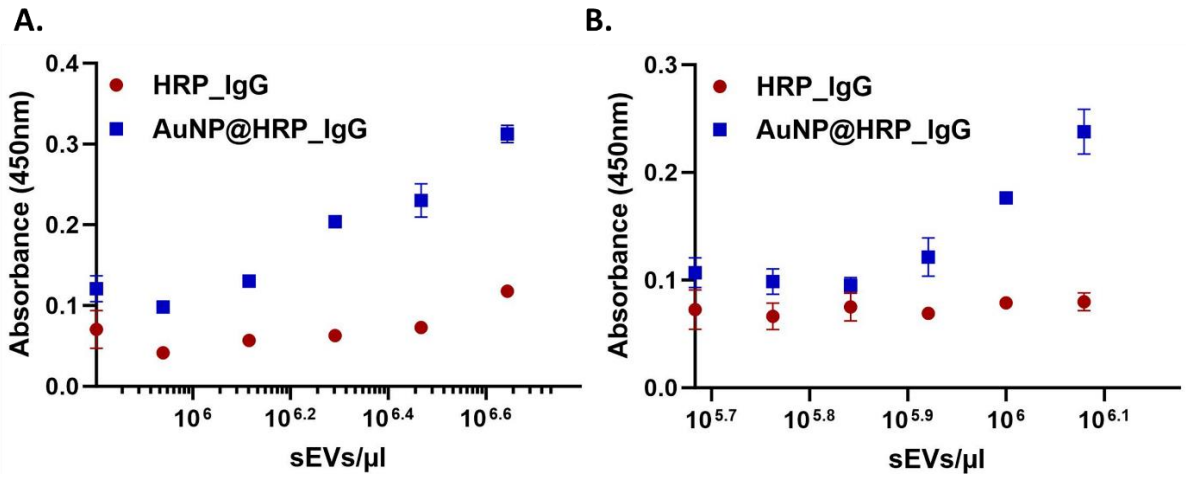

Fig 29: Detection of CD63 on the surface of sEVs isolated from (a.) H1975 and (b.) MSTO-211H cells. Samples were prepared with sEVs at varying concentrations (~ 10^5 – 10^6 sEVs/µL) and analysed using the conventional and AuNP-enhanced ELISA. The AuNP-ELISA generated higher absorbance readings and allowed for enhanced sensitivity in the detection of sEV CD63. For H1975 and MSTO sEVs, it was able to detect CD63 at concentrations as low as 1.87 × 10^6 sEVs/µL and 8.21 × 10^5 sEVs/µL, respectively. Data plotted as mean ± standard deviation (S.D). (n=3)

The colorimetric ELISA system was also employed to detect PD-L1 antigen at a concentration range of 0.39 ng/mL – 50 ng/mL, corresponding to a molar concentration range of 0.0155 nM – 1.992 nM (Fig 35). Consistent with the CD63 antigen findings, the AuNP-ELISA generated higher absorbance readings compared to the traditional ELISA, resulting in more improved detection of target analytes (Fig 30). Subsequently, sEV samples were prepared at varying concentrations (~ 10^5 – 10^6 sEVs/µL) to quantitate the PD-L1 on the surface of sEVs. While the AuNP ELISA did generate higher colorimetric signals compared to the conventional ELISA, the absorbance readings generated were too low and inconsistent to be quantitated accurately (Fig 31). CD63 is an sEV structural surface marker, but a disease-specific, low-abundant sEV marker like PD-L1 necessitates a detection system with higher sensitivity to facilitate its accurate detection and quantitation.

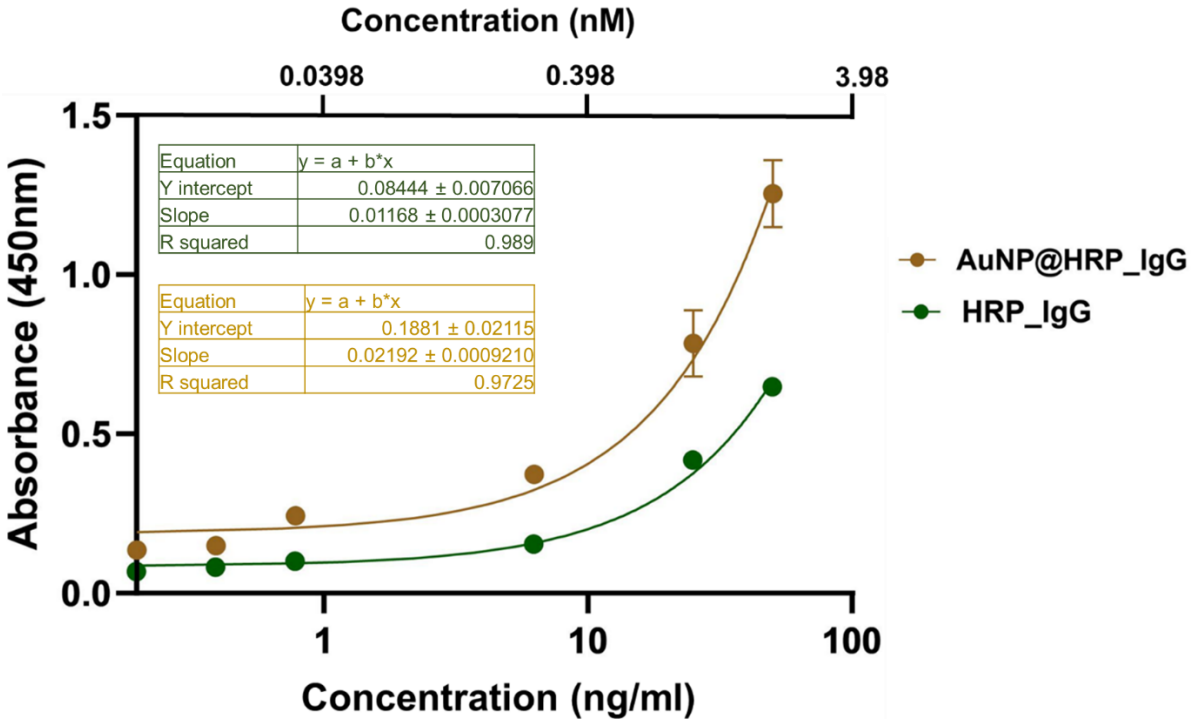

Fig 30: Detection of PD-L1 antigen using the (green) conventional colorimetric ELISA and the (gold) AuNP-enhanced ELISA. Calibration curves for detecting CD63 at concentrations of 0.39 ng/mL–50 ng/mL, corresponding to a molar concentration range of 0.0155 nM – 1.992 nM. The absorbance readings showed a proportional increase with increasing concentration of the protein between this concentration range [(a.) R^2=0.9890; (b.) R^2=0.9725]. Data plotted as Mean ± S.D. The AuNP ELISA clearly generated higher colorimetric signals than the conventional ELISA format, resulting in enhanced sensitivity towards detection of PD-L1 antigen. The AuNP ELISA produced colorimetric signals in 10 minutes, compared to the conventional ELISA, which took up to 30 minutes for colour development. Data plotted as mean ± standard deviation (S.D). (n=3)

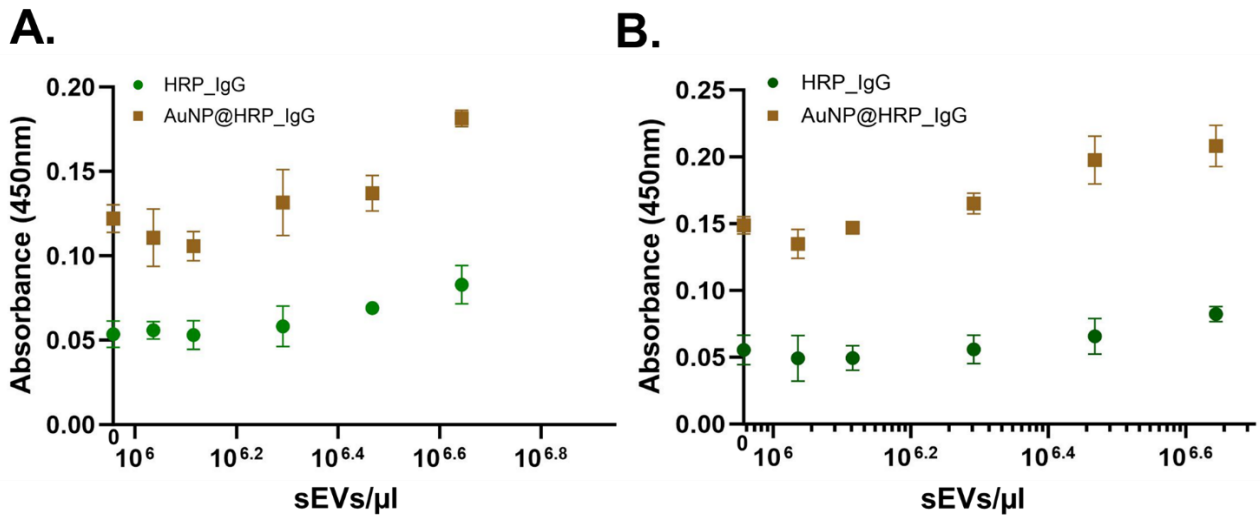

Fig 31: Detection of PD-L1 on the surface of sEVs isolated from (a.) H1975 and (b.) MSTO-211H cells. Samples were prepared with sEVs at varying concentrations (~ 10^5 – 10^6 sEVs/µL) and analysed using the conventional and AuNP-enhanced ELISA. While the AuNP ELISA did generate higher colorimetric

signals compared to the conventional ELISA, the absorbance readings generated were too low and inconsistent to be quantitated accurately. Data plotted as mean ± standard deviation (S.D). (n=3)

The use of AuNP-HRP conjugates allowed for more HRP signalling molecules to catalyze the TMB substrate, resulting in higher absorbance readings and a ~2-fold improvement in the detection sensitivity of CD63 compared to conventional ELISA. The application of the AuNP-ELISA system in a portable, hand-held plate reader has significant implications for POC applications, particularly in resource-limited settings, for the sensitive detection of sEV markers. While the AuNP-ELISA demonstrated proficiency in detecting CD63, its sensitivity towards low-abundance and disease-specific sEV markers such as PD-L1 needs further enhancement. This highlights the importance of rigorously optimising assay parameters, which is inherently more refined in commercial ELISA kits but challenging to replicate in lab-assembled systems, particularly when integrating NP-based detection platforms like AuNP-ELISA.

Commercial ELISA kits are rigorously optimised through industrial refinement and standardisation, making them highly effective for enzyme-based detection systems [499, 500]. Precision-engineered microplate wells feature uniform geometries and specialised coatings, such as high-binding polystyrene or covalent attachments, to ensure consistent antigen-antibody immobilisation and minimise nonspecific binding [501]. These kits employ strategies to orient capture antibodies correctly, maximising antigen binding efficiency, while lab-assembled ELISAs, relying on passive adsorption, often result in random antibody orientations that reduce sensitivity [502]. Reagents in commercial kits, such as capture and detection antibodies, substrates, and enzyme conjugates, are meticulously purified and thoroughly standardised to ensure consistent quality and reproducibility across batches [503]. Proprietary blocking and wash buffers are tailored to minimise nonspecific interactions and maintain compatibility with complex sample matrices, whereas lab-prepared buffers often lack this

refinement [504]. Antibody pairs are extensively validated for optimal stoichiometry, specificity, and sensitivity, ensuring consistent performance across diverse samples [505]. Enzyme-substrate kinetics and dynamic range are optimised to enhance signal generation and provide precise quantification [502]. Additionally, pre-validated protocols, built-in controls, and advanced signal amplification strategies contribute to the robustness and reliability of commercial kits [472]. Despite these optimisations, the proprietary design and enzyme-specific nature of commercial kits make them impractical for integrating NP-based systems like AuNP-ELISA without significant re-engineering [473].

4.2.4. UCNP-based microplate Sandwich Immunoassay

The UCNP-based microplate immunoassay operates similarly to conventional ELISA, but it employs a UCNP-conjugated detector antibody as a direct luminescent reporter, replacing the need for a chromogen-labelled antibody and substrate to produce a coloured assay readout. The optimised sandwich ELISA conditions were implemented for the UCNP microplate immunoassay, with the HRP-Antibody replaced by a UCNP-conjugated detector antibody functioning as a probe. Black-walled microplates were used to minimise signal bleed-through between adjacent wells and improve the reliability of the assay. A customised microplate reader integrated with a 980 nm laser to excite the UCNP probes in individual wells and the resultant luminescent emission signals were recorded. CD63 antigen at a concentration range of 0.1 ng/mL – 1000 ng/mL, corresponding to a molar concentration range of 4.39×10^{-3} nM – 43.9 nM was analysed and the results showed a proportional increase of signal intensity with increasing antigen concentration (R^2= 0.9606) (Fig 32). The LOD for CD63 antigen with the UCNP microplate immunoassay was found to be 0.036 ng/mL, corresponding to a molar concentration of 1.578 pM, making it ~10-fold more sensitive than the colorimetric AuNP-ELISA format.

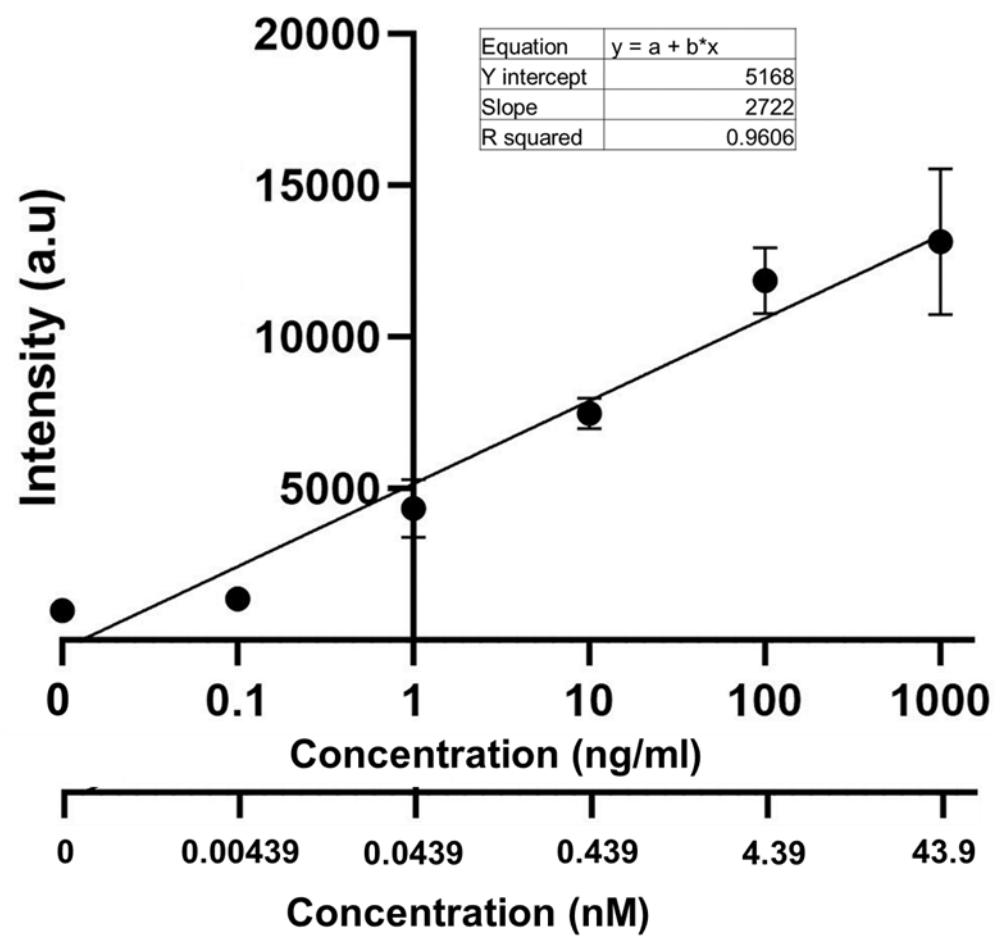

Fig 32: Detection of CD63 antigen using the UCNP-based microplate immunoassay system. Calibration curve for detection of CD63 protein at concentrations of 0.1, 1, 10, 100 and 1000 ng/mL, R^2= 0.9606. The signal intensity showed a proportional increase with increasing CD63 antigen concentration. Data plotted as mean ± standard deviation (S.D). (n=3)

The background noise observed in blank (no antigen) samples with UCNPs stems from multiple factors inherent to the assay system. The residual luminescence of UCNPs, which emit light upon excitation even without specific binding events, contributes significantly to the baseline signal [506]. This is further amplified by the 980 nm laser used for UCNP excitation, as higher laser power enhances upconversion efficiency but simultaneously increases baseline

luminescence [507]. Another contributing factor is autofluorescence from assay components, such as the microplate materials or buffer constituents [508]. Although black-walled microplates are designed to minimise reflectivity, the clear-bottom section may emit weak autofluorescence under NIR excitation [509]. Additionally, some chemical or biological components, such as stabilisers or proteins in the buffer, may weakly fluoresce, adding to the background signal [510]. Non-specific adsorption of UCNPs to the plate surface and incomplete removal of unbound UCNPs during washing further amplify the noise, as even trace amounts of highly luminescent UCNPs can contribute a detectable signal [511].

Mitigation strategies to reduce this background noise include fine-tuning the laser power to balance sensitivity and baseline noise, implementing more stringent or automated washing protocols to ensure the complete removal of free UCNPs, and optimising blocking agents to minimise non-specific UCNP adsorption [512, 513]. Additionally, time-gated detection systems can help differentiate true UCNP signals from background noise by capturing their unique emissions while excluding short-lived autofluorescence or stray excitation light [514]. Although normalising signals would reduce the apparent baseline signal, the relative raw signals between blank and antigen-containing samples remain consistent due to the use of arbitrary relative units (a.u.), ensuring reliable differentiation between samples.

sEV samples were prepared in concentrations between ~10^4 – 10^6 sEVs/µL and analysed in the UCNP microplate immunoassay. For H1975 and MSTO sEVs, the system was successful at detecting CD63 at concentrations as low as 1.44×10^5 sEVs/µL and 6.06×10^5 sEVs/µL, respectively (Fig 33), which represents an improved sensitivity over the colorimetric AuNP-ELISA (Table 3). The use of high quality luminescent UCNPs as a signalling probe substantially enhanced the sensitivity of the microplate-based immunoassay and represents a more sensitive system for accurate detection of target analytes.

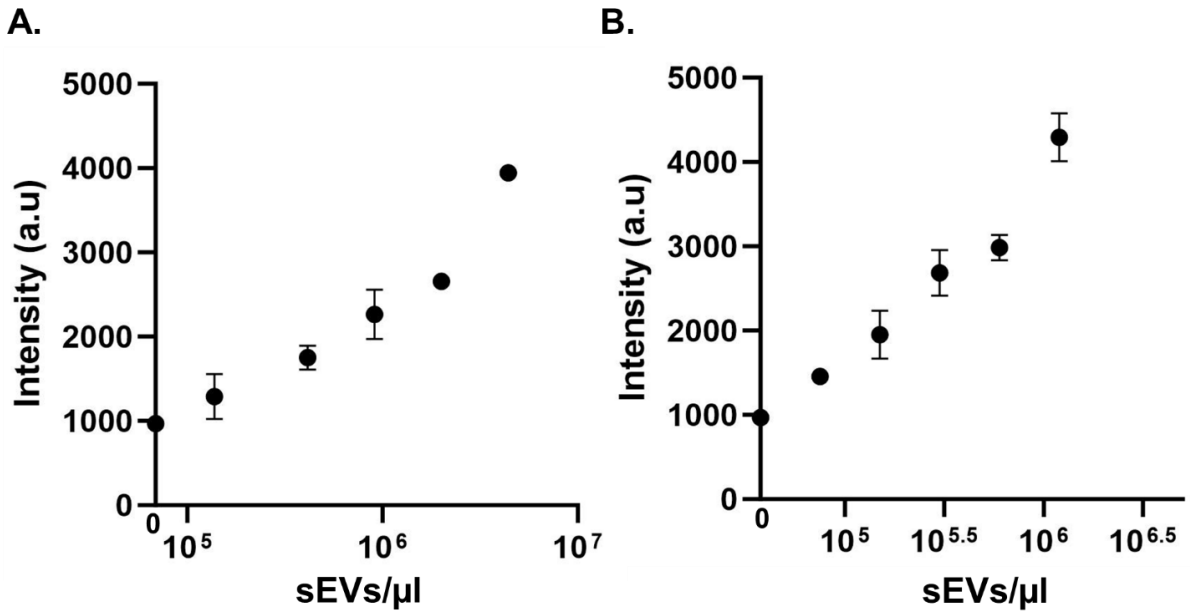

Fig 33: Detection of CD63 on the surface of sEVs isolated from (a.) H1975 and (b.) MSTO cells. sEV samples were prepared in concentrations ranging from ~10^4 – 10^6 sEVs/µL and analysed using the UCNP microplate assay. For H1975 and MSTO sEVs, it was able to detect CD63 at concentrations as low as 1.44 × 10^5 sEVs/µL and 6.06 × 10^4 sEVs/µL, respectively. Data plotted as mean ± standard deviation (S.D). (n=3)

Table 3: Comparison of detection performance between AuNP-ELISA vs UCNP microplate immunoassay.

	Lowest sEV concentration detected	
sEVs	**AuNP-ELISA**	**UCNP Microplate Assay**
H1975	1.87 × 10^6 sEVs/µL	1.44 × 10^5 sEVs/µL
MSTO	8.21 × 10^5 sEVs/µL	6.06 × 10^4 sEVs/µL

Compared to other reported UCNP-based systems, our UCNP microplate immunoassay represents a more operationally uncomplicated, ELISA-like approach towards detecting sEV surface markers (Table 4). Huang et al. achieved a detection limit of 1.8 × 10^3 EVs/µL using

UCNP-based TIRF microscopy, a highly advanced imaging technique that allowed single EV detection, requiring specialised instrumentation [407]. Chen et al. and Wang et al. utilised LRET-based aptasensors, achieving detection limits of 1.1×10^3 particles/μL and 80 sEVs/μL, respectively, through mechanisms that depend on precise energy transfer setups [397, 398]. Zhang et al. attained the highest sensitivity (<10 sEVs/μL) by employing UCNP-AuNP conjugates with ICP-MS, a sophisticated single-particle detection system that requires substantial instrumentation and expertise [515]. While our UCNP microplate assay is comparatively less sensitive than these advanced systems, it allows a simpler, more accessible format with the potential for scalability.

The UCNP microplate assay can also be expanded to detect and quantify other disease-specific sEV surface markers, including PD-L1, EGFR, GPC-1, EpCAM, PSA, EGFR and others, to provide a more comprehensive understanding of the diagnostic landscape. However, while the colorimetric ELISAs were performed on a portable, hand-held plate reader setup, the UCNP microplate assay format required a custom-built plate reader specifically designed for UCNP detection. The detection of UCNPs necessitates a specific analytical system that can excite the nanoparticles at 980 nm and record the resulting emissions at ~ 654 nm, and the UCNP microplate immunoassay used in this study was a benchtop system that is not applicable as a POC testing system. With the continuous development of the UCNP microplate assay system, a miniaturised, hand-held version of this customised plate reader, if developed, would enable the sensitive detection of more disease-specific sEV markers, including the analysis of clinical samples, and enhance the diagnostic applicability of the technology, particularly in resource-limited settings.

Table 4: Comparison of detection performance between UCNP microplate assay with other UCNP-based sEV analytical studies

Study	Principle	Lowest sEV concentration detected
Huang et al. [407]	UCNP-based TIRF microscopy	1.8×10^3 EVs/μL
Chen et al. [397]	Paper aptasensor based on LRET from UCNPs to AuNRs	1.1×10^3 particles/μL
Wang et al. [398]	aptasensor based on LRET from UCNPs to tetramethyl rhodamine	80 sEVs/μL
Zhang et al. [515]	UCNP-AuNP nanosatellite detection in inductively coupled plasma–mass spectrometry	< 10 sEVs/μL
This work	UCNP-based microplate immunoassay	6.06×10^4 sEVs/μL - 1.44×10^5 sEVs/μL (CD63)

4.3. Discussion and Conclusion

ELISA is recognised for its convenience in detecting target analytes, presenting a well-established and user-friendly platform. Traditional ELISAs often struggle with low sensitivity, hindering their effectiveness in detecting low-abundance analytes [429]. The study focussed on developing nanoparticle-integrated ELISA systems with potential POC applications that enable the detection and quantification of sEV surface markers. In the first technique, we incorporated the use of AuNP-conjugated signalling antibodies to improve the sensitivity of the conventional ELISA in a portable, hand-held colorimetric plate reader. The high surface-to-volume ratio, substantial loading capacity, and biocompatibility of AuNPs served as carriers for the HRP antibody in the ELISA format. Although studies have reported the improved detection sensitivity of target analytes using AuNP-ELISA, they have not been applied to the detection of sEV surface markers, particularly within an analytical system suitable for potential POC applications [429, 430]. The AuNP-ELISA successfully generated higher absorbance readings and improved CD63 antigen and sEV-CD63 detection sensitivity in H1975 and

MSTO cell-derived sEVs (~2-fold) compared to the conventional ELISA. Although this in-house ELISA method demonstrated success in detecting CD63, for the application of this technology towards accurate quantitation of low-abundance disease-specific sEV markers like PD-L1, especially from complex biological samples, the detection limit needs to be enhanced substantially.

In this project, initial attempts were made to incorporate the AuNP-ELISA and UCNP microplate assay formats into commercial ELISA kits to utilise their pre-optimized components and protocols. However, these efforts failed due to fundamental incompatibilities, as commercial kits are optimised for enzyme-antibody interactions and not designed for NP-based systems. Adapting commercial ELISA kits to AuNP- or UCNP-based detection systems is impractical due to the lack of transparency in their pre-optimized components and protocols, which are specifically designed for enzymatic detection methods [501]. Key information, such as the density of capture antibodies on the plate, the composition and concentration of blocking and wash buffers, and the working concentrations of detector antibodies and HRP conjugates, is proprietary and undisclosed [516]. Without these details, it is impossible to adjust critical parameters for NP-based systems, which have unique requirements such as maintaining colloidal stability, optimising surface interactions, and balancing nanoparticle-antibody stoichiometry [517, 518]. Commercial wash and blocking buffers, optimised for enzyme-antibody systems, may not account for the physical and chemical properties of NPs, potentially causing aggregation or nonspecific binding [519]. This issue is particularly critical, as NP aggregation in incompatible buffers can lead to signal loss, high background noise, and reduced sensitivity [520]. Additionally, commercial kits are designed as closed systems with standardised protocols for incubation times and temperatures tailored for enzyme-antibody kinetics. These fixed conditions are incompatible with the slower binding dynamics and distinct optical properties of NPs like AuNPs and UCNPs [521]. Given the inflexible design of

commercial kits and their reliance on pre-validated reagents and substrates, modifying them for NP-based ELISAs would negate the benefits of their optimisation and require extensive re-engineering [522]. These limitations are amplified when dealing with scarce analytes, as achieving optimal sensitivity requires fine-tuned assay conditions that commercial kits cannot accommodate. As a result, building a custom NP-based ELISA and/or microplate immunoassay from the ground up was the only feasible solution to ensure compatibility, maintain NP stability, and achieve reliable and sensitive detection of low-abundance markers like sEV surface proteins.

Colorimetric ELISA formats rely on the spectroscopic detection of a chromogenic substrate, producing a measurable colorimetric product directly proportional to the concentration of the target analyte. However, the sensitivity of colorimetric readout is comparatively lower than alternative signal readouts like fluorescence, which diminishes the efficacy of colorimetric ELISAs. Furthermore, potential interference from compounds in biological samples adds another layer of complexity to the colorimetric signal readout [523-525]. The UCNP microplate immunoassay format leveraged the superior bio-analytical performance of high-quality UCNPs to sensitively detect CD63 in a microplate-based immunoassay format at an improved sensitivity (~10-fold) compared to the AuNP-ELISA. Moreover, the UCNP microplate assay achieved a detection performance comparable to other reported UCNP-based analytical studies that sensitively detected sEVs. As discussed earlier, incorporating the use of UCNP-conjugated probes in commercial ELISA kits that have undergone more specific immunoassay optimisations and the continuous advancement of the UCNP-based plate reader technology will allow for better reproducibility and be implemented towards the detection of more low-abundance, disease-specific sEV analytes from diverse sample types. However, while the colorimetric ELISA was performed using a hand-held plate reader, the UCNP microplate assay required a custom-built benchtop plate reader, which is unsuitable for POC settings. With the

continuous development of UCNP microplate technology, there is hope that the system can be miniaturised into a compact hand-held device suitable for POC applications, enabling the sensitive detection of sEV markers. To address this, in Chapters 5 and 6, we investigated using a novel, quantitative UCNP-based LFA assay technology to detect and quantify sEV surface markers sensitively. Nevertheless, the technologies discussed in this chapter represent ongoing scientific innovation towards developing sensitive bio-analytical approaches to establish sEV-based diagnostics.

5. Up-conversion Nanoparticle-Integrated Lateral Flow Assay for Detecting Small Extracellular Vesicles (sEV) PD-L1

Abstract

Small extracellular vesicles (sEVs) derived from cancer cells are enriched cargo of biomolecules, including proteins and nucleic acids, making them important sources of disease-specific biomarkers. Notably, sEV proteins like PD-L1 are clinically significant biomarkers enriched in multiple cancer types and implicated with cancer progression. However, conventional technologies are operationally complex and limited in their sensitivity. Herein, for the first time, we present a novel quantitative lateral flow assay (LFA) for sensitive detection of sEV-PD-L1 using highly doped ($NaYF_4$:40%Yb^{3+}, 4%Er^{3+}) UCNPs. The UCNP-LFA demonstrated highly sensitive and specific detection and quantification of CD63 and PD-L1 antigens, with limits of detection (LOD) of 58 pg/mL (2.546 pM) and 10 pg/mL (0.398 pM), respectively and was successful at detecting sEV-CD63 and sEV-PD-L1 in H1975, MM05 and MSTO-211H cell-derived sEVs. The findings demonstrate a significant advancement towards developing a simple, reliable and sensitive sEV-derived biomarker detection platform for point of care (POC) testing. The UCNP-LFA holds promise as a powerful tool for early diagnosis and disease monitoring of cancer and other diseases.

5.1. Introduction

sEVs originating from cancer cells reflect the molecular information of tumour and its microenvironment, offering valuable diagnostic and prognostic insights as non-invasive biomarkers [526]. Analysing the protein and nucleotide cargoes of sEVs allows the identification of specific cancer signatures, facilitating early-stage detection, disease monitoring and predicting treatment responses [527]. Specific sEV proteins like programmed death ligand 1 (PD-L1) have been found in multiple cancer types, including breast, lung,

glioblastoma and head and neck cancers, which can be harnessed towards the development of cancer diagnostic approaches [55, 527, 528].

The PD-1/PD-L1 signalling pathway plays a critical role in tumour immune invasion [529]. PD-L1, as a key immune checkpoint protein, inhibits the activation and proliferation of T cells, thereby weakening their cytotoxicity against tumor cells [530-532]. Studies have demonstrated the role of sEV-PD-L1 in tumor progression, where PD-L1-positive sEVs contribute to immune evasion by inhibiting cytokines and inducing apoptosis in $CD8^+$ T cells [533]. High PD-L1 expression in pleural mesothelioma (PM) has been consistently correlated with the nonepitheliod histological subtype that has poor disease prognosis [534] and several clinical trials are currently exploring the PD-1/PD-L1 therapeutic approach in combination with chemotherapy [535]. sEV-PD-L1 is positively associated with overall disease stage in multiple cancers and has proven to be more clinically useful than soluble PD-L1 [536, 537]. The role of sEV PD-L1 in tumour progression is significant and targeting it can be an effective therapeutic strategy, particularly in predicting treatment responses of immunotherapy [538, 539]. The sensitive detection and quantification of sEV-PD-L1 levels can be a reliable cancer diagnostic medium in clinical settings [540, 541].

Conventional methods like Western Blotting, ELISA and Flow Cytometry have been implemented to detect sEV proteins, like PD-L1. However, the relatively small size and low abundance of sEVs in early cancer stages prevents the implementation of these methods, which have limited sensitivity, require large sample volumes and do not adequately represent the heterogeneity of sEVs [537, 542, 543]. Imaging techniques have also been applied for sEV analysis, but a majority of these approaches are label-based and heavily reliant on the use of fluorescent dyes which have limited signal intensity and photo stability for long-term characterisation [544]. These complexities and the limited sensitivity of conventional strategies prevent the implementation of sEV diagnostics in clinical settings [545].

Lateral flow assays (LFAs) are a well-established and versatile technology for rapidly detecting target analytes. They are ideal for use as POC diagnostics, presenting several advantages compared to other analytical methods, which include their rapid and cost-effective nature, as they do not require any sophisticated equipment [298]. However, the visual interpretation of colorimetric tests used in most LFAs is not quantitative, and these tests are limited by the low sensitivity of traditional reporters such as colloidal gold nanoparticles [311, 312]. Integrating highly stable and sensitive fluorescent nanoparticles into LFAs can overcome these limitations and contribute to developing high-performance quantitative analytical assays. Lanthanide-doped upconversion nanoparticles (UCNPs) are particularly useful in this regard, as they can combine two or more lower-energy photons into one higher-energy photon, making them ideal for single-molecule biosensing and bioimaging applications [177]. The nonbleaching, nonblinking and anti-Stokes emissions of UCNPs and their tuneable colours make them ideal for use as probes for multiplexed assays [313-317]. UCNP-based LFAs have been implemented in multiple studies to detect disease-specific target biomarkers with enhanced accuracy and sensitivity, with significant POC testing applications [318-321].

In this study, for the first time, we have developed a highly doped ($NaYF_4$:40%Yb^{3+}, 4%Er^{3+}) UCNP-based lateral flow assay (UCNP-LFA) for the sensitive detection and quantification of specific sEV biomarkers. The UCNP-LFA was implemented to detect CD63, an integral structural marker for sEVs, and PD-L1, a cancer-specific marker on sEVs, in human mesothelioma and lung cancer cell lines (MM05, MSTO-211H and H1975) (Fig 34). This innovative technology is a significant step towards the development of a simple, reliable, and sensitive sEV biomarker detection system that could be implemented in clinical settings as a sEV based diagnostic tool.

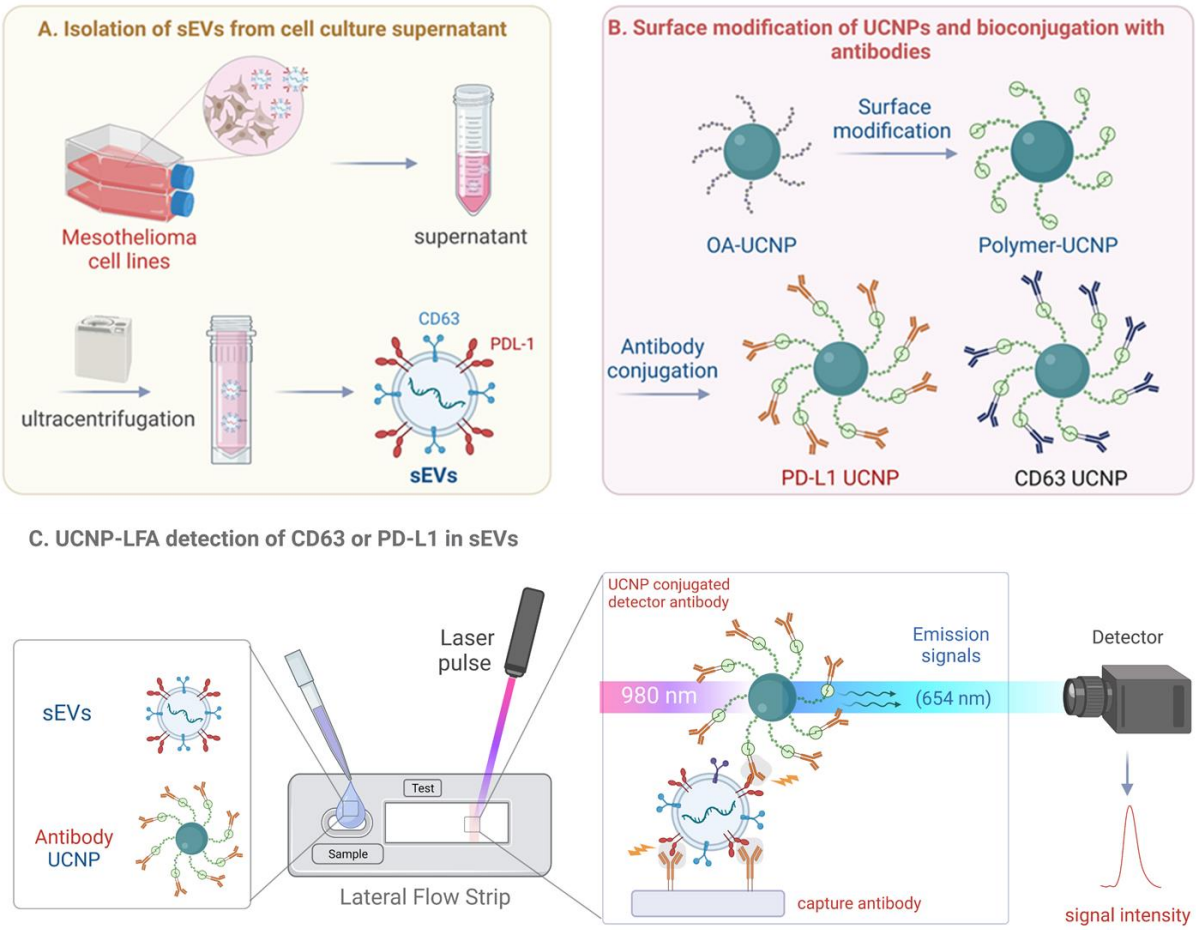

Fig 34: Schematic representation of the UCNP-LFA detection system for detection of sEV surface markers. (**a**) sEVs are isolated from cell culture conditioned medium by ultracentrifugation and consequently analysed by the UCNP lateral flow system. (**b**) High-quality UCNPs were synthesised with oleic acid (OA) as a surface ligand and surface modified with polymers containing anchoring ligands. The surface-modified UCNPs were bio-conjugated with monoclonal CD63 or PD-L1 antibodies to form UCNP probes. (**c**) UCNP conjugated probes were complexed with sEV samples and introduced into the sample pad of the lateral flow strips. CD63 and PD-L1 in the samples were detected in separate strips coated with the corresponding capture antibody. The solution flows through the conjugate pad onto the nitrocellulose membrane, where target analytes are recognised by immobilised antibodies at the test line. The laser-integrated strip reader excites the UCNPs at 980nm, and the resulting emission signals at 654nm are recorded, which is proportional to the concentration of target analytes in the sample.

5.2. Experimental Results

5.2.1. sEV characterisation

The sEVs used in the study were isolated from three different cell lines (H1975, MM05 and MSTO-211H) using ultracentrifugation, which is the gold standard method for sEV isolation [10]. Particle size and concentration were evaluated by NTA and the protein expression was

evaluated by Western Blotting. NTA revealed that the majority of sEVs derived from the three cell lines had a mean size of 50-200 nm. The average sizes of the sEVs from H1975, MM05 and MSTO-211H were measured to be 139.7 nm, 133.3 nm and 141 nm, respectively. The concentration of sEVs from H1975, MM05 and MSTO-211H was found to be 3.7×10^9 particles/mL, 3×10^9 particles/mL, and 2.7×10^9 particles/mL, respectively (Fig 35). TEM image of the isolated sEVs additionally validated the morphology of sEVs as bilayer sphere-shaped vesicles, consistent with previous observations (Fig 36a). The presence of common sEV markers CD63, CD9, and CD81 proteins (tetraspanins) was confirmed in the isolated sEV samples using Western Blotting (Fig 36b). These findings further establish the successful isolation and characterisation of sEVs isolated from the cells.

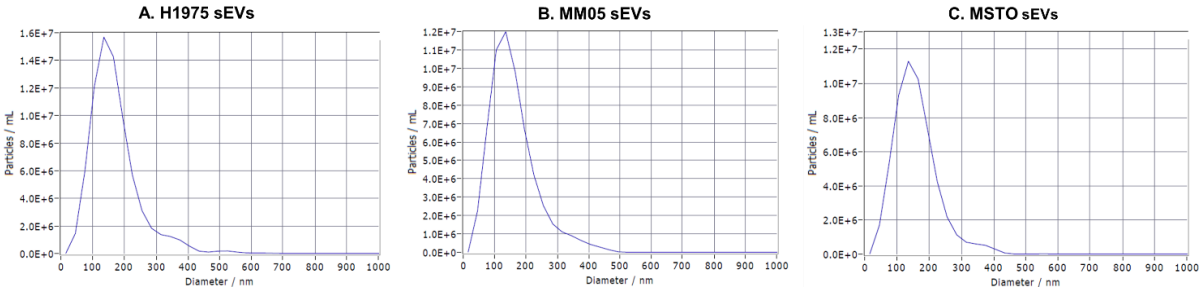

Fig 35: Characterization of cancer-cell derived sEVs. The size distribution of sEVs derived from H1975 (**A**), MM05 (**B**) and MSTO-211H (**C**), the concentration of sEVs were 3.7×10^9 particles/mL, 3×10^9 particles/mL and 2.7×10^9 particles/mL based on NTA analysis.

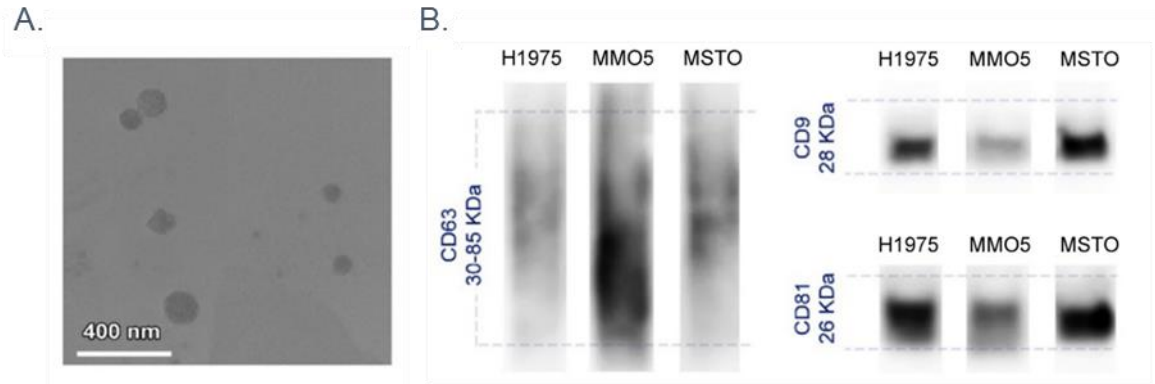

Fig 36: (**A.**) TEM image of the sEVs derived from MM05. (**B.**) Western Blot analysis of the CD63, CD9, and CD81 on the surface of sEVs, sEVs were loaded on SDS-PAGE and immunoblotted for

antibodies against anti-CD63, anti-CD9 and anti-CD81. A gel was run under non-reducing conditions with 2×10^8 particles; ~5µg. The exposure time was 35 seconds.

5.2.2. Detection of CD63 and PD-L1 proteins using UCNP-LFA

To assess the performance of the UCNP-LFA system in detecting surface markers on sEVs, it was important to establish the detection sensitivity of the target analytes. Additionally, the heterogeneity in the size distribution of isolated sEVs and the variability in surface biomarker expression necessitated an accurate estimation of the UCNP-LFA system's detection performance and sensitivity.

Paired capture and detector antibodies for CD63 and PD-L1 were used in the study; detector antibodies were conjugated with surface-modified UCNPs to generate UCNP reporter probes and capture antibodies were immobilised on the test line of nitrocellulose (NC) membranes. CD63 and PD-L1 were detected parallelly on separate LFA strips with the corresponding capture antibody coated on the test lines. In the presence of target epitopes in the samples, the UCNP probes complexed with the targets, which were recognised by the immobilised antibodies in the membrane. In the position of the test line, a laser beam, when triggered, excited the UCNP reporters at 980nm, and the machine recorded the UCNP emission signal peaks at 654nm, which was proportional to the concentration of the target analytes present in the sample, thus enabling the detection and quantification of target epitopes (Fig 40). In the analysis of target analytes with the UCNP-LFA, we adopted the wet method, which entails incubating the sample with UCNP probes prior to analysis on the LFA strips. This preliminary incubation step, conducted on a shaker at 800 rpm for 10 minutes at 30°C before applying the sample onto the strips, facilitates the formation of immunocomplexes between the UCNP probes and the target analytes. This process enhances the comprehensiveness and accuracy of the analysis conducted with the UCNP-LFA.

Fig 37a illustrates the trend in signal intensity ratio across varying CD63 antigen concentrations (0-100 ng/mL). The intensity ratio is calculated by comparing the signal intensity measured at the test line, where UCNP-sEV-antibody complexes bind to the immobilised capture antibodies, to the signal intensity at a reference region of the lateral flow strip. This reference region is located downstream, away from the test line, where UCNP complexes flow but have not encountered or bound to the immobilised antibodies. Using this approach, the ratio provides an accurate and reliable measure of the binding events at the test line while accounting for background signals or variations in UCNP distribution along the strip. This method ensures that the calculated intensity ratio reflects specific binding at the test line, offering a robust analytical measure of assay performance. The analysis exhibited a proportional relationship with CD63 protein concentration between 0.1-100 ng/mL, corresponding to the molar concentration range of 4.39×10^{-3} – 4.39 nM (R^2= 0.97826). The limit of detection (LOD) for CD63 antigen was determined to be 58 pg/mL, which in molar concentration is 2.546 pM. Similarly, the signal intensity for PD-L1 antigen was measured within the concentration range of 0.01-100 ng/mL, corresponding to a molar concentration of 3.98×10^{-4} – 3.98 nM (R^2= 0.9969) (Fig 37b). The signal intensity exhibited a proportional relationship with increasing PD-L1 antigen concentration, and the LOD was determined to be 10 pg/mL, which in molar concentration is 0.398 pM. The LODs were calculated as per the standard formula reported in the literature [497, 498]. The low detection limit of CD63 and PD-L1 in the UCNP-LFA potentiates the implementation of this technology towards ultrasensitive detection of cancer-specific PD-L1 on the surface of sEVs.

The UCNP-LFA data for CD63 detection was fitted with linear regression because the signal intensity increased proportionally with antigen concentration within the tested range (0.1–100 ng/mL). In contrast, the data for PD-L1 detection required exponential regression due to a non-linear, accelerating signal trend observed over the 0.01–100 ng/mL range. A linear model for

PD-L1 would have failed to capture this rapid signal amplification and misrepresented its detection sensitivity. The high-affinity paired antibody used for PD-L1 detection contributed to this behaviour, as it enabled strong binding at low analyte concentrations, enhancing sensitivity while saturating at higher antigen concentrations, leading to the exponential trend [546]. Additionally, epitope accessibility and antigen properties may have influenced the differences: CD63, as a tetraspanin protein, presents uniformly accessible epitopes, supporting a proportional, linear response. In contrast, PD-L1, a membrane-bound ligand, exhibits more complex epitope presentation and potential clustering, contributing to the non-linear signal amplification at higher concentrations [547, 548].

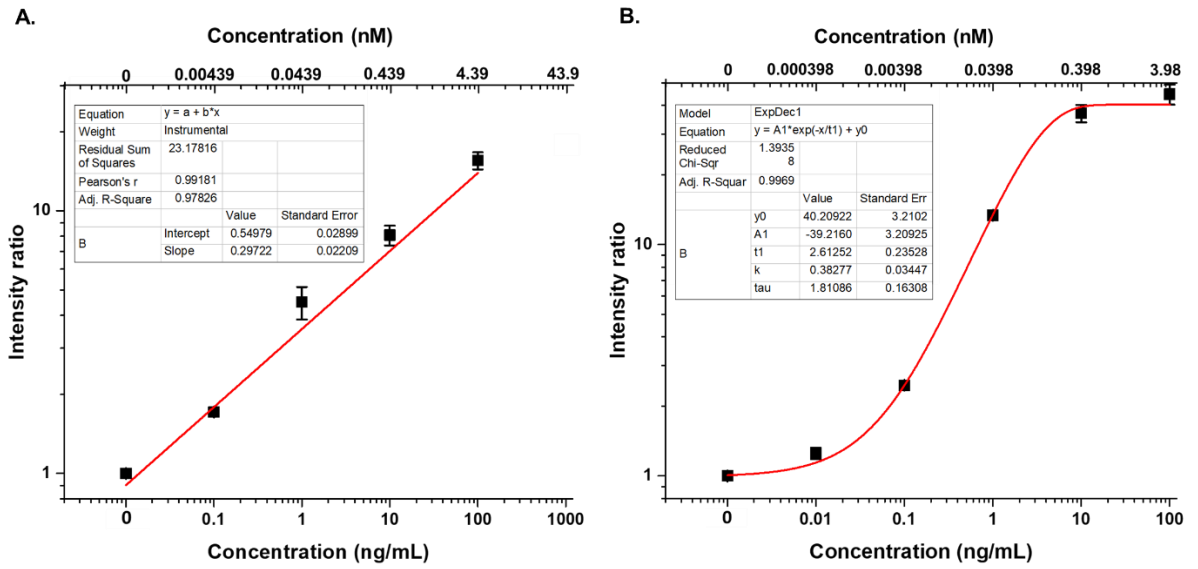

Fig 37: Detection of CD63 and PD-L1 antigens with the UCNP-LFA system. (a.) (b.) Calibration curve of the CD63-UCNPs LFA for detecting CD63 protein at concentrations of 0.01, 0.1, 1, 10, and 100 ng/mL (4.39×10^{-3} – 4.39 nM), R^2= 0.97826. Calibration curve of the PD-L1-UCNPs LFA for the detection of PD-L1 protein at concentrations of 0.01, 0.1, 1, 10, 100 and 100 ng/mL (3.98×10^{-4} – 3.98 nM), R^2= 0.9969. The signal intensities showed a proportional increase with increasing concentration of the proteins. Data plotted as mean ± standard deviation (S.D). (n=3)

Since sEVs possess multiple structural and cancer-specific biomarkers on their surface, it is crucial for an sEV-based detection platform to maintain high specificity in detecting sEV-specific target analytes. It was important to ensure the absence of cross-reactivity that could disrupt the detection of PD-L1 and CD63 on the surface of sEVs. The results showed that the

signal intensities of the control and 40 ng/mL CD63 antigen were indistinguishable when detected in test strips with the PD-L1 antibody in the test line. Furthermore, there was negligible difference in signal intensities between 40 pg/mL PD-L1 antigen and 40 ng/mL CD63 + 40 pg/mL PD-L1 antigens. Similarly, in CD63 lateral flow strips, there was negligible difference between the control and 100 ng/mL PD-L1 antigen, as well as between 1 ng/mL CD63 and 1 ng/mL CD63 + 100 ng/mL PD-L1 antigens (Fig 38a, 38b). These findings demonstrate the high specificity of the UCNP-LFA system in detecting target analytes.

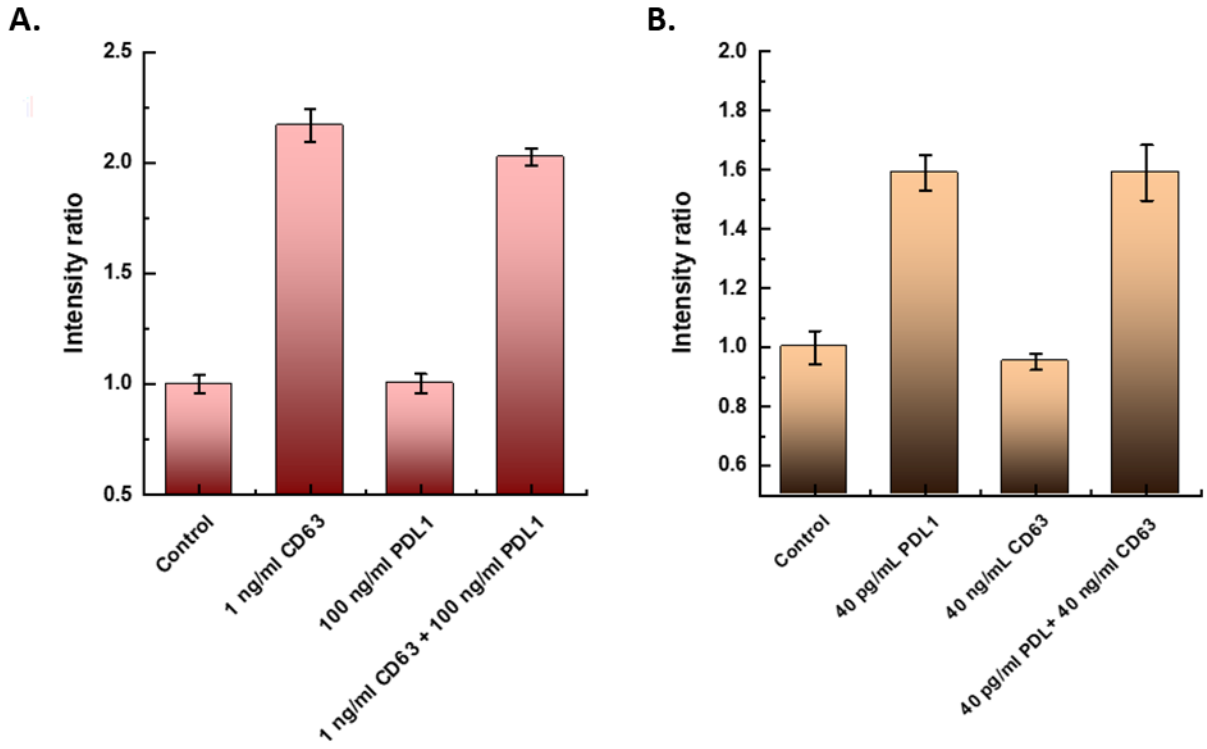

Fig 38: (a.) (b.) Establishing specificity in the detection of target analytes with UCNP-LFA. For the strips with the CD63 antibody pair, there was no positive signal in the presence of high concentrations of PD-L1 (100 ng/mL), and the same concentration of PD-L1 did not interfere with the detection of 1 ng/mL CD63. Similarly, the strips with the PDL1 antibody pair did not yield a positive signal in the presence of high concentrations of CD63 (40 ng/mL), and the same concentration of CD63 did not impact the detection of 40 pg/mL PD-L1. Data plotted as mean ± standard deviation (S.D). (n=3)

To ensure the reliable performance of the UCNP-LFA system, multiple parameters were systematically considered, tested, and optimised. These efforts were informed by both existing literature on sEV-based LFA technologies [308, 310, 549] and the ongoing process refinements

carried out by our group in applying UCNP-LFA technology across multiple studies [370, 371]. Careful selection of the lateral flow strip components, including the sample pad, conjugation pad, nitrocellulose (NC) membrane, and absorbent pad, was critical for ensuring efficient sample flow and signal consistency. The pore size of each component was a key consideration, as it directly influenced flow dynamics, analyte migration, and overall assay sensitivity. The NC membrane, in particular, required precise control of pore size to balance flow rates and ensure optimal antigen-antibody interactions at the test line. Similarly, uniform deposition of reagents on the test and control lines of the NC membrane was critical, as uneven coating could lead to signal variability and inconsistent results. Buffer pH and ionic strength were also optimised to ensure compatibility with the lateral flow components, stabilise UCNP conjugates, and enhance antigen-antibody interactions, further improving assay reproducibility. Sample volume was optimised to ensure sufficient analyte availability for immunocomplex formation while avoiding excessive volumes that could disrupt flow dynamics or result in overflow. Measurement timing was standardised to 10 minutes after sample application, providing enough time for analytes to bind recognition antibodies at the test line and produce reliable and consistent signals. A key optimisation involved comparing the ‘wet method’ and the ‘dry method’ for incorporating UCNP-conjugated antibody probes. In the wet method, UCNP probes were pre-incubated with the sample for 10 minutes before application to the lateral flow strip. This pre-incubation step allowed immunocomplexes to form prior to being introduced to the lateral flow strip, significantly improving sensitivity, particularly for low-abundance analytes, and ensuring reproducibility. Conversely, the dry method, where UCNP probes were immobilised on the conjugate pad and only the sample was applied to the sample pad, produced inconsistent and less reliable results. The wet method was thus adopted as the standard protocol for UCNP-LFA.

Overall, these extensive optimisation efforts highlight the critical considerations that went into developing the UCNP-LFA system and reflect the substantial work undertaken to ensure its reliability and sensitivity. By addressing factors such as material selection, sample volume, incubation protocols, and timing, we established a robust framework for applying UCNP-LFA in sEV detection.

5.2.3. Detection of CD63 and PD-L1 biomarkers on the surface of sEVs

The UCNP-LFA facilitates both the detection and quantitation of target analytes and is performed without any sample enrichment or sample pre-amplification step. Therefore, it represents a more reliable biomarker detection strategy than other colorimetric lateral flow assay systems-based strategies for sEV biomarker detection [215, 305].

Having established the UCNP-LFA's detection sensitivity of CD63 and PD-L1 antigen, the same was implemented to detect sEV-CD63 and sEV-PD-L1 in sEVs isolated from H1975, MM05 and MSTO-211H cells. H1975 is a lung cancer cell line, and MM05 and MSTO-211H are human mesothelioma cell lines, and studies have established the expression of PD-L1 in sEVs isolated from these cells [533, 550]. sEV samples were prepared at concentrations ranging from ~10^2 – 10^7 sEVs/µL and analysed using the UCNP-LFA to establish a broad detection range of sEV markers. In the case of sEV-CD63 detection, the signal intensity ratio at the highest sEV concentrations was found to be between ~ 1.5 – 3.5, corresponding to ~ 0.1 – 1 ng/mL (4.389×10^{-3} – 4.389×10^{-2} nM) across the three distinct cell-derived sEVs. Similarly, for the detection of sEV-PD-L1, the signal intensity ratio at the highest sEV concentrations was found to be between ~ 1.5 – 2.5, corresponding to ~ 0.02 – 0.08 ng/mL (7.968×10^{-4} – 3.187×10^{-3} nM) across the three cell-derived sEVs (Fig 39). However, within the concentration range of ~10^2 – 10^6 sEVs/µL, the signal intensity ratios in the UCNP-LFA

did not exhibit adequate linearity. This lack of linearity hindered the precise determination of the detection limit for sEV-CD63 and sEV-PD-L1 within the sEVs derived from each cell type.

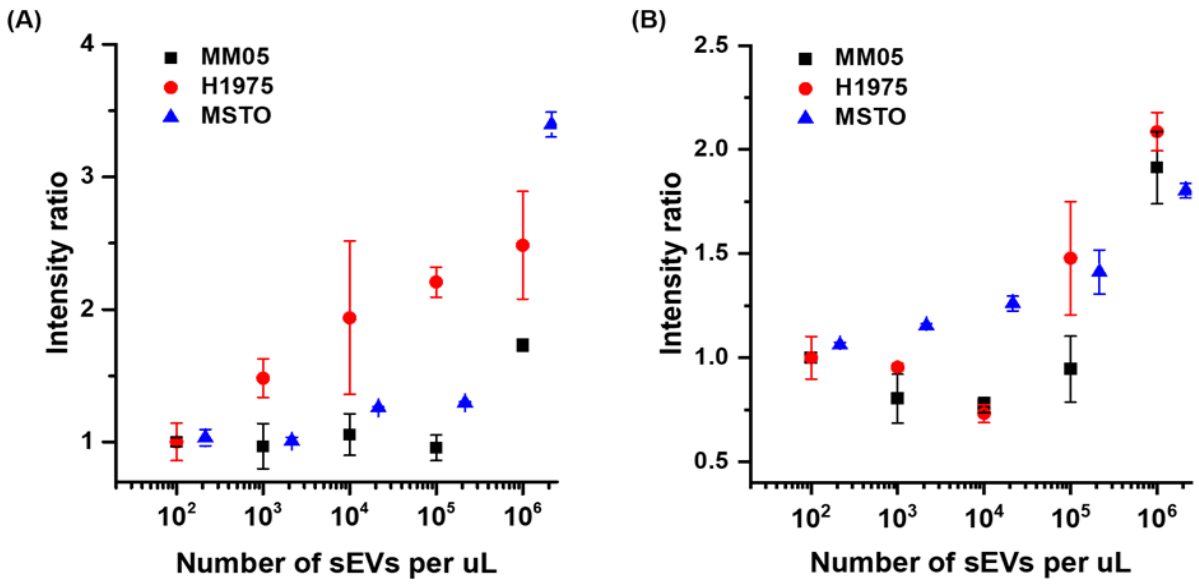

Fig 39: Detection of CD63 (A) and PD-L1 (B) on the surface of sEVs isolated from H1975, MM05 and MSTO-211H cell lines with concentrations ranging from ~10^2 – 10^6 sEVs/µL. For sEV-CD63 detection (A), the intensity ratio at the highest concentrations of the cell-derived sEVs was between ~ 1.5 – 3.5, corresponding to ~ 0.1 – 1 ng/mL. For sEV-PD-L1 detection (B), the intensity ratio at the highest concentrations of the cell-derived sEVs was between ~ 1.5 – 2.5, corresponding to ~ 0.02 – 0.08 ng/mL. Data plotted as mean ± standard deviation (S.D). (n=3)

Challenges in estimating the detection limit of sEV-CD63 and sEV-PD-L1 on H1975, MM05 and MSTO sEVs: At concentrations < 10^5 sEVs/µL, the intensity ratio for CD63 and PD-L1 did not exhibit proportionality across all three cell-derived sEVs. Given the heterogeneity of sEVs in terms of size, morphology, and surface marker composition, serial dilution of sEV samples at lower concentrations allowed Brownian motion to compromise the accurate quantification of sEV surface markers [551, 552]. Brownian motion is when sEVs in suspension undergo constant random motion collisions with solvent molecules and with each other [553]. In LFAs, this poses a challenge to the precise positioning of sEVs as they migrate along the lateral flow strip [554]. Serial dilution of sEV samples cannot adequately account for the dynamic nature of Brownian motion, which is influenced by multiple factors, including

storage conditions, solvent properties, and external forces, affecting sEV dispersion and quantification accuracy [555, 556]. Diluting sEV concentrations increases the spacing between individual sEVs in the sample, reducing the frequency of sEV-sEV collisions but amplifying the relative impact of Brownian motion on each sEV's trajectory in the LFA strips [557]. As a result, sEV samples at low concentrations limits the interactions between the sEV surface markers with the capture antibody at the test line, resulting in inconsistent signal intensities and compromised quantification accuracy [555, 558]. Furthermore, reduced sEV concentrations in diluted samples affect the kinetics of sEV-capture antibody interactions on the lateral flow strip, with lower sEV concentrations slowing down the rate of antibody-sEV binding, thus prolonging the interaction time needed for sEVs to bind with the capture antibody at the test line [559]. Therefore, while serial dilution of sEV samples is a common strategy to expand the dynamic range of detection in LFAs, it presents significant limitations to the accurate quantification of sEVs, particularly at lower concentrations. And despite adequate optimization of the UCNP-LFA process, the inherent randomness of sEV diffusion and interactions within the lateral flow strip can explain the high variability and reduced linearity at concentrations < 10^5 sEVs/µL.

For Chapter 5, the concentration range of ~10^2 – 10^6 sEVs/µL was selected for analysis on the UCNP-LFA to establish a comparison with other UCNP-based sEV studies. However, as evidenced by the UCNP-LFA analysis, the intensity ratio of CD63 and PD-L1 at concentrations <10^5 sEVs/µL were inconsistent, displaying high variability and making their accurate quantification difficult with the UCNP-LFA. Additionally, the inherent diversity in size, morphology, and surface marker composition of sEVs was anticipated to disrupt signal intensity and linearity consistency across a broad concentration range. Hence, the detection sensitivity of the UCNP-LFA was first established using CD63 and PD-L1 proteins, to use as

a reference for quantifying their expression in the sEV samples. Therefore, for Chapter 6, sEVs were not diluted at concentrations below 10^5 sEVs/µL to quantify sEV surface markers.

Validation of sEV-CD63 and sEV-PD-L1 expression using commercial ELISA kits: In addition to the sEVs analysis conducted by UCNP-LFA, the sEVs also underwent parallel analysis using commercial CD63 and PD-L1 ELISA kits (Fig. 40). Notably, both kits successfully detected CD63 and PD-L1 on sEVs from H1975, MM05, and MSTO cell lines at concentrations in the range of ~10^6 sEVs/µL. Although the UCNP-LFA did not yield a linear signal intensity ratio across varying concentrations of the three cell-derived sEVs, hindering the accurate determination of the LOD for sEV-CD63 and sEV-PD-L1, it nonetheless demonstrated the ability to detect these markers at concentrations comparable to those detected by the commercial ELISA kits.

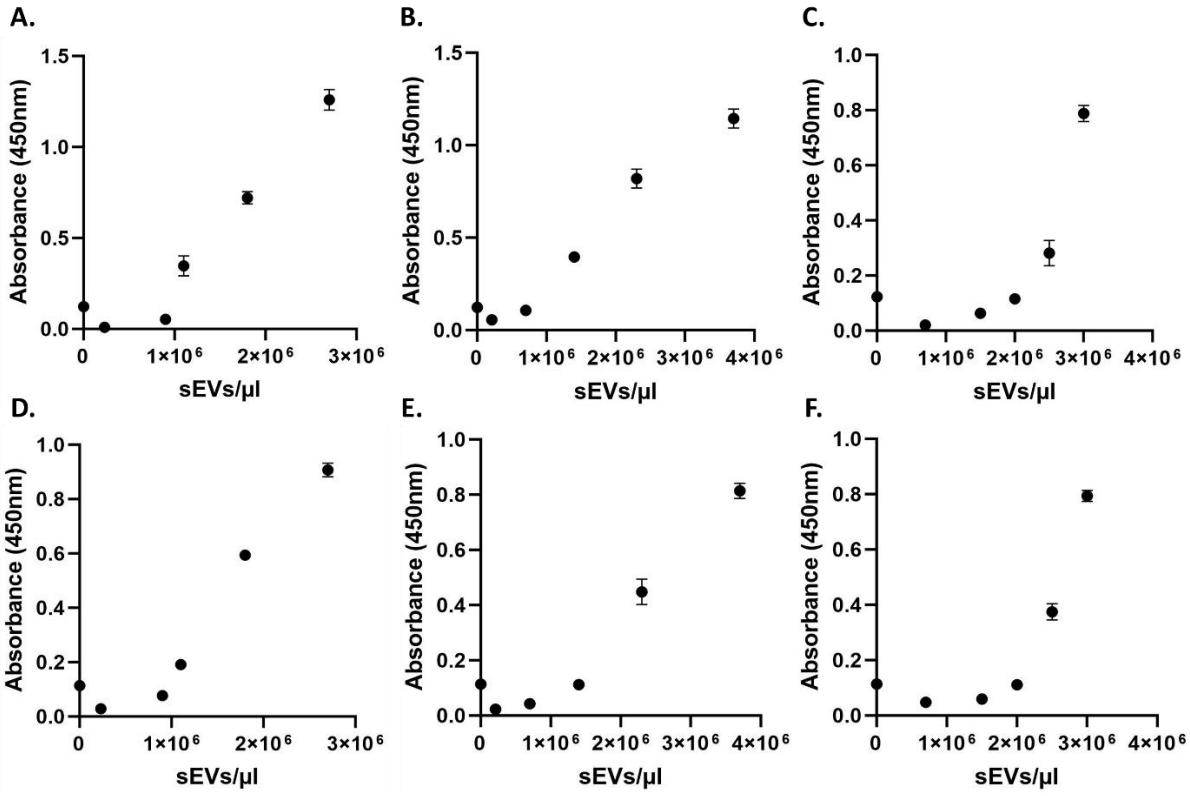

Fig 40: Commercial CD63 ELISA-based detection of CD63 from the surface of sEVs isolated from (A) MSTO-211H, (B) H1975 and (C) MM05 cell lines. The lowest sEV concentrations at which the ELISA could detect sEV-CD63 were 1.2 × 10^6 particles/µL (A), 1.43 × 10^6 particles/µL (B) and 2.13 × 10^6 particles/µL (C), respectively. Commercial PD-L1 ELISA-based detection of PD-L1 from the surface of sEVs isolated from (D) MSTO-211H, (E) H1975 and (F) MM05 cell lines. The lowest sEV

concentrations at which the ELISA could detect sEV surface PD-L1 were 1.25×10^6 particles/μL (D), 1.47×10^6 particles/μL (E) and 2.5×10^6 particles/μL (F), respectively. Data plotted as mean ± standard deviation (S.D). (n=3)

We further validated the performance of the UCNP-LFA by detecting CD63 and PD-L1 in sEVs isolated from healthy plasma. sEVs from biological samples often exhibit a complex mixture of vesicles originating from diverse cell types and physiological conditions. This inherent heterogeneity can result in a high background of non-target sEVs, posing a challenge for sEV analytical systems. Therefore, it is crucial to ensure that any analytical system can differentiate between target and non-target sEVs to establish the system's reliability and accuracy. The sEVs derived from healthy plasma were characterised by NTA, revealing similar size distribution with a majority of the sEVs ranging from 50-200 nm. The concentration of sEVs was found to be ~ 10^9 sEVs/mL (Fig 41). The UCNP-LFA successfully detected CD63, since it is a structural sEV marker, but detected no PD-L1 in the sEVs isolated from samples, indicating their absence in healthy plasma (Fig 42). Additionally, these sEVs were spiked with PD-L1 antigen to assess whether the detection performance was impacted when the target analytes were present in samples with a high background of non-target sEVs. The results showed that the signal intensities of the spiked samples were identical to the calibration curve of PD-L1 antigen without any background sEVs, indicating negligible non-specific binding (Fig 43). These results establish the potential of the UCNP-LFA technology to be further developed into a sensitive sEV-based diagnostic platform for implementation in clinical settings.

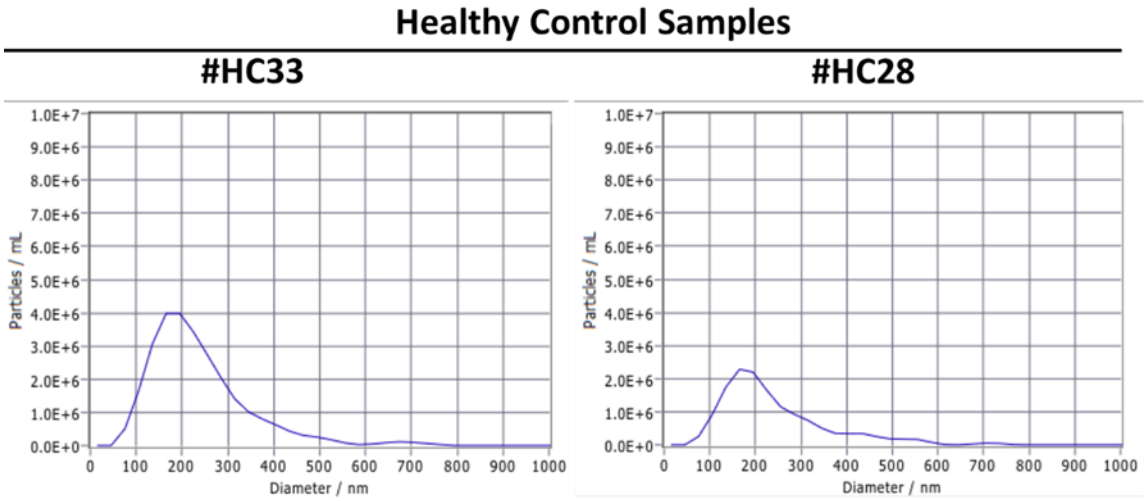

Fig 41: A. The size distribution of healthy patient-derived sEVs. Samples #HC33 and #HC28 showed sharp peaks at 188.2 ± 5.7 nm and 177 ± 3.7 nm (Mean ± standard error), respectively. The concentration of sEVs was 1.4×10^9 particles/mL and 2.7×10^9 particles/mL, respectively.

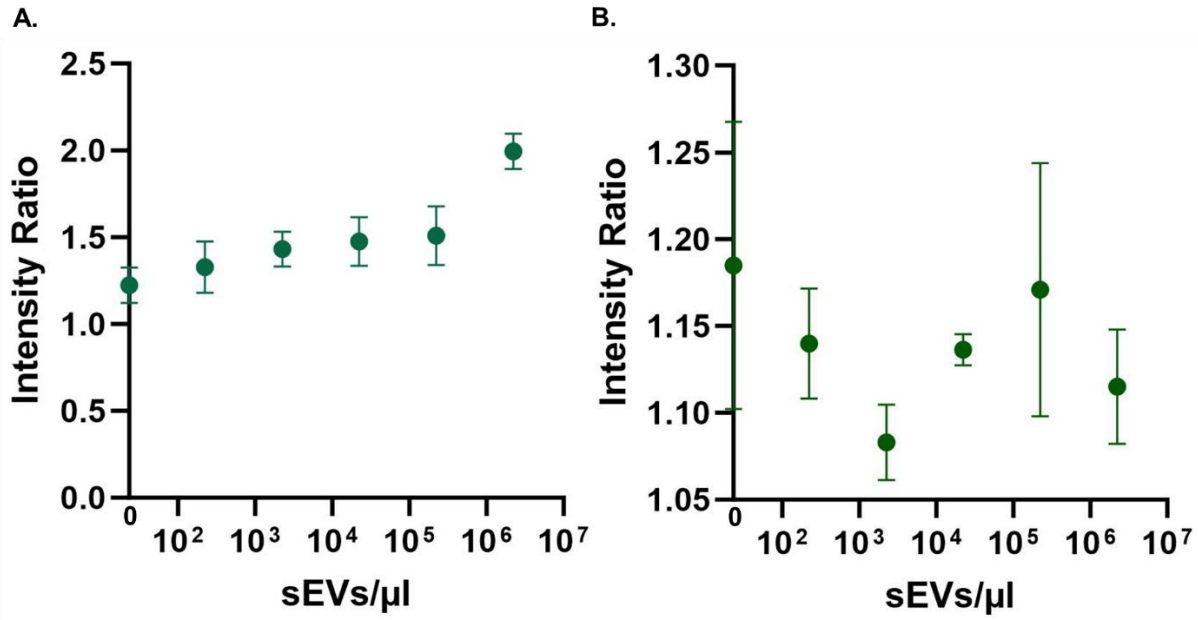

Fig 42: Detection of CD63 (a) and PD-L1 (b) from the surface of sEVs isolated from healthy plasma samples. CD63, a structural marker of sEVs was detected in healthy control sEVs while there was negligible expression of PD-L1. Data plotted as mean ± standard deviation (S.D). (n=3)

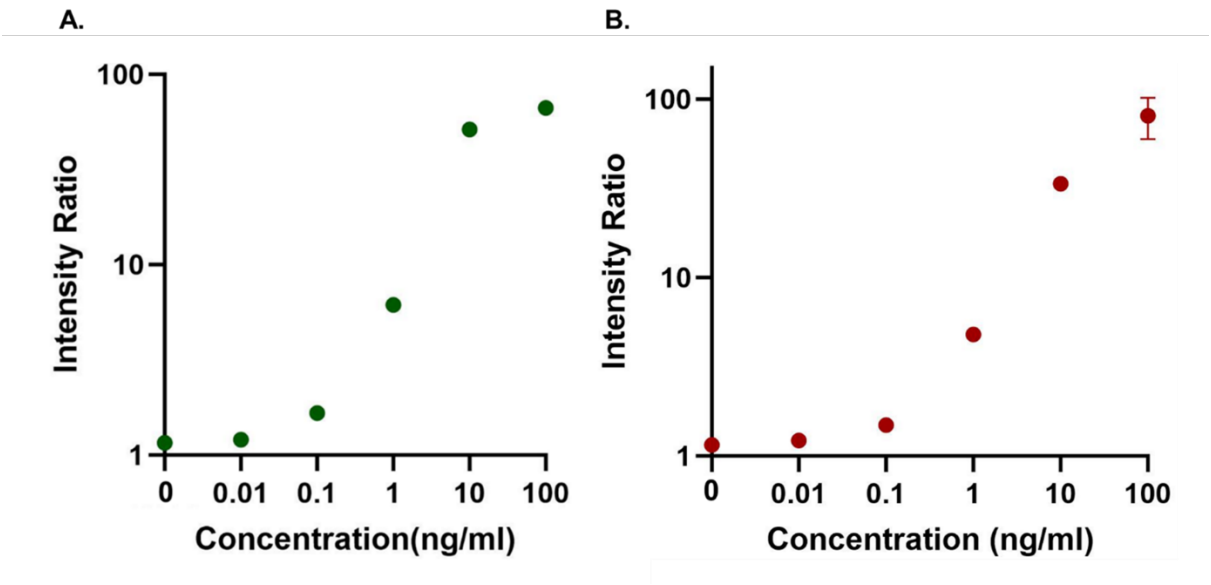

Fig 43: Detection of PD-L1 antigen spiked in healthy control sEVs (a) and PD-L1 antigen (b) within the UCNP-LFA. The signal intensity trend is identical to the intensity trend of the PD-L1 antigen in the buffer, establishing that the detection performance is not impacted when the target analytes are present in a complex background of heterogeneous sEV populations. Data plotted as mean ± standard deviation (S.D). (n=3)

5.3. Discussion and Conclusion

The role of sEV PD-L1 in tumour progression, particularly in immune response, has been well-established [560, 561]. Studies have consistently reported that elevated levels of sEV-PD-L1 contribute to T cell dysfunction in cancer cells [562, 563]. However, the limited sensitivity and operational complexity of conventional analytical methods, such as ELISA and Western Blot hinder the application of sEV biomarker detection strategies in clinical and diagnostic settings. Additionally, there is a significant research gap in the development of reliable and sensitive sEV detection systems that have POC applications. Some studies have utilized gold nanoparticles (AuNPs) and magnetic nanoparticles (MNPs) to develop colorimetric lateral flow assays (LFAs) for the detection of sEV markers [307, 564, 565]. Rodriguez et al. was the first to develop an AuNP-based LFA for detection of tetraspanins as targets from purified sEVs from cell culture supernatants of Ma-Mel-86c melanoma cells. They employed anti-CD63 as

detection antibody and a combination of anti-CD9 and anti-CD81 as capture antibodies to detect sEVs at an LOD of 8.54×10^8 sEVs/mL [215].

In this study, we introduced the first UCNP-based lateral flow testing system for sensitive detection and quantification of sEV-PD-L1. The approach harnessed the unique properties of UCNPs, including nonbleaching, high brightness, and uniformity in size, to develop a sensitive and quantitative LFA technology [359, 566]. Previous research from our group achieved single sEV quantification using UCNPs in a total internal reflection fluorescence (TIRF) imaging technique [567]. Although studies have demonstrated the efficacy of UCNP-LFAs for sensitive detection of target analytes in biofluids such as blood [319, 402, 568, 569], their implementation towards the detection of surface markers on sEVs has not been explored extensively. The UCNP-LFA represents a more operationally simpler strategy for sEV marker detection and quantification and holds promise for early-stage cancer detection, particularly when disease-specific sEVs are scarce. Furthermore, it enables the detection of multiple surface markers on sEVs in resource-limited settings. The UCNP-LFA detected two biomarkers, CD63 and PD-L1, on sEVs derived from human mesothelioma and lung cancer cells, without any sample enrichment or sample pre-amplification step. While we could not establish a reliable detection limit of the UCNP-LFA for sEV-CD63 and sEV-PD-L1, the study demonstrated a comparable detection performance of the system to commercial ELISA kits. Additionally, the analyses of healthy sEV samples established that the UCNP-LFA can detect target markers in samples with a high background of non-target markers.

The continuous advancement of UCNP-LFA strip reader technology will enable the simultaneous detection of multiple sEV markers on a single strip, facilitating multiplexed detection of different sEV subpopulations and investigating their heterogeneity. Moreover, the range of detectable targets can be expanded to include other mesothelioma and lung cancer-specific functional biomarkers like mesothelin, Her-2, EGFR and CD151, allowing for the

testing of a panel of sEV markers [570, 571]. Future studies should analyse a comprehensive panel of sEVs isolated from clinical samples to establish the diagnostic applicability of this technology. The study aligns with the growing research trend of sEV diagnostic platforms that can reliably detect cancer-specific markers and aid in disease detection, treatment selection, and treatment monitoring.

6. Detecting Small Extracellular Vesicles (sEV) GPC-1 using a quantitative, up-conversion nanoparticle-based quantitative lateral flow assay (UCNP-LFA) technology

Abstract

Glypican-1 (GPC-1) is a cell surface proteoglycan that is found to be elevated in multiple cancer types and its high expression is associated with tumour growth, angiogenesis and metastasis. Studies have established the clinical significance of sEV-GPC-1 in pancreatic, prostate and colorectal cancer, potentiating their use as a disease-specific biomarker. In this study, we employed the UCNP-based lateral flow assay technology to sensitively detect sEV-GPC-1 and sEV-PD-L1. The technology demonstrated high sensitivity and specificity towards the detection and quantification of GPC-1 in sEVs isolated from LnCap, DU145 and HCT-116 cell lines. It achieved a detection limit of 0.0363 ng/mL (0.9612 pM) and could accurately quantify sEV-GPC-1 at a ~10-fold enhanced sensitivity, compared to a commercial GPC-1 ELISA kit. This is the first study that explored a quantitative LFA technology to detect and quantify sEV-GPC-1, potentiating the application of this technology towards the development of sEV-based clinical diagnostics.

6.1. Introduction

Prostate cancer and colorectal cancer are prevalent types of cancer in men, ranking among the leading causes of cancer-related deaths in the United States [572, 573]. The prognosis of both these cancers are very poor with current diagnostic methods having been found to be inconclusive and resulting in false negatives [574-577]. Glypicans are a subgroup within the heparan sulfate proteoglycans (HSPGs) family, which represent a diverse set of macromolecules abundantly present on cell surfaces, extracellular matrices and connective tissues [578]. These versatile HSPGs play essential roles in multiple cellular functions,

encompassing cell recognition, cell growth, proliferation and morphogenesis and their involvement in these processes contribute to maintaining cellular balance. The dysregulation of HSPG expression has been observed across multiple human malignancies [579, 580].

Glypican-1 (GPC-1) is one such cell surface proteoglycan that is elevated in some types of cancers, such as breast cancer, pancreatic cancer and gliomas [579, 581]. Its high expression has also been associated with poor disease outcomes in prostate cancer and colorectal cancer, and studies have shown that GPC-1 facilitates tumour growth and angiogenesis [92, 582, 583]. Melo et al. reported that GPC-1-positive sEVs were highly expressed in early and late-stage pancreatic cancer serum samples compared to healthy controls and benign pancreatic disease samples, establishing the potential for sEV-GPC-1 as a marker for early-stage pancreatic cancer [11]. Studies have also demonstrated that sEV-GPC-1 is enriched both in plasma and tissues of colorectal cancer patients [584] and can be utilised in clinical management as a marker for relapse in patients with Stage 3 colorectal cancer [585]. GPC-1 is also considered a potential biomarker for prostate cancer, with GPC-1 preferred as a more reliable marker over PSA, which is associated with false negatives and inconclusive test results [586]. The identification of sEV-GPC-1 isolated from blood and urine potentiates targeted personalised therapy based on based on specific genetic and proteomic mutations [92]. Studies have explored both conventional methods like Flow Cytometry and ELISA [587, 588] and novel nano-sensor technologies to detect sEV-GPC-1 [589, 590]. In this context, the UCNP-LFA platform would allow for rapid and sensitive detection of these important cancer specific markers. The combination of high-binding antibodies coupled with high-quality UCNP reporters can facilitate detection and quantitation of sEV-GPC-1 with improved accuracy and allow for future POC testing applications.

The study employs the use of the UCNP-LFA system to detect sEV-GPC-1 and sEV-PD-L1 in sEVs isolated from LnCap, DU145 and HCT116 cell lines (Fig 44). LnCap and DU145 are

prostate cancer lines with varying metastatic potentials and HCT116 is a highly metastatic colon cancer cell line [591, 592]. To the best of our knowledge, this is the first study of its kind and represents a push towards the development of sEV-based diagnostic systems that facilitate non-invasive and dynamic analyses of early-stage cancer biomarkers, particularly in clinical settings.

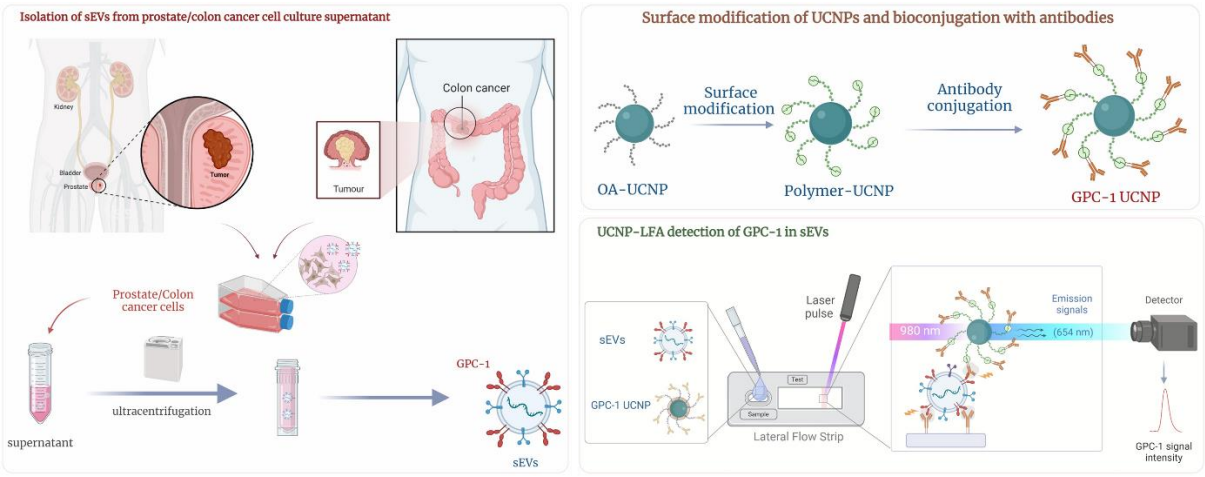

Fig 44: UCNP-LFA-based detection of sEV GPC-1. (a) sEVs were isolated from the cell culture conditioned medium of LnCap, DU145 and HCT116 cells by ultracentrifugation and analysed by the UCNP-LFA. (b). High-quality UCNPs were synthesised and surface-modified with polymers containing anchoring ligands and subsequently bio-conjugated with GPC-1 antibodies to form UCNP probes. (c). UCNP conjugated probes were complexed with sEVs and introduced into the sample pad of the lateral flow strips. The solution flows through the conjugate pad onto the nitrocellulose membrane, where GPC-1 in the samples were detected in strips with the corresponding capture antibody coated at the test line. The laser-integrated strip reader excites the UCNPs at 980nm, and the resulting emission signals at 654nm are recorded, which is proportional to the concentration of GPC-1 in the sample.

6.2. Experimental Results

6.2.1. Characterisation of isolated sEVs

The conditioned cell culture supernatant from the LnCap, DU145 and HCT116 cells were subjected to ultracentrifugation to isolate sEVs. The sEVs were characterised using NTA to determine their particle size and concentration and their functional protein expression was assessed using Western Blotting. The NTA findings indicated that the majority of sEVs

exhibited a mean size range of 50-200 nm. The mean sizes of sEVs from LnCap, DU145 and HCT116 were measured at 107.9 nm, 154.5 and 111.1 nm, and their concentrations were determined to be 8.4×10^8 particles/mL, 3.6×10^9 particles/mL and 5.1×10^9 particles/mL, respectively (Fig. 45). The morphology of the isolated sEVs was validated by TEM, which was consistent with prior observations. Western Blotting confirmed the presence of common sEV markers CD63, CD9, and CD81 proteins (tetraspanins) in the isolated sEV samples (Fig 46), reinforcing the successful isolation and identification of the utilized sEVs in the study.

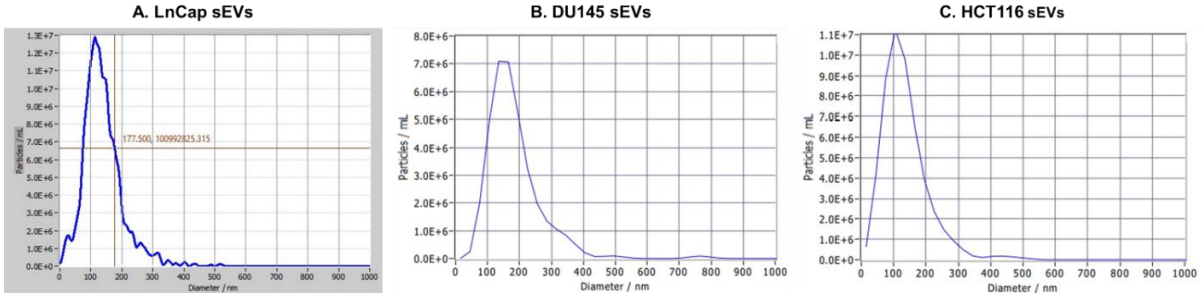

Fig 45: Characterisation of (a.) LnCaP, (b.) DU145 and (c.) HCT116 cell-derived sEVs. The NTA analysis determined the concentration of the three sEVs to be 8.4×10^8 particles/mL, 3.6×10^9 particles/mL and 5.1×10^9 particles/mL, respectively. The average sizes of the sEVs from LnCap, DU145 and HCT116 were measured to be 107.9 nm, 154.5 and 111.1 nm, respectively

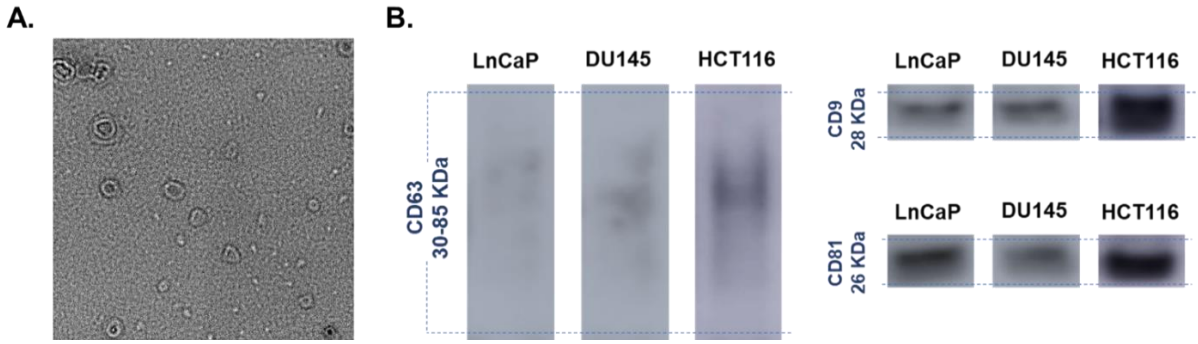

Fig 46: (A) TEM image of the sEVs derived from DU145. (B) Western Blot analysis of the CD63, CD9, and CD81 on the surface of sEVs, sEVs were loaded on SDS-PAGE and immunoblotted for antibodies against anti-CD63, anti-CD9 and anti-CD81. A gel was run under non-reducing conditions with an exposure time of 35 seconds.

6.2.2. Detection of GPC-1, PD-L1 and PSA in sEVs using commercial ELISA kits

In Chapter 5, our investigation established that the detection sensitivity of the UCNP-LFA was comparable to that of commercial ELISA kits. Selecting a broad concentration range of sEVs (~10^2 – 10^6 sEVs/μL) generated inconsistent signal intensity readings, lacking linearity and hindering the accurate estimation of the LOD for the sEVs analysed. To address this, for Chapter 6, we first verified the expression of GPC-1, PD-L1 and PSA in sEVs isolated from LnCap, DU145 and HCT-116 cell lines. The GPC-1 commercial ELISA kit successfully identified sEV-GPC-1 in the three cell-derived sEVs at concentrations between 10^5 – 10^6 sEVs/μL, with the GPC-1 expression being higher in DU145 and HCT-116 sEVs compared to LnCap sEVs. These findings were consistent with previous findings on GPC-1 expression of sEVs from these cell sources [593, 594] (Fig 47). Similarly, the PD-L1 commercial ELISA kit detected sEV-PD-L1 in DU145 and HCT-116 sEVs at concentrations in the range of ~10^6 sEVs/μL, but the absorbance values for LnCap sEVs were too low to quantify accurately, consistent with current literature [595, 596] (Fig 48). Initially intending to detect sEV-PSA using the UCNP-LFA on the cell-derived sEVs, we employed the PSA ELISA kit to identify the expression of sEV-PSA first. The commercial ELISA kit was successful at detecting sEV-PSA in LnCap sEVs, but the absorbance values for DU145 and HCT-116 sEVs were too low to be accurately quantified, consistent with previous findings [597] (Fig 49). Based on these findings, we decided to perform the UCNP-LFA analysis at concentrations ranging between ~10^4 -10^6 sEVs/μL.

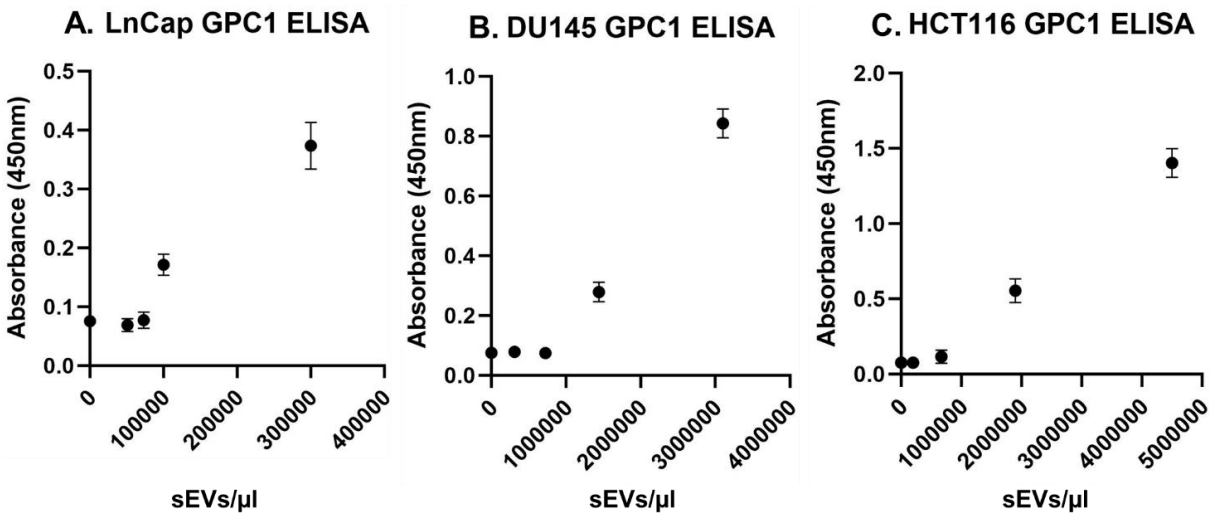

Fig 47: Commercial GPC-1 ELISA-based detection of GPC-1 from the surface of sEVs isolated from (A) LnCap (B) DU145 and (C) HCT116 cells. The lowest sEV concentrations at which the ELISA could accurately detect sEV GPC-1 were 1.1×10^5 sEVs/µL, 1.44×10^6 sEVs/µL and 1.9×10^6 sEVs/µL. Data plotted as mean ± standard deviation (S.D). (n=3)

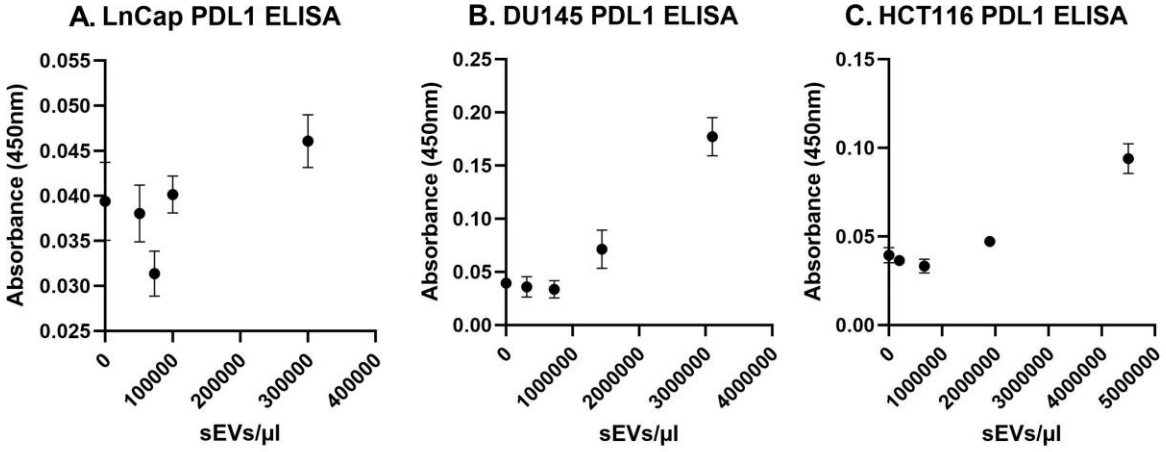

Fig 48: Commercial PD-L1 ELISA-based detection of PD-L1 from the surface of sEVs isolated from (A) LnCap (B) DU145 and (C) HCT116 cells. For LnCap sEVs, the ELISA was not successful at accurately detecting PD-L1. For DU145 sEVs and HCT116 sEVs, the lowest concentration at which PD-L1 was detected were 3.1×10^6 sEVs/µL and 4.5×10^6 sEVs/µL, respectively. Data plotted as mean ± standard deviation (S.D). (n=3)

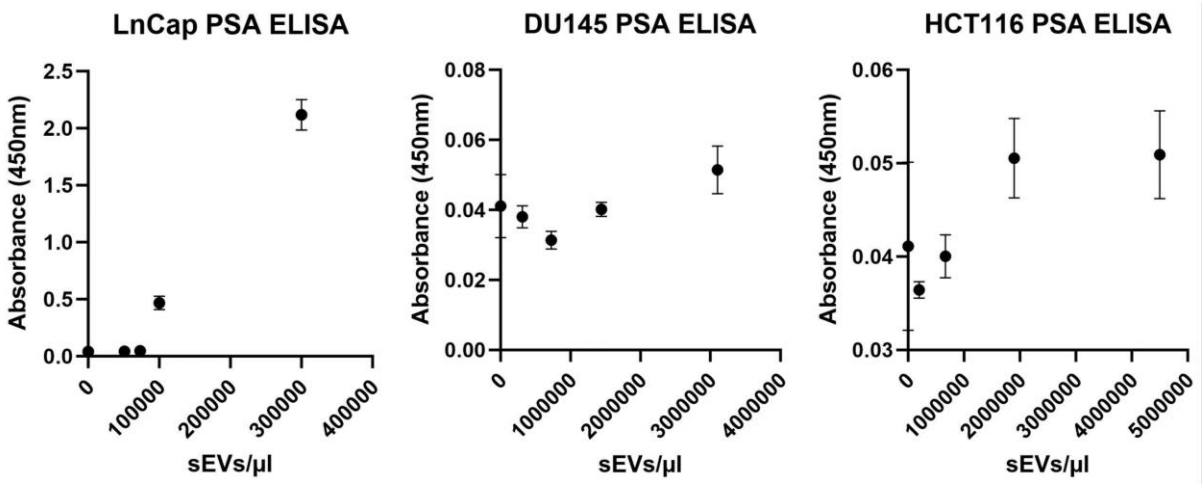

Fig 49: Commercial PSA ELISA-based detection of PD-L1 from the surface of sEVs isolated from LnCap, DU145 and HCT116 cells. The concentration of PSA in DU145 and HCT116 sEVs were too low to be accurately detected and quantitated by the ELISA kit. Among the samples tested, only the LnCap sEVs exhibited elevated levels of PSA expression. Data plotted as mean ± standard deviation (S.D). (n=3)

6.2.3. UCNP-LFA-based detection of GPC-1 and PD-L1 antigens

Before detecting and quantitating GPC-1 in sEV samples, it was imperative to establish the detection sensitivity of the GPC-1 antigen using the UCNP-LFA system. The operational process was the same as previously discussed, where the GPC-1 capture antibody was immobilised on the test line of lateral flow strips while the detector antibody was conjugated to polymer-modified UCNPs. The 'wet method' was implemented for GPC-1 detection, where UCNP-Antibody probes were incubated with the samples before being introduced into strips. In the presence of GPC-1 in samples, the UCNP probes formed a complex with the target analyte and were recognized by the immobilized antibody in the test line. At the test line, a triggered laser beam excited the UCNP reporters at 980 nm and recorded the resultant emission signal peaks at 654nm, which was proportionate to the concentration of the target analyte in the sample, facilitating the detection and quantification of GPC-1 in the samples.

As illustrated in Fig 50a, the intensity ratio was proportional to the concentration of GPC-1 antigen in the range of 0.01 ng/mL - 100 ng/mL, which corresponds to the molar concentration

of 2.67×10^{-4} – 2.67 nM (Fig 50a.). Similar to Chapter 5, the intensity ratio is determined by comparing the signal intensity at the test line, where UCNP-sEV-antibody complexes interact with immobilised capture antibodies, to the signal intensity at a reference region of the lateral flow strip downstream of the test line. This ratio offers a precise and dependable assessment of binding events at the test line while compensating for background signals or variations in the distribution of UCNPs along the strip. The LOD for detection of GPC-1 antigen in the UCNP-LFA was found to be 0.0363 ng/mL, which in molar concentration is 0.9612 pM. This enhanced sensitivity was implemented to accurately detect and quantitate GPC-1 on the surface of sEVs used in this study. Additionally, we also used the UCNP-LFA to establish a calibration curve of PD-L1 antigen at the concentration range of 0.01 ng/mL – 100 ng/mL (4.39×10^{-3} – 4.39 nM) to be used as a reference to quantify sEV-PD1 in the sEV samples and to establish specificity in the detection of target analytes from sEVs (Fig 50b).

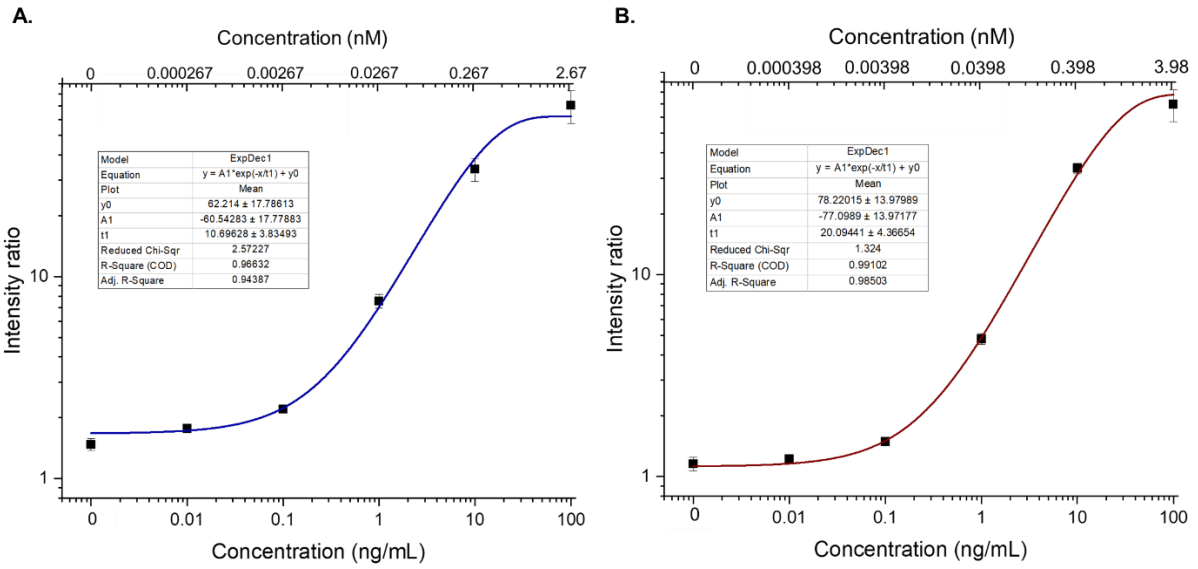

Fig 50: Detection of GPC-1 and PD-L1 antigens with the UCNP-LFA system. (a.) Calibration curve of the GPC-1-UCNPs LFA for the detection of GPC-1 protein at concentrations of 0.01, 0.1, 1, 10, and 100 ng/mL (2.67×10^{-4} – 2.67 nM), R^2= 0.96632. (b.) Calibration curve of the PD-L1-UCNPs LFA for the detection of PD-L1 protein at concentrations of 0.01, 0.1, 1, 10, 100 and 100 ng/mL (4.39×10^{-3} – 4.39 nM), R^2= 0.99102. The signal intensities showed a proportional increase with increasing concentration of the proteins. (n=3)

The precision in the detection of GPC-1 on sEV surfaces necessitated an investigation of potential cross-reactivity between the target analytes, which could compromise the specificity in the detection of GPC-1. The findings showed that on GPC-1 antibody-coated strips, the signal intensities of the control and 100 pg/mL PD-L1 were indistinguishable, and there were negligible variations in the signal readings between samples containing 1 ng/mL GPC1 antigen and 100 pg/mL PD-L1 + 1 ng/mL GPC-1 antigens (Fig 51a.). Likewise, on PD-L1 strips, marginal distinctions were evident between control and 1 ng/mL GPC-1 antigen as well as between 100 pg/mL PD-L1 and 1 ng/mL GPC-1 + 100 pg/mL PD-L1 antigens (Fig 51b.). These results distinctly showcase the UCNP-LFA system's high specificity in detecting the target analytes without cross-reactivity.

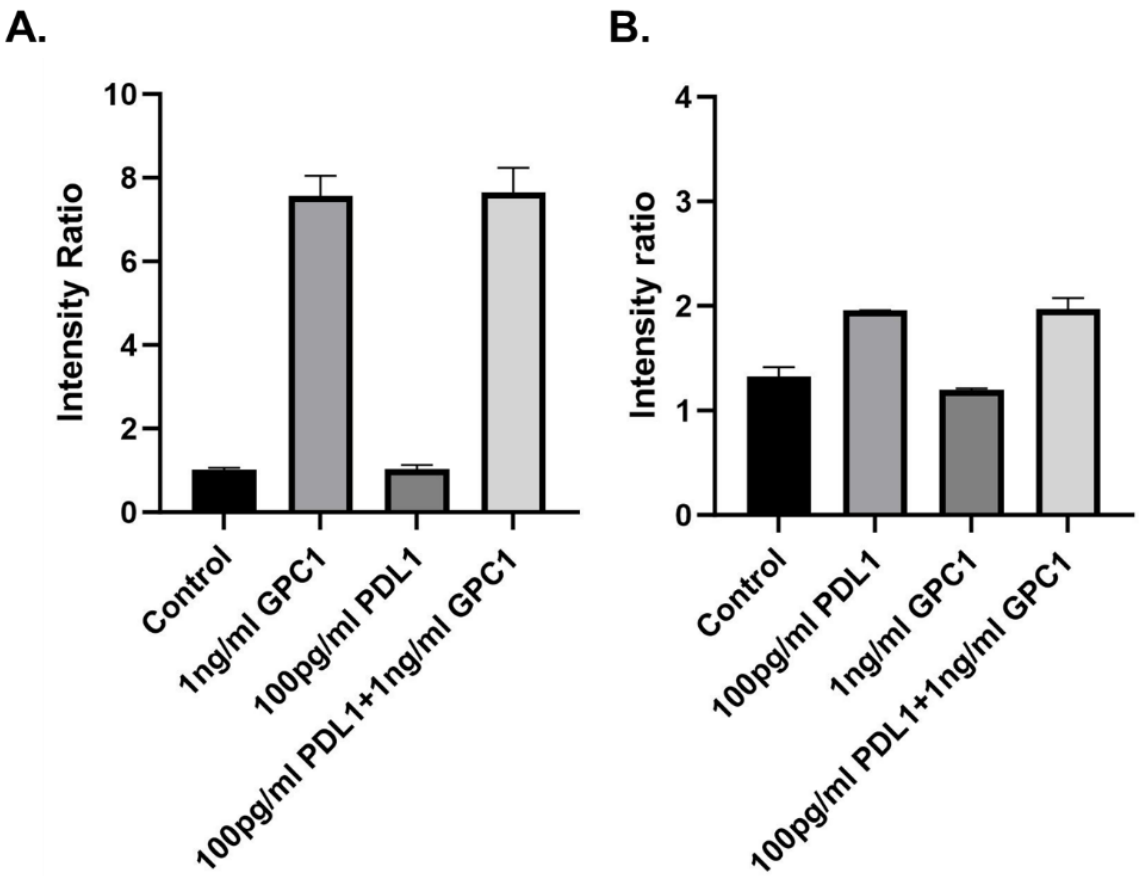

Fig 51: Establishing specificity in detection of target analytes with UCNP-LFA. The strips with the GPC-1 antibody pair did not yield a positive signal in the presence of high concentrations of PD-L1 (100 pg/mL) and the same concentration of PD-L1 did not impact the detection of 1 ng/mL GPC-1. Similarly, for the strips with the PD-L1 antibody pair, there was no positive signal in the presence of

high concentrations of GPC-1 (1 ng/mL) and the same concentration of GPC-1 did not interfere with the detection of 1 ng/mL GPC-1. Data plotted as mean ± standard deviation (S.D). (n=3)

6.2.4. Detection of sEV-GPC-1 and sEV-PD-L1 using the UCNP-LFA

Having established the UCNP-LFA's enhanced detection sensitivity, it was implemented to detect sEV-GPC-1 on the LnCap, DU145 and HCT116 cell lines. LnCap and DU145 are prostate cancer cell lines, and HCT116 is a colon cancer cell line, and the presence of GPC-1 on sEVs isolated from these cells can be a potential cancer biomarker that can be exploited for informing therapeutic options [81, 92]. sEV samples from these cells were prepared at concentrations ranging from ~10^4 – 10^6 sEVs/µL. The signal intensity ratios were found to be proportional to the concentration of sEVs in the samples. The lowest concentrations at which GPC-1 was detected on sEVs from LnCaP, DU145 and HCT116 cells were 2.08×10^4 sEVs/µL, 1.265×10^5 sEVs/µL and 1.544×10^5 sEVs/µL respectively (Fig 52), displaying a ~ 10-fold improvement in detection sensitivity of sEV-GPC-1 compared to the commercial ELISA kit. The expression of sEV-GPC-1 was found to be higher in DU145 and HCT-116 sEVs compared to LnCap sEVs, consistent with the commercial ELISA readings and consistent with previous literature [593, 594].

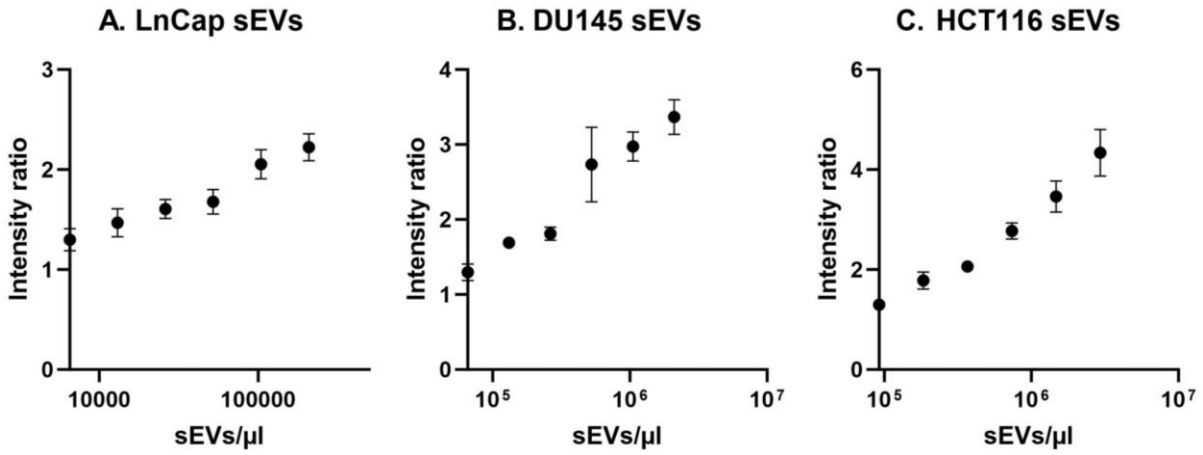

Fig 52: UCNP-LFA detection of GPC-1 on the surface of sEVs isolated from LnCaP, DU145 and HCT116 cell lines with concentrations ranging from ~10^4 – 10^6 sEVs/µL. The lowest concentrations at which GPC-1 was detected on sEVs from LnCaP, DU145 and HCT116 cells were 2.08×10^4 sEVs/µL, 1.265×10^5 sEVs/µL and 1.544×10^5 sEVs/µL respectively. Data plotted as mean ± standard deviation (S.D). (n=3)

The UCNP-LFA was also used to detect sEV-PD-L1 on the surface of LnCap, DU145 and HCT116 sEVs. The clinical utility of sEV-PD-L1 has been established with it being associated with multiple types of cancers [540, 598]. sEV samples with concentrations ranging from ~10^4 – 10^6 sEVs/µL were analysed with the UCNP-LFA. For LnCap sEVs, the UCNP-LFA could not accurately quantify the expression of PD-L1, which was consistent with the commercial ELISA findings. For HCT116 sEVs, while PD-L1 was detected at the highest concentration tested (2.94×10^6 sEVs/µL), the intensity values at this point overlapped within the error range of the adjacent concentrations, indicating that accurate quantification of sEV-PD-L1 was not achievable. Moreover, at lower concentrations, the signals lacked the linearity required for reliable quantification of the expression of sEV-PD-L1. In contrast, DU145 sEVs demonstrated better linearity, and the lowest concentration at which the UCNP-LFA could detect PD-L1 sEVs was 3.61×10^5 sEVs/µL (Fig 53). The findings were generally consistent with the commercial ELISA results and previously reported findings [595, 599].

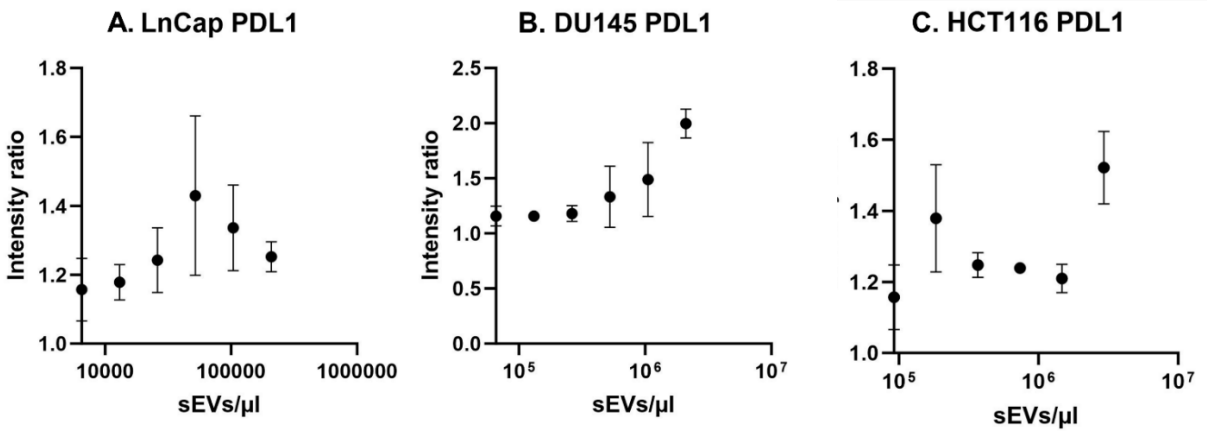

Fig 53: UCNP-LFA detection of PD-L1 on the surface of sEVs isolated from (a.) LnCaP, (b.) DU145 and (c.) HCT116 cell lines with concentrations ranging from ~10^4 – 10^6 sEVs/µL. For LnCaP sEVs, the UCNP-LFA failed to detect PD-L1 reliably, as the intensity ratio did not show a consistent increase with higher sEV concentrations, aligning with the findings of the commercial ELISA. For HCT116 sEVs, PD-L1 was detected at the highest concentration tested (2.94×10^6 sEVs/µL), but the signal at this concentration fell within the error range of adjacent data points, making accurate quantification unreliable. At lower concentrations, the lack of signal linearity further hindered reliable quantification. DU145 sEVs exhibited better linearity, with PD-L1 detection achieved at a minimum concentration of 3.61×10^5 sEVs/µL. Data plotted as mean ± standard deviation (S.D). (n=3)

Since we used LnCap and DU145 sEVs, which are both prostate cancer-specific cell lines, we also attempted to analyse the expression of PSA in the cell-derived sEVs. Detecting the level of PSA in body fluids is one of the most common prostate cancer diagnostic tests. However, they are often found to be inconclusive and can result in false negatives [574, 575]. Studies have shown that the detection of sEV associated with PSA in combination with other sEV-specific markers has more clinical relevance than the levels of circulating PSA in serum [600]. The commercial PSA ELISA kit was successful at detecting sEV-PSA in LnCap sEVs, but the absorbance values for the DU145 and HCT-116 sEVs were too low to be quantified accurately, consistent with previous findings [597]. However, the UCNP-LFA failed to generate a reliable calibration curve for PSA antigen detection, rendering it unsuitable for accurate PSA estimation in the sEV samples. The inadequacy stemmed from the antigen-antibody pair's low affinity and poor compatibility, which was confirmed separately by validation immunoassay experiments.

This significantly compromised the functionality of the system in reliably detecting PSA (Fig 54) and could not be implemented towards detection of sEV-PSA.

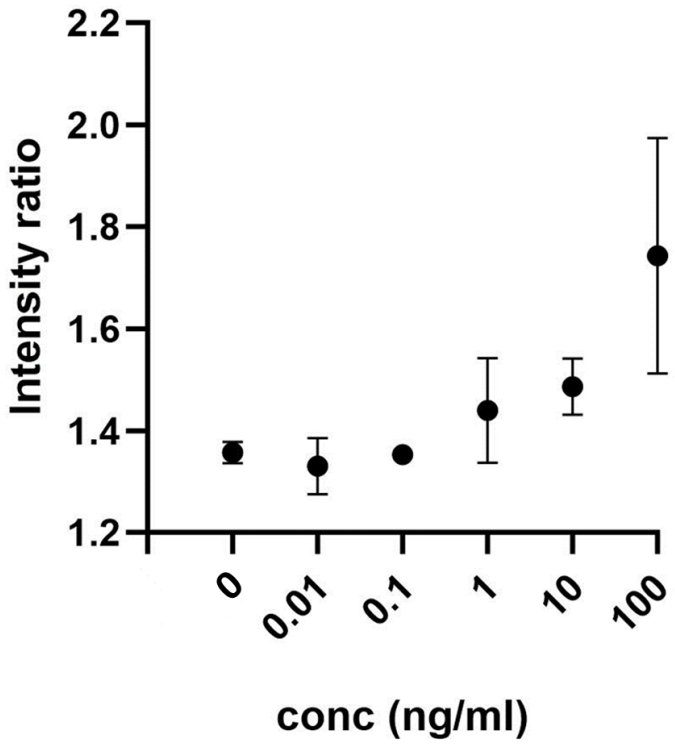

Fig 54: Calibration curve of the PSA-UCNP LFA for the detection of PSA protein at concentrations of 0.01, 0.1, 1, 10, and 100 ng/mL. The UCNP-LFA analysis demonstrated poor linearity in the detection of PSA antigen and hence cannot be used as a reliable calibration curve to accurately quantify sEV-PSA. Data plotted as mean ± standard deviation (S.D). (n=3)

6.3. Discussion and Conclusion

The significant potential of sEVs to function as both diagnostic and prognostic biomarkers has been thoroughly established. This has prompted the development of sEV-based biopsy tests, including the ExoDx Prostate Test that detects prostate cancer-specific RNA in sEVs to predict high-grade prostate cancer [601]. GPC-1 has garnered significant attention owing to its vital role in cellular signalling and tumour growth-promoting functions [602, 603]. The enrichment of sEV-GPC-1 in multiple cancer types, including prostate and colorectal cancer, makes it a potential diagnostic indicator that can be applied towards early-stage cancer detection and

disease monitoring [587, 593]. However, the minimal sensitivity of conventional techniques like Flow Cytometry and Western Blotting limits the implementation of sEV-GPC-1 detection systems in clinical settings.

In this study, for the first time we used a quantitative UCNP-LFA system to sensitively detect sEV-GPC-1 in sEVs isolated from LnCap, DU145 and HCT116 cell lines. The UCNP-LFA leveraged the benefits of high-quality UCNPs and high binding antibodies to achieve sensitive detection of sEV-GPC-1, demonstrating a detection limit at least ~10-fold better than that of a commercial GPC-1 ELISA kit (Table 5). The study simultaneously analysed the expression of PD-L1 in isolated sEVs, considering its clinical significance in promoting tumour progression and its therapeutic relevance, particularly in immunotherapy [595, 604]. The findings were consistent with previous studies, where the sEV-PD-L1 expression was found to be higher in DU145 and HCT116 sEVs compared to LnCap sEVs [595, 605].

The UCNP-LFA demonstrated the capability to detect disease-specific sEV surface markers within detection ranges that align with or exceed several other LFA-based sEV analysis studies reported in the literature (Table 6). While the sensitivity achieved by the UCNP-LFA is comparable and/or higher than that reported in studies using conventional AuNP, magnetic-based and aptamer-based LFAs, Wu et al. employed a double-conjugate AuNP-based LFA to achieve exceptional sensitivity (~ 10^3 sEVs/μL) [305, 565, 606, 607]. Importantly, the UCNP-LFA achieves this detection level without needing sample enrichment or pre-amplification, making it a simpler, more accessible alternative for quantitative sEV analysis.

The ongoing development of the UCNP-LFA technology will empower the concurrent identification of multiple sEV markers, and establish POC sEV-based cancer diagnostics. The UCNP-LFA has the capability to detect sEV-GPC-1 in patient samples, and its user-friendly functioning could be leveraged to detect other clinically significant biomarkers like PSA and

prostate-specific membrane antigen (PSMA) for prostate cancer [600]. The technology can also be expanded to detect sEV-nucleic acids specific to prostate and colon cancers to represent a more holistic disease-specific biomarker expression profile in patient samples. The simultaneous detection of a panel of sEV markers holds the potential to establish the diagnostic applicability of this technology.

Table 5: Comparison of detection performance between Commercial ELISA kit and the UCNP-LFA for sEVs isolated from LnCap, DU145 and HCT116 sEVs. The lowest sEV concentration that was accurately detected using both systems are indicated in the table.

sEVs	**Commercial ELISA**		**UCNP-LFA**	
	GPC-1	**PDL1**	**GPC-1**	**PDL1**
LnCap	1.1×10^5 sEVs/μL	N/A	2.08×10^4 sEVs/μL	N/A
DU145	1.44×10^6 sEVs/μL	3.1×10^6 sEVs/μL	1.26×10^5 sEVs/μL	3.61×10^5 sEVs/μL
HCT116	1.9×10^6 sEVs/μL	4.5×10^6 sEVs/μL	1.54×10^5 sEVs/μL	N/A

Table 6: Comparison of detection performance of UCNP-LFA with other LFA-based sEV studies

Study	**Principle**	**Lowest sEV concentration detected**
Rodriguez et al. [606]	AuNP based LFA	8.54×10^5 sEVs/μL
Moyano et al. [305]	Magnetic based LFA	10^7 sEVs/μL
Yu et al. [607]	Aptamer based AuNP LFA	6.4×10^5 sEVs/μL
Wu et al. [565]	Double conjugates based AuNP LFA	1.3×10^3 sEVs/μL
This project	Quantitative UCNP-LFA	$3.61 \times 10^5 – 2.29 \times 10^6$ sEVs/μL (PD-L1) $2.08 \times 10^4 – 1.54 \times 10^5$ sEVs/μL (GPC-1)

7. Conclusion, Perspectives and Future Directions

7.1. Thesis Summary

The focus of this thesis was to leverage the unique properties of NPs and their superior bio-analytical performance to introduce novel approaches to enable the detection of sEV surface markers with high sensitivity and specificity.

In the sequential order of the results chapters, in Chapter 3, I first present the experimental results validating the structural and functional characterisation of AuNPs and UCNPs used in the AuNP-ELISA, UCNP microplate immunoassay, and UCNP-LFA. For AuNPs, we investigated their size and discussed the bioconjugation process to HRP signalling antibodies and the functional characterisation of these conjugates for use in the AuNP-ELISA, detailed in Chapter 4. For UCNPs, the results cover their synthesis, surface modification, and bioconjugation with antibodies for use in the UCNP microplate assay in Chapter 4 and the UCNP-LFA systems detailed in Chapters 5 and 6. Specifically, these results address the synthesis of core and core@shell UCNPs, their surface engineering, and their application as probes for both the UCNP microplate immunoassay and the UCNP-LFA.

In Chapter 4, we explored the integration of AuNP and UCNP functionalised labels towards improving the detection sensitivity of a conventional ELISA format, with potential applications as a POC testing system. An in-house ELISA method was developed by initially optimising the various components of a sandwich microplate-based ELISA format. In the first technique, HRP labelled antibodies were functionalised on the surface of AuNPs by physical adsorption, and the modified AuNP-ELISA performed in a portable, hand-held plate reader generated higher colorimetric absorbance signals and achieved a ~ 2-fold improvement in the detection

limit of sEV-CD63. In the second technique, instead of a colorimetric immunoassay, the CD63 detector antibody was conjugated to polymer-modified UCNPs and used as signalling labels in a microplate immunoassay format. The UCNP microplate assay was performed in a bench-top, customised microplate reader suitable for quantifying the luminescent labels of UCNP probes and achieved a ~10-fold improvement in the detection limit of sEV-CD63 compared to the colorimetric AuNP-ELISA. While the UCNP microplate immunoassay exhibited enhanced detection performance of sEV-CD63, it necessitated a custom-built benchtop plate reader, which is unsuitable for application in POC settings. The findings of this results chapter establish the utility of nanoparticles in enhancing the sensitivity of conventional immunoassay formats that can be implemented to detect other cancer-specific sEV markers.

In Chapter 5, we introduced a system for rapid, reliable and sensitive sEV biomarker detection using high-quality UCNPs integrated with a lateral flow assay, with potential for application in POC settings. The functionality of the UCNP-LFA as a reliable sEV marker-detecting sensor was first established by detecting both CD63 and PD-L1 antigens and establishing the system's detection range and limit. The heterogeneity of sEVs with multiple surface markers also necessitated a high level of specificity in the detection of target analytes, which the UCNP-LFA did. Following this, the sensor was used to target and sensitively quantitate CD63, an integral structural surface sEV marker and PD-L1, a cancer-specific sEV surface marker with substantial clinical significance [560, 561], in sEVs isolated from H1975, MM05 and MSTO-211H cell lines. Encouraged by the superior bioanalytical performance of UCNPs, Chapter 5 analysed sEV samples at concentrations ranging from ~10^3 to 10^6 sEVs/μL to establish a broad detection range for the UCNP-LFA. While the UCNP-LFA successfully detected and quantified sEV-CD63 and sEV-PD-L1 at the highest concentrations, at concentrations < 10^5 sEVs/μL, the signal intensity ratios were inconsistent and exhibited high variability, preventing accurate estimation of the LOD for sEV-CD63 and sEV-PD-L1 across all cell-derived sEVs.

Nevertheless, the UCNP-LFA was successful at detecting sEV-CD63 and sEV-PD-L1 at detection sensitivities comparable to that of parallelly run analyses using commercial ELISA kits.

Finally in Chapter 6, we extended the use of UCNP-LFA to sensitively detect and quantify GPC-1 and PD-L1 on sEVs isolated from LnCap, DU145 and HCT116 cell lines. sEV-GPC-1 has been identified as a key player in tumour progression, metastasis and therapeutic resistance [608, 609]. This is the first study of its kind that has implemented a quantitative lateral flow assay system to detect sEV-PD-L1. Consistent with the previous results chapter, we first established the sensitivity and specificity of the UCNP-LFA in detecting the GPC-1 analyte, to be implemented towards detection of the same marker in sEVs. The UCNP-LFA achieved atleast a ~10-fold improvement in detection limits of sEV-GPC-1 and sEV-PD-L1 compared to parallelly run analyses using commercial ELISA kits. Moreover, the detection performance was discussed in comparison to other colorimetric LFA studies on sEV detection, with the UCNP-LFA enjoying the advantage of allowing quantitative detection of sEV markers [305, 307, 606]. The findings of these two result chapters advance the implementation of quantitative UCNP-LFA systems towards sensitive and accurate detection of cancer-specific sEV markers. Future research needs to prioritise the implementation of the UCNP-LFA technology in the detection of a comprehensive panel of disease-relevant sEV markers, particularly from complex biofluids in diagnostic settings.

The major milestones achieved during my PhD study include, but not limited to:

1. Isolation and characterisation of sEVs: In my research, a key experimental step involved isolating and characterising small extracellular vesicles (sEVs) for subsequent analysis in sensor technologies. We induced hypoxic stress conditions in the cell culture to simulate the tumour microenvironment, prompting the release of sEVs [610]. Additionally, I

conducted ultracentrifugation on the conditioned medium from various cell lines to isolate sEVs and employed techniques such as Nanoparticle Tracking Analysis (NTA), Western Blotting, and Transmission Electron Microscopy (TEM) for comprehensive structural, functional, and morphological characterization of the isolated sEVs.

2. AuNP characterisation and optimisation of bio-conjugation conditions: In my projects, employing AuNPs required thorough characterisation using techniques such as DLS, Zeta Potential measurements and UV-Vis Spectroscopy. Since I used physical adsorption for bio-conjugation with labelling antibodies, I conducted multiple experiments to identify the optimal pH and loading concentration of antibodies. This was essential to prevent aggregation and ensure the stability of AuNP-antibody conjugates, and it contributed to strong bio-analytical performance in the modified ELISA format.
3. Characterisation of UCNPs: In my thesis, the importance of UCNPs necessitated the synthesis of heavily doped ($NaYF_4$:40%Yb,4%Er) core and core@shell UCNPs, followed by their characterisation using TEM. Additionally, surface modification of UCNPs with polymers containing anchoring ligands was crucial to facilitate optimal conditions for bio-conjugation with specific antibodies, forming highly sensitive probes. I also gained proficiency in various nanoparticle characterisation techniques such as DLS, Zeta Potential measurements, and FTIR.
4. Optimising the sandwich ELISA components was a critical milestone, ensuring high sensitivity and specificity for detecting low-abundance sEV surface markers. A homemade ELISA platform was developed, integrating AuNP-HRP conjugates to amplify the colorimetric signal through their enhanced surface area and optical properties. Similarly, the UCNP microplate immunoassay employed luminescent UCNP-antibody conjugates as highly efficient probes to achieve sensitive detection with minimal background interference. Key parameters, including antibodies, blocking buffers, and washing steps,

were systematically refined to ensure reliable antigen capture and signal amplification across both platforms.

Additional optimisations included selecting high-binding polystyrene plates for consistent antibody immobilisation and using stabilising coating buffers to prevent aggregation of conjugates. Washing steps with a mild detergent were refined to minimise background noise, while longer incubation times improved sensitivity by allowing sufficient time for immunocomplex formation. Cross-reactivity tests validated the specificity of both platforms, demonstrating reliable detection of target sEV markers, such as CD63 and PD-L1, without interference from non-target analytes.

These refinements addressed challenges associated with homemade assay systems, such as variability in surface chemistries and the detection of low-abundance analytes. The iterative optimisation process delivered robust, reproducible platforms capable of supporting bioanalytical applications with high performance, while insights from these optimisations provide a foundation for extending these assays to other targets and detection systems.

5. Design, Fabrication, and Optimisation of UCNP-LFA Strips: The development and optimisation of the UCNP-LFA system represented a crucial milestone in this thesis, requiring a thoughtful design process and systematic refinement of its components. Each part of the lateral flow strip—including the sample pad, conjugation pad, nitrocellulose (NC) membrane, and absorbent pad—was carefully selected and configured to ensure efficient analyte migration, reliable flow dynamics, and consistent signal generation. Particular attention was given to the pore sizes of these components, especially the NC membrane, to optimise flow rates and promote effective antigen-antibody interactions at the test line, thereby enhancing sensitivity and reproducibility. Additionally, uniform deposition of capture antibodies onto the test line was critical to minimise signal variability and ensure robust assay performance.

Buffers were carefully optimised to maintain compatibility with the lateral flow strip components and to stabilise the UCNP-conjugated probes, thereby enhancing the efficiency of antigen-antibody interactions. The 'wet method,' which involved pre-incubating UCNP probes with the sample before applying it to the strip, was found to be more effective than the 'dry method,' where UCNP probes were immobilised on the conjugate pad. This pre-incubation step enhanced assay sensitivity by allowing immunocomplex formation prior to application and significantly improved reproducibility, particularly for detecting low-abundance analytes.

These extensive efforts in component selection, buffer optimisation, and incubation protocols collectively contributed to a robust and sensitive UCNP-LFA platform. The optimised system demonstrated high specificity and consistent performance, underscoring the substantial work undertaken to establish its reliability for detecting sEV-specific markers and advancing its potential applications in biosensing technologies.

7.2. Technical Limitations

The confluence of my health condition, with its enduring impact on my daily life, coupled with the constraints imposed by the pandemic and persistent funding challenges, proved to be significant hurdles in advancing my research. Regrettably, these factors hindered me from fully realizing the comprehensive research objectives set forth at the outset of my doctoral studies. Despite my unwavering commitment, these unforeseen circumstances hampered the attainment of the intended milestones and posed formidable challenges to the seamless progression of my research endeavours.

The nanoparticle modified ELISAs (AuNP-ELISA and UCNP microplate assay) successfully detected CD63 at enhanced detection limits compared to the conventional ELISA. While the AuNP-ELISA achieved an improved detection limit of CD63 compared to the conventional

ELISA, the detection of low abundance, cancer specific sEV markers require even more improved sensitivity. The UCNP microplate immunoassay achieved enhanced detection sensitivity compared to the colorimetric formats, which is a consequence of the superior bio-analytical performance offered by high-quality UCNPs. Incorporating nanoparticle-based immunoassay formats into commercial ELISA kits, that offer very specific standardisation and optimisation, a process challenging to replicate in academic research settings, will potentiate improved detection performance beyond what is discussed in this thesis. While the colorimetric ELISAs were performed in a portable, hand-held plate reader, the UCNP microplate assay was performed in a bench-top, customised plate reader, with limited application in POC settings. Although this version of the UCNP microplate assay may not inherently offer the same versatility as POC solutions like LFAs or portable analytical systems, developing this technology into a compact hand-held device or integrating similar nanoparticle-assisted ELISA formats into on-chip systems through innovative approaches can enhance its adaptability in clinical settings. Future research should broaden the spectrum of sEV detection to encompass various disease-specific markers and clinical samples to evaluate the technology's potential in diagnostic settings.

The UCNP-LFA utilised in my projects successfully quantified sEV markers from cell lines with comparable sensitivities to commercial ELISA kits. Despite this success, assessing clinical samples is crucial for validating biosensor technologies in real-world diagnostic scenarios, as samples like blood or urine mimic the complexity of biological environments. The primary aim of employing LFAs was to create a 'sample-to-answer' system suitable for clinical implementation. However, the operational process in my projects necessitated a prerequisite step that involved isolating sEVs initially from conditioned media or complex biofluid samples before their detection and in the UCNP-LFA. Moreover, as we saw in Chapter 5, at lower sEV concentrations, Brownian motion and the inherent heterogeneity in size,

morphology, and biomarker composition do not consistently correspond with serial dilution of samples. This means that diluting sEV samples does not necessarily result in proportionately lower amounts of sEV target analytes. This inconsistency can lead to high variability, making it challenging to accurately estimate the detection limit of an analytical system. Additionally, steps like ultracentrifugation can result in particle loss during isolation and can be affected by storage conditions and solvent chemistry. Therefore, an integrated system that combines both sEV isolation and detection would address these issues. Future research should focus on developing integrated approaches that enable both the isolation of sEVs and their subsequent analysis using the UCNP-LFA within a single functioning sensor. In my thesis, the UCNP-LFA demonstrated its effectiveness in detecting sEV markers like CD63, PD-L1, and GPC-1 individually on separate LFA strips. However, to enable a more comprehensive diagnostic analysis, the UCNP-LFA should be capable of multiplexed detection on a single strip. Furthermore, expanding the biomarker panel to include additional cancer-specific sEV markers such as Her2, mesothelin, EGFR, and PSA would provide a thorough understanding of patients' diagnostic profiles. In addition to surface protein markers on sEVs, the nucleic acids associated with sEVs, particularly miRNAs and mRNAs, have established themselves as disease-specific biomarkers. Their stability in bodily fluids, such as blood, potentiate their application in non-invasive diagnostics [611]. Concurrently, there is a need for further development of the UCNP-LFA to enable the detection of sEV-miRNA and sEV-mRNA with sensitivity and specificity that is comparable to qRT-PCR.

7.3. Perspectives and Future Research Directions

Liquid biopsy circumvents the limitations of conventional tissue biopsy by allowing minimal invasiveness, easy acquisition of samples and dynamic analysis. The potential of sEVs serving as diagnostic and prognostic biomarkers has been extensively investigated, but their inherent heterogeneity and size have posed as hindrances to decoding the complexity of their molecular

interactions. Strategies that exploit physical or biological characteristics have been implemented for sEV isolation, however there is no standardised method that allows for high throughput, high purity with minimal damage isolation of sEVs from complex body fluids [612, 613]. Prompted by the stable circulation of sEVs, a few liquid biopsy systems targeting sEV nucleic acids have been tested in clinical trials. ExoDX^{TM} Lung (ALX) was the first sEV based liquid biopsy that allowed for isolation and analysis of sEV RNA from blood samples. The system was successful at accurately detecting EML4-ALK mutations with 88% sensitivity and 100% specificity in NSCLC patients, which was more sensitive than detection of genetic aberrations in cfDNA [614]. A similar sEV based diagnostic system, the ExoDx Prostate IntelliScore system was validated by the FDA for screening of prostate cancer (PCa), without the need for invasive tissue collection. Based on the detection of PCa specific RNA in sEVs, the system provides a risk score to predict patients' chances of developing high grade prostate cancer [615]. One of the key challenges of sEV-based diagnostics is in achieving efficient isolation of cancer cell-derived sEVs. To address this, integrated systems have been developed to allow for comprehensive screening of cancers based on sEV analysis. The MedOncAlyzer 170 (Exosome Diagnostics) is one such liquid biopsy system that combines the detection of sEV RNA and ctDNA in a single system. The system successfully identified functional mutations in multiple cancer types from as low as 0.5mL of blood or plasma [616].

While miniaturised and nanoparticle-integrated systems have established themselves as promising platforms for analysing sEV biomarkers, a major limitation is the poor translation of these techniques to clinical settings. The inherent heterogeneity of sEVs requires the combined screening of multiple biomarkers (preferably in a panel) to enhance diagnostic accuracy. For clinical settings, it is essential to develop platforms that facilitate simplified isolation and detection modules for sEVs, while minimising sample loss. To achieve rapid, reliable and reproducible sEV biomarker analysis, it is important to standardise the design and

operation of sensitive nanoparticle-integrated devices. The intrinsic complexity in the design of complex sensors often reduces the reliability of testing performance. It is important to ensure that complex sensor designs do not compromise the clinical value. Additionally, the automated operation of these systems with minimal intervention, particularly in clinical settings, allows for reproducible analysis of high volumes of samples. Standardised modular designs of different components in a sensor, integrated with machine learning and artificial intelligence modules, allow for more automated operation.

Apart from the sEV detection approaches extensively discussed in Chapter 1, there are additional strategies for sEV detection and analysis that enable more accurate and ultrasensitive detection and quantification of sEVs and their cargoes. These advanced methods hold significant potential for integration into automated systems and have important implications for sEV-based diagnostics.

CRISPR/Cas based sEV detection

CRISPR/Cas (Clustered regularly interspaced short palindromic repeats) is an adaptive immune mechanism originally found in bacteria and archaea, and is the most widely used gene editing system [617, 618]. These systems offer unique advantages, including high sensitivity and specificity, particularly when integrated with isothermal nucleic acid amplification strategies, surpassing the detection sensitivity of conventional PCR methods, making them promising for the development of POC diagnostics [619].

Leveraging the high accuracy and sensitivity offered by CRISPR/Cas systems, can enable the sensitive detection of sEVs and their associated cargoes. For instance, Zhao et al. combined a CD63 aptamer-based target recognition with the signal amplification of CRISPR/Cas12a to achieve rapid and sensitive detection of sEVs. The CD63 aptamer, integrated with a blocker, was immobilized on magnetic beads. Upon encountering $CD63^+$ sEVs, the aptamer now bound to the sEVs released the blocker. This triggered the activation of the CRISPR/Cas system,

leading to the cleavage of reporter ssDNA and enabling a sensitive detection range from 3×10^3 to 6×10^7 particles/mL [620]. A similar CRISPR/Cas12a-aptamer sensor strategy was reported for the sensitive identification of disease specific $CD109^+$ and $EGFR^+$ sEVs in both cells and complex biofluids (Fig 55) [621]. He et al. developed a novel method for ultrasensitive detection of sEV-PD-L1 by combining aptamer-CRISPR/Cas13a with dual amplification steps. Mechanistically, the study involved amplifying a DNA aptamer specific to sEV-PD-L1 by recombinase polymerase amplification (RPA) and transcription-mediated amplification (TMA), to facilitate real-time detection by the CRISPR/Cas13a system. The strategy achieved a detection limit of 10 particles/mL and offered a convenient approach for dynamically monitoring tumour progression in patients undergoing immunotherapy [622].

The ability of CRISPR/Cas systems to detect target oligonucleotide markers with high selectivity and precision has prompted the adoption of the technology towards detection of sEV-nucleic acids [623, 624]. The CRISPR/Cas12a system combined with RCA achieved a detection limit of 34.7 fM for sEV-miR-21, potentiating the application of the technology in clinical settings [625]. In a similar approach, Wang et al. employed an RCA-assisted CRISPR/Cas9 cleavage (RACE) system to sensitively detect multiple sEV-miRNAs (miR-21, miR-221, and miR-222). The system achieved single-base resolution through dual-specific recognition from padlock probe-mediated ligation and protospacer adjacent motif (PAM)-triggered cleavage. The method's detection performance of sEV-miRNAs was validated by parallel RT-qPCR analysis, highlighting its robustness and potential for use in multiplexed POC diagnostics [626]. The customisability of CRISPR/Cas systems has prompted their integration into electrochemical chip-based platforms and has also facilitated rapid, accurate and sensitive detection of specific nucleic acids without the need for bulky, sophisticated equipment, particularly in POC settings [627, 628].

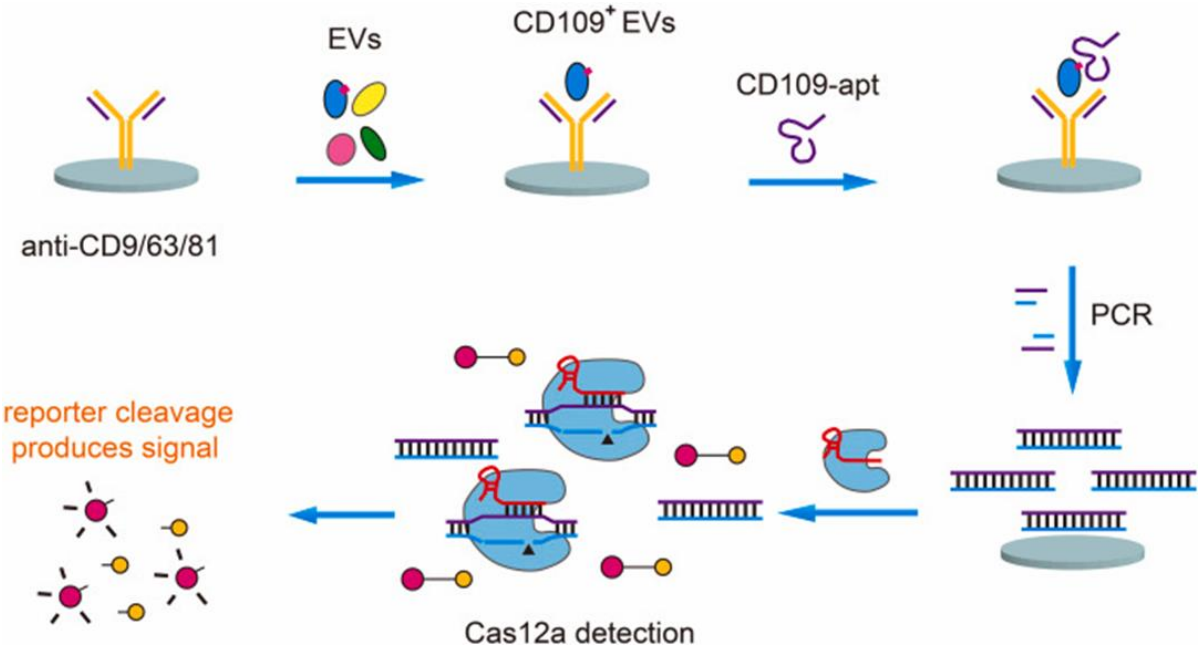

Fig 55: Schematic illustration of the aptamer-CRISPR/Cas12a assay. The system combined aptamers, PCR-based exponential amplification, and CRISPR/Cas12a real-time DNA detection to identify $CD109^+$ and $EGFR^+$ tumor-derived sEVs in cell lines and complex biofluids. This platform achieves highly sensitive detection of $CD109^+$ and $EGFR^+$ sEVs, with a detection limit as low as 100 particles/mL and a linear range spanning 6 orders of magnitude (10^2-10^8 particles/mL), making it suitable for direct detection of sEV proteins in low-volume samples (50 µl). Reproduced with permission from ref [629].

Machine Learning based EV analysis

Machine learning involves the prediction and analysis of unknown data based on models of known data. Being a crucial aspect of artificial intelligence, machine learning has been explored for multiplexed profiling of sEV markers [45]. Algorithms like linear discriminant analysis (LDA), principal component analysis (PCA), neural network (NN), support vector machine (SVM) and random forests (RF) have been implemented to classify multivariate data into a typical classification model, which are then applied for prediction and grouping of unknown biological data [630]. LDA makes predictions by estimating the probability such that a new set of inputs belongs to each class and has been implemented to determine upto 7-8 sEV markers with high accuracy from as low as 1 µL of plasma [631, 632]. PCA is an algorithm that changes a group of related variables into a series of linearly unrelated variables through

orthogonal transformation. Towards this, Shin et al. used PCA based machine learning model to differentiate normal and lung cancer derived sEVs to accurately predict lung cancer in sampled cohorts [633]. Algorithms like RF, NN and SVM have also been implemented to analyse multiple sEV associated mRNAs of breast cancer patients and enhanced the overall diagnostic performance of the platform [634].

Analysis of the generated data by machine learning has facilitated multimodal monitoring and data acquisition instrumentation [635, 636]. The development of integrated on-chip devices have potentiated the rise of next generation autonomous platforms that are operated by data driven models [637]. Towards this, Ko et al. designed a novel multichannel nanofluidic system that integrated machine learning with nanofluidics to diagnose pancreatic cancer using sEVs. The study used an sEV track-etched magnetic nanopore chip (ExoTENPO) that rotated conventional nanofluidic sorting by 90º to form magnetic traps at the edges of pores instead of in channels. Using this platform, sEVs were isolated from healthy and diseased murine and clinical cohorts to analyse their RNA and a machine learning algorithm (LDA) was implemented to generate predictive panels that classified cancer and pre cancer mice as well as pancreatic cancer patients from healthy controls in blinded studies [638]. An LDA based machine learning integrated system has also been successful at assessing EV heterogeneity at the single EV level. This was the first DNA-mediated approach simultaneously that sorted and detected individual EV subpopulations. The platform was successful at deciphering single EVs and differentiating breast cancer samples from controls on the basis of HER2 expressing EV signatures [639]. More recently, Zhang et al devised a nano-engineered microfluidic platform for multiparametric analysis of EV concentration in circulation, subtype and enzymolytic activity (EV-CLUE) with high sensitivity requiring minimal sample input, allowing longitudinal monitoring of in vivo tumour growth in mice. The study implemented a high-resolution colloidal inkjet printing method to develop a 3D nanopatterned device that enabled

integrative functional and molecular phenotyping of tumour associated EVs. The platform also analysed the expression and proteolytic activity of matrix metalloproteases (MMPs) on EVs, which are key regulators of extracellular matrix (ECM), to detect in vitro cell invasiveness and monitor in vivo tumour metastasis using both cancer cell lines and mouse models. The study integrated an LDA based machine learning diagnostic with the chip based functional EV analysis to enhance the clinical sensitivity and specificity for patient classification. The EV-CLUE chip was successful at sensitively detecting expression and phenotypes of MMP^+ sEVs in cell lines, mouse models and clinical plasma and its performance was validated by comparison to standard analytical methods [640].

7.4. Conclusion

The findings of this PhD thesis establish the utility of nanoparticle-assisted sensors towards sensitive detection of sEV markers. The projects were motivated by the clinical significance of sEVs coupled with the current lack of simple and highly sensitive sEV detection systems. The technologies introduced in this thesis and its findings have the potential to make a significant impact on both the development and use of innovative technologies, as well as facilitate informed decisions on therapeutic regimens by sensitively detecting early-stage cancer biomarkers. Leveraging these technologies in diverse sensor modules, as explored in the literature review, especially electrochemical, SERS and single sEV analysis sensors, will foster the development of ultrasensitive sEV detection systems that allow non-invasive and dynamic analyses of early-stage cancer biomarkers, particularly in clinical POC settings. Ultrasensitive sEV-based diagnostics present an ideal diagnostic and prognostic option for molecular diagnosis of cancer and promise a shift in medical paradigms towards personalised medicine and show promise of revolutionising diagnostic and disease monitoring applications.

8. Appendix

During the candidature of my PhD, I have also authored and published two papers on topics that were beyond the scope of the overall aim of my thesis.

1. P. Bordhan, S. Razavi Bazaz, D. Jin and M. E. Warkiani. "Advances and enabling technologies for phase-specific cell cycle synchronisation" Lab on a chip. DOI: 10.1039/D1LC00724F
2. V.Y. Naei, P. Bordhan, F. Mirakhorli, M. Khorrami, J. Shrestha, H. Nazari, A. Kulasinghe, M.E. Warkiani, "Advances in novel strategies for isolation, characterization and analysis of CTCs and ctDNA", Therapeutic Advances in Medical Oncology, DOI:10.1177/17588359231192401

I was the main author of the first paper indicated here, which presented a comprehensive review on discussing the conventional and microfluidic-based methods for achieving phase-specific cell cycle synchronisation, which has significant implications in targeted gene editing, drug efficacy and studying specific cell cycle events and regulatory mechanisms. For the second published paper, I was a co-author (2^{nd} author), which presented a comprehensive review of the advances in isolation and characterisation and analysis of CTCs and ctDNA. Engaging in these projects provided me with valuable experience in writing comprehensive reviews on relevant scientific topics and familiarised me with the complexities of publishing works in reputable scientific journals.

9. References

1. *Global Cancer Observatory*. 2022; Available from: https://gco.iarc.fr/today/en/fact-sheets-cancers.
2. Li, W., et al., *Emerging nanotechnologies for liquid biopsy: The detection of circulating tumor cells and extracellular vesicles.* Advanced Materials, 2019. **31**(45): p. 1805344.
3. Munzone, E., et al., *Changes of HER2 status in circulating tumor cells compared with the primary tumor during treatment for advanced breast cancer.* Clinical breast cancer, 2010. **10**(5): p. 392-397.
4. Guarneri, V., et al., *Comparison of HER-2 and hormone receptor expression in primary breast cancers and asynchronous paired metastases: impact on patient management.* The oncologist, 2008. **13**(8): p. 838-844.
5. Ohannesian, N., et al., *Commercial and emerging technologies for cancer diagnosis and prognosis based on circulating tumor exosomes.* Journal of Physics: Photonics, 2020. **2**(3): p. 032002.
6. Gerlinger, M., et al., *Intratumor heterogeneity and branched evolution revealed by multiregion sequencing.* N Engl j Med, 2012. **366**: p. 883-892.
7. Iliescu, F.S., et al., *Recent advances in microfluidic methods in cancer liquid biopsy.* Biomicrofluidics, 2019. **13**(4): p. 041503.
8. McGranahan, N. and C. Swanton, *Biological and therapeutic impact of intratumor heterogeneity in cancer evolution.* Cancer cell, 2015. **27**(1): p. 15-26.
9. Mittelbrunn, M., et al., *Unidirectional transfer of microRNA-loaded exosomes from T cells to antigen-presenting cells.* Nature communications, 2011. **2**(1): p. 1-10.
10. Wang, J., et al., *Towards microfluidic-based exosome isolation and detection for tumor therapy.* Nano Today, 2021. **37**: p. 101066.
11. Melo, S.A., et al., *Glypican-1 identifies cancer exosomes and detects early pancreatic cancer.* Nature, 2015. **523**(7559): p. 177-182.
12. Nawaz, M., et al., *The emerging role of extracellular vesicles as biomarkers for urogenital cancers.* Nature Reviews Urology, 2014. **11**(12): p. 688.
13. Szabo, G. and F. Momen-Heravi, *Extracellular vesicles in liver disease and potential as biomarkers and therapeutic targets.* Nature reviews Gastroenterology & hepatology, 2017. **14**(8): p. 455.
14. Dawson, S.-J., et al., *Analysis of circulating tumor DNA to monitor metastatic breast cancer.* New England Journal of Medicine, 2013. **368**(13): p. 1199-1209.
15. Gall, T.M., et al., *Circulating tumor cells and cell-free DNA in pancreatic ductal adenocarcinoma.* The American journal of pathology, 2019. **189**(1): p. 71-81.
16. Eyles, J., et al., *Tumor cells disseminate early, but immunosurveillance limits metastatic outgrowth, in a mouse model of melanoma.* The Journal of clinical investigation, 2010. **120**(6): p. 2030-2039.
17. Zhand, S., et al., *Improving capture efficiency of human cancer cell derived exosomes with nanostructured metal organic framework functionalized beads.* Applied Materials Today, 2021. **23**: p. 100994.
18. Belotti, Y. and C.T. Lim, *Microfluidics for Liquid Biopsies: Recent Advances, Current Challenges, and Future Directions.* Analytical Chemistry, 2021. **93**(11): p. 4727-4738.
19. Khoo, B.L., et al., *Single‐cell profiling approaches to probing tumor heterogeneity.* International journal of cancer, 2016. **139**(2): p. 243-255.
20. Song, Y., et al., *Enrichment and single-cell analysis of circulating tumor cells.* Chemical science, 2017. **8**(3): p. 1736-1751.
21. Alix-Panabières, C. and K. Pantel, *Clinical applications of circulating tumor cells and circulating tumor DNA as liquid biopsy.* Cancer discovery, 2016. **6**(5): p. 479-491.

22. Thiery, J.P., et al., *Epithelial-mesenchymal transitions in development and disease.* cell, 2009. **139**(5): p. 871-890.
23. Ferreira, M.M., V.C. Ramani, and S.S. Jeffrey, *Circulating tumor cell technologies.* Molecular oncology, 2016. **10**(3): p. 374-394.
24. Marrinucci, D., et al., *Case study of the morphologic variation of circulating tumor cells.* Human pathology, 2007. **38**(3): p. 514-519.
25. Merker, J.D., et al., *Circulating tumor DNA analysis in patients with cancer: American Society of Clinical Oncology and College of American Pathologists joint review.* Archives of pathology & laboratory medicine, 2018. **142**(10): p. 1242-1253.
26. Stewart, C.M., et al., *The value of cell‐free DNA for molecular pathology.* The Journal of pathology, 2018. **244**(5): p. 616-627.
27. Gauri, S. and M.R. Ahmad, *ctDNA detection in microfluidic platform: A promising biomarker for personalized cancer chemotherapy.* Journal of Sensors, 2020. **2020**.
28. Haber, D.A. and V.E. Velculescu, *Blood-Based Analyses of Cancer: Circulating Tumor Cells and Circulating Tumor DNABlood-Based Analysis of Cancer.* Cancer discovery, 2014. **4**(6): p. 650-661.
29. Moati, E., et al., *Role of circulating tumor DNA in gastrointestinal cancers: current knowledge and perspectives.* Cancers, 2021. **13**(19): p. 4743.
30. Bronkhorst, A.J., V. Ungerer, and S. Holdenrieder, *The emerging role of cell-free DNA as a molecular marker for cancer management.* Biomolecular detection and quantification, 2019. **17**: p. 100087.
31. Rijavec, E., et al., *Liquid biopsy in non-small cell lung cancer: highlights and challenges.* Cancers, 2019. **12**(1): p. 17.
32. Keller, L., et al., *Clinical relevance of blood-based ctDNA analysis: mutation detection and beyond.* British Journal of Cancer, 2021. **124**(2): p. 345-358.
33. Ai, B., et al., *Circulating cell-free DNA as a prognostic and predictive biomarker in non-small cell lung cancer.* Oncotarget, 2016. **7**(28): p. 44583.
34. Bettegowda, C., et al., *Detection of circulating tumor DNA in early-and late-stage human malignancies.* Science translational medicine, 2014. **6**(224): p. 224ra24-224ra24.
35. Phallen, J., et al., *Direct detection of early-stage cancers using circulating tumor DNA.* Science translational medicine, 2017. **9**(403): p. eaan2415.
36. Szpechcinski, A., et al., *Cell-free DNA levels in plasma of patients with non-small-cell lung cancer and inflammatory lung disease.* British journal of cancer, 2015. **113**(3): p. 476-483.
37. Elazezy, M. and S.A. Joosse, *Techniques of using circulating tumor DNA as a liquid biopsy component in cancer management.* Computational and structural biotechnology journal, 2018. **16**: p. 370-378.
38. Théry, C., L. Zitvogel, and S. Amigorena, *Exosomes: composition, biogenesis and function.* Nature reviews immunology, 2002. **2**(8): p. 569-579.
39. Cazzoli, R., et al., *microRNAs derived from circulating exosomes as noninvasive biomarkers for screening and diagnosing lung cancer.* Journal of thoracic oncology, 2013. **8**(9): p. 1156-1162.
40. Hoshino, A., et al., *Tumour exosome integrins determine organotropic metastasis.* Nature, 2015. **527**(7578): p. 329-335.
41. Zhang, L., et al., *Microenvironment-induced PTEN loss by exosomal microRNA primes brain metastasis outgrowth.* Nature, 2015. **527**(7576): p. 100-104.
42. Théry, C., *Biogenesis, secretion, and intercellular interactions of exosomes and other extracellular vesicles.* Annu. Rev. Cell Dev. Biol, 2014. **30**: p. 255-89.
43. Crowley, E., et al., *Liquid biopsy: monitoring cancer-genetics in the blood.* Nature reviews Clinical oncology, 2013. **10**(8): p. 472-484.
44. Lin, B., et al., *Microfluidic‐Based Exosome Analysis for Liquid Biopsy.* Small Methods, 2021. **5**(3): p. 2001131.

45. Yu, D., et al., *Exosomes as a new frontier of cancer liquid biopsy.* Molecular Cancer, 2022. **21**(1): p. 1-33.
46. Shao, H., et al., *New Technologies for Analysis of Extracellular Vesicles.* Chemical Reviews, 2018. **118**(4): p. 1917-1950.
47. Van Niel, G., et al., *Exosomes: a common pathway for a specialized function.* Journal of biochemistry, 2006. **140**(1): p. 13-21.
48. Cao, L.-q., et al., *Correction to: Exosomal miR-21 regulates the TETs/PTENp1/PTEN pathway to promote hepatocellular carcinoma growth.* Molecular Cancer, 2020. **19**(1): p. 1-2.
49. Liu, C., et al., *Sensitive detection of exosomal proteins via a compact surface plasmon resonance biosensor for cancer diagnosis.* ACS sensors, 2018. **3**(8): p. 1471-1479.
50. Zhou, Y.G., et al., *Interrogating circulating microsomes and exosomes using metal nanoparticles.* Small, 2016. **12**(6): p. 727-732.
51. Gusachenko, O., M. Zenkova, and V. Vlassov, *Nucleic acids in exosomes: disease markers and intercellular communication molecules.* Biochemistry (Moscow), 2013. **78**(1): p. 1-7.
52. Behera, J. and N. Tyagi, *Exosomes: mediators of bone diseases, protection, and therapeutics potential.* Oncoscience, 2018. **5**(5-6): p. 181.
53. Hannafon, B.N. and W.-Q. Ding, *Intercellular communication by exosome-derived microRNAs in cancer.* International journal of molecular sciences, 2013. **14**(7): p. 14240-14269.
54. Mitchell, P.S., et al., *Circulating microRNAs as stable blood-based markers for cancer detection.* Proceedings of the National Academy of Sciences, 2008. **105**(30): p. 10513-10518.
55. Taylor, D.D. and C. Gercel-Taylor, *MicroRNA signatures of tumor-derived exosomes as diagnostic biomarkers of ovarian cancer.* Gynecologic Oncology, 2008. **110**(1): p. 13-21.
56. Di, H., et al., *Nanozyme-assisted sensitive profiling of exosomal proteins for rapid cancer diagnosis.* Theranostics, 2020. **10**(20): p. 9303.
57. Preis, M., et al., *MicroRNA-10b expression correlates with response to neoadjuvant therapy and survival in pancreatic ductal adenocarcinoma.* Clinical Cancer Research, 2011. **17**(17): p. 5812-5821.
58. Wu, W., et al., *Surface plasmon resonance imaging-based biosensor for multiplex and ultrasensitive detection of NSCLC-associated exosomal miRNAs using DNA programmed heterostructure of Au-on-Ag.* Biosensors and Bioelectronics, 2021. **175**: p. 112835.
59. Lee, J.U., et al., *Quantitative and specific detection of exosomal miRNAs for accurate diagnosis of breast cancer using a surface‐enhanced Raman scattering sensor based on plasmonic head‐flocked gold nanopillars.* Small, 2019. **15**(17): p. 1804968.
60. Gerlach, J.Q., et al., *Urinary nanovesicles captured by lectins or antibodies demonstrate variations in size and surface glycosylation profile.* Nanomedicine, 2017. **12**(11): p. 1217-1229.
61. Costa, J., *Glycoconjugates from extracellular vesicles: Structures, functions and emerging potential as cancer biomarkers.* Biochimica et Biophysica Acta (BBA)-Reviews on Cancer, 2017. **1868**(1): p. 157-166.
62. Cummings, Richard D. and J.M. Pierce, *The Challenge and Promise of Glycomics.* Chemistry & Biology, 2014. **21**(1): p. 1-15.
63. Nakai, W., et al., *A novel affinity-based method for the isolation of highly purified extracellular vesicles.* Scientific reports, 2016. **6**(1): p. 1-11.
64. Xu, H., et al., *Magnetic-based microfluidic device for on-chip isolation and detection of tumor-derived exosomes.* Analytical chemistry, 2018. **90**(22): p. 13451-13458.
65. Nayak, S., et al., *Point-of-Care Diagnostics: Recent Developments in a Connected Age.* Analytical Chemistry, 2017. **89**(1): p. 102-123.
66. El Andaloussi, S., et al., *Extracellular vesicles: biology and emerging therapeutic opportunities.* Nature Reviews Drug Discovery, 2013. **12**(5): p. 347-357.
67. Hofmann, L., et al., *The Emerging Role of Exosomes in Diagnosis, Prognosis, and Therapy in Head and Neck Cancer.* International Journal of Molecular Sciences, 2020. **21**(11): p. 4072.

68. Zhao, R., et al., *Exosomal long noncoding RNA HOTTIP as potential novel diagnostic and prognostic biomarker test for gastric cancer.* Molecular Cancer, 2018. **17**(1): p. 68.
69. Wei, S., et al., *Exosomal transfer of miR-15b-3p enhances tumorigenesis and malignant transformation through the DYNLT1/Caspase-3/Caspase-9 signaling pathway in gastric cancer.* Journal of Experimental & Clinical Cancer Research, 2020. **39**(1): p. 32.
70. Lee, Y.R., et al., *Circulating exosomal noncoding RNAs as prognostic biomarkers in human hepatocellular carcinoma.* International Journal of Cancer, 2019. **144**(6): p. 1444-1452.
71. Cao, L.-q., et al., *Correction to: Exosomal miR-21 regulates the TETs/PTENp1/PTEN pathway to promote hepatocellular carcinoma growth.* Molecular Cancer, 2020. **19**(1): p. 59.
72. Nakano, T., et al., *Circulating exosomal miR-92b: Its role for cancer immunoediting and clinical value for prediction of posttransplant hepatocellular carcinoma recurrence.* American Journal of Transplantation, 2019. **19**(12): p. 3250-3262.
73. Di, H., et al., *Nanozyme-assisted sensitive profiling of exosomal proteins for rapid cancer diagnosis.* Theranostics, 2020. **10**(20): p. 9303-9314.
74. Joshi, G.K., et al., *Label-Free Nanoplasmonic-Based Short Noncoding RNA Sensing at Attomolar Concentrations Allows for Quantitative and Highly Specific Assay of MicroRNA-10b in Biological Fluids and Circulating Exosomes.* ACS Nano, 2015. **9**(11): p. 11075-11089.
75. Pang, Y., et al., *Dual-SERS biosensor for one-step detection of microRNAs in exosome and residual plasma of blood samples for diagnosing pancreatic cancer.* Biosensors and Bioelectronics, 2019. **130**: p. 204-213.
76. Melo, S.A., et al., *Glypican-1 identifies cancer exosomes and detects early pancreatic cancer.* Nature, 2015. **523**(7559): p. 177-182.
77. Lewis, J.M., et al., *Integrated Analysis of Exosomal Protein Biomarkers on Alternating Current Electrokinetic Chips Enables Rapid Detection of Pancreatic Cancer in Patient Blood.* ACS Nano, 2018. **12**(4): p. 3311-3320.
78. Carmicheal, J., et al., *Label-free characterization of exosome via surface enhanced Raman spectroscopy for the early detection of pancreatic cancer.* Nanomedicine: Nanotechnology, Biology and Medicine, 2019. **16**: p. 88-96.
79. Ma, D., et al., *Quantitative detection of exosomal microRNA extracted from human blood based on surface-enhanced Raman scattering.* Biosensors and Bioelectronics, 2018. **101**: p. 167-173.
80. Wei, P., et al., *Plasma extracellular vesicles detected by Single Molecule array technology as a liquid biopsy for colorectal cancer.* Journal of Extracellular Vesicles, 2020. **9**(1): p. 1809765.
81. Li, J., et al., *The mechanisms underlying the enrichment and action of glypican-1-positive exosomes in colorectal cancer cells.* Transl Oncol, 2023. **32**: p. 101655.
82. Fan, Y., et al., *High-sensitive and multiplex biosensing assay of NSCLC-derived exosomes via different recognition sites based on SPRi array.* Biosensors and Bioelectronics, 2020. **154**: p. 112066.
83. Liu, C., et al., *Sensitive Detection of Exosomal Proteins via a Compact Surface Plasmon Resonance Biosensor for Cancer Diagnosis.* ACS Sensors, 2018. **3**(8): p. 1471-1479.
84. Munson, P.B., et al., *Exosomal miR-16-5p as a target for malignant mesothelioma.* Scientific Reports, 2019. **9**(1): p. 11688.
85. Ahmadzada, T., et al., *Extracellular vesicles as biomarkers in malignant pleural mesothelioma: A review.* Critical Reviews in Oncology/Hematology, 2020. **150**: p. 102949.
86. Fang, S., et al., *Clinical application of a microfluidic chip for immunocapture and quantification of circulating exosomes to assist breast cancer diagnosis and molecular classification.* PLOS ONE, 2017. **12**(4): p. e0175050.
87. Kwizera, E.A., et al., *Molecular Detection and Analysis of Exosomes Using Surface-Enhanced Raman Scattering Gold Nanorods and a Miniaturized Device.* Theranostics, 2018. **8**(10): p. 2722-2738.

88. Cao, Y., et al., *Identification of programmed death ligand-1 positive exosomes in breast cancer based on DNA amplification-responsive metal-organic frameworks.* Biosensors and Bioelectronics, 2020. **166**: p. 112452.
89. Lu, F., et al., *The Clinical Application Value of RDW, CA153, and MPV in Breast Cancer.* Clinical Laboratory, 2021(2).
90. Lee, J.U., et al., *Quantitative and Specific Detection of Exosomal miRNAs for Accurate Diagnosis of Breast Cancer Using a Surface-Enhanced Raman Scattering Sensor Based on Plasmonic Head-Flocked Gold Nanopillars.* Small, 2019. **15**(17): p. 1804968.
91. Tian, F., et al., *Protein analysis of extracellular vesicles to monitor and predict therapeutic response in metastatic breast cancer.* Nature Communications, 2021. **12**(1): p. 2536.
92. Truong, Q., et al., *Glypican-1 as a Biomarker for Prostate Cancer: Isolation and Characterization.* J Cancer, 2016. **7**(8): p. 1002-9.
93. Zhou, C., et al., *Functional Implication of Exosomal miR-217 and miR-23b-3p in the Progression of Prostate Cancer.* OncoTargets and Therapy, 2020. **13**(null): p. 11595-11606.
94. Li, S., et al., *Exosomal ephrinA2 derived from serum as a potential biomarker for prostate cancer.* J Cancer, 2018. **9**(15): p. 2659-2665.
95. Zhou, Y.-G., et al., *Interrogating Circulating Microsomes and Exosomes Using Metal Nanoparticles.* Small, 2016. **12**(6): p. 727-732.
96. Zhu, S., et al., *Exosomal TUBB3 mRNA expression of metastatic castration-resistant prostate cancer patients: Association with patient outcome under abiraterone.* Cancer Medicine, 2021. **10**(18): p. 6282-6290.
97. Im, H., et al., *Label-free detection and molecular profiling of exosomes with a nano-plasmonic sensor.* Nature Biotechnology, 2014. **32**(5): p. 490-495.
98. Zhao, Z., et al., *A microfluidic ExoSearch chip for multiplexed exosome detection towards blood-based ovarian cancer diagnosis.* Lab on a Chip, 2016. **16**(3): p. 489-496.
99. Zhang, P., et al., *Ultrasensitive detection of circulating exosomes with a 3D-nanopatterned microfluidic chip.* Nature biomedical engineering, 2019. **3**(6): p. 438-451.
100. Liu, J., et al., *Plasma-derived exosomal miR-4732-5p is a promising noninvasive diagnostic biomarker for epithelial ovarian cancer.* Journal of Ovarian Research, 2021. **14**(1): p. 59.
101. Onukwugha, N.-E., Y.-T. Kang, and S. Nagrath, *Emerging micro-nano technologies for extracellular vesicles in immuno-oncology: from specific isolations to immunomodulation.* Lab on a Chip, 2022.
102. Gandham, S., et al., *Technologies and standardization in research on extracellular vesicles.* Trends in biotechnology, 2020. **38**(10): p. 1066-1098.
103. Wu, M., et al., *Isolation of exosomes from whole blood by integrating acoustics and microfluidics.* Proceedings of the National Academy of Sciences, 2017. **114**(40): p. 10584-10589.
104. Lin, S., et al., *Progress in Microfluidics‐Based Exosome Separation and Detection Technologies for Diagnostic Applications.* Small, 2020. **16**(9): p. 1903916.
105. Gámez-Valero, A., et al., *Size-Exclusion Chromatography-based isolation minimally alters Extracellular Vesicles' characteristics compared to precipitating agents.* Scientific reports, 2016. **6**(1): p. 1-9.
106. Böing, A.N., et al., *Single-step isolation of extracellular vesicles by size-exclusion chromatography.* Journal of extracellular vesicles, 2014. **3**(1): p. 23430.
107. de Menezes-Neto, A., et al., *Size-exclusion chromatography as a stand-alone methodology identifies novel markers in mass spectrometry analyses of plasma-derived vesicles from healthy individuals.* Journal of extracellular vesicles, 2015. **4**(1): p. 27378.
108. Livshits, M.A., et al., *Isolation of exosomes by differential centrifugation: Theoretical analysis of a commonly used protocol.* Scientific reports, 2015. **5**(1): p. 1-14.

109. Contreras-Naranjo, J.C., H.-J. Wu, and V.M. Ugaz, *Microfluidics for exosome isolation and analysis: enabling liquid biopsy for personalized medicine.* Lab on a Chip, 2017. **17**(21): p. 3558-3577.
110. Wang, X., et al., *A fluorescence assay for exosome detection based on bivalent cholesterol anchor triggered target conversion and enzyme-free signal amplification.* Analytical Chemistry, 2021. **93**(24): p. 8493-8500.
111. Yoshioka, Y., et al., *Ultra-sensitive liquid biopsy of circulating extracellular vesicles using ExoScreen.* Nature communications, 2014. **5**(1): p. 1-8.
112. Eldh, M., et al., *Importance of RNA isolation methods for analysis of exosomal RNA: evaluation of different methods.* Molecular immunology, 2012. **50**(4): p. 278-286.
113. Li, M., et al., *Analysis of the RNA content of the exosomes derived from blood serum and urine and its potential as biomarkers.* Philosophical Transactions of the Royal Society B: Biological Sciences, 2014. **369**(1652): p. 20130502.
114. Sidhom, K., P.O. Obi, and A. Saleem, *A review of exosomal isolation methods: is size exclusion chromatography the best option?* International journal of molecular sciences, 2020. **21**(18): p. 6466.
115. Lötvall, J., et al., *Minimal experimental requirements for definition of extracellular vesicles and their functions: a position statement from the International Society for Extracellular Vesicles*. 2014, Wiley Online Library.
116. Gorgun, C., et al., *Isolation and flow cytometry characterization of extracellular‐vesicle subpopulations derived from human mesenchymal stromal cells.* Current protocols in stem cell biology, 2019. **48**(1): p. e76.
117. Sharma, P., et al., *Immunoaffinity‐based isolation of melanoma cell‐derived exosomes from plasma of patients with melanoma.* Journal of extracellular vesicles, 2018. **7**(1): p. 1435138.
118. Campos-Silva, C., et al., *High sensitivity detection of extracellular vesicles immune-captured from urine by conventional flow cytometry.* Scientific reports, 2019. **9**(1): p. 1-12.
119. Gurunathan, S., et al., *Review of the Isolation, Characterization, Biological Function, and Multifarious Therapeutic Approaches of Exosomes.* Cells, 2019. **8**(4): p. 307.
120. Xu, H. and B.-C. Ye, *Integrated microfluidic platforms for tumor-derived exosome analysis.* TrAC Trends in Analytical Chemistry, 2022: p. 116860.
121. Robinson, H., et al. *Extracellular vesicles for precision medicine in prostate cancer–Is it ready for clinical translation?* in *Seminars in Cancer Biology*. 2023. Elsevier.
122. Willms, E., et al., *Extracellular vesicle heterogeneity: subpopulations, isolation techniques, and diverse functions in cancer progression.* Frontiers in immunology, 2018. **9**: p. 738.
123. Khosla, N.K., et al., *Simplifying the complex: accessible microfluidic solutions for contemporary processes within in vitro diagnostics.* Lab on a Chip, 2022. **22**(18): p. 3340-3360.
124. Berlanda, S.F., et al., *Recent advances in microfluidic technology for bioanalysis and diagnostics.* Analytical chemistry, 2020. **93**(1): p. 311-331.
125. Lopes, L.C., A. Santos, and P.R. Bueno, *An outlook on electrochemical approaches for molecular diagnostics assays and discussions on the limitations of miniaturized technologies for point-of-care devices.* Sensors and Actuators Reports, 2022. **4**: p. 100087.
126. Suea-Ngam, A., et al., *Enzyme-assisted nucleic acid detection for infectious disease diagnostics: moving toward the point-of-care.* ACS sensors, 2020. **5**(9): p. 2701-2723.
127. Whitesides, G.M., *The origins and the future of microfluidics.* nature, 2006. **442**(7101): p. 368-373.
128. Liga, A., et al., *Exosome isolation: a microfluidic road-map.* Lab on a Chip, 2015. **15**(11): p. 2388-2394.
129. Gomez-Marquez, J. and K. Hamad-Schifferli, *Local development of nanotechnology-based diagnostics.* Nature Nanotechnology, 2021. **16**(5): p. 484-486.
130. Howes, P.D., R. Chandrawati, and M.M. Stevens, *Colloidal nanoparticles as advanced biological sensors.* Science, 2014. **346**(6205): p. 1247390.

131. Bleeker, E.A., et al., *Considerations on the EU definition of a nanomaterial: science to support policy making.* Regulatory toxicology and pharmacology, 2013. **65**(1): p. 119-125.
132. Kairdolf, B.A., X. Qian, and S. Nie, *Bioconjugated nanoparticles for biosensing, in vivo imaging, and medical diagnostics.* Analytical chemistry, 2017. **89**(2): p. 1015-1031.
133. Malik, P., et al., *Nanobiosensors: concepts and variations.* International Scholarly Research Notices, 2013. **2013**.
134. Ramesh, M., et al., *Nanotechnology-Enabled Biosensors: A Review of Fundamentals, Design Principles, Materials, and Applications.* Biosensors (Basel), 2022. **13**(1).
135. Mehrotra, P., *Biosensors and their applications–A review.* Journal of oral biology and craniofacial research, 2016. **6**(2): p. 153-159.
136. Chamorro-Garcia, A. and A. Merkoçi, *Nanobiosensors in diagnostics.* Nanobiomedicine, 2016. **3**: p. 1849543516663574.
137. Jeong, S., et al., *Integrated magneto–electrochemical sensor for exosome analysis.* ACS nano, 2016. **10**(2): p. 1802-1809.
138. Attaallah, R., et al., *Nanobiosensors for bioclinical applications: pros and cons.* Green Nanoparticles: Synthesis and Biomedical Applications, 2020: p. 117-149.
139. Aro, K., et al., *Saliva liquid biopsy for point-of-care applications.* Frontiers in public health, 2017. **5**: p. 77.
140. Fu, H., et al., *A paper-based microfluidic platform with shape-memory-polymer-actuated fluid valves for automated multi-step immunoassays.* Microsystems & nanoengineering, 2019. **5**(1): p. 1-12.
141. Zhao, C. and X. Liu, *A portable paper-based microfluidic platform for multiplexed electrochemical detection of human immunodeficiency virus and hepatitis C virus antibodies in serum.* Biomicrofluidics, 2016. **10**(2): p. 024119.
142. Dincer, C., et al., *Multiplexed Point-of-Care Testing – xPOCT.* Trends in Biotechnology, 2017. **35**(8): p. 728-742.
143. Vashist, S.K., *Point-of-care diagnostics: Recent advances and trends.* Biosensors, 2017. **7**(4): p. 62.
144. Syedmoradi, L., et al., *Point of care testing: The impact of nanotechnology.* Biosensors and Bioelectronics, 2017. **87**: p. 373-387.
145. Gaikwad, P.S. and R. Banerjee, *Advances in point-of-care diagnostic devices in cancers.* Analyst, 2018. **143**(6): p. 1326-1348.
146. Geng, H., et al., *Noble Metal Nanoparticle Biosensors: From Fundamental Studies toward Point-of-Care Diagnostics.* Accounts of Chemical Research, 2022. **55**(5): p. 593-604.
147. Sivaram, A.J., et al., *Recent advances in the generation of antibody–nanomaterial conjugates.* Advanced healthcare materials, 2018. **7**(1): p. 1700607.
148. Montenegro, J.-M., et al., *Controlled antibody/(bio-) conjugation of inorganic nanoparticles for targeted delivery.* Advanced drug delivery reviews, 2013. **65**(5): p. 677-688.
149. Peterson, V.M., et al., *Orthogonal amplification of nanoparticles for improved diagnostic sensing.* ACS nano, 2012. **6**(4): p. 3506-3513.
150. Saha, B., et al., *The influence of covalent immobilization conditions on antibody accessibility on nanoparticles.* Analyst, 2017. **142**(22): p. 4247-4256.
151. Haun, J.B., et al., *Magnetic nanoparticle biosensors.* WIREs Nanomedicine and Nanobiotechnology, 2010. **2**(3): p. 291-304.
152. Tamanaha, C.R., et al., *Magnetic labeling, detection, and system integration.* Biosensors and Bioelectronics, 2008. **24**(1): p. 1-13.
153. Konry, T., et al., *Particles and microfluidics merged: perspectives of highly sensitive diagnostic detection.* Microchimica Acta, 2012. **176**(3): p. 251-269.
154. Valentini, F., M. Carbone, and G. Palleschi, *Carbon nanostructured materials for applications in nano-medicine, cultural heritage, and electrochemical biosensors.* Analytical and Bioanalytical Chemistry, 2013. **405**(2): p. 451-465.

155. Vamvakaki, V. and N.A. Chaniotakis, *Carbon nanostructures as transducers in biosensors.* Sensors and Actuators B: Chemical, 2007. **126**(1): p. 193-197.
156. Battigelli, A., et al., *Endowing carbon nanotubes with biological and biomedical properties by chemical modifications.* Advanced Drug Delivery Reviews, 2013. **65**(15): p. 1899-1920.
157. Ménard-Moyon, C., et al., *Functionalized Carbon Nanotubes for Probing and Modulating Molecular Functions.* Chemistry & Biology, 2010. **17**(2): p. 107-115.
158. Wang, J., *Carbon-Nanotube Based Electrochemical Biosensors: A Review.* Electroanalysis, 2005. **17**(1): p. 7-14.
159. Le Goff, A., M. Holzinger, and S. Cosnier, *Enzymatic biosensors based on SWCNT-conducting polymer electrodes.* Analyst, 2011. **136**(7): p. 1279-1287.
160. Li, Y., H.J. Schluesener, and S. Xu, *Gold nanoparticle-based biosensors.* Gold Bulletin, 2010. **43**(1): p. 29-41.
161. Biju, V., *Chemical modifications and bioconjugate reactions of nanomaterials for sensing, imaging, drug delivery and therapy.* Chemical Society Reviews, 2014. **43**(3): p. 744-764.
162. Hao, E., G.C. Schatz, and J.T. Hupp, *Synthesis and Optical Properties of Anisotropic Metal Nanoparticles.* Journal of Fluorescence, 2004. **14**(4): p. 331-341.
163. Kelly, K.L., et al., *The Optical Properties of Metal Nanoparticles: The Influence of Size, Shape, and Dielectric Environment.* The Journal of Physical Chemistry B, 2003. **107**(3): p. 668-677.
164. Chen, S., et al., *Plasmon-Enhanced Colorimetric ELISA with Single Molecule Sensitivity.* Nano Letters, 2011. **11**(4): p. 1826-1830.
165. Hossain, M.K., et al., *Characteristics of surface-enhanced Raman scattering and surface-enhanced fluorescence using a single and a double layer gold nanostructure.* Physical Chemistry Chemical Physics, 2009. **11**(34): p. 7484-7490.
166. Lim, D.-K., et al., *Highly uniform and reproducible surface-enhanced Raman scattering from DNA-tailorable nanoparticles with 1-nm interior gap.* Nature Nanotechnology, 2011. **6**(7): p. 452-460.
167. Saha, K., et al., *Gold Nanoparticles in Chemical and Biological Sensing.* Chemical Reviews, 2012. **112**(5): p. 2739-2779.
168. Murray, C.B., D.J. Norris, and M.G. Bawendi, *Synthesis and characterization of nearly monodisperse CdE (E = sulfur, selenium, tellurium) semiconductor nanocrystallites.* Journal of the American Chemical Society, 1993. **115**(19): p. 8706-8715.
169. Resch-Genger, U., et al., *Quantum dots versus organic dyes as fluorescent labels.* Nature Methods, 2008. **5**(9): p. 763-775.
170. Clapp, A.R., I.L. Medintz, and H. Mattoussi, *Förster Resonance Energy Transfer Investigations Using Quantum-Dot Fluorophores.* ChemPhysChem, 2006. **7**(1): p. 47-57.
171. Zhang, C.-Y., et al., *Single-quantum-dot-based DNA nanosensor.* Nature Materials, 2005. **4**(11): p. 826-831.
172. Freeman, R., J. Girsh, and I. Willner, *Nucleic Acid/Quantum Dots (QDs) Hybrid Systems for Optical and Photoelectrochemical Sensing.* ACS Applied Materials & Interfaces, 2013. **5**(8): p. 2815-2834.
173. Dyadyusha, L., et al., *Quenching of CdSe quantum dot emission, a new approach for biosensing.* Chemical Communications, 2005(25): p. 3201-3203.
174. Dai, Z., et al., *Adaption of Au Nanoparticles and CdTe Quantum Dots in DNA Detection* *Supported by the Natural Science Foundation of Tianjin(Nos.06TXTJJC14400, 07JCYBJC15900) and Young Teacher Foundation of Tianjin Polytechnic University (No.029624).* Chinese Journal of Chemical Engineering, 2007. **15**(6): p. 791-794.
175. Ha, T. and P. Tinnefeld, *Photophysics of fluorescent probes for single-molecule biophysics and super-resolution imaging.* Annual review of physical chemistry, 2012. **63**(1): p. 595-617.
176. Stennett, E.M., M.A. Ciuba, and M. Levitus, *Photophysical processes in single molecule organic fluorescent probes.* Chemical Society Reviews, 2014. **43**(4): p. 1057-1075.

177. Bao, G., et al., *Learning from lanthanide complexes: The development of dye-lanthanide nanoparticles and their biomedical applications.* Coordination Chemistry Reviews, 2021. **429**: p. 213642.
178. Wang, Y., et al., *Remote manipulation of upconversion luminescence.* Chemical Society Reviews, 2018. **47**(17): p. 6473-6485.
179. Lu, Y., et al., *Tunable lifetime multiplexing using luminescent nanocrystals.* Nature Photonics, 2014. **8**(1): p. 32-36.
180. Michalet, X., et al., *Quantum dots for live cells, in vivo imaging, and diagnostics.* science, 2005. **307**(5709): p. 538-544.
181. Genovese, D., et al., *Energy transfer processes in dye-doped nanostructures yield cooperative and versatile fluorescent probes.* Nanoscale, 2014. **6**(6): p. 3022-3036.
182. Gnach, A. and A. Bednarkiewicz, *Lanthanide-doped up-converting nanoparticles: Merits and challenges.* Nano Today, 2012. **7**(6): p. 532-563.
183. Reisch, A. and A.S. Klymchenko, *Fluorescent Polymer Nanoparticles Based on Dyes: Seeking Brighter Tools for Bioimaging.* Small, 2016. **12**(15): p. 1968-1992.
184. Li, K. and B. Liu, *Polymer-encapsulated organic nanoparticles for fluorescence and photoacoustic imaging.* Chemical Society Reviews, 2014. **43**(18): p. 6570-6597.
185. Méallet-Renault, R., et al., *Fluorescent nanoparticles as selective Cu (II) sensors.* Photochemical & Photobiological Sciences, 2006. **5**: p. 300-310.
186. Reisch, A., et al., *Collective fluorescence switching of counterion-assembled dyes in polymer nanoparticles.* Nature Communications, 2014. **5**(1): p. 4089.
187. Eliseeva, S.V. and J.-C.G. Bünzli, *Lanthanide luminescence for functional materials and bio-sciences.* Chemical Society Reviews, 2010. **39**(1): p. 189-227.
188. Bünzli, J.-C.G., *Lanthanide Luminescence for Biomedical Analyses and Imaging.* Chemical Reviews, 2010. **110**(5): p. 2729-2755.
189. Cheignon, C., et al., *Dye-sensitized lanthanide containing nanoparticles for luminescence based applications.* Nanoscale, 2022. **14**(38): p. 13915-13949.
190. Bünzli, J.-C.G. and C. Piguet, *Taking advantage of luminescent lanthanide ions.* Chemical Society Reviews, 2005. **34**(12): p. 1048-1077.
191. Butler, S.J., et al., *EuroTracker® dyes: design, synthesis, structure and photophysical properties of very bright europium complexes and their use in bioassays and cellular optical imaging.* Dalton Transactions, 2015. **44**(11): p. 4791-4803.
192. Garfield, D.J., et al., *Enrichment of molecular antenna triplets amplifies upconverting nanoparticle emission.* Nature Photonics, 2018. **12**(7): p. 402-407.
193. Hardy, D.A., et al., *Structure–Function Correlation: Engineering High Quantum Yields in Down-Shifting Nanophosphors.* Journal of the American Chemical Society, 2019. **141**(51): p. 20416-20423.
194. Sun, G., et al., *Lanthanide upconversion and downshifting luminescence for biomolecules detection.* Nanoscale Horizons, 2021. **6**(10): p. 766-780.
195. I, Y.L., et al., *808 nm light triggered lanthanide nanoprobes with enhanced down-shifting emission beyond 1500 nm for imaging-guided resection surgery of tumor and vascular visualization.* Theranostics, 2020. **10**(15): p. 6875-6885.
196. Liang, L., et al., *Continuous-wave near-infrared stimulated-emission depletion microscopy using downshifting lanthanide nanoparticles.* Nature Nanotechnology, 2021. **16**(9): p. 975-980.
197. Shao, W., et al., *Dramatic enhancement of quantum cutting in lanthanide-doped nanocrystals photosensitized with an aggregation-induced enhanced emission dye.* Nano Letters, 2018. **18**(8): p. 4922-4926.
198. Wisser, M.D., et al., *Improving quantum yield of upconverting nanoparticles in aqueous media via emission sensitization.* Nano letters, 2018. **18**(4): p. 2689-2695.

199. Wang, Z. and A. Meijerink, *Dye-sensitized downconversion.* The journal of physical chemistry letters, 2018. **9**(7): p. 1522-1526.
200. Chen, G., et al., *Efficient broadband upconversion of near-infrared light in dye-sensitized core/shell nanocrystals.* Advanced Optical Materials, 2016. **4**(11): p. 1760-1766.
201. Wang, F., et al., *Simultaneous phase and size control of upconversion nanocrystals through lanthanide doping.* nature, 2010. **463**(7284): p. 1061-1065.
202. Chen, G., et al., *Upconversion nanoparticles: design, nanochemistry, and applications in theranostics.* Chemical reviews, 2014. **114**(10): p. 5161-5214.
203. Loo, J.F.-C., et al., *Upconversion and downconversion nanoparticles for biophotonics and nanomedicine.* Coordination Chemistry Reviews, 2019. **400**: p. 213042.
204. Gerelkhuu, Z., Y.I. Lee, and T.H. Yoon, *Upconversion Nanomaterials in Bioimaging and Biosensor Applications and Their Biological Response.* Nanomaterials (Basel), 2022. **12**(19).
205. Liu, C., et al., *Single-Exosome-Counting Immunoassays for Cancer Diagnostics.* Nano Letters, 2018. **18**(7): p. 4226-4232.
206. Lin, B., et al., *Microfluidic-Based Exosome Analysis for Liquid Biopsy.* Small Methods, 2021. **5**(3): p. 2001131.
207. Cordonnier, M., et al., *Exosomes in cancer theranostic: Diamonds in the rough.* Cell Adhesion & Migration, 2017. **11**(2): p. 151-163.
208. Zhang, Y., et al., *Exosomes: biogenesis, biologic function and clinical potential.* Cell & bioscience, 2019. **9**(1): p. 1-18.
209. Huang, X., et al., *Characterization of human plasma-derived exosomal RNAs by deep sequencing.* BMC genomics, 2013. **14**(1): p. 1-14.
210. Boriachek, K., et al., *Biological functions and current advances in isolation and detection strategies for exosome nanovesicles.* Small, 2018. **14**(6): p. 1702153.
211. Im, H., et al., *Novel nanosensing technologies for exosome detection and profiling.* Lab on a Chip, 2017. **17**(17): p. 2892-2898.
212. Taylor, M.L., et al., *Nanomaterials for Molecular Detection and Analysis of Extracellular Vesicles.* Nanomaterials (Basel), 2023. **13**(3).
213. Kwon, Y. and J. Park, *Methods to analyze extracellular vesicles at single particle level.* Micro and Nano Systems Letters, 2022. **10**(1): p. 14.
214. Amrhein, K., et al., *Dual Imaging Single Vesicle Surface Protein Profiling and Early Cancer Detection.* ACS applied materials & interfaces, 2023. **15**(2): p. 2679-2692.
215. Oliveira-Rodríguez, M., et al., *Development of a rapid lateral flow immunoassay test for detection of exosomes previously enriched from cell culture medium and body fluids.* Journal of extracellular vesicles, 2016. **5**(1): p. 31803.
216. Lobb, R.J., et al., *Optimized exosome isolation protocol for cell culture supernatant and human plasma.* Journal of extracellular vesicles, 2015. **4**(1): p. 27031.
217. Son, K.J., et al., *Microfluidic compartments with sensing microbeads for dynamic monitoring of cytokine and exosome release from single cells.* Analyst, 2016. **141**(2): p. 679-688.
218. Liang, L.-G., et al., *An integrated double-filtration microfluidic device for isolation, enrichment and quantification of urinary extracellular vesicles for detection of bladder cancer.* Scientific reports, 2017. **7**(1): p. 1-10.
219. Hisey, C.L., et al., *Microfluidic affinity separation chip for selective capture and release of label-free ovarian cancer exosomes.* Lab on a Chip, 2018. **18**(20): p. 3144-3153.
220. Wang, Y., et al., *Rapid differentiation of host and parasitic exosome vesicles using microfluidic photonic crystal biosensor.* ACS sensors, 2018. **3**(9): p. 1616-1621.
221. Issadore, D., et al., *Miniature magnetic resonance system for point-of-care diagnostics.* Lab on a Chip, 2011. **11**(13): p. 2282-2287.
222. Zhang, P., M. He, and Y. Zeng, *Ultrasensitive microfluidic analysis of circulating exosomes using a nanostructured graphene oxide/polydopamine coating.* Lab on a Chip, 2016. **16**(16): p. 3033-3042.

223. Kanwar, S.S., et al., *Microfluidic device (ExoChip) for on-chip isolation, quantification and characterization of circulating exosomes.* Lab on a Chip, 2014. **14**(11): p. 1891-1900.
224. Fang, S., et al., *Clinical application of a microfluidic chip for immunocapture and quantification of circulating exosomes to assist breast cancer diagnosis and molecular classification.* PloS one, 2017. **12**(4): p. e0175050.
225. Zhao, W., et al., *Microsphere mediated exosome isolation and ultra-sensitive detection on a dielectrophoresis integrated microfluidic device.* Analyst, 2021. **146**(19): p. 5962-5972.
226. Lu, Y., et al., *Integrated microfluidic system for isolating exosome and analyzing protein marker PD-L1.* Biosensors and Bioelectronics, 2022. **204**: p. 113879.
227. Bai, Y., et al., *Rapid Isolation and Multiplexed Detection of Exosome Tumor Markers Via Queued Beads Combined with Quantum Dots in a Microarray.* Nano-Micro Letters, 2019. **11**(1): p. 59.
228. Dobhal, G., et al., *Cadmium-free quantum dots as fluorescent labels for exosomes.* Sensors, 2018. **18**(10): p. 3308.
229. Zong, S., et al., *Single molecule localization imaging of exosomes using blinking silicon quantum dots.* Nanotechnology, 2018. **29**(6): p. 065705.
230. Jiang, X., et al., *Gold–carbon dots for the intracellular imaging of cancer-derived exosomes.* Nanotechnology, 2018. **29**(17): p. 175701.
231. He, F., et al., *Quantification of Exosome Based on a Copper-Mediated Signal Amplification Strategy.* Analytical Chemistry, 2018. **90**(13): p. 8072-8079.
232. Gao, M.-L., B.-C. Yin, and B.-C. Ye, *Construction of a DNA-AuNP-based satellite network for exosome analysis.* Analyst, 2019. **144**(20): p. 5996-6003.
233. Zhang, J., et al., *A ratiometric electrochemical biosensor for the exosomal microRNAs detection based on bipedal DNA walkers propelled by locked nucleic acid modified toehold mediate strand displacement reaction.* Biosensors and Bioelectronics, 2018. **102**: p. 33-40.
234. Lee, L.J., et al., *Extracellular mRNA detected by tethered lipoplex nanoparticle biochip for lung adenocarcinoma detection.* American journal of respiratory and critical care medicine, 2016. **193**(12): p. 1431-1433.
235. Liu, C., et al., *Non-invasive detection of exosomal MicroRNAs via tethered cationic lipoplex nanoparticles (tCLN) biochip for lung cancer early detection.* Frontiers in genetics, 2020. **11**.
236. Hu, J., et al., *Overhang molecular beacons encapsulated in tethered cationic lipoplex nanoparticles for detection of single-point mutation in extracellular vesicle-associated RNAs.* Biomaterials, 2018. **183**: p. 20-29.
237. Cao, H., X. Zhou, and Y. Zeng, *Microfluidic exponential rolling circle amplification for sensitive microRNA detection directly from biological samples.* Sensors and Actuators B: Chemical, 2019. **279**: p. 447-457.
238. Lee, J.H., et al., *Simultaneous and multiplexed detection of exosome microRNAs using molecular beacons.* Biosensors and Bioelectronics, 2016. **86**: p. 202-210.
239. Lee, J.H., et al., *In situ single step detection of exosome microRNA using molecular beacon.* Biomaterials, 2015. **54**: p. 116-125.
240. Hu, J., et al., *A signal-amplifiable biochip quantifies extracellular vesicle-associated RNAs for early cancer detection.* Nature communications, 2017. **8**(1): p. 1683.
241. Yang, Y., et al., *An immuno-biochip selectively captures tumor-derived exosomes and detects exosomal RNAs for cancer diagnosis.* ACS applied materials & interfaces, 2018. **10**(50): p. 43375-43386.
242. Li, G., W. Tang, and F. Yang, *Cancer liquid biopsy using integrated microfluidic exosome analysis platforms.* Biotechnology Journal, 2020. **15**(5): p. 1900225.
243. Xia, Y., et al., *A visible and colorimetric aptasensor based on DNA-capped single-walled carbon nanotubes for detection of exosomes.* Biosensors and Bioelectronics, 2017. **92**: p. 8-15.

244. Wang, Y.-M., et al., *Enhancement of the Intrinsic Peroxidase-Like Activity of Graphitic Carbon Nitride Nanosheets by ssDNAs and Its Application for Detection of Exosomes.* Analytical Chemistry, 2017. **89**(22): p. 12327-12333.
245. Martín-Gracia, B., et al., *Nanoparticle-based biosensors for detection of extracellular vesicles in liquid biopsies.* Journal of Materials Chemistry B, 2020. **8**(31): p. 6710-6738.
246. Ko, J., E. Carpenter, and D. Issadore, *Detection and isolation of circulating exosomes and microvesicles for cancer monitoring and diagnostics using micro-/nano-based devices.* Analyst, 2016. **141**(2): p. 450-460.
247. He, F., et al., *Direct exosome quantification via bivalent-cholesterol-labeled DNA anchor for signal amplification.* Analytical chemistry, 2017. **89**(23): p. 12968-12975.
248. Zhang, Y., et al., *Sensitive multicolor visual detection of exosomes via dual signal amplification strategy of enzyme-catalyzed metallization of Au nanorods and hybridization chain reaction.* ACS sensors, 2019. **4**(12): p. 3210-3218.
249. Boriachek, K., et al., *Avoiding pre-isolation step in exosome analysis: direct isolation and sensitive detection of exosomes using gold-loaded nanoporous ferric oxide nanozymes.* Analytical chemistry, 2019. **91**(6): p. 3827-3834.
250. Gholizadeh, S., et al., *Microfluidic approaches for isolation, detection, and characterization of extracellular vesicles: current status and future directions.* Biosensors and Bioelectronics, 2017. **91**: p. 588-605.
251. Chen, Z., et al., *Detection of exosomes by ZnO nanowires coated three-dimensional scaffold chip device.* Biosensors and Bioelectronics, 2018. **122**: p. 211-216.
252. Woo, H., et al., *ACS Nano 2017, 11, 1360–1370*. DOI.
253. Woo, H.-K., et al., *Exodisc for rapid, size-selective, and efficient isolation and analysis of nanoscale extracellular vesicles from biological samples.* ACS nano, 2017. **11**(2): p. 1360-1370.
254. Liang, L.-G., et al., *An integrated double-filtration microfluidic device for isolation, enrichment and quantification of urinary extracellular vesicles for detection of bladder cancer.* Scientific Reports, 2017. **7**(1): p. 46224.
255. Xu, L., et al., *Optical, electrochemical and electrical (nano) biosensors for detection of exosomes: a comprehensive overview.* Biosensors and Bioelectronics, 2020. **161**: p. 112222.
256. Kaushal, S., et al., *Strategies for the development of metallic‐nanoparticle‐based label‐free biosensors and their biomedical applications.* ChemBioChem, 2020. **21**(5): p. 576-600.
257. Alim, S., et al., *Recent uses of carbon nanotubes & gold nanoparticles in electrochemistry with application in biosensing: A review.* Biosensors and Bioelectronics, 2018. **121**: p. 125-136.
258. Boriachek, K., et al., *Quantum dot-based sensitive detection of disease specific exosome in serum.* Analyst, 2017. **142**(12): p. 2211-2219.
259. Boriachek, K., et al., *Avoiding Pre-Isolation Step in Exosome Analysis: Direct Isolation and Sensitive Detection of Exosomes Using Gold-Loaded Nanoporous Ferric Oxide Nanozymes.* Analytical Chemistry, 2019. **91**(6): p. 3827-3834.
260. Doldán, X., et al., *Electrochemical sandwich immunosensor for determination of exosomes based on surface marker-mediated signal amplification.* Analytical chemistry, 2016. **88**(21): p. 10466-10473.
261. Zhou, Q., et al., *Development of an aptasensor for electrochemical detection of exosomes.* Methods, 2016. **97**: p. 88-93.
262. Wang, S., et al., *Aptasensor with expanded nucleotide using DNA nanotetrahedra for electrochemical detection of cancerous exosomes.* ACS nano, 2017. **11**(4): p. 3943-3949.
263. Wang, F., et al., *Precise Molecular Profiling of Circulating Exosomes Using a Metal–Organic Framework-Based Sensing Interface and an Enzyme-Based Electrochemical Logic Platform.* Analytical Chemistry, 2022. **94**(2): p. 875-883.
264. Wang, S., et al., *Aptasensor with Expanded Nucleotide Using DNA Nanotetrahedra for Electrochemical Detection of Cancerous Exosomes.* ACS Nano, 2017. **11**(4): p. 3943-3949.

265. Xu, X., et al., *Near‐field enhanced plasmonic‐magnetic bifunctional nanotubes for single cell bioanalysis.* Advanced Functional Materials, 2013. **23**(35): p. 4332-4338.
266. Le Ru, E.C., et al., *Surface enhanced Raman scattering enhancement factors: a comprehensive study.* The Journal of Physical Chemistry C, 2007. **111**(37): p. 13794-13803.
267. Song, F., et al., *Enrichment-Detection Integrated Exosome Profiling Biosensors Promising for Early Diagnosis of Cancer*. 2021, ACS Publications.
268. Fu, J.H., et al., *SERS‐active MIL‐100 (Fe) sensory array for ultrasensitive and multiplex detection of VOCs.* Angewandte Chemie, 2020. **132**(46): p. 20670-20679.
269. Tao, L., et al., *1T′ transition metal telluride atomic layers for plasmon-free SERS at femtomolar levels.* Journal of the American Chemical Society, 2018. **140**(28): p. 8696-8704.
270. Zong, S., et al., *Facile detection of tumor-derived exosomes using magnetic nanobeads and SERS nanoprobes.* Analytical Methods, 2016. **8**(25): p. 5001-5008.
271. Wang, Z., et al., *Screening and multiple detection of cancer exosomes using an SERS-based method.* Nanoscale, 2018. **10**(19): p. 9053-9062.
272. Lee, C., et al., *3D plasmonic nanobowl platform for the study of exosomes in solution.* Nanoscale, 2015. **7**(20): p. 9290-9297.
273. Dong, S., et al., *Beehive-Inspired Macroporous SERS Probe for Cancer Detection through Capturing and Analyzing Exosomes in Plasma.* ACS Applied Materials & Interfaces, 2020. **12**(4): p. 5136-5146.
274. Liu, Z., et al., *Microfluidics for production of particles: mechanism, methodology, and applications.* Small, 2020. **16**(9): p. 1904673.
275. Kang, Y.T., et al., *Isolation and profiling of circulating tumor‐associated exosomes using extracellular vesicular lipid‐protein binding affinity based microfluidic device.* Small, 2019. **15**(47): p. 1903600.
276. Zhao, Y., et al., *A microfluidic surface-enhanced Raman scattering (SERS) sensor for microRNA in extracellular vesicles with nucleic acid-tyramine cascade amplification.* Chinese Chemical Letters, 2022. **33**(4): p. 2101-2104.
277. De La Escosura-Muniz, A., C. Parolo, and A. Merkoçi, *Immunosensing using nanoparticles.* Materials today, 2010. **13**(7-8): p. 24-34.
278. Grasso, L., et al., *Molecular screening of cancer-derived exosomes by surface plasmon resonance spectroscopy.* Analytical and bioanalytical chemistry, 2015. **407**: p. 5425-5432.
279. Homola, J., *Surface plasmon resonance sensors for detection of chemical and biological species.* Chemical reviews, 2008. **108**(2): p. 462-493.
280. Zhu, L., et al., *Label-free quantitative detection of tumor-derived exosomes through surface plasmon resonance imaging.* Analytical chemistry, 2014. **86**(17): p. 8857-8864.
281. Sina, A.A.I., et al., *Real time and label free profiling of clinically relevant exosomes.* Scientific reports, 2016. **6**(1): p. 30460.
282. Rupert, D.L., et al., *Determination of exosome concentration in solution using surface plasmon resonance spectroscopy.* Analytical chemistry, 2014. **86**(12): p. 5929-5936.
283. Di Noto, G., et al., *Merging colloidal nanoplasmonics and surface plasmon resonance spectroscopy for enhanced profiling of multiple myeloma-derived exosomes.* Biosensors and Bioelectronics, 2016. **77**: p. 518-524.
284. Zhu, F., et al., *Microfluidics-based technologies for the analysis of extracellular vesicles at the single-cell level and single-vesicle level.* Chinese Chemical Letters, 2021.
285. Ko, J., et al., *Sequencing-based protein analysis of single extracellular vesicles.* ACS nano, 2021. **15**(3): p. 5631-5638.
286. Salipante, S.J. and K.R. Jerome, *Digital PCR—an emerging technology with broad applications in microbiology.* Clinical chemistry, 2020. **66**(1): p. 117-123.
287. Coccaro, N., et al., *Digital PCR: a reliable tool for analyzing and monitoring hematologic malignancies.* International journal of molecular sciences, 2020. **21**(9): p. 3141.

288. Akama, K., K. Shirai, and S. Suzuki, *Droplet-free digital enzyme-linked immunosorbent assay based on a tyramide signal amplification system.* Analytical chemistry, 2016. **88**(14): p. 7123-7129.
289. Wu, C., T.J. Dougan, and D.R. Walt, *High-Throughput, High-Multiplex Digital Protein Detection with Attomolar Sensitivity.* ACS nano, 2022. **16**(1): p. 1025-1035.
290. Lin, B., et al., *Tracing Tumor‐Derived Exosomal PD‐L1 by Dual‐Aptamer Activated Proximity‐Induced Droplet Digital PCR.* Angewandte Chemie International Edition, 2021. **60**(14): p. 7582-7586.
291. Yang, Z., et al., *Ultrasensitive Single Extracellular Vesicle Detection Using High Throughput Droplet Digital Enzyme-Linked Immunosorbent Assay.* Nano Letters, 2022.
292. Chang, L., et al., *Single molecule enzyme-linked immunosorbent assays: theoretical considerations.* Journal of immunological methods, 2012. **378**(1-2): p. 102-115.
293. Fraser, K., et al., *Characterization of single microvesicles in plasma from glioblastoma patients.* Neuro-oncology, 2019. **21**(5): p. 606-615.
294. Wu, D., et al., *Profiling surface proteins on individual exosomes using a proximity barcoding assay.* Nature communications, 2019. **10**(1): p. 1-10.
295. Lee, K., et al., *Multiplexed profiling of single extracellular vesicles.* ACS nano, 2018. **12**(1): p. 494-503.
296. Raghu, D., et al., *Nanoplasmonic pillars engineered for single exosome detection.* PloS one, 2018. **13**(8): p. e0202773.
297. Yang, Z., et al., *Ultrasensitive Single Extracellular Vesicle Detection Using High Throughput Droplet Digital Enzyme-Linked Immunosorbent Assay.* Nano Letters, 2022. **22**(11): p. 4315-4324.
298. Martín-Gracia, B., et al., *Nanoparticle-based biosensors for detection of extracellular vesicles in liquid biopsies.* Journal of Materials Chemistry B, 2020. **8**(31): p. 6710-6738.
299. Liu, J., et al., *A lateral flow assay for the determination of human tetanus antibody in whole blood by using gold nanoparticle labeled tetanus antigen.* Microchimica Acta, 2018. **185**(2): p. 1-7.
300. Lu, Z., et al., *Rapid diagnostic testing platform for iron and vitamin A deficiency.* Proceedings of the National Academy of Sciences, 2017. **114**(51): p. 13513-13518.
301. Hsieh, H.V., J.L. Dantzler, and B.H. Weigl, *Analytical tools to improve optimization procedures for lateral flow assays.* Diagnostics, 2017. **7**(2): p. 29.
302. Koczula, K.M. and A. Gallotta, *Lateral flow assays.* Essays in biochemistry, 2016. **60**(1): p. 111-120.
303. López-Cobo, S., et al., *Immunoassays for scarce tumour-antigens in exosomes: detection of the human NKG2D-Ligand, MICA, in tetraspanin-containing nanovesicles from melanoma.* Journal of nanobiotechnology, 2018. **16**: p. 1-12.
304. Oliveira-Rodríguez, M., et al., *Point-of-care detection of extracellular vesicles: Sensitivity optimization and multiple-target detection.* Biosensors and Bioelectronics, 2017. **87**: p. 38-45.
305. Moyano, A., et al., *Magnetic Lateral Flow Immunoassay for Small Extracellular Vesicles Quantification: Application to Colorectal Cancer Biomarker Detection.* Sensors, 2021. **21**(11): p. 3756.
306. Dong, D., et al., *Simple and rapid extracellular vesicles quantification via membrane biotinylation strategy coupled with fluorescent nanospheres-based lateral flow assay.* Talanta, 2019. **200**: p. 408-414.
307. Wang, B., et al., *Nanozyme-Based Lateral Flow Immunoassay (LFIA) for Extracellular Vesicle Detection.* Biosensors (Basel), 2022. **12**(7).
308. Wu, T., et al., *Enhanced lateral flow assay with double conjugates for the detection of exosomes.* Science China Chemistry, 2018. **61**: p. 1423-1429.
309. Kim, S., et al., *DNA barcode-based detection of exosomal microRNAs using nucleic acid lateral flow assays for the diagnosis of colorectal cancer.* Talanta, 2022. **242**: p. 123306.

310. Yu, Q., et al., *Development of a lateral flow aptamer assay strip for facile identification of theranostic exosomes isolated from human lung carcinoma cells.* Analytical biochemistry, 2020. **594**: p. 113591.
311. Choi, D.H., et al., *A dual gold nanoparticle conjugate-based lateral flow assay (LFA) method for the analysis of troponin I.* Biosensors and Bioelectronics, 2010. **25**(8): p. 1999-2002.
312. Lee, S., S. Mehta, and D. Erickson, *Two-color lateral flow assay for multiplex detection of causative agents behind acute febrile illnesses.* Analytical chemistry, 2016. **88**(17): p. 8359-8363.
313. Wang, F., et al., *Microscopic inspection and tracking of single upconversion nanoparticles in living cells.* Light: Science & Applications, 2018. **7**(4): p. 18007-18007.
314. Pei, P., et al., *X-ray-activated persistent luminescence nanomaterials for NIR-II imaging.* Nature Nanotechnology, 2021. **16**(9): p. 1011-1018.
315. Pei, P., et al., *NIR-II ratiometric lanthanide-dye hybrid nanoprobes doped bioscaffolds for in situ bone repair monitoring.* Nano Letters, 2022. **22**(2): p. 783-791.
316. Wang, F., et al., *Upconversion nanoparticles in biological labeling, imaging, and therapy.* Analyst, 2010. **135**(8): p. 1839-1854.
317. Liao, J., et al., *Optical fingerprint classification of single upconversion nanoparticles by deep learning.* The Journal of Physical Chemistry Letters, 2021. **12**(41): p. 10242-10248.
318. Wang, W., et al., *Smartphone enabled upconversion nanoparticle-based lateral flow strip for ultra-low concentration of methamphetamine detection.* Sensors and Actuators B: Chemical, 2022. **370**: p. 132421.
319. Ji, T., et al., *Point of care upconversion nanoparticles-based lateral flow assay quantifying myoglobin in clinical human blood samples.* Sensors and Actuators B: Chemical, 2019. **282**: p. 309-316.
320. Bayoumy, S., et al., *Sensitive and quantitative detection of cardiac troponin I with upconverting nanoparticle lateral flow test with minimized interference.* Scientific Reports, 2021. **11**(1): p. 18698.
321. Martiskainen, I., et al., *Upconverting nanoparticle reporter–based highly sensitive rapid lateral flow immunoassay for hepatitis B virus surface antigen.* Analytical and Bioanalytical Chemistry, 2021. **413**(4): p. 967-978.
322. Liu, Y., et al., *Ultrasensitive and Highly Specific Lateral Flow Assays for Point-of-Care Diagnosis.* ACS Nano, 2021. **15**(3): p. 3593-3611.
323. Dong, S., et al., *Beehive-inspired macroporous SERS probe for cancer detection through capturing and analyzing exosomes in plasma.* ACS applied materials & interfaces, 2020. **12**(4): p. 5136-5146.
324. Moyano, A., et al., *Magnetic lateral flow immunoassay for small extracellular vesicles quantification: application to colorectal cancer biomarker detection.* Sensors, 2021. **21**(11): p. 3756.
325. Wang, B., et al., *Nanozyme-Based Lateral Flow Immunoassay (LFIA) for Extracellular Vesicle Detection.* Biosensors, 2022. **12**(7): p. 490.
326. Su, Q., et al., *Resonance energy transfer in upconversion nanoplatforms for selective biodetection.* Accounts of chemical research, 2017. **50**(1): p. 32-40.
327. Zhou, J., et al., *Upconversion luminescent materials: advances and applications.* Chemical reviews, 2015. **115**(1): p. 395-465.
328. Zhu, X., et al., *Anti-Stokes shift luminescent materials for bio-applications.* Chemical Society Reviews, 2017. **46**(4): p. 1025-1039.
329. Zhu, X., et al., *Recent progress of rare‐earth doped upconversion nanoparticles: synthesis, optimization, and applications.* Advanced Science, 2019. **6**(22): p. 1901358.
330. Yin, H., W. Xue, and D.G. Anderson, *CRISPR–Cas: a tool for cancer research and therapeutics.* Nature Reviews Clinical Oncology, 2019. **16**(5): p. 281-295.

331. Gong, S., et al., *CRISPR/Cas-based in vitro diagnostic platforms for cancer biomarker detection*. 2021, ACS Publications.
332. Yang, Y., et al., *CRISPR/Cas: advances, limitations, and applications for precision cancer research.* Frontiers in medicine, 2021. **8**: p. 649896.
333. Zhou, J., et al., *Dual-modality in vivo imaging using rare-earth nanocrystals with near-infrared to near-infrared (NIR-to-NIR) upconversion luminescence and magnetic resonance properties.* Biomaterials, 2010. **31**(12): p. 3287-3295.
334. Schroter, A. and T. Hirsch, *Control of Luminescence and Interfacial Properties as Perspective for Upconversion Nanoparticles.* Small, 2024. **20**(14): p. 2306042.
335. Bünzli, J.-C.G., *Benefiting from the Unique Properties of Lanthanide Ions.* Accounts of Chemical Research, 2006. **39**(1): p. 53-61.
336. dos Santos, C.M.G., et al., *Recent developments in the field of supramolecular lanthanide luminescent sensors and self-assemblies.* Coordination Chemistry Reviews, 2008. **252**(23): p. 2512-2527.
337. Bünzli, J.-C.G., et al., *Lanthanide Bimetallic Helicates forin VitroImaging and Sensing.* Annals of the New York Academy of Sciences, 2008. **1130**(1): p. 97-105.
338. Montgomery, C.P., et al., *Cell-Penetrating Metal Complex Optical Probes: Targeted and Responsive Systems Based on Lanthanide Luminescence.* Accounts of Chemical Research, 2009. **42**(7): p. 925-937.
339. Yang, J., et al., *Highly Stretchable and Fast Self-Healing Luminescent Materials.* ACS Applied Materials & Interfaces, 2020. **12**(11): p. 13239-13247.
340. Wang, L., et al., *Lanthanide-Doped Inorganic Nanoprobes for Luminescent Assays of Biomarkers.* Accounts of Materials Research, 2023. **4**(2): p. 193-204.
341. Dawson, P. and M. Romanowski, *Excitation Modulation of Upconversion Nanoparticles for Switch-like Control of Ultraviolet Luminescence.* Journal of the American Chemical Society, 2018. **140**(17): p. 5714-5718.
342. Ma, X., et al., *Highly Thermostable One-Dimensional Lanthanide(III) Coordination Polymers Constructed from Benzimidazole-5,6-dicarboxylic Acid and 1,10-Phenanthroline: Synthesis, Structure, and Tunable White-Light Emission.* Crystal Growth & Design, 2012. **12**(11): p. 5227-5232.
343. Wang, M., et al., *Upconversion nanoparticles: synthesis, surface modification and biological applications.* Nanomedicine, 2011. **7**(6): p. 710-29.
344. Pawlik, N., et al., *Studies of energy transfer process between Gd3+ and Eu3+ ions in oxyfluoride sol-gel materials.* Ceramics International, 2023. **49**(24, Part B): p. 41041-41053.
345. Zhang, B., et al., *Color-tunable phosphor of Sr3YNa(PO4)3F:Tb3+ via interionic cross-relaxation energy transfer.* RSC Advances, 2018. **8**(45): p. 25378-25386.
346. Kovacs, D., et al., *Eu(III) and Tb(III) Complexes of Octa- and Nonadentate Macrocyclic Ligands Carrying Azide, Alkyne, and Ester Reactive Groups.* Inorganic Chemistry, 2020. **59**(1): p. 106-117.
347. Hosseinpour, M., et al., *Alpha sensing, NIR to green light emission in Er3+ doped PbWO4 nanoparticles with modification of calcination atmosphere.* Journal of Alloys and Compounds, 2025. **1010**: p. 177189.
348. Blackburn, O.A., et al., *Luminescence and upconversion from thulium(iii) species in solution.* Physical Chemistry Chemical Physics, 2012. **14**(38): p. 13378-13384.
349. Sy, M., et al., *Lanthanide-based luminescence biolabelling.* Chemical Communications, 2016. **52**(29): p. 5080-5095.
350. Wu, X., et al., *Upconversion nanoparticles: a versatile solution to multiscale biological imaging.* Bioconjug Chem, 2015. **26**(2): p. 166-75.
351. Heer, S., et al., *Highly efficient multicolour upconversion emission in transparent colloids of lanthanide ‐doped NaYF4 nanocrystals.* Advanced Materials, 2004. **16**(23 ‐ 24): p. 2102-2105.

352. Esipova, T.V., et al., *Dendritic upconverting nanoparticles enable in vivo multiphoton microscopy with low-power continuous wave sources.* Proceedings of the National Academy of Sciences, 2012. **109**(51): p. 20826-20831.
353. Kataria, M., et al., *Multifunctional Laser-Induced Bubble Microresonator for Upconversion Emission Enhancement.* The Journal of Physical Chemistry C, 2023. **127**(16): p. 7752-7761.
354. Jin, J., et al., *Polymer-Coated NaYF4:Yb3+, Er3+ Upconversion Nanoparticles for Charge-Dependent Cellular Imaging.* ACS Nano, 2011. **5**(10): p. 7838-7847.
355. Ryu, J., et al., *Facile Synthesis of Ultrasmall and Hexagonal NaGdF4: Yb3+, Er3+ Nanoparticles with Magnetic and Upconversion Imaging Properties.* The Journal of Physical Chemistry C, 2010. **114**(49): p. 21077-21082.
356. Sedlmeier, A. and H.H. Gorris, *Surface modification and characterization of photon-upconverting nanoparticles for bioanalytical applications.* Chemical Society reviews, 2015. **44 6**: p. 1526-60.
357. Tu, L., et al., *Excitation energy migration dynamics in upconversion nanomaterials.* Chemical Society Reviews, 2015. **44**(6): p. 1331-1345.
358. Chen, X., et al., *Photon upconversion in core–shell nanoparticles.* Chemical Society Reviews, 2015. **44**(6): p. 1318-1330.
359. Wen, S., et al., *Advances in highly doped upconversion nanoparticles.* Nature Communications, 2018. **9**(1): p. 2415.
360. Zuo, J., et al., *Employing shells to eliminate concentration quenching in photonic upconversion nanostructure.* Nanoscale, 2017. **9**(23): p. 7941-7946.
361. Johnson, N.J., et al., *Direct evidence for coupled surface and concentration quenching dynamics in lanthanide-doped nanocrystals.* Journal of the American Chemical Society, 2017. **139**(8): p. 3275-3282.
362. Wang, F., J. Wang, and X. Liu, *Direct evidence of a surface quenching effect on size-dependent luminescence of upconversion nanoparticles.* Angew. Chem. Int. Ed, 2010. **49**(41): p. 7456-7460.
363. Zhao, J., et al., *Single-nanocrystal sensitivity achieved by enhanced upconversion luminescence.* Nature nanotechnology, 2013. **8**(10): p. 729-734.
364. Wen, S., et al., *Power-Dependent Optimal Concentrations of Tm3+ and Yb3+ in Upconversion Nanoparticles.* The Journal of Physical Chemistry Letters, 2022. **13**(23): p. 5316-5323.
365. Li, X., et al., *Engineering homogeneous doping in single nanoparticle to enhance upconversion efficiency.* Nano letters, 2014. **14**(6): p. 3634-3639.
366. Qian, H.-S. and Y. Zhang, *Synthesis of Hexagonal-Phase Core−Shell NaYF4 Nanocrystals with Tunable Upconversion Fluorescence.* Langmuir, 2008. **24**(21): p. 12123-12125.
367. Peng, P., et al., *Biodegradable Inorganic Upconversion Nanocrystals for In Vivo Applications.* ACS Nano, 2020. **14**(12): p. 16672-16680.
368. Li, C., et al., *Highly Uniform and Monodisperse β-NaYF4:Ln3+ (Ln = Eu, Tb, Yb/Er, and Yb/Tm) Hexagonal Microprism Crystals: Hydrothermal Synthesis and Luminescent Properties.* Inorganic Chemistry, 2007. **46**(16): p. 6329-6337.
369. Liu, J.-L., et al., *First Dimethyltin-Functionalized Rare-Earth Incorporated Tellurotungstates Consisting of {B-α-TeW7O28} and {W5O18} Mixed Building Units.* Inorganic Chemistry, 2018. **57**(20): p. 12509-12520.
370. Zhang, L., et al., *Ultrasensitive Rapid Antigen Test by Geometric Lateral Flow Assays and Highly Doped Upconversion Nanoparticles.* Analytical Chemistry, 2024. **96**(42): p. 16581-16589.
371. Masoumeh Ghorbanpour, S., et al., *Quantitative Point of Care Tests for Timely Diagnosis of Early-Onset Preeclampsia with High Sensitivity and Specificity.* Angewandte Chemie International Edition, 2023. **62**(26): p. e202301193.
372. Wilhelm, S., et al., *Water dispersible upconverting nanoparticles: effects of surface modification on their luminescence and colloidal stability.* Nanoscale, 2015. **7**(4): p. 1403-1410.

373. Ye, X., et al., *Morphologically controlled synthesis of colloidal upconversion nanophosphors and their shape-directed self-assembly.* Proceedings of the National Academy of Sciences, 2010. **107**(52): p. 22430-22435.
374. Sedlmeier, A. and H.H. Gorris, *Surface modification and characterization of photon-upconverting nanoparticles for bioanalytical applications.* Chemical Society Reviews, 2015. **44**(6): p. 1526-1560.
375. Zhang, Y., et al., *Tuning sub-10 nm single-phase NaMnF 3 nanocrystals as ultrasensitive hosts for pure intense fluorescence and excellent T 1 magnetic resonance imaging.* Chemical Communications, 2012. **48**(83): p. 10322-10324.
376. Wang, M., et al., *Upconversion nanoparticles: synthesis, surface modification and biological applications.* Nanomedicine: Nanotechnology, Biology and Medicine, 2011. **7**(6): p. 710-729.
377. Boyer, J.-C., et al., *Surface modification of upconverting NaYF4 nanoparticles with PEG–phosphate ligands for NIR (800 nm) biolabeling within the biological window.* Langmuir, 2010. **26**(2): p. 1157-1164.
378. Jia, X., et al., *Polyacrylic acid modified upconversion nanoparticles for simultaneous pH-triggered drug delivery and release imaging.* Journal of biomedical nanotechnology, 2013. **9**(12): p. 2063-2072.
379. Kumar, R., et al., *Combined optical and MR bioimaging using rare earth ion doped NaYF4 nanocrystals.* Advanced Functional Materials, 2009. **19**(6): p. 853-859.
380. Wei, Z., et al., *Cysteine modified rare-earth up-converting nanoparticles for in vitro and in vivo bioimaging.* Biomaterials, 2014. **35**(1): p. 387-392.
381. Zhang, Q., et al., *Hexanedioic acid mediated surface–ligand-exchange process for transferring NaYF4: Yb/Er (or Yb/Tm) up-converting nanoparticles from hydrophobic to hydrophilic.* Journal of colloid and interface science, 2009. **336**(1): p. 171-175.
382. Chen, Z., et al., *Versatile synthesis strategy for carboxylic acid− functionalized upconverting nanophosphors as biological labels.* Journal of the American Chemical Society, 2008. **130**(10): p. 3023-3029.
383. Wang, M., et al., *Two-phase solvothermal synthesis of rare-earth doped NaYF4 upconversion fluorescent nanocrystals.* Materials Letters, 2009. **63**(2): p. 325-327.
384. Bogdan, N., et al., *Synthesis of Ligand-Free Colloidally Stable Water Dispersible Brightly Luminescent Lanthanide-Doped Upconverting Nanoparticles.* Nano Letters, 2011. **11**(2): p. 835-840.
385. Bogdan, N., et al., *Bio-functionalization of ligand-free upconverting lanthanide doped nanoparticles for bio-imaging and cell targeting.* Nanoscale, 2012. **4**(12): p. 3647-3650.
386. Ferrara, K.W., M.A. Borden, and H. Zhang, *Lipid-Shelled Vehicles: Engineering for Ultrasound Molecular Imaging and Drug Delivery.* Accounts of Chemical Research, 2009. **42**(7): p. 881-892.
387. Wagner, A., et al., *GMP Production of Liposomes—A New Industrial Approach.* Journal of Liposome Research, 2006. **16**(3): p. 311-319.
388. Li, L.L., et al., *Biomimetic surface engineering of lanthanide-doped upconversion nanoparticles as versatile bioprobes.* Angew Chem Int Ed Engl, 2012. **51**(25): p. 6121-5.
389. Wu, S., et al., *Non-blinking and photostable upconverted luminescence from single lanthanide-doped nanocrystals.* Proceedings of the National Academy of Sciences, 2009. **106**(27): p. 10917-10921.
390. Yi, G.-S. and G.-M. Chow, *Water-Soluble NaYF4:Yb,Er(Tm)/NaYF4/Polymer Core/Shell/Shell Nanoparticles with Significant Enhancement of Upconversion Fluorescence.* Chemistry of Materials, 2007. **19**(3): p. 341-343.
391. Chen, D., et al., *Ultra-broadband near-infrared excitable upconversion core/shell nanocrystals.* Chemical Communications, 2012. **48**(47): p. 5898-5900.

392. Soukka, T., T. Rantanen, and K. Kuningas, *Photon Upconversion in Homogeneous Fluorescence-based Bioanalytical Assays.* Annals of the New York Academy of Sciences, 2008. **1130**(1): p. 188-200.
393. Tian, Z., et al., *Autofluorescence-free in vivo multicolor imaging using upconversion fluoride nanocrystals.* Lasers in Medical Science, 2010. **25**(4): p. 479-484.
394. Hou, Z., et al., *Electrospinning Preparation and Drug-Delivery Properties of an Up-conversion Luminescent Porous NaYF4:Yb3+, Er3+@Silica Fiber Nanocomposite.* Advanced Functional Materials, 2011. **21**(12): p. 2356-2365.
395. Duan, C., et al., *Recent progress in upconversion luminescence nanomaterials for biomedical applications.* Journal of Materials Chemistry B, 2018. **6**(2): p. 192-209.
396. Guo, H., et al., *Direct Detection of Circulating Tumor Cells in Whole Blood Using Time‐Resolved Luminescent Lanthanide Nanoprobes.* Angewandte Chemie International Edition, 2019. **58**(35): p. 12195-12199.
397. Chen, X., et al., *A paper-supported aptasensor based on upconversion luminescence resonance energy transfer for the accessible determination of exosomes.* Biosensors and Bioelectronics, 2018. **102**: p. 582-588.
398. Wang, Y., et al., *An aptasensor based on upconversion nanoparticles as LRET donors for the detection of exosomes.* Sensors and Actuators B: Chemical, 2019. **298**: p. 126900.
399. Zhang, X.W., et al., *Integral Multielement Signals by DNA-Programmed UCNP-AuNP Nanosatellite Assemblies for Ultrasensitive ICP-MS Detection of Exosomal Proteins and Cancer Identification.* Anal Chem, 2021. **93**(16): p. 6437-6445.
400. Ju, Q., U. Uddayasankar, and U. Krull, *Paper-Based DNA Detection Using Lanthanide-Doped LiYF4 Upconversion Nanocrystals As Bioprobe.* Small, 2014. **10**(19): p. 3912-3917.
401. He, M., et al., *Portable Upconversion Nanoparticles-Based Paper Device for Field Testing of Drug Abuse.* Analytical Chemistry, 2016. **88**(3): p. 1530-1534.
402. He, H., et al., *Quantitative Lateral Flow Strip Sensor Using Highly Doped Upconversion Nanoparticles.* Analytical Chemistry, 2018. **90**(21): p. 12356-12360.
403. Wang, C., et al., *Simultaneous isolation and detection of circulating tumor cells with a microfluidic silicon-nanowire-array integrated with magnetic upconversion nanoprobes.* Biomaterials, 2015. **54**: p. 55-62.
404. Kale, V., et al., *Spectrally and Spatially Multiplexed Serological Array-in-Well Assay Utilizing Two-Color Upconversion Luminescence Imaging.* Analytical Chemistry, 2016. **88**(8): p. 4470-4477.
405. Lan, J., et al., *Upconversion luminescence assay for the detection of the vascular endothelial growth factor, a biomarker for breast cancer.* Microchimica Acta, 2016. **183**(12): p. 3201-3208.
406. Farka, Z., et al., *Single molecule upconversion-linked immunosorbent assay with extended dynamic range for the sensitive detection of diagnostic biomarkers.* Analytical chemistry, 2017. **89**(21): p. 11825-11830.
407. Huang, G., et al., *Single Small Extracellular Vesicle (sEV) Quantification by Upconversion Nanoparticles.* Nano Letters, 2022. **22**(9): p. 3761-3769.
408. Huang, G., et al., *Upconversion nanoparticles for super-resolution quantification of single small extracellular vesicles.* eLight, 2022. **2**(1): p. 20.
409. Wen, S., et al., *Nanorods with multidimensional optical information beyond the diffraction limit.* Nature communications, 2020. **11**(1): p. 6047.
410. Maddahfar, M., et al., *Stable and Highly Efficient Antibody–Nanoparticles Conjugation.* Bioconjugate Chemistry, 2021. **32**(6): p. 1146-1155.
411. Wang, A., et al., *Detection of the potential tumor marker of AFP using surface-enhanced Raman scattering-based immunoassay.* Journal of Raman Spectroscopy, 2013. **44**(12): p. 1649-1653.
412. Kastner, S., et al., *The effect of layer thickness and immobilization chemistry on the detection of CRP in LSPR assays.* Scientific Reports, 2022. **12**(1): p. 836.

413. Chen, L., et al., *Design of Silica-protected Surface-enhanced Raman Scattering Nanoprobe for Immunosorbent Assay#.* Bulletin of the Korean Chemical Society, 2015. **36**(3): p. 930-935.
414. Kurdekar, A., et al., *Sub-picogram level sensitivity in HIV diagnostics achieved with the europium nanoparticle immunoassay through metal enhanced fluorescence.* Nanoscale Advances, 2019. **1**(1): p. 273-280.
415. Chopra, A., G. Mohanta, and S. Sarkar Pal, *Exploring metal-molecule-metal nanoparticles (MMNP) configuration for introducing specificity in SPR biosensors*. SPIE Future Sensing Technologies. Vol. 13083. 2024: SPIE.
416. Ding, Q., et al., *Theranostic Upconversion Nanobeacons for Tumor mRNA Ratiometric Fluorescence Detection and Imaging-Monitored Drug Delivery.* Small, 2016. **12**(43): p. 5944-5953.
417. Li, R., et al., *Multifunctional Nanoprobe for the Delivery of Therapeutic siRNA and Real-Time Molecular Imaging of Parkinson's Disease Biomarkers.* ACS Applied Materials & Interfaces, 2021. **13**(10): p. 11609-11620.
418. Du, R., et al., *Ultrasensitive Detection of Low-Abundance Protein Biomarkers by Mass Spectrometry Signal Amplification Assay.* Analytical Chemistry, 2016. **88**(13): p. 6767-6772.
419. Qiu, F., et al., *Evaluation of two high-abundance protein depletion kits and optimization of downstream isoelectric focusing.* Mol Med Rep, 2015. **12**(5): p. 7749-7755.
420. Gangadharan, B., et al., *New Approaches for Biomarker Discovery: The Search for Liver Fibrosis Markers in Hepatitis C Patients.* Journal of Proteome Research, 2011. **10**(5): p. 2643-2650.
421. Lichtenauer, A.M., et al., *Equalizer technology followed by DIGE-based proteomics for detection of cellular proteins in artificial peritoneal dialysis effluents.* ELECTROPHORESIS, 2014. **35**(10): p. 1387-1394.
422. Chen, X., et al., *Entropy-driven strand displacement reaction for ultrasensitive detection of circulating tumor DNA based on upconversion and Fe3O4 nanocrystals.* Science China Materials, 2021. **64**(10): p. 2593-2600.
423. Taylor, M.L., et al., *Nanomaterials for Molecular Detection and Analysis of Extracellular Vesicles.* Nanomaterials, 2023. **13**(3): p. 524.
424. Kim, M.S., et al., *Development of exosome-encapsulated paclitaxel to overcome MDR in cancer cells.* Nanomedicine: Nanotechnology, Biology and Medicine, 2016. **12**(3): p. 655-664.
425. Wang, Y., et al., *Mass Spectrometry Imaging of Mass Tag Immunoassay Enables the Quantitative Profiling of Biomarkers from Dozens of Exosomes.* Analytical Chemistry, 2021. **93**(2): p. 709-714.
426. Angeloni, N.L., et al., *Pathways for Modulating Exosome Lipids Identified By High-Density Lipoprotein-Like Nanoparticle Binding to Scavenger Receptor Type B-1.* Scientific Reports, 2016. **6**(1): p. 22915.
427. Lee, C., et al., *SERS analysis of selectively captured exosomes using an integrin-specific peptide ligand.* Journal of Raman Spectroscopy, 2017. **48**(12): p. 1771-1776.
428. Zhang, H., et al., *Immunoassay-aptasensor for the determination of tumor-derived exosomes based on the combination of magnetic nanoparticles and hybridization chain reaction.* RSC Advances, 2021. **11**(9): p. 4983-4990.
429. Ambrosi, A., F. Airò, and A. Merkoçi, *Enhanced Gold Nanoparticle Based ELISA for a Breast Cancer Biomarker.* Analytical Chemistry, 2010. **82**(3): p. 1151-1156.
430. Zhan, L., et al., *Gold nanoparticle-based enhanced ELISA for respiratory syncytial virus.* New Journal of Chemistry, 2014. **38**(7): p. 2935-2940.
431. Ciaurriz, P., et al., *Comparison of four functionalization methods of gold nanoparticles for enhancing the enzyme-linked immunosorbent assay (ELISA).* Beilstein J Nanotechnol, 2017. **8**: p. 244-253.
432. Tan, Y.H., et al., *A nanoengineering approach for investigation and regulation of protein immobilization.* ACS Nano, 2008. **2**(11): p. 2374-84.

433. Rennke, H.G. and M.A. Venkatachalam, *Chemical modification of horseradish peroxidase. Preparation and characterization of tracer enzymes with different isoelectric points.* J Histochem Cytochem, 1979. **27**(10): p. 1352-3.
434. Lu, Z.-Y. and Y.-H. Chan, *The importance of antibody orientation for enhancing sensitivity and selectivity in lateral flow immunoassays.* Sensors & Diagnostics, 2024. **3**(10): p. 1613-1634.
435. Trilling, A.K., J. Beekwilder, and H. Zuilhof, *Antibody orientation on biosensor surfaces: a minireview.* Analyst, 2013. **138**(6): p. 1619-1627.
436. Dykman, L. and N. Khlebtsov, *Gold nanoparticles in biomedical applications: recent advances and perspectives.* Chemical Society Reviews, 2012. **41**(6): p. 2256-2282.
437. Pilch, A., et al., *Shaping Luminescent Properties of Yb3+ and Ho3+ Co-Doped Upconverting Core–Shell β-NaYF4 Nanoparticles by Dopant Distribution and Spacing.* Small, 2017. **13**(47): p. 1701635.
438. Karami, A., et al., *Facile Multistep Synthesis of ZnO-Coated β-NaYF4:Yb/Tm Upconversion Nanoparticles as an Antimicrobial Photodynamic Therapy for Persistent Staphylococcus aureus Small Colony Variants.* ACS Applied Bio Materials, 2021. **4**(8): p. 6125-6136.
439. Li, D., et al., *Highly Doped Upconversion Nanoparticles for In Vivo Applications Under Mild Excitation Power.* Analytical Chemistry, 2020. **92**(16): p. 10913-10919.
440. Boyer, J.-C. and F.C.J.M. van Veggel, *Absolute quantum yield measurements of colloidal NaYF4: Er3+, Yb3+ upconverting nanoparticles.* Nanoscale, 2010. **2**(8): p. 1417-1419.
441. Li, F., et al., *Size-dependent lanthanide energy transfer amplifies upconversion luminescence quantum yields.* Nature Photonics, 2024. **18**(5): p. 440-449.
442. Lin, G. and D. Jin, *Responsive Sensors of Upconversion Nanoparticles.* ACS Sensors, 2021. **6**(12): p. 4272-4282.
443. Wang, J., et al., *Enhancing multiphoton upconversion through energy clustering at sublattice level.* Nature materials, 2014. **13**(2): p. 157-162.
444. Huang, X., et al., *Enhancing solar cell efficiency: the search for luminescent materials as spectral converters.* Chemical Society Reviews, 2013. **42**(1): p. 173-201.
445. Auzel, F., *Upconversion and anti-stokes processes with f and d ions in solids.* Chemical reviews, 2004. **104**(1): p. 139-174.
446. Liu, D., et al., *Three-dimensional controlled growth of monodisperse sub-50 nm heterogeneous nanocrystals.* Nature Communications, 2016. **7**(1): p. 10254.
447. Liu, D., et al., *Three-dimensional controlled growth of monodisperse sub-50 nm heterogeneous nanocrystals.* Nature communications, 2016. **7**(1): p. 1-8.
448. Liu, Y., et al., *Amplified stimulated emission in upconversion nanoparticles for super-resolution nanoscopy.* Nature, 2017. **543**(7644): p. 229-233.
449. Zhang, L., et al., *Optimizing the polymer cloak for upconverting nanoparticles: an evaluation of bioactivity and optical performance.* ACS Applied Materials & Interfaces, 2021. **13**(14): p. 16142-16154.
450. Porstmann, T. and S. Kiessig, *Enzyme immunoassay techniques an overview.* Journal of immunological methods, 1992. **150**(1-2): p. 5-21.
451. Self, C.H. and D.B. Cook, *Advances in immunoassay technology*. Current opinion in biotechnology, 1996. **7**(1): p. 60-65.
452. Kwong, G.A., et al., *Mass-encoded synthetic biomarkers for multiplexed urinary monitoring of disease.* Nature biotechnology, 2013. **31**(1): p. 63-70.
453. Deshpande, S., *Enzyme immunoassays: from concept to product development*. 2012: Springer Science & Business Media.
454. Quan, Y., et al., *Development of an enhanced chemiluminescence ELISA for the rapid detection of acrylamide in food products.* Journal of agricultural and food chemistry, 2011. **59**(13): p. 6895-6899.
455. Yuan, L., L. Xu, and S. Liu, *Integrated tyramide and polymerization-assisted signal amplification for a highly-sensitive immunoassay.* Anal Chem, 2012. **84**(24): p. 10737-44.

456. Ruktanonchai, U., et al., *Signal amplification of microarray-based immunoassay by optimization of nanoliposome formulations.* Anal Biochem, 2012. **429**(2): p. 142-7.
457. Lin, H., et al., *Modified enzyme-linked immunosorbent assay strategy using graphene oxide sheets and gold nanoparticles functionalized with different antibody types.* Anal Chem, 2013. **85**(13): p. 6228-32.
458. Saha, K., et al., *Gold nanoparticles in chemical and biological sensing.* Chem Rev, 2012. **112**(5): p. 2739-79.
459. Niu, Y., Y. Zhao, and A. Fan, *Conformational switching immobilized hairpin DNA probes following subsequent expanding of gold nanoparticles enables visual detecting sequence-specific DNA.* Anal Chem, 2011. **83**(19): p. 7500-6.
460. Liu, D., et al., *Gold nanoparticle-based activatable probe for sensing ultralow levels of prostate-specific antigen.* ACS Nano, 2013. **7**(6): p. 5568-76.
461. Singh, H., et al., *A handy field-portable ELISA system for rapid onsite diagnosis of infectious diseases.* Japanese journal of infectious diseases, 2016. **69**(5): p. 435-438.
462. Thiha, A. and F. Ibrahim, *A colorimetric enzyme-linked immunosorbent assay (ELISA) detection platform for a point-of-care dengue detection system on a lab-on-compact-disc.* Sensors, 2015. **15**(5): p. 11431-11441.
463. Hlavacek, A., P. Bouchal, and P. Skládal, *Biotinylation of quantum dots for application in fluoroimmunoassays with biotin-avidin amplification.* Microchimica Acta, 2012. **176**: p. 287-293.
464. Osterfeld, S.J., et al., *Multiplex protein assays based on real-time magnetic nanotag sensing.* Proceedings of the National Academy of Sciences, 2008. **105**(52): p. 20637-20640.
465. Wang, L., et al., *Watching silica nanoparticles glow in the biological world*. 2006, ACS Publications.
466. Haase, M. and H. Schäfer, *Upconverting nanoparticles.* Angewandte Chemie International Edition, 2011. **50**(26): p. 5808-5829.
467. Schietinger, S., et al., *Plasmon-enhanced upconversion in single NaYF4: Yb3+/Er3+ codoped nanocrystals.* Nano letters, 2010. **10**(1): p. 134-138.
468. Li, X., F. Zhang, and D. Zhao, *Lab on upconversion nanoparticles: optical properties and applications engineering via designed nanostructure.* Chemical Society Reviews, 2015. **44**(6): p. 1346-1378.
469. Gorris, H.H., et al., *Tuning the dual emission of photon‐upconverting nanoparticles for ratiometric multiplexed encoding.* Advanced Materials, 2011. **23**(14): p. 1652-1655.
470. Zhou, C., et al., *Lanthanide-Doped Upconversion-Linked Immunosorbent Assay for the Sensitive Detection of Carbohydrate Antigen 19-9.* Frontiers in Chemistry, 2021. **8**: p. 592445.
471. Hlaváček, A., et al., *Competitive Upconversion-Linked Immunosorbent Assay for the Sensitive Detection of Diclofenac.* Analytical Chemistry, 2016. **88**(11): p. 6011-6017.
472. Martin, L.J., B. Akhavan, and M.M.M. Bilek, *Electric fields control the orientation of peptides irreversibly immobilized on radical-functionalized surfaces.* Nature Communications, 2018. **9**(1): p. 357.
473. Batra, G., et al., *Evaluation of envelope domain III-based single chimeric tetravalent antigen and monovalent antigen mixtures for the detection of anti-dengue antibodies in human sera.* BMC Infectious Diseases, 2011. **11**(1): p. 64.
474. Siddiqui, M.F., Z.A. Khan, and S. Park, *Detection of C-Reactive Protein Using Histag-HRP Functionalized Nanoconjugate with Signal Amplified Immunoassay.* Nanomaterials, 2020. **10**(6): p. 1240.
475. Lakshmipriya, T., S.C.B. Gopinath, and T.-H. Tang, *Biotin-Streptavidin Competition Mediates Sensitive Detection of Biomolecules in Enzyme Linked Immunosorbent Assay.* PLOS ONE, 2016. **11**(3): p. e0151153.

476. Ivens, K.O., et al., *The Effect of Different Methods of Fermentation on the Detection of Milk Protein Residues in Retail Cheese by Enzyme-Linked Immunosorbent Assay (ELISA).* Journal of Food Science, 2017. **82**(11): p. 2752-2758.
477. Wang, L., et al., *Development of an effective one-step double-antigen sandwich ELISA based on p72 to detect antibodies against African swine fever virus.* Frontiers in Veterinary Science, 2023. **10**.
478. Tsurusawa, N., et al., *Modified ELISA for Ultrasensitive Diagnosis.* Journal of Clinical Medicine, 2021. **10**(21): p. 5197.
479. Lei, J., et al., *Development and application of nsp5-ELISA for the detection of antibody to infectious bronchitis virus.* Journal of Virological Methods, 2017. **243**: p. 182-189.
480. Sun, D.-d., et al., *Quality Evaluation of Five Commercial Enzyme Linked Immunosorbent Assay Kits for Detecting Aflatoxin B1 in Feedstuffs.* Asian-Australas J Anim Sci, 2015. **28**(5): p. 691-696.
481. Patel, P., U. Kuzmanov, and S. Mital, *Avoiding false discovery in biomarker research.* BMC Biochemistry, 2016. **17**(1): p. 17.
482. Nandi, S., et al., *Comparative assessment of commercial ELISA kits for detection of HIV in India.* BMC Research Notes, 2014. **7**(1): p. 436.
483. Enayati, H., J. Mohammadnejad, and A. Nikfarjam, *Development of enzyme-linked immunosorbent assay (ELISA) based on covalent immobilization of antibody on plate for measurement of digoxin.* Acta Biochimica Iranica, 2023. **1**(3): p. 139-144.
484. Varghese, K., et al., *A New Electrochemiluminescence-Based Multiplex Assay for the Assessment of Human Antibody Responses to Bordetella pertussis Vaccines.* Infectious Diseases and Therapy, 2021. **10**(4): p. 2539-2561.
485. Kim, S.-H., *ELISA for Quantitative Determination of Hepatitis B Virus Surface Antigen.* Immune Netw, 2017. **17**(6): p. 451-459.
486. Štimac, A., T. Kurtović, and B. Halassy, *Multi-Detection Size Exclusion Chromatography as an Advanced Tool for Monitoring Enzyme–Antibody Conjugation Reaction and Quality Control of a Final Product.* Molecules, 2023. **28**(11): p. 4567.
487. Safdari, Y., et al., *Protein L: A Robust Enzyme-Conjugated Molecule for Detection of Humanized Single Chain Antibodies.* Monoclonal Antibodies in Immunodiagnosis and Immunotherapy, 2013. **32**(6): p. 409-412.
488. Logozzi, M., et al., *Chapter Nine - Immunocapture-based ELISA to characterize and quantify exosomes in both cell culture supernatants and body fluids*, in *Methods in Enzymology*, S. Spada and L. Galluzzi, Editors. 2020, Academic Press. p. 155-180.
489. Khodashenas, S., S. Khalili, and M. Forouzandeh Moghadam, *A cell ELISA based method for exosome detection in diagnostic and therapeutic applications.* Biotechnology Letters, 2019. **41**(4): p. 523-531.
490. Lee, J., et al., *Enhanced paper-based ELISA for simultaneous EVs/exosome isolation and detection using streptavidin agarose-based immobilization.* Analyst, 2020. **145**(1): p. 157-164.
491. Leister, K.P., et al., *Two high throughput screen assays for measurement of TNF-α in THP-1 cells.* Current chemical genomics, 2011. **5**: p. 21.
492. Kim, S.-J., et al., *Preprogrammed, Parallel On-Chip Immunoassay Using System-Level Capillarity Control.* Analytical Chemistry, 2013. **85**(14): p. 6902-6907.
493. DeCotes, D., et al., *Highly mutated monoclonal antibody 3F2 targets a conformational and strain-restricted epitope in human immunodeficiency virus gp41 with significant antibody-dependent cell cytotoxicity.* Archives of Virology, 2022. **167**(11): p. 2193-2201.
494. Khachornsakkul, K., W. Dungchai, and N. Pamme, *Distance-Based All-In-One Immunodevice for Point-of-Care Monitoring of Cytokine Interleukin-6.* ACS Sensors, 2022. **7**(8): p. 2410-2419.
495. Zhang, C., et al., *Toxicity and Immunogenicity of Enterotoxigenic Escherichia coli Heat-Labile and Heat-Stable Toxoid Fusion 3xSTaA14Q-LTS63K/R192G/L211A in a Murine Model.* PLOS ONE, 2013. **8**(10): p. e77386.

496. Ghoshdastidar, S., et al., *Plate-Adherent Nanosubstrate for Improved ELISA of Small Molecules: A Proof of Concept Study.* Analytical Chemistry, 2020. **92**(16): p. 10952-10956.
497. Tripathi, P., et al., *Aptamer-gold nanozyme based competitive lateral flow assay for rapid detection of CA125 in human serum.* Biosensors and Bioelectronics, 2020. **165**: p. 112368.
498. Wang, X.-M., et al., *Triple quantitative detection of three inflammatory biomarkers with a biotin-streptavidin-phycoerythrin based lateral flow immunoassay.* Analytical Biochemistry, 2022. **657**: p. 114915.
499. Min, J., et al., *A Recombinant Secondary Antibody Mimic as a Target-specific Signal Amplifier and an Antibody Immobilizer in Immunoassays.* Scientific Reports, 2016. **6**(1): p. 24159.
500. Bronshtein, A., et al., *Development of a Multianalyte Enzyme-Linked Immunosorbent Assay for Permethrin and Aroclors and Its Implementation for Analysis of Soil/Sediment and House Dust Extracts.* Journal of Agricultural and Food Chemistry, 2012. **60**(17): p. 4235-4242.
501. Wang, C., T. Lakshmipriya, and S.C.B. Gopinath, *Amine-Aldehyde Chemical Conjugation on a Potassium Hydroxide-Treated Polystyrene ELISA Surface for Nanosensing an HIV-p24 Antigen.* Nanoscale Research Letters, 2019. **14**(1): p. 21.
502. Chuang, K.-H., et al., *Development of an Anti-Methoxy Poly(ethylene glycol) (α-mPEG) Cell-Based Capture System to Measure mPEG and mPEGylated Molecules.* Macromolecules, 2014. **47**(19): p. 6880-6888.
503. Chen, Y.-J., et al., *Development of a highly sensitive enzyme-linked immunosorbent assay (ELISA) through use of poly-protein G-expressing cell-based microplates.* Scientific Reports, 2018. **8**(1): p. 17868.
504. Wang, X., et al., *Understanding LRRK2 kinase activity in preclinical models and human subjects through quantitative analysis of LRRK2 and pT73 Rab10.* Scientific Reports, 2021. **11**(1): p. 12900.
505. Seo, J.-s., S. Lee, and C.D. Poulter, *Regioselective Covalent Immobilization of Recombinant Antibody-Binding Proteins A, G, and L for Construction of Antibody Arrays.* Journal of the American Chemical Society, 2013. **135**(24): p. 8973-8980.
506. Cai, J., et al., *Temperature Sensing Using Thermal Population of Low-Lying Energy Levels with (Sm0.01Gd0.99)VO4.* Inorganic Chemistry, 2017. **56**(7): p. 4039-4046.
507. Lipchik, A.M. and L.L. Parker, *Time-Resolved Luminescence Detection of Spleen Tyrosine Kinase Activity through Terbium Sensitization.* Analytical Chemistry, 2013. **85**(5): p. 2582-2588.
508. Devkota, A.K., et al., *Development of a High-Throughput Lysyl Hydroxylase (LH) Assay and Identification of Small-Molecule Inhibitors against LH2.* SLAS Discovery, 2019. **24**(4): p. 484-491.
509. Hagan, A.K. and T. Zuchner, *Lanthanide-based time-resolved luminescence immunoassays.* Analytical and Bioanalytical Chemistry, 2011. **400**(9): p. 2847-2864.
510. Gabr, M.T. and F.C. Pigge, *Expanding the Toolbox for Label-Free Enzyme Assays: A Dinuclear Platinum(II) Complex/DNA Ensemble with Switchable Near-IR Emission.* Molecules, 2019. **24**(23): p. 4390.
511. Li, C.-Y., et al., *Combining Holographic Optical Tweezers with Upconversion Luminescence Encoding: Imaging-Based Stable Suspension Array for Sensitive Responding of Dual Cancer Biomarkers.* Analytical Chemistry, 2018. **90**(4): p. 2639-2647.
512. Shao, Q., et al., *Emission color tuning of core/shell upconversion nanoparticles through modulation of laser power or temperature.* Nanoscale, 2017. **9**(33): p. 12132-12141.
513. Liu, W., et al., *A green, versatile, and facile strategy for anti-biofouling surface with ultra-high graft density polyethylene glycol.* Journal of Nanobiotechnology, 2024. **22**(1): p. 746.
514. Wilhelm, S., et al., *Multicolor upconversion nanoparticles for protein conjugation.* Theranostics, 2013. **3**(4): p. 239-48.
515. Zhang, X.-W., et al., *Integral Multielement Signals by DNA-Programmed UCNP–AuNP Nanosatellite Assemblies for Ultrasensitive ICP–MS Detection of Exosomal Proteins and Cancer Identification.* Analytical Chemistry, 2021. **93**(16): p. 6437-6445.

516. Korbakis, D., et al., *Preclinical evaluation of a TEX101 protein ELISA test for the differential diagnosis of male infertility.* BMC Medicine, 2017. **15**(1): p. 60.
517. Oh, J., et al., *Detection of Anti-Extractable Nuclear Antigens in Patients with Systemic Rheumatic Disease via Fluorescence Enzyme Immunoassay and Its Clinical Utility.* Yonsei Med J, 2020. **61**(1): p. 73-78.
518. Qiu, X., et al., *Development of indirect competitive ELISA for determination of dehydroabietic acid in duck skin and comparison with the HPLC method.* Poultry Science, 2020. **99**(6): p. 3280-3285.
519. Gabriel, M., et al., *Development and evaluation of antibody-capture immunoassays for detection of Lassa virus nucleoprotein-specific immunoglobulin M and G.* PLOS Neglected Tropical Diseases, 2018. **12**(3): p. e0006361.
520. Blacksell, S.D., et al., *Diagnostic Accuracy of the InBios Scrub Typhus Detect Enzyme-Linked Immunoassay for the Detection of IgM Antibodies in Northern Thailand.* Clinical and Vaccine Immunology, 2016. **23**(2): p. 148-154.
521. Bystryak, S. and R. Santockyte, *Increased Sensitivity of HIV-1 p24 ELISA Using a Photochemical Signal Amplification System.* JAIDS Journal of Acquired Immune Deficiency Syndromes, 2015. **70**(2): p. 109-114.
522. Hyldgaard, J., et al., *Comparison of two different methods for measuring anti-mullerian hormone in a clinical series.* Reproductive Biology and Endocrinology, 2015. **13**(1): p. 107.
523. Gao, Y., Y. Zhou, and R. Chandrawati, *Metal and metal oxide nanoparticles to enhance the performance of enzyme-linked immunosorbent assay (ELISA).* ACS Applied Nano Materials, 2019. **3**(1): p. 1-21.
524. Xianyu, Y., Z. Wang, and X. Jiang, *A plasmonic nanosensor for immunoassay via enzyme-triggered click chemistry.* Acs Nano, 2014. **8**(12): p. 12741-12747.
525. Tong, S., et al., *Tiny grains give huge gains: nanocrystal-based signal amplification for biomolecule detection.* ACS nano, 2013. **7**(6): p. 5142-5150.
526. Dorayappan, K.D.P., et al., *The biological significance and clinical applications of exosomes in ovarian cancer.* Gynecologic oncology, 2016. **142**(1): p. 199-205.
527. Theodoraki, M.-N., et al., *Clinical Significance of PD-L1+ Exosomes in Plasma of Head and Neck Cancer Patients.* Clinical Cancer Research, 2018. **24**(4): p. 896-905.
528. Psyrri, A., T.Y. Seiwert, and A. Jimeno, *Molecular pathways in head and neck cancer: EGFR, PI3K, and more.* American Society of Clinical Oncology educational book / ASCO. American Society of Clinical Oncology. Meeting, 2013: p. 246-255.
529. Azadi, S., et al., *Upregulation of PD-L1 expression in breast cancer cells through the formation of 3D multicellular cancer aggregates under different chemical and mechanical conditions.* Biochimica et Biophysica Acta (BBA)-Molecular Cell Research, 2019. **1866**(12): p. 118526.
530. Chen, D.S. and I. Mellman, *Elements of cancer immunity and the cancer–immune set point.* Nature, 2017. **541**(7637): p. 321-330.
531. Gibney, G.T., L.M. Weiner, and M.B. Atkins, *Predictive biomarkers for checkpoint inhibitor-based immunotherapy.* The Lancet Oncology, 2016. **17**(12): p. e542-e551.
532. Zou, W., J.D. Wolchok, and L. Chen, *PD-L1 (B7-H1) and PD-1 pathway blockade for cancer therapy: Mechanisms, response biomarkers, and combinations.* Science translational medicine, 2016. **8**(328): p. 328rv4-328rv4.
533. Kim, D.H., et al., *Exosomal PD-L1 promotes tumor growth through immune escape in non-small cell lung cancer.* Experimental & Molecular Medicine, 2019. **51**(8): p. 1-13.
534. Tartarone, A., R. Lerose, and M. Aieta, *Is there a role for immunotherapy in malignant pleural mesothelioma?* Medical Oncology, 2018. **35**(7): p. 98.
535. Cinausero, M., et al., *Emerging therapies in malignant pleural mesothelioma.* Critical Reviews in Oncology/Hematology, 2019. **144**: p. 102815.
536. Zhang, J., et al., *Biochemical aspects of PD-L1 regulation in cancer immunotherapy.* Trends in biochemical sciences, 2018. **43**(12): p. 1014-1032.

537. Mansfield, A., et al., *Temporal and spatial discordance of programmed cell death-ligand 1 expression and lymphocyte tumor infiltration between paired primary lesions and brain metastases in lung cancer.* Annals of Oncology, 2016. **27**(10): p. 1953-1958.
538. Kim, D.H., et al., *Exosomal PD-L1 promotes tumor growth through immune escape in non-small cell lung cancer.* Experimental & molecular medicine, 2019. **51**(8): p. 1-13.
539. Poggio, M., et al., *Suppression of exosomal PD-L1 induces systemic anti-tumor immunity and memory.* Cell, 2019. **177**(2): p. 414-427. e13.
540. Li, C., et al., *Clinical significance of PD-L1 expression in serum-derived exosomes in NSCLC patients.* Journal of translational medicine, 2019. **17**: p. 1-10.
541. Ricklefs, F.L., et al., *Immune evasion mediated by PD-L1 on glioblastoma-derived extracellular vesicles.* Science advances, 2018. **4**(3): p. eaar2766.
542. Tian, Y., et al., *Protein profiling and sizing of extracellular vesicles from colorectal cancer patients via flow cytometry.* ACS nano, 2018. **12**(1): p. 671-680.
543. Görgens, A., et al., *Optimisation of imaging flow cytometry for the analysis of single extracellular vesicles by using fluorescence-tagged vesicles as biological reference material.* Journal of extracellular vesicles, 2019. **8**(1): p. 1587567.
544. Huang, G., et al., *Emerging technologies for profiling extracellular vesicle heterogeneity.* Lab on a Chip, 2020. **20**(14): p. 2423-2437.
545. Mathieu, M., et al., *Specificities of secretion and uptake of exosomes and other extracellular vesicles for cell-to-cell communication.* Nature Cell Biology, 2019. **21**(1): p. 9-17.
546. Martomo, S.A. and J. Patel, *Evaluation of the clinical molecule anti-human-PD-L1/IL-15 KD033 in the human-PD-1/PD-L1-expressing murine model demonstrates PD-L1 targeting of IL-15 in vivo.* Cancer Immunology, Immunotherapy, 2023. **72**(6): p. 1941-1950.
547. Lee, H.T., et al., *Molecular mechanism of PD-1/PD-L1 blockade via anti-PD-L1 antibodies atezolizumab and durvalumab.* Scientific Reports, 2017. **7**(1): p. 5532.
548. Broos, K., et al., *Single Domain Antibody-Mediated Blockade of Programmed Death-Ligand 1 on Dendritic Cells Enhances CD8 T-cell Activation and Cytokine Production.* Vaccines, 2019. **7**(3): p. 85.
549. Oliveira-Rodríguez, M., et al., *Development of a rapid lateral flow immunoassay test for detection of exosomes previously enriched from cell culture medium and body fluids.* Journal of extracellular vesicles, 2016. **5**(1): p. 31803.
550. Ahmadzada, T., et al., *Small and Large Extracellular Vesicles Derived from Pleural Mesothelioma Cell Lines Offer Biomarker Potential.* Cancers, 2023. **15**(8): p. 2364.
551. Avni, Y., S. Komura, and D. Andelman, *Brownian motion of a charged colloid in restricted confinement.* Physical Review E, 2021. **103**(4): p. 042607.
552. Zeming, K.K., et al., *Real-time modulated nanoparticle separation with an ultra-large dynamic range.* Lab on a Chip, 2016. **16**(1): p. 75-85.
553. Li, X., et al., *Challenges and opportunities in exosome research-Perspectives from biology, engineering, and cancer therapy.* APL Bioeng, 2019. **3**(1): p. 011503.
554. Chen, X., et al., *Tailoring noble metal nanoparticle designs to enable sensitive lateral flow immunoassay.* Theranostics, 2022. **12**(2): p. 574-602.
555. Ahmad, M.A., *Electrical Detection, Identification, and Quantification of Exosomes.* IEEE Access, 2018. **6**: p. 22817-22826.
556. Yakubovich, E.I., A.G. Polischouk, and V.I. Evtushenko, *Principles and Problems of Exosome Isolation from Biological Fluids.* Biochem (Mosc) Suppl Ser A Membr Cell Biol, 2022. **16**(2): p. 115-126.
557. Akama, K., et al., *Wash- and Amplification-Free Digital Immunoassay Based on Single-Particle Motion Analysis.* ACS Nano, 2019. **13**(11): p. 13116-13126.
558. Kim, J., et al., *Orientational binding modes of reporters in a viral-nanoparticle lateral flow assay.* Analyst, 2017. **142**(1): p. 55-64.

559. Ren, W., et al., *Magnetic Focus Lateral Flow Sensor for Detection of Cervical Cancer Biomarkers.* Analytical Chemistry, 2019. **91**(4): p. 2876-2884.
560. Qiu, Y., et al., *Activated T cell-derived exosomal PD-1 attenuates PD-L1-induced immune dysfunction in triple-negative breast cancer.* Oncogene, 2021. **40**(31): p. 4992-5001.
561. Ye, L., et al., *The Importance of Exosomal PD-L1 in Cancer Progression and Its Potential as a Therapeutic Target.* Cells, 2021. **10**(11).
562. Chen, S.E. and M.B. Pace, *Malignant pleural mesothelioma.* American Journal of Health-System Pharmacy, 2012. **69**(5): p. 377-385.
563. Bian, X., et al., *Microvesicles and chemokines in tumor microenvironment: mediators of intercellular communications in tumor progression.* Molecular Cancer, 2019. **18**(1): p. 50.
564. López-Cobo, S., et al., *Immunoassays for scarce tumour-antigens in exosomes: detection of the human NKG2D-Ligand, MICA, in tetraspanin-containing nanovesicles from melanoma.* Journal of Nanobiotechnology, 2018. **16**(1): p. 47.
565. Wu, T., et al., *Enhanced lateral flow assay with double conjugates for the detection of exosomes.* Science China Chemistry, 2018. **61**(11): p. 1423-1429.
566. Di, X., et al., *Spatiotemporally mapping temperature dynamics of lysosomes and mitochondria using cascade organelle-targeting upconversion nanoparticles.* Proceedings of the National Academy of Sciences, 2022. **119**(45): p. e2207402119.
567. Huang, G., et al., *Single Small Extracellular Vesicle (sEV) Quantification by Upconversion Nanoparticles.* Nano Letters, 2022. **22**(9): p. 3761-3769.
568. Ali, M., et al., *A fluorescent lateral flow biosensor for the quantitative detection of Vaspin using upconverting nanoparticles.* Spectrochimica Acta Part A: Molecular and Biomolecular Spectroscopy, 2020. **226**: p. 117610.
569. Juntunen, E., et al., *Lateral flow immunoassay with upconverting nanoparticle‐based detection for indirect measurement of interferon response by the level of MxA.* Journal of medical virology, 2017. **89**(4): p. 598-605.
570. Clayton, A., et al., *Human tumor-derived exosomes selectively impair lymphocyte responses to interleukin-2.* Cancer research, 2007. **67**(15): p. 7458-7466.
571. Reclusa, P., et al., *Exosomes as diagnostic and predictive biomarkers in lung cancer.* J Thorac Dis, 2017. **9**(Suppl 13): p. S1373-s1382.
572. Truong, Q., et al., *Glypican-1 as a biomarker for prostate cancer: isolation and characterization.* Journal of Cancer, 2016. **7**(8): p. 1002.
573. Sung, H., et al., *Global cancer statistics 2020: GLOBOCAN estimates of incidence and mortality worldwide for 36 cancers in 185 countries.* CA: a cancer journal for clinicians, 2021. **71**(3): p. 209-249.
574. Dijkstra, S., P. Mulders, and J. Schalken, *Clinical use of novel urine and blood based prostate cancer biomarkers: a review.* Clinical biochemistry, 2014. **47**(10-11): p. 889-896.
575. Bratt, O. and H. Lilja, *Serum markers in prostate cancer detection.* Current opinion in urology, 2015. **25**(1): p. 59.
576. Siegel, R.L., et al., *Cancer statistics, 2021.* Ca Cancer J Clin, 2021. **71**(1): p. 7-33.
577. Kahi, C.J., et al., *Colonoscopy surveillance after colorectal cancer resection: recommendations of the US Multi-Society Task Force on Colorectal Cancer.* Gastroenterology, 2016. **150**(3): p. 758-768. e11.
578. Perrimon, N. and M. Bernfield, *Specificities of heparan sulphate proteoglycans in developmental processes.* Nature, 2000. **404**(6779): p. 725-728.
579. Matsuda, K., et al., *Glypican-1 is overexpressed in human breast cancer and modulates the mitogenic effects of multiple heparin-binding growth factors in breast cancer cells.* Cancer research, 2001. **61**(14): p. 5562-5569.
580. Su, G., et al., *Glypican-1 is frequently overexpressed in human gliomas and enhances FGF-2 signaling in glioma cells.* The American journal of pathology, 2006. **168**(6): p. 2014-2026.

581. Kleeff, J., et al., *The cell-surface heparan sulfate proteoglycan glypican-1 regulates growth factor action in pancreatic carcinoma cells and is overexpressed in human pancreatic cancer.* The Journal of clinical investigation, 1998. **102**(9): p. 1662-1673.
582. Wang, S., Y. Qiu, and B. Bai, *The expression, regulation, and biomarker potential of glypican-1 in cancer.* Frontiers in oncology, 2019. **9**: p. 614.
583. Lu, F., et al., *GPC1 promotes the growth and migration of colorectal cancer cells through regulating the TGF-β1/SMAD2 signaling pathway.* Plos one, 2022. **17**(6): p. e0269094.
584. Li, J., et al., *GPC1 exosome and its regulatory miRNAs are specific markers for the detection and target therapy of colorectal cancer.* Journal of Cellular and Molecular Medicine, 2017. **21**(5): p. 838-847.
585. Li, J., et al., *The clinical significance of circulating GPC1 positive exosomes and its regulative miRNAs in colon cancer patients.* Oncotarget, 2017. **8**(60).
586. Shore, N., et al., *PII-LBA3 GLYPICAN-1 AS A BIOMARKER FOR PROSTATE CANCER.* Journal of Urology, 2015. **193**(4S): p. e496-e496.
587. Zhao, J., et al., *Serum exosomal and serum glypican-1 are associated with early recurrence of pancreatic ductal adenocarcinoma.* Frontiers in Oncology, 2022. **12**: p. 992929.
588. Huang, M., et al., *Combining fluorescent cell sorting and single b cell amplification to screen the monoclonal antibody gene against human glypican-1 in pancreatic cancer.* Journal of Oncology, 2021. **2021**.
589. Huang, X., et al., *Glypican-1-antibody-conjugated Gd–Au nanoclusters for FI/MRI dual-modal targeted detection of pancreatic cancer.* International Journal of Nanomedicine, 2018: p. 2585-2599.
590. Li, J., et al., *Highly Sensitive Exosome Detection for Early Diagnosis of Pancreatic Cancer Using Immunoassay Based on Hierarchical Surface‐Enhanced Raman Scattering Substrate.* Small Methods, 2022. **6**(6): p. 2200154.
591. Lee, H.M., et al., *Legacy effect of high glucose on promoting survival of HCT116 colorectal cancer cells by reducing endoplasmic reticulum stress response.* Am J Cancer Res, 2021. **11**(12): p. 6004-6023.
592. Lima, A.R., et al., *Discrimination between the human prostate normal and cancer cell exometabolome by GC-MS.* Scientific Reports, 2018. **8**(1): p. 5539.
593. Quach, N.D., et al., *Paradoxical role of glypican-1 in prostate cancer cell and tumor growth.* Scientific reports, 2019. **9**(1): p. 11478.
594. Li, J., et al., *GPC 1 exosome and its regulatory mi RNA s are specific markers for the detection and target therapy of colorectal cancer.* Journal of cellular and molecular medicine, 2017. **21**(5): p. 838-847.
595. Li, D., et al., *Prostate cancer cells synergistically defend against CD8+ T cells by secreting exosomal PD‐L1.* Cancer Medicine, 2023. **12**(15): p. 16405-16415.
596. Gao, Y., et al., *Cancer-associated fibroblasts promote the upregulation of PD-L1 expression through akt phosphorylation in colorectal cancer.* Frontiers in Oncology, 2021. **11**: p. 748465.
597. Mitchell, P.J., et al., *Can urinary exosomes act as treatment response markers in prostate cancer?* Journal of Translational Medicine, 2009. **7**(1): p. 4.
598. Chen, G., et al., *Exosomal PD-L1 contributes to immunosuppression and is associated with anti-PD-1 response.* Nature, 2018. **560**(7718): p. 382-386.
599. Yin, Y., et al., *Colorectal cancer‐derived small extracellular vesicles promote tumor immune evasion by upregulating PD‐L1 expression in tumor‐associated macrophages.* Advanced Science, 2022. **9**(9): p. 2102620.
600. Logozzi, M., et al., *Increased PSA expression on prostate cancer exosomes in in vitro condition and in cancer patients.* Cancer letters, 2017. **403**: p. 318-329.
601. McKiernan, J., et al., *A prospective adaptive utility trial to validate performance of a novel urine exosome gene expression assay to predict high-grade prostate cancer in patients with*

prostate-specific antigen 2–10 ng/ml at initial biopsy. European urology, 2018. **74**(6): p. 731-738.
602. Pan, J. and M. Ho, *Role of glypican-1 in regulating multiple cellular signaling pathways.* American Journal of Physiology-Cell Physiology, 2021. **321**(5): p. C846-C858.
603. Huang, G., et al., *α3 Chains of type V collagen regulate breast tumour growth via glypican-1.* Nature communications, 2017. **8**(1): p. 14351.
604. Wu, F., et al., *PD-L1 detection on circulating tumor-derived extracellular vesicles (T-EVs) from patients with lung cancer.* Transl Lung Cancer Res, 2021. **10**(6): p. 2441-2451.
605. Yin, Y., et al., *Colorectal Cancer-Derived Small Extracellular Vesicles Promote Tumor Immune Evasion by Upregulating PD-L1 Expression in Tumor-Associated Macrophages.* Advanced Science, 2022. **9**(9): p. 2102620.
606. Oliveira-Rodríguez, M., et al., *Development of a rapid lateral flow immunoassay test for detection of exosomes previously enriched from cell culture medium and body fluids.* J Extracell Vesicles, 2016. **5**: p. 31803.
607. Yu, Q., et al., *Development of a lateral flow aptamer assay strip for facile identification of theranostic exosomes isolated from human lung carcinoma cells.* Anal Biochem, 2020. **594**: p. 113591.
608. Li, J., et al., *The clinical significance of circulating GPC1 positive exosomes and its regulative miRNAs in colon cancer patients.* Oncotarget, 2017. **8**(60): p. 101189-101202.
609. Zhao, J., et al., *Serum exosomal and serum glypican-1 are associated with early recurrence of pancreatic ductal adenocarcinoma.* Frontiers in Oncology, 2022. **12**.
610. Shao, C., et al., *Role of hypoxia-induced exosomes in tumor biology.* Mol Cancer, 2018. **17**(1): p. 120.
611. Wang, J., et al., *Exosomal RNAs: Novel Potential Biomarkers for Diseases-A Review.* Int J Mol Sci, 2022. **23**(5).
612. Zhang, X., et al., *Exosomes in cancer: small particle, big player.* Journal of hematology & oncology, 2015. **8**(1): p. 1-13.
613. Van Niel, G., G. d'Angelo, and G. Raposo, *Shedding light on the cell biology of extracellular vesicles.* Nature reviews Molecular cell biology, 2018. **19**(4): p. 213-228.
614. Jayaseelan, V.P., *Emerging role of exosomes as promising diagnostic tool for cancer.* Cancer Gene Therapy, 2020. **27**(6): p. 395-398.
615. McKiernan, J., et al., *A novel urine exosome gene expression assay to predict high-grade prostate cancer at initial biopsy.* JAMA oncology, 2016. **2**(7): p. 882-889.
616. Wu, K., et al., *Extracellular vesicles as emerging targets in cancer: Recent development from bench to bedside.* Biochimica et Biophysica Acta (BBA)-Reviews on Cancer, 2017. **1868**(2): p. 538-563.
617. Jiang, F. and J.A. Doudna, *CRISPR-Cas9 structures and mechanisms.* Annu Rev Biophys, 2017. **46**(1): p. 505-529.
618. Gong, S., et al., *An in vitro site-specific cleavage assay of CRISPR-Cas9 using a personal glucose meter.* Chemical Communications, 2020. **56**(62): p. 8850-8853.
619. Pickar-Oliver, A. and C.A. Gersbach, *The next generation of CRISPR–Cas technologies and applications.* Nature reviews Molecular cell biology, 2019. **20**(8): p. 490-507.
620. Zhao, X., et al., *Rapid and sensitive exosome detection with CRISPR/Cas12a.* Analytical and bioanalytical chemistry, 2020. **412**(3): p. 601-609.
621. Li, H., et al., *Aptamer-based CRISPR/Cas12a assay for the ultrasensitive detection of extracellular vesicle proteins.* Talanta, 2021. **221**: p. 121670.
622. He, Y., et al., *Applying CRISPR/Cas13 to Construct Exosomal PD-L1 Ultrasensitive Biosensors for Dynamic Monitoring of Tumor Progression in Immunotherapy.* Advanced Therapeutics, 2020. **3**(10): p. 2000093.
623. Blondal, T., et al., *Verification of CRISPR editing and finding transgenic inserts by Xdrop indirect sequence capture followed by short-and long-read sequencing.* Methods, 2021. **191**: p. 68-77.

624. Park, J.S., et al., *Digital CRISPR/Cas‐Assisted assay for rapid and sensitive detection of SARS‐CoV‐2.* Advanced Science, 2021. **8**(5): p. 2003564.
625. Zhang, G., et al., *CRISPR-Cas12a enhanced rolling circle amplification method for ultrasensitive miRNA detection.* Microchemical Journal, 2020. **158**: p. 105239.
626. Wang, R., et al., *Rolling circular amplification (RCA)-Assisted CRISPR/Cas9 cleavage (RACE) for highly specific detection of multiple extracellular vesicle MicroRNAs.* Analytical chemistry, 2019. **92**(2): p. 2176-2185.
627. Bruch, R., et al., *CRISPR/Cas13a-Powered Electrochemical Microfluidic Biosensor for Nucleic Acid Amplification-Free miRNA Diagnostics.* Advanced Materials, 2019. **31**(51): p. 1905311.
628. Sheng, Y., et al., *A CRISPR/Cas13a-powered catalytic electrochemical biosensor for successive and highly sensitive RNA diagnostics.* Biosensors and Bioelectronics, 2021. **178**: p. 113027.
629. Li, H., et al., *Aptamer-based CRISPR/Cas12a assay for the ultrasensitive detection of extracellular vesicle proteins.* Talanta, 2021. **221**: p. 121670.
630. LeCun, Y., Y. Bengio, and G. Hinton, *Deep learning.* nature, 2015. **521**(7553): p. 436-444.
631. Liu, C., et al., *Low-cost thermophoretic profiling of extracellular-vesicle surface proteins for the early detection and classification of cancers.* Nature biomedical engineering, 2019. **3**(3): p. 183-193.
632. Tian, F., et al., *Protein analysis of extracellular vesicles to monitor and predict therapeutic response in metastatic breast cancer.* Nature communications, 2021. **12**(1): p. 1-13.
633. Shin, H., et al., *Early-stage lung cancer diagnosis by deep learning-based spectroscopic analysis of circulating exosomes.* ACS nano, 2020. **14**(5): p. 5435-5444.
634. Liu, C., et al., *Multiplexed analysis of small extracellular vesicle-derived mRNAs by droplet digital PCR and machine learning improves breast cancer diagnosis.* Biosensors and Bioelectronics, 2021. **194**: p. 113615.
635. Zheng, J., et al., *Exploiting machine learning for bestowing intelligence to microfluidics.* Biosensors and Bioelectronics, 2021. **194**: p. 113666.
636. Srikanth, S., et al., *Droplet based microfluidics integrated with machine learning.* Sensors and Actuators A: Physical, 2021. **332**: p. 113096.
637. Galan, E.A., et al., *Intelligent microfluidics: The convergence of machine learning and microfluidics in materials science and biomedicine.* Matter, 2020. **3**(6): p. 1893-1922.
638. Ko, J., et al., *Combining machine learning and nanofluidic technology to diagnose pancreatic cancer using exosomes.* ACS nano, 2017. **11**(11): p. 11182-11193.
639. Liu, C., et al., *λ-DNA-and aptamer-mediated sorting and analysis of extracellular vesicles.* Journal of the American Chemical Society, 2019. **141**(9): p. 3817-3821.
640. Zhang, P., et al., *Molecular and functional extracellular vesicle analysis using nanopatterned microchips monitors tumor progression and metastasis.* Science translational medicine, 2020. **12**(547): p. eaaz2878.